# Slug Flow-Induced Vibration and Vortex-Induced Vibration of Catenary Risers

**Bowen Ma**

A thesis submitted in partial fulfilment of the requirements for the degree of Doctor of Philosophy

School of Engineering

Newcastle University

January 2020

# Abstract

Subsea risers are widely used in the offshore oil and gas industry for deep-water productions where hydrocarbon flows of multiple phases may appear in several flow patterns. Characterized by the alternating liquid- and gas-dominant regions, slug flows are practically problematic due to a fluctuation in flow momenta and pressure potentially causing slug flow-induced vibration (SIV). Compared with a single-phase flow-induced vibration, fundamental understanding of SIV phenomena and the associated effects on the dynamics of catenary risers are still lacking.

Therefore, the present thesis aims to investigate SIV of flexible catenary risers subject to external excitations by the vortex-induced vibration (VIV). The literature of multiphase flows (gas-liquid flow patterns, flow maps) and flow-induced vibrations (SIV, VIV) is reviewed. A mechanistic steady-state slug model is considered to provide the slug flow-induced loads with a two-dimensional continuum riser model. A numerical study for fundamental planar dynamics of an inclined curved flexible riser carrying slug gas-liquid flows is conducted. Results demonstrate several SIV features and effects of slug flow characteristics (slug unit length, translational velocity and fluctuation frequencies) on the riser resonant dynamics. These fundamental observations enable a further study with combined VIV-SIV phenomena.

To incorporate the VIV effect, a phenomenological model based on wake oscillators is used and first implemented for an elastically mounted rigid cylinder in uniform flows subject to cross-flow/in-line VIV. The dynamical system described by coupled nonlinear cylinder-wake oscillators is solved by a numerical-analytical approach. Several important VIV characteristics are captured, highlighting abilities of this semi-empirical model in VIV prediction. By applying the distributed van der Pol wake-oscillators, this low-order model is then extended to the analysis of cross-flow-only VIV of a catenary riser under uniform flows perpendicular to its initial curvature plane. Some experimentally observed VIV features of flexible cylinders are numerically predicted. By comparing VIV-only with VIV-SIV responses, VIV is found to prevail in the combined external-internal excitation cases. Slug flows generally result in a significant multi-mode VIV, which becomes more pronounced at higher external flow velocities: this is attributed to the effect of softening stiffness of the pipe caused by internal slug flow mass and pressure leading to a higher-mode VIV.

To validate the numerical model of SIV, a small-scale flexible pipe conveying gas-liquid flows has been investigated experimentally for a catenary configuration. The experiment is carried out in an air-water test loop with a hanging tube section made of silica gel. Both slug

flow-induced pipe motions and gas-liquid flow patterns are recorded simultaneously using non-intrusive high-speed cameras. Pressure variations are also measured at the pipe inlet and outlet by two pressure transducers. The flow-transporting system is tested by employing different gas-liquid flow rates. Occurrence of slug flows is captured at the relatively high ratios of the gas to liquid superficial velocities rendering a large-amplitude SIV of the flexible pipe. Under different flow conditions, slug flow characteristics are observed to vary significantly in terms of the travelling velocities, lengths and frequencies of different slug units. These entail the unsteady SIV with modulated amplitudes and frequencies. Some qualitative aspects of slug characteristics and SIV responses from numerical predictions are captured in the laboratory tests. Through comparisons of riser vibration responses and frequencies between numerical and experimental results, the prediction abilities of the mathematical model are recognized.

In summary, this thesis has investigated fundamental and potential SIV effects on catenary risers. A significant role of the slug unit length and the slug translational velocity should be considered individually for determining large-amplitude SIV which is of practical importance from a design viewpoint. Possible amplifications of riser responses due to slug flows are remarked in combined VIV-SIV scenarios. This is meaningful for the riser stress, fatigue and failure assessment. Although the present numerical model is limited to steady-state slug flows, it paves a way for a future development of computationally efficient tools benefiting the screening analysis of subsea risers transporting gas-liquid slug flows.

# Acknowledgements

First of all, I would like to express my sincere gratitude to my supervisor Dr Narakorn Srinil for his continuous support, patience, guidance, trust and encouragement throughout my PhD life. His excellence and knowledge in academic calibre as well as enthusiasm and diligence in work are highly admirable. His brilliant supervision directs and motivates me to develop as a researcher. I feel deeply honoured to be his PhD student.

I would like to extend my great appreciation to Prof. Hongjun Zhu at the Southwest Petroleum University for his invaluable support and advice during the experiment work. My thanks also go to my fellow students at the Southwest Petroleum University, especially to Mr Honglei Zhao, Ms Yue Gao and Mr Tao Tang who kindly helped me in preparing and conducting the experiments. The enjoyable time spent in Chengdu is unforgettable.

I would like to thank Dr Hossein Zanganeh, Dr Konstantinos Bakis and Dr Victoria Kurushina for sharing their research experience and knowledge. The discussions with them are always inspiring and shedding lights on my path towards improving my research.

I am grateful to study in the Marine, Offshore and Subsea Technology Group at Newcastle University and to meet all my fellow colleagues and friends, especially Dr Yibo Liang, Dr Weichao Shi, Dr Chang Li, Dr Serena Lim, Dr Xiangyin Meng, Dr Maria Syrigou, Dr Jaime Torres, Mr Xutian Xue, Mr Ankang Cheng, Mr Junyi Wu, Mr Zhizun Xu, Mr Bruno Soares, Mr Inima Tamunodienye and Mr Joshua Abam. Special thanks to my office mate, Mr Pierre-Adrien Opinel, for his endless support as well as the great time during lunches, drinks and tours.

During my time in Newcastle, I have met a lot of friends who truly make my life filled with happiness, especially Mr Tiehan Han, Mr Hugo Huang, Mr Zifei Han, Mr Mike Jiang, Mr Loh Chao, Mr Mingyi Zhai, Ms Chenfeng Hu, Mr Lue Wang, Mr Tony Gong, Ms Xiang Sui, Ms Kate Ouyang. Special thanks to Ms Yuying Xie who always motivates and supports me.

Finally, I would like to express my deepest appreciation to my beloved parents, Xiaoyan Wang and Ruijun Ma, for their unconditional love, understanding, encouragement and support. I love you all with my heart and soul.

# Table of Contents

**Abstract** ..... **i**

**Acknowledgements** ..... **v**

**Table of Contents** ..... **vii**

**List of Figures** ..... **xi**

**List of Tables** ..... **xix**

**Nomenclature** ..... **xxi**

**List of Publications** ..... **xxv**

**Chapter 1. Introduction** ..... **1**

1.1 Background ..... 1

1.2 Aims and Objectives of the Thesis ..... 5

1.3 Outline of the Thesis ..... 6

1.4 Scope of the Thesis ..... 7

**Chapter 2. Literature Review** ..... **9**

2.1 Gas-Liquid Flow Features and Maps ..... 9

2.1.1 Common flow patterns in horizontal and vertical tubes ..... 9

2.1.2 Gas-liquid flow maps for different flow directions ..... 12

2.2 Slug Flow-Induced Vibrations ..... 16

2.2.1 SIV investigation by idealized model ..... 16

2.2.2 SIV investigation by mechanistic model ..... 19

2.2.3 Experimental investigations on SIV ..... 23

2.3 Vortex-Induced Vibrations ..... 24

2.3.1 Experimental studies on VIV of catenary risers ..... 24

2.3.2 Numerical studies on VIV of catenary risers ..... 26

2.4 Summary ..... 28

**Chapter 3. Planar Dynamics of Catenary Riser Carrying Slug Flows ..... 29**

3.1 Mechanical Model of Curved Pipe Conveying Slug Flows ..... 29

3.2 Mechanistic Model of Slug Gas-Liquid Flows ..... 34

3.2.1 Governing equations ..... 34

3.2.2 Slug flow variables and solution steps ..... 36

3.3. Fundamental Pipe Properties and Slug Flow Characteristics ..... 38

3.4. Mechanisms of Curved Flexible Pipe Transporting Slug Flows ..... 47

3.4.1 Slug flow-induced fluctuation frequencies ..... 48

3.4.2 Slug flow-induced transient drifts ..... 51

3.4.3 Slug flow-induced mean displacements ..... 54

3.4.4 Slug flow-induced planar vibrations ..... 57

3.4.5 Slug flow-induced bending and axial stresses ..... 66

3.5. Summary ..... 71

**Chapter 4. Two-Dimensional VIV of Rigid Cylinders ..... 73**

4.1 Nonlinear Fluid-Structure Dynamic Model ..... 73

4.2 Analytical Prediction of VIV Responses ..... 77

4.3 Parametric Investigation and Discussion ..... 81

4.3.1 Model calibration and validation ..... 81

4.3.2 Frequencies, motion trajectories, phases and static drifts ..... 85

4.3.3 Influence of control gain, geometrically nonlinear coupling and mass ratio ..... 89

4.3.4 Comparison of power requirement ..... 92

4.4 Summary ..... 94

**Chapter 5. Catenary Riser Responses Subject to Combined VIV and SIV ..... 97**

5.1 Mechanical Model and Governing Equations ..... 97

5.2 Validation of VIV Model for Flexible Risers ..... 101
5.3 Numerical Results and Discussion ..... 105
5.3.1 Dynamics responses under various current velocities: VIV vs. VIV-SIV ..... 105
5.3.2 Influence of SIV in VIV-SIV at low and high current velocities ..... 111
5.3.3 Stress evaluation: VIV vs. VIV-SIV ..... 117
5.4 Summary ..... 124
**Chapter 6. Experimental Investigation on Slug Flow-Induced Vibration ..... 127**
6.1 Experimental Setup ..... 127
6.2 Data Acquisition ..... 130
6.3 Free Decay Tests ..... 134
6.4 SIV Results and Discussion ..... 136
6.4.1 Riser response amplitudes and frequencies ..... 137
6.4.2 Non-uniform slug flow characteristics ..... 143
6.4.3 SIV responses under various flow conditions ..... 147
6.5 Experimental vs. Numerical Results ..... 159
6.6 Summary ..... 164
**Chapter 7. Conclusions ..... 167**
7.1 Slug Flow-Induced Vibration ..... 167
7.2 Combined Vortex-Induced Vibration and Slug Flow-Induced Vibration ..... 169
7.3 Recommendation for Future Research ..... 169
**References ..... 171**

# List of Figures

**Figure 1.1:** FIV problems in offshore engineering considered in the present research work. ..1

**Figure 1.2:** Schematic of deep-water subsea production system potentially subject to currents and slug flows. ..3

**Figure 1.3:** Illustration of the scope in the present research. ..7

**Figure 2.1:** Illustration of (a) typical subsea oil and gas production systems (source: GENESIS) (b) conveying multiphase gas-liquid flow (source: SINTEF). ..9

**Figure 2.2:** Gas-liquid flow patterns in horizontal pipes adapted from Rouhani and Sohal (1983). ..10

**Figure 2.3 :** Gas-liquid flow patterns in vertical pipes adapted from Rouhani and Sohal (1983). ..11

**Figure 2.4:** Flow pattern maps adapted from Spedding and Nguyen (1980) for (a) horizontal, (b) 45°, (c) 70°, (d) upward vertical, (e) -6.17° and (f) -44.75° flows: SL, DB, S, A, D represent slug, dispersed bubble, stratified, annular and droplet flow. ..14

**Figure 2.5:** Illustration of slug flow shapes from (a) sinusoidal function and (b-d) pulse train function in case of $L_s$=0.5$L_u$, $L_s$=0.25$L_u$ and $L_s$=0.75$L_u$. ..19

**Figure 3.1:** A planar dynamic model of an inclined curved flexible riser conveying slug gas-liquid flows. ..30

**Figure 3.2:** Properties associated with initial static profile of catenary riser: (a) $\tilde{x}$-$\tilde{y}$ coordinates, (b) local inclination angles, (c) pre-tensions, (d) curvatures: blue and red dashed lines denote the results of present study and OrcaFlex (Orcina, 2016). ..39

**Figure 3.3:** Influence of $U_t$ (6, 9, 12, 16, 20 m/s) on (a) $h_f/d$, (b) $R$, (c) $u_L$ and (d) $u_G$ for a slug unit with $L_u/d$ = 80, $u_{ls}$=2 m/s and $\beta$=30°. ..42

**Figure 3.4:** Influence of $L_u/d$ (63, 80, 120, 140, 208) on (a) $h_f/d$, (b) $R$, (c) $u_L$ and (d) $u_G$ for a slug unit with $u_{gs}$=10.3 m/s, $u_{ls}$=2 m/s and $\beta$=30°. ..43

**Figure 3.5:** Influence of $\beta$ (2°, 15°, 30°, 51°) on (a) $h_f/d$, (b) $R$, (c) $u_L$ and (d) $u_G$ for a slug unit with $u_{gs}$=4.5 m/s, $u_{ls}$=2 m/s and $L_u/d$=80. ..45

**Figure 3.6:** Illustration of space-time varying profiles (a) $R$, (b) $u_L$, (c) $u_G$ and (d) $P$ based on $L_u/d$ = 80, $U_t$ =16 m/s. Dashed lines in (d) denote $P_m$. ..49

**Figure 3.7:** Frequency spectra of slug fluctuations based on $L_u/d$= 80 and varying $U_t$. ..50

**Figure 3.8:** Frequency spectra of slug fluctuations based on $U_t$ = 16 m/s and varying $L_u/d$. ..50

**Figure 3.9:** Frequency spectra of slug fluctuations based on $U_t$ = 9 m/s and $L_u/d$ = 80 with varying $\beta$. ..... 51

**Figure 3.10:** Space-time varying (a, c, e) *u/d* and (b, d, f) *v/d* during initial transient slug initiation and subsequent steady state in the case of varying (a, b) $U_t$, (c, d) $L_u/d$ and (e, f) $\beta$. 52

**Figure 3.11:** Space-time varying (a, c, e, g) *u* and (b, d, f, h) *v* inclusive of mean drifts during steady-state SIV for $L_u/d$= 80 at (a, b) $U_t$ = 6 m/s, (c, d) 9 m/s, (e, f) 16 m/s and (g, h) 20 m/s. ..... 55

**Figure 3.12:** Spatial profiles of mean drifts in (a, c, e, g) *X* and (b, d, f, h) *Y* directions in the case of varying (a, b) $U_t$, (c, d) $L_u/d$, (e, f) $\beta$ and (g, h) $f_s$..... 56

**Figure 3.13:** Space-time varying (a, c, e, g) *u* and (b, d, f, h) *v* in mm exclusive of mean drifts during steady-state SIV for $L_u/d$= 80 at (a, b) $U_t$ = 6 m/s, (c, d) 9 m/s, (e, f) 16 m/s, (g, h) 20 m/s. ..... 58

**Figure 3.14:.** Spatial profiles of oscillation frequencies associated with responses in Figure 3.13..... 59

**Figure 3.15:** Space-time varying (a, c, e, g) *u* and (b, d, f, h) *v* in mm exclusive of mean drifts during steady-state SIV for (a, b & e, f) $L_u/d$ = 120, (c, d & g, h) $L_u/d$ = 208 at (a, b & c, d) $U_t$ = 16 m/s and (e, f & g, h) $U_t$ = 6 m/s. ..... 61

**Figure 3.16:** Spatial profiles of oscillation frequencies associated with responses in Figure 3.15..... 62

**Figure 3.17:.** Illustrative spatial modal profiles in (a, c) *X* and (b, d) *Y* directions for $L_u/d$ = 120 at $U_t$ = 6 m/s dominated by lower (a, b) and higher (c, d) modes. ..... 63

**Figure 3.18:** Phase plane trajectories associated with spatially maximum (a, c, e, g) $u_{rms}$ and (b, d, f, h) $v_{rms}$ for (a, b) $L_u/d$ = 80 and $U_t$ = 6 m/s; (c, d) $L_u/d$ = 80 and $U_t$ = 16 m/s; (e, f) $L_u/d$ = 208 and $U_t$ = 16 m/s, (g, h) $L_u/d$= 120 and $U_t$ = 6 m/s. ..... 64

**Figure 3.19:** Variations of spatially maximum (a, c, e) $u_{rms}$ and (b, d, f) $v_{rms}$ in the case of (a, b) varying $U_t$ for $L_u/d$ = 80, (c, d) varying $L_u/d$ for $U_t$ = 6 m/s and (e, f) varying $L_u/d$ for $U_t$ = 16 m/s. ..... 65

**Figure 3.20:** Space-time varying (a, c, e, g) $\sigma_u$ and (b, d, f, h) $\sigma_v$ inclusive of mean components: a, b (c, d) for $L_u/d$ = 80 (120) at $U_t$ = 6 m/s; e, f (g, h) for $L_u/d$ = 80 (208) at $U_t$ = 16 m/s. ..... 67

**Figure 3.21:** Space-time varying $\sigma_a$ (a, c, e, g) with and (b, d, f, h) exclusive of mean components: a, b (c, d) for $L_u/d$ = 80 (120) at $U_t$ = 6 m/s; e, f (g, h) for $L_u/d$ = 80 (208) at $U_t$ = 16 m/s. ..... 68

**Figure 3.22:** Space-time varying $\sigma_t$ in (a, c) $X$ and (b, d) $Y$ directions for (a, b) $L_u/d$ = 80 and $U_t$ = 6 m/s and (c, d) $L_u/d$ = 208 at $U_t$ = 16 m/s. ..... 69

**Figure 4.1:** (a) An active velocity feedback control model of an elastically mounted circular cylinder undergoing 2D VIV; (b) a block diagram of active control strategy. ..... 75

**Figure 4.2:** Comparisons of response amplitudes in the absence of control with numerical (triangles), analytical (circles) and experimental (squares) results for cylinder with $m^*$ = 2.6 and $\xi$ = 0.00361. ..... 82

**Figure 4.3:** Comparisons of non-controlled and controlled amplitudes for cylinder with $m^*$ = 2.6 and $\xi$ = 0.00361: lines with circles (crosses) and triangles (stars) denote numerical (analytical) results ..... 83

**Figure 4.4:** Comparison of oscillation frequency ratios (a, b) and resonant frequencies (c, d) for cylinder with $m^*$ = 2.6, $\xi$ = 0.00361 and $\beta_K = \gamma_G$ = 0.5: lines (symbols) denote controlled (non-controlled) results. Higher $x$ and lower $y$ frequencies are shown in (a, b) with Strouhal rule (dotted lines). ..... 84

**Figure 4.5:** Phase plane portraits for cylinder with $m^*$ = 2.6, $\xi$ = 0.00361, $\beta_K = \gamma_G$ = 0.5 and $V_r$ = 7: a dot represents the moment of control activation. ..... 86

**Figure 4.6:** Two-dimensional $\tilde{X}$-$\tilde{Y}$ motion trajectories at $V_r$ = 7 (a, b) and $V_r$ = 4 (c, d) for cylinder with $m^*$ = 2.6, $\xi$ = 0.00361 and $\beta_K = \gamma_G$ = 0.5: a dot represents the moment of control activation. ..... 87

**Figure 4.7:** Comparisons of phase relationships (a-d) and mean drift effect (e, f) for cylinder with $m^*$ = 2.6, $\xi$ = 0.00361 and $\beta_K = \gamma_G$ = 0.5: lines (circles) denote non-controlled (controlled) results; squares denote experimental free-vibration data ..... 88

**Figure 4.8:** Influence of control gain on response amplitudes (a-d) and maximum amplitude reduction percentage $R_m$ (e, f) for cylinder with $m^*$ = 1.2, $\xi$ = 0.00361, $\beta_K$ and $\gamma_G$ being increased from 0 to 0.1, 0.2, 0.3, 0.4 and 0.8, respectively. ..... 90

**Figure 4.9:** Influence of geometrically nonlinear coefficient ($\alpha_y$) on controlled amplitudes for cylinder with $m^*$ = 1.2, $\xi$ = 0.00361 and $\beta_K = \gamma_G$ = 0.1. ..... 91

**Figure 4.10:** Influence of $m^*$ on controlled amplitudes for cylinder with $\xi$ = 0.00361 and $\beta_K = \gamma_G$ =0.1. ..... 92

**Figure 4.11:** Comparisons of response amplitudes at ideal perfect lock-in condition with varying $m^*$ for cylinder with $\xi$ = 0.00361, $\beta_K$ and $\gamma_G$ being increased from 0 to 0.25, 0.5, respectively. ..... 93

**Figure 4.12:** Comparisons of averaged power requirement with the targeted reduced amplitudes with LC (dots) vs NC (lines): (a) $m^*$ = 2.6 and $\xi$ = 0.00361, (b) $m^*$ = 6.9 and $\xi$ = 0.00361, (c) $m^*$ = 1 and $\xi$ = 0; (d) showing the zoomed results in (c). ..... 94

**Figure 5.1:** (a) A planar dynamic model of an inclined curved flexible riser conveying slug gas-liquid flows and undergoing VIV with (b) illustration of hydrodynamic forces for a cross section. ..... 98

**Figure 5.2:** Comparison of numerical (blue squares) and experimental (red circles) results of (a, c, e) maximum and (b, d, f) RMS amplitudes at varying $U_o$ in case of (a, b) $T$ = 600 N, (c, d) 700 N and (e, f) 800 N. ..... 102

**Figure 5.3:** (a, c, e) Modal distribution and (b, d, f) comparison of numerical (blue squares) and experimental (red circles) results of dominant modes at varying $U_o$ in case of (a, b) $T$ = 600 N, (c, d) 700 N and (e, f) 800 N. ..... 104

**Figure 5.4:** Comparison of numerical and experimental results with dominant frequency at varying $U_o$ in case of (a) $T$ = 600 N, (b) 700 N and (c) 800 N: black line represents the Strouhal rule. ..... 105

**Figure 5.5:** Comparison of (a, b) maximum and (c, d,) RMS amplitudes of (a, c) $u$ and (b, d) $v$ at varying $U_o$ in case of VIV-only (blue squares), VIV-SIV for $L_u/d$=80, $U_t$ = 6 m/s (red triangles) and VIV-SIV for $L_u/d$=80, $U_t$ = 16 m/s (black circles). ..... 106

**Figure 5.6:** Illustration of normalized riser mode shapes for mode (a) 5, (b) 10, (c) 15, (d) 20, (e) 25, (f) 30: solid (dashed) lines denote the shapes in $X$ ($Y$), respectively. ..... 107

**Figure 5.7:** Modal distribution in (a, c, e) $u$ and (b, d, f) $v$ at varying $U_o$ in case of (a, b) VIV-only, (c, d) VIV-SIV for $L_u/d$=80, $U_t$ = 6 m/s and (e, f) VIV-SIV for $L_u/d$=80, $U_t$ = 16 m/s: red and blue markers represent dominant and secondary modes, respectively..... 109

**Figure 5.8:** Comparison of dominant $f_o$ for (a) $u$ and (b) $v$ at varying $U_o$ in case of VIV-only (blue squares), VIV-SIV for $L_u/d$=80, $U_t$ = 6 m/s (red triangles) and VIV-SIV for $L_u/d$=80, $U_t$ = 16 m/s (black circles): black line represents the Strouhal rule. ..... 110

**Figure 5.9:** Space-time varying (a, c, e) $u$ and (b, d, f) $v$ exclusive of mean at $U_o$ = 0.2 m/s, for (a, b) VIV-only, (c, d) VIV-SIV: $L_u/d$ = 80 at $U_t$ = 6 m/s and (e, f) VIV-SIV: $L_u/d$ = 80 at $U_t$ = 16 m/s. ..... 111

**Figure 5.10:** Spatial profiles of oscillation frequencies associated with responses in Figure 5.8. ..... 112

**Figure 5.11:** Space-time varying (a, c, e) $u$ and (b, d, f) $v$ exclusive of mean at $U_o$ = 0.5 m/s for (a, b) VIV-only, (c, d) VIV-SIV: $L_u/d$ = 80 at $U_t$ = 6 m/s and (e, f) VIV-SIV: $L_u/d$ = 80 at $U_t$ = 16 m/s. ..... 113

**Figure 5.12:** Spatial profiles of oscillation frequencies associated with responses in Figure 5.10. ..... 114

**Figure 5.13:** Spatial distribution of (a, c) $u_{rms}$ and (b, d) $v_{rms}$ in case of (a, b) $U_o$ = 0.2 m/s and (c, d) $U_o$ = 0.5 m/s. ..... 115

**Figure 5.14:** Space-time varying (a, c, e) $\sigma_u$ and (b, d, f) $\sigma_v$ exclusive of mean components at $U_o$ = 0.2 m/s for (a, b) VIV-only, (c, d) VIV-SIV: $L_u/d$ = 80 at $U_t$ = 6 m/s and (e, f) VIV-SIV: $L_u/d$ = 80 at $U_t$ = 16 m/s. ..... 118

**Figure 5.15:** Space-time varying (a, c, e) $\sigma_u$ and (b, d, f) $\sigma_v$ exclusive of mean components at $U_o$ = 0.5 m/s, for (a, b) VIV-only, (c, d) VIV-SIV: $L_u/d$ = 80 at $U_t$ = 6 m/s and (e, f) VIV-SIV: $L_u/d$ = 80 at $U_t$ = 16 m/s. ..... 119

**Figure 5.16:** Spatial distribution of (a, c) $\sigma_{u.rms}$ and (b, d) $\sigma_{v.rms}$ in case of (a, b) $U_o$ = 0.2 m/s and (c, d) $U_o$ = 0.5 m/s. ..... 120

**Figure 5.17:** Space-time varying $\sigma_a$ exclusive of mean components at (a, c, e) $U_o$ = 0.2 and (b, d, f) 0.5 m/s, for (a, b) VIV-only, (c, d) VIV-SIV: $L_u/d$ = 80 at $U_t$ = 6 m/s and (e, f) VIV-SIV: $L_u/d$ = 80 at $U_t$ = 16 m/s. ..... 121

**Figure 5.18:** Spatial distribution of $\sigma_{a.rms}$ in case of (a) $U_o$ = 0.2 m/s and (b) $U_o$ = 0.5 m/s... 122

**Figure 5.19:** Space-time varying $\sigma_t$ at (a, c, e) $U_o$ = 0.2 and (b, d, f) 0.5 m/s, for (a, b) VIV-only, (c, d) VIV-SIV: $L_u/d$ = 80 at $U_t$ = 6 m/s and (e, f) VIV-SIV: $L_u/d$ = 80 at $U_t$ = 16 m/s. 123

**Figure 6.1:** A schematic plot of SIV test loop. ..... 128

**Figure 6.2:** In-plane view of the riser segment. ..... 128

**Figure 6.3:** Key devices along flowlines: (a) air compressor, (b) float flowmeter, (c) water pump, (d) electromagnetic flowmeter, (e) air-water mixing point, (f) pressure transducers. 130

**Figure 6.4:** (a) High-speed cameras, (b) record view in front of the riser segment and (c) operation panel for data acquisition. ..... 131

**Figure 6.5:** Software interface for (a) cameras and (b) pressure transducers, respectively... 132

**Figure 6.6:** Illustrative plot of makers and image post-processing process by comparing different frames. ..... 133

**Figure 6.7:** Time histories and frequency spectra of free decay tests for (a-c) air-filled and (d-f) water-filled riser in ($u$, $v$) in-plane and ($z$) out-of-plane directions. ..... 135

**Figure 6.8:** Time histories of riser responses for (a) $u$ and (b) $v$ before and after low-pass filtering (case 10). ..... 137

**Figure 6.9:** Time-varying spatial profiles (solid lines) with associated spatial RMS displacements (dashed lines) in (a) $X$ and (b) $Y$ for case 10. ..... 138

**Figure 6.10:** Time histories of (a, c, e, g, i, k, m) $u$ and (b, d, f, h, j, l, n) $v$ at different locations of riser for case 10. ..... 139

**Figure 6.11:** Frequency spectra associated with the responses in Figure 6.10. ..... 140

**Figure 6.12:** Phase plane trajectories associated with the responses of M14, M24, M30 and M33 in Figure 6.10..... 142

**Figure 6.13:** Illustration of $U_t$ measurement by a slug travelling path in five consecutive frames (a-e) for ($t_1$-$t_5$) in case 10..... 144

**Figure 6.14:** (a) Selected responses (30 s < $t$ < 42 s) for case 10 and their associated (b-d) flow information at three time instants (A-A: $t$ = 34 s, B-B: $t$ =37.5 s, C-C: $t$ =40.3 s): red arrows highlight slug units in the frames with estimated $L_u$, $L_f$, $L_s$..... 145

**Figure 6.15:** (a) Selected responses (55 s < $t$ < 70 s) for case 10 and their associated (b-d) flow information at three time instants (D-D: $t$= 56.4 s, E-E: $t$=61.6 s, F-F: $t$=65.5 s): red arrows highlight slug units in the frames with estimated $L_u$, $L_f$, $L_s$..... 146

**Figure 6.16:** Space-time varying (a, b, c, d) $u$ and (e, f, g, h) $v$ of SIV for (a, e) case 7, (b, f) case 8, (c, g) case 9, (d, h) case 10. ..... 148

**Figure 6.17:** Spatial profiles of oscillation frequencies associated with responses in Figure 6.16..... 149

**Figure 6.18:** Representative flow information for (a) case 7, (b) case 8, (c) case 9 and (d) case 10: red arrows highlight slug units in the frames with estimated $L_u$, $L_f$, $L_s$..... 151

**Figure 6.19:** Response time histories of (a, c, e, g) $u$ and (b, d, f, h) $v$ associated with spatially maximum RMS displacements for (a, b) case 7, (c, d) case 8, (e, f) case 9 and (g, h) case 10. ..... 152

**Figure 6.20:** Wavelet contour plots associated with response time histories in Figure 6.19. 153

**Figure 6.21:** Spatial distribution of RMS responses for (a, b) case 3-5 in Set 1, (b, d) case 7-10 in Set 2 and (e, f) case 12-15 in Set 3. ..... 155

**Figure 6.22:** $P_{std}$ of (a) riser top and (b) bottom and (c) $dP$ associated for Set 1-3 at $R_{GL}$ = 3-5. ..... 158

**Figure 6.23:** Comparison between (a, b) simulation and (c, d) experimental results (C5) via space-time varying responses and time-history displacements in (a, c, e) *X* and (b, d, f) *Y*: blue solid and red dashed lines denote results from model and experiment, respectively. ..... 160

**Figure 6.24:** Comparison between (a, b) simulation and (c, d) experimental results (C10) via space-time varying responses and time-history displacements in (a, c, e) *X* and (b, d, f) *Y*: blue solid and red dashed lines denote results from model and experiment, respectively. ..... 161

**Figure 6.25:** Comparison between (a, b) simulation and (c, d) experimental results (C15) via space-time varying responses and time-history displacements in (a, c, e) *X* and (b, d, f) *Y*: blue solid and red dashed lines denote results from model and experiment, respectively. ..... 162

**Figure 6.26:** Comparison of (a, c, e) $u_{rms}$ and (b, d, f) $v_{rms}$: red line and circles denote numerical and experimental results, respectively. ..... 163

# List of Tables

**Table 2.1:** Summary of experimental and theoretical studies characterizing gas-liquid flow regimes. ..... 15

**Table 2.2:** Review of some relevant studies on SIV modelling and analysis with key observations. ..... 22

**Table 2.3:** Summary of experimental and numerical studies of flexible catenary risers subject to VIV. ..... 27

**Table 3.1:** Validation of the present model and numerical simulations through comparison of natural frequencies of production riser with previously published results. ..... 33

**Table 3.2:** Specified slug flow parameters for SIV case studies with $u_{ls}$ = 2 m/s. ..... 41

**Table 3.3:** Slug flow profile properties in cases of varying (a) $U_t$, (b) $L_w/d$ and (c) $\beta$. ..... 41

**Table 3.4:** Pressure drop components, bottom pressure and resulting pre-tension variations in cases of varying (a) $U_t$, (b) $L_w/d$ and (c) $\beta$. ..... 44

**Table 3.5:** Maximum amplified mean drifts during transient and steady states in cases of varying (a) $U_t$, (b) $L_w/d$ and (c) $\beta$. ..... 53

**Table 3.6:** Modified mean tensions associated with pipe equilibrium reconfigurations during steady SIV ..... 57

**Table 3.7:** Maximum/minimum bending, axial and total stresses in MPa corresponding to (a) Figure 3.20, (b) Figure 3.21 and (c) Figure 3.22, respectively. ..... 70

**Table 5.1:** Summary of main outputs in SIV vs. VIV-SIV responses for $U_o$=0.2 m/s and $U_o$=0.5 m/s. ..... 124

**Table 6.1:** Key parameters of the riser segment. ..... 129

**Table 6.2:** Natural frequencies and damping ratios of the riser. ..... 136

**Table 6.3:** Test cases with observed FIV and flow patterns. ..... 136

**Table 6.4:** Summary of key flow characteristics and maxima of riser RMS responses. ..... 156

**Table 6.5:** Comparison of key experimental setups and SIV aspects between different studies. ..... 159

# Nomenclature

## Abbreviations

| | |
|---|---|
| 1D | one-dimensional |
| 2D | two-dimensional |
| CF | cross-flow |
| CFD | computational fluid dynamics |
| DOF | degree of freedom |
| FIV | flow-induced vibration |
| IL | in-line |
| RMS | root-mean-squared |
| SIV | slug flow-induced vibration |
| VIV | vortex-induced vibration |

## Roman symbols

| | |
|---|---|
| $A_o$ ($A$) | riser outer (inner) area |
| $a_1$-$a_{10}$ | analytical solution coefficients |
| $A_f$ ($A_g$) | cross-sectional liquid film (gas) area |
| $A_r$ | riser cross-sectional area |
| $A_x$, $A_y$, $A_n$ | cylinder response amplitude |
| $B$, $C$, $C_{fg}$, $n_o$, $j_o$ | empirical coefficients for slug flow model |
| $c$ ,$c_f$, $c_s$ | damping coefficient |
| $C_a$ | added mass coefficient |
| $\bar{C}_D$, $C_D$, $C_L$ | mean drag, fluctuating drag, fluctuating lift force coefficients |
| $C_{D0}$ ($C_{L0}$) | drag (lift) coefficient of stationary cylinder |
| $D$ ($d$) | cylinder outer (inner) diameter |
| $D_{hf}$ ($D_{hg}$) | liquid (gas) hydraulic diameter |
| $dP$ | pressure drop |
| $dP_f$ | film pressure drop |
| $dP_g$ | gravitational pressure drop |
| $dP_s$ | liquid slug pressure drop |
| $dP_u$ | slug unit pressure drop |
| $D_t$ | mean drift effect caused by geometric nonlinear coupling |
| $E$ | Young's modulus of elasticity |
| $F_{yc}^*$ | dimensional control force |
| $F_b$, $F_n$ | hydrodynamic forces in bi-normal and normal directions |
| $f_f$ | liquid-wall frictional factor |
| $f_g$ | gas-wall frictional factor |
| $f_i$ | interfacial frictional factor |
| $F_L$ ($F_D$) | hydrodynamic lift (drag) force |
| $f_n$ | natural frequency in air/water |
| $f_{n1}$ | fundamental frequency |

| | |
|---|---|
| $f_o$ | oscillation frequency |
| $f_s$ | slug characteristic frequency |
| $F_X$ ($F_Y$) | horizontal (vertical) lift force component |
| $F_x^*$, $F_y^*$ | dimensional fluid force |
| $F_{yc}$ | dimensionless control force |
| $g$ | gravitational acceleration |
| $G$ | dimensional nonlinear gain |
| $G_l$ ($G_g$) | liquid (gas) mass flow rate |
| $h_c$ | critical film height |
| $h_f$ | film height along a slug unit |
| $h_s$ | initial film height |
| $i$ | phase index |
| $I$ | moment of area |
| $j$,$J$ | spatial node |
| $k$ | pressure fluctuation factor |
| $k_s$ | slug wave number in idealized slug flow model |
| $K$ | cylinder stiffness |
| $L$ | riser length |
| $L_f$ | film length |
| $L_s$ | liquid slug length |
| $L_u$ | slug unit length |
| $m^*$ | mass ratio |
| $m_a$ | fluid added mass per unit length |
| $m_i$ | phase mass per unit length |
| $m_s$ | structure mass per unit length |
| $m_t$ | total mass per unit length |
| $n$, $N$ | mode order |
| $N_s$ | slug number |
| $P$ | internal fluid pressure |
| $P_b$ | internal fluid mean pressure at riser bottom |
| $P_{\text{drop}}$ | pressure drop from riser bottom to top |
| $P_m$ | internal fluid mean pressure |
| $P_o$ | external hydrostatic pressure |
| $P_{std}$ | standard deviation of fluid pressure |
| $P_t$ | internal fluid mean pressure at riser outlet |
| $P_w$ | dimensionless average power |
| $Q$ | dimensional linear gain |
| $q$, $q_x$ $q_y$ $q_n$ ,$q_0$ | wake variables |
| $Q_l$ ($Q_g$) | liquid (gas) volumetric flow rate |
| $q_M$, $x_M$, $y_M$ | dimensionless amplitude at ideal lock-in frequency ($\delta$=$\omega$=1) |
| $R$ | cross-sectional holdup |
| $\tilde{R}$ | normalized holdup |
| Re | Reynolds number |
| $R_f$ | film holdup |

| | |
|---|---|
| $R_{GL}$ | ratio of gas to liquid superficial velocities |
| $R_m$ | maximum amplitude reduction percentage |
| $R_s$ | liquid slug holdup |
| $s$ | arc-length coordinate |
| $S_f$ | liquid wetted perimeter |
| $S_g$ | gas wetted perimeter |
| $S_i$ | liquid-gas wetted perimeter |
| St | Strouhal number |
| $s_t$, $s_n$, $s_b$ | local tangential, normal, bi-normal directions |
| $T$ | wall tension |
| $t$ | dimensional time |
| $T_b$ | bottom tension |
| $T_{drop}$ | tension drop from riser top to bottom |
| $T_m$ | mean tension |
| $u$ ($v$) | horizontal (vertical) displacement |
| $U_0$ | bubble stagnant drift velocity |
| $U_\infty$ | bubble rising velocity |
| $U_d$ | bubble drift velocity |
| $U_f$ ($U_g$) | liquid (gas) velocity in film zone |
| $U_i$ | internal fluid velocity |
| $U_l$ ($U_b$) | liquid (small bubble) velocity in liquid slug |
| $u_L$ ($u_G$) | liquid (gas) local velocity |
| $u_{ls}$ ($u_{gs}$) | liquid (gas) superficial velocity |
| $u_{max}$ ($v_{max}$) | maximum horizontal (vertical) displacement |
| $U_o$ | uniform flow velocity |
| $U_{rel}$ | relative velocity |
| $u_{rms}$ ($v_{rms}$) | root-mean-squared horizontal (vertical) displacement |
| $U_s$ ($U_t$) | mixture (translational) velocity |
| $\tilde{v}$ | response vector |
| $V_g$ ($V_f$) | relative gas (liquid film) velocity |
| $V_r$ | reduced flow velocity |
| $w$ | normal displacement |
| We | Weber number |
| $W_n$ | modal weight |
| $X$ ($\tilde{x}$) | horizontal axis (coordinate) |
| $\tilde{X}$ ($x$) | dimensional (dimensionless) in-line displacement |
| $x_0$, $y_0$ | dimensionless amplitudes |
| $Y$ ($\tilde{y}$) | vertical axis (coordinate) |
| $\tilde{Y}$ ($y$) | dimensional (dimensionless) cross-flow displacement |
| $Y_i$ | span-wise coordinate |
| $Z$ ($z$) | perpendicular axis (coordinate) to x-y |
| $z_s$ | slug unit coordinate |

## Greek symbols

| | |
|---|---|
| $\alpha$ | dynamic angle |
| $\alpha^*_x\ \beta^*_x\ \alpha^*_y\ \beta^*_y$ | geometrically nonlinear coefficients in dimensional form |
| $\alpha_f$ | film zone void fraction |
| $\alpha_s$ | liquid slug void fraction |
| $\alpha_u$ | average void fraction |
| $\alpha_{\text{vol}}$ | volumetric void fraction |
| $\alpha_x\ \beta_x\ \alpha_y\ \beta_y$ | geometrically nonlinear coefficients in dimensionless form |
| $\alpha_{xq},\ \alpha_{yq}$ | hydrodynamic force coefficients |
| $\beta$ | riser local inclination angle |
| $\beta_K$ | dimensionless linear control gain |
| $\gamma$ | stall parameter |
| $\gamma_{\text{G}}$ | dimensionless nonlinear control gain |
| $\delta$ | cylinder-to-vortex shedding frequency ratio |
| $\varepsilon_x,\ \Lambda_{\text{x}},\ \varepsilon_y,\ \Lambda_{\text{y}},\ \lambda$ | wake oscillator empirical coefficients |
| $\Theta,\ \Phi_{\text{n}}$ | mode shape matrix and vector |
| $\theta_{\text{s}}$ | arbitrary phase in idealized slug flow model |
| $\theta_{xy}\ ,\ \theta_{qy}$ | relative phase angles |
| $\kappa$ | riser static curvature |
| $\mu$ | dimensionless mass parameter |
| $\nu$ | Poisson's ratio |
| $\nu_l\ (\nu_g)$ | liquid (gas) kinematic viscosity |
| $\xi$ | structural damping ratio |
| $\rho_l\ (\rho_g)$ | liquid (gas) density |
| $\rho_o$ | external fluid density |
| $\rho_u$ | slug unit density |
| $\sigma$ | interfacial surface tension |
| $\sigma_a$ | axial stress |
| $\sigma_{a.\text{rms}},\ \sigma_{u.\text{rms}}\ \sigma_{v.\text{rms}}$ | root-mean-squared stress components |
| $\sigma_t$ | total stress |
| $\sigma_u,\ \sigma_v$ | bending stresses |
| $\tau\ ,\ T$ | dimensionless time |
| $\tau_f$ | liquid-wall friction forces |
| $\tau_g$ | gas-wall friction forces |
| $\tau_i$ | interfacial friction forces |
| $\phi$ | liquid film geometric angle |
| $\phi_{n,}\ \phi_{u,}\ \phi_v$ | modal shape vector |
| $X_{tt}$ | Lockhart-Martinelli parameter |
| $\psi,\ \psi_m,\ \psi_s,\ \psi_{Ns}$ | slug function in idealized slug flow model |
| $\omega$ | dimensionless oscillation frequency in analytical solution |
| $\omega_n$ | angular natural frequency |
| $\omega_{st}$ | vortex-shedding angular frequency |

# List of Publications

## Journal papers

**Ma B**, Srinil N. Two-dimensional vortex-induced vibration suppression through the cylinder transverse linear/nonlinear velocity feedback. *Acta Mechanica* 2017, **228**(12), 4369-4389.

**Ma B**, Srinil N. Planar dynamics of inclined curved flexible riser carrying slug liquid-gas flows. *Submitted.*

**Ma B**, Srinil N, Zhu H. Experimental investigation on large-amplitude vibration of flexible catenary pipe conveying intermittent slug liquid-gas flows. *Under preparation.*

**Ma B**, Srinil N. Dynamic modelling and analysis of extensible/bendable catenary risers subject to combined slug flow-induced vibration and vortex-induced vibration. *Under preparation.*

Srinil N, **Ma B**, Zhang L. Experimental investigation on in-plane/out-of-plane vortex-induced vibrations of curved cylinder in parallel and perpendicular flows. *Journal of Sound and Vibration* 2018, **421**, 275-299.

## Conference papers

**Ma B**, Srinil N. Suppression of two-dimensional vortex-induced vibration with active velocity feedback controller. *In: The 13th International Conference on Motion & Vibration Control and 12th International Conference on Recent Advances in Structural Dynamics*. 2016, Southampton.

Srinil N, **Ma B**, Zhang L. Vortex-induced vibration of J-shaped cylinder by towing experiments. *In: 11th International Conference on Flow-Induced Vibration*. 2016, The Hague, Netherlands.

**Ma B**, Srinil N. Dynamic characteristics of deep-water risers carrying multiphase flows, *In: ASME 2018 37th International Conference on Ocean, Offshore & Arctic Engineering (OMAE2018)*. 2018, Madrid.

**Ma B**, Srinil N, Zhu H. Experiment on the effect of superficial gas-liquid velocities on slug FIV in an inclined sagged riser, *ASME 2020 39th International Conference on Ocean, Offshore & Arctic Engineering (OMAE2020)*. *Under preparation.*

# Chapter 1. Introduction

## 1.1 Background

With the rising energy demand for modern society, oil and gas development is playing an important role in supplying fossil fuels. Offshore sources from shallow water, deep water and ultra-deep water are responsible for around one third in the total shares (Maribus, 2014). However, as many shallow-water source fields become exhausted, the industry has moved into new areas with greater water depths to exploit hydrocarbon reservoirs. The ventures into harsher and remoter deep-water regions result in challenges in subsea design and operation, especially for those facilities which may experience severe environmental conditions. Deep-water riser and pipelines are the key subsea production systems in the offshore oil and gas industry for conveying the hydrocarbon flows from the seabed wells to the ocean surface platforms. Since these structures are inherently long, flexible and extensible, they tend to undergo large flow-induced motions and vibrations due to the environmental loads such as waves, currents as well as some internal effects from the conveyed product flows. These inevitable factors can lead to serious flow-induced vibration (FIV) phenomena concerning the integrity and reliability of subsea systems. The related fatigue failures can be catastrophic, causing personnel safety issues, environmental degradation and costly production downtime.

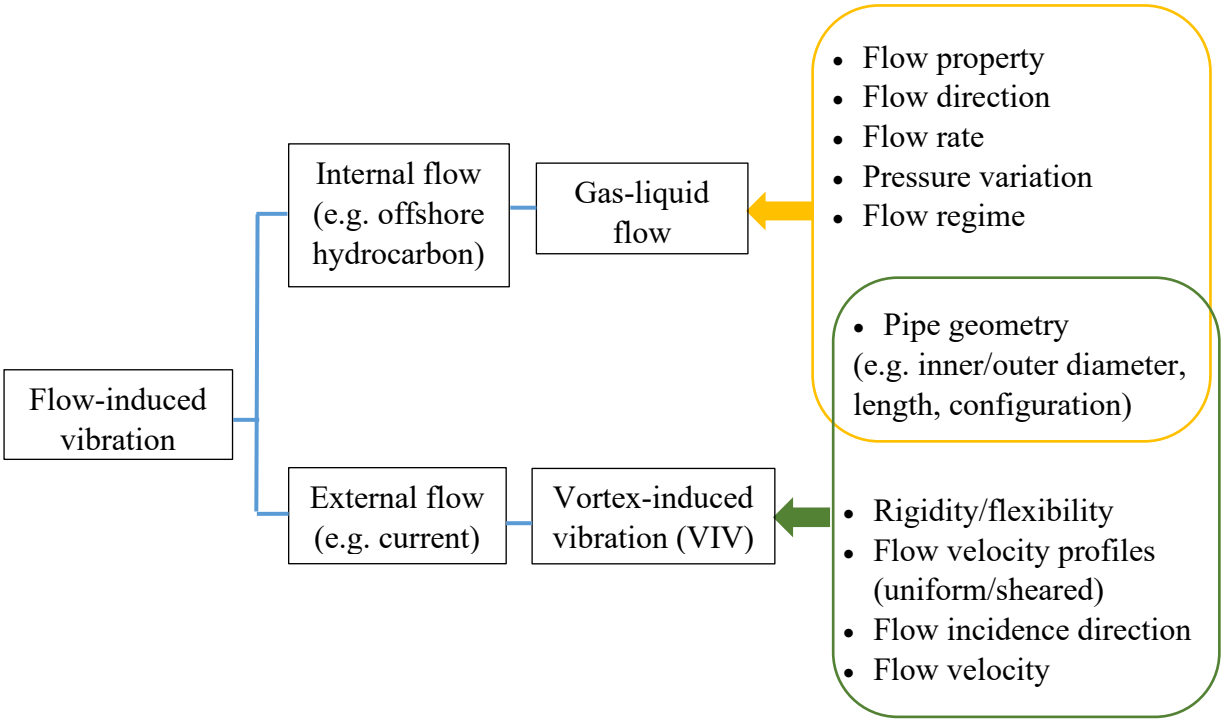


**Figure 1.1:** FIV problems in offshore engineering considered in the present research work.

FIV may take place in various branches of offshore and subsea engineering such as platforms, mooring lines, subsea risers, pipelines, umbilicals and jumpers. Such a flow-related vibration mechanism was pioneered by Blevins in 1977, describing the dynamic behaviours due to the interaction between fluid and structure. The fluid and solid bodies are interrelated through the fluid forces, which in turn may be altered and affected by the reaction forces from the moving or deformed structure (Blevins, 1990). Based on different types of flows, FIV mechanisms can be dramatically different and generally classified into single-phase and multiphase flow-induced vibrations (Blevins, 1990; Kaneko et al., 2013). The single-phase flow can further be categorized into steady and unsteady flows, in which the fluid-structure interaction and turbulence forces play dominant roles. On the other hand, as a flowing mixture of different fluids, a multiphase flow may excite structural vibrations by its time-varying characteristics in flow momentum and pressure. As for offshore oil and gas development, the sources of structural excitations may come from the internal and external flows. Further, the combined effects can lead to more complex and challenging FIV situations. Figure 1.1 illustrates the FIV problems concerned in the present study with some key physical parameters, which play significant roles in determining fluid loads and resultant flow-induced structural dynamics.

Subsea risers may be subject to internal FIV due to the transported hydrocarbons. The product flows from the subsea well are typically multiphase flows, which are highly complicated in nature with features of time-space randomness and variability. Depending on the composition of the petroleum reservoir, such multiphase flows may consist of two leading gas and liquid (oil and/or water) phases which are known as the two-fluid, gas-liquid flows. Even without considering the dynamics of piping systems, gas-liquid flows are recognised as a complex phenomenon as it may appear in diverse geometrical configurations of phase interfaces, referred to as flow patterns, based on several flow-pipe parameters such as the pipe orientations, diameters, flow directions, physical fluid properties and operating conditions (Yadigaroglu and Hewitt, 2017). Pertaining to gas-liquid flows, some major flow patterns for a tube can be classified into separated (e.g. stratified flow), dispersed (e.g. bubble flow) and intermittent flows (e.g. slug flow). More detailed information regarding the flow characteristics in various flow regimes will be presented in the following chapter.

Among different flow regimes, the slug flow is one of the most common and undesirable gas-liquid two-phase flows due to its unsteadiness, intermittency and high pressure drop by nature. In the contest of oil and gas production systems in deep water as illustrated in Figure 1.2, the slug flow may occur in subsea jumpers, pipelines and risers and it can be induced by various factors such as hydrodynamic instabilities, pipe geometry and operational conditions.

Generally, the slug flow can be classified into hydrodynamic slugs, terrain-induced slugs and operation-induced slugs as described below:

- Hydrodynamic slugs

This type of slugging is caused by the instability of interfacial waves between the liquid and gas phases. Under certain flow conditions, a liquid slug is formed when the amplitude of the liquid wave grows and becomes large enough to bridge the whole pipe cross-section.

- Terrain-induced slugs

Terrain-induced slugs are initiated by the liquid accumulation at the lowest point of the pipeline, resulting in a growing liquid slug in the pipeline-riser system. It is then pushed out of the riser as the upstream gas pressure becomes larger than the hydrostatic head and expands. Such slug formation, growth, blowout and liquid fall-back process can be cyclic, leading to severe pressure variations and flow surges.

- Operation-induced slugs

Such type of slug flow is caused by transient operations such as a start-up process, where slugs are formed due to a transient liquid accumulation from a steady state. Also, other operations like pigging and change of flow rates may result in slugging problems. The former pushes the liquid inventory ahead out of the pipeline as liquid slugs, whereas the latter may lead to the development of slug flows from a steady flow pattern, e.g. stratified flow, when the gas flow rate is increased.

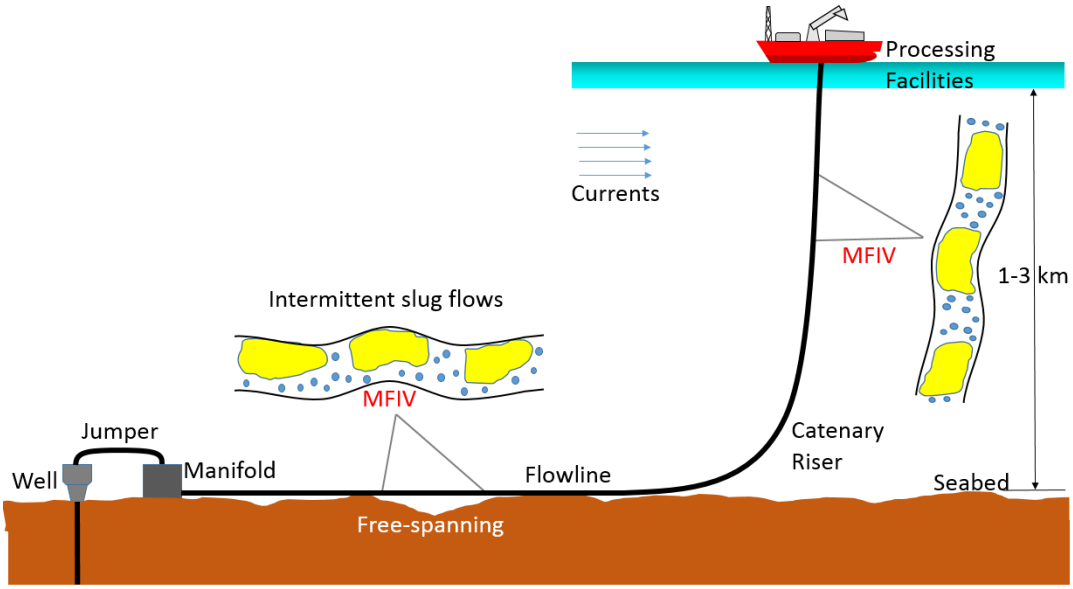


**Figure 1.2:** Schematic of deep-water subsea production system potentially subject to currents and slug flows.

The slug flow pattern is characterized by an alternate distribution of liquid- and gas-dominant sections, termed as liquid slug and gas bubble regions. Unlike some homogeneous flow regimes, this discontinuous two-phase flow leads to sudden changes in masses, flow momenta and pressure within the pipe. Consequently, fluctuating dynamic forces can be led by the slug flow with excitation frequencies which may potentially resonate with the structural natural frequencies, resulting in significant FIV. Moreover, additional time-varying loads can also be induced due to the change of flow direction when the slug flow is transported through bends, elbows or highly curved risers. Such a SIV phenomena are widely recognized by the oil and gas industry, being a common and problematic issue causing excessive and cyclic stresses, reduction of fatigue life or even catastrophic system failures. For instance, an underwater survey by remotely operated vehicles was conducted after the Macondo incident in 2010. It was then reported by Zaldivar (2014) that a section of the broken-down riser was subject to regular motions on the seafloor because of oil-gas slug flows, in which the riser oscillation frequency matches the one of slug flows. Nowadays, the dynamic effects of deep-water flexible risers due to the slug flow have been incorporated in the current rules and standards for riser analysis as stated in DNVGL-ST-F201. The standard addresses possible SIV for long and flexible risers with high curvature by the time-varying loading associated with slug flow weight, centrifugal and Coriolis forces. Besides, a large quasistatic re-configuration of riser due to additional slug mass and potential resonance due to slug-riser frequency coincidence should be considered carefully.

As for the external FIV, one of the most major and crucial vibration sources for subsea structures comes from vortex-induced vibration (VIV). Such a complex fluid-structure interaction process may develop when flows pass a movable bluff body, shedding vortices behind and consequently inducing coupled periodic drag and lift forces on the body. In particular, the hydrodynamic forces can be significantly increased when the frequency of vortex shedding becomes close to the structural natural frequency, which leads to a resonance state in the so-called lock-in range with generating large vibration amplitudes. The complexities of VIV phenomena are more pronounced when considering the long-distance offshore risers, where the slender and flexible structures are potentially vulnerable to three-dimensional VIV in streamwise, transverse and longitudinal directions. Although the effects of external flows leading to VIV has been well studied and documented in the literature (Sarpkaya, 2004; Wu et al., 2012), textbooks (Blevins, 1990; Sumer and Fredsøe, 2006), and recommended practice (DNVGL-RP-C205; DNVGL-RP-F105; DNVGL-RP-F204), it is still a challenging topic due to the complex nature in the fluid-structure interaction, especially, when it refers to practical

deep-water applications with curved geometries such as catenary, S-shaped or lazy-wave risers. The non-straight configuration is observed to result in more complicated vortex wake along the structure due to the effects of flow incidence, which in turn renders different VIV behaviours from those observed in the straight ones.

From an industrial perspective, a scenario of combined internal and external FIV brings greater complications and unknowns in offshore design and fatigue assessment. For a practical consideration of water depths greater than 1000 m, a large-diameter, long and compliant riser, transporting the mixed gas-liquid phases upwardly under a certain flow rate, may be simultaneously subject to the external current and internal multiphase flow excitations, resulting in both VIV and SIV of the riser. Apart from potentially amplifying overall riser vibrations and stresses, such complex flow-pipe interactions could lead to a flow assurance issue, operational interruption and greater engineering solution cost. As stated in the recommended practice API-RP-1111, dynamic loads both from VIV and SIV should be addressed for the fatigue assessment of all subsea components such as risers and flowlines. The internal slug flow can potentially subject subsea risers to vibration and lead to more complex structural dynamics when VIV is involved. Insights into interrelationships between slug flow characteristics and SIV as well as understanding of combined internal-external FIV phenomena are meaningful for a reliable design of subsea systems. Despite the practical importance of these phenomena in the field, investigations into SIV and combined VIV-SIV mechanism of the subsea structures, which fundamentally shed light on the associated stress and fatigue assessment, are still lacking. The presently recognized gap drives the present research.

### 1.2 Aims and Objectives of the Thesis

The present thesis aims to investigate SIV of flexible catenary risers subject to external excitations by VIV with focusing on the mechanical effects of slug gas-liquid flow characteristics, including slug unit length, translational velocity and slug frequency, on the riser dynamics and the roles of SIV versus (vs.) VIV in the combined internal-external flow situations. To achieve this, a mechanistic steady-state slug flow model is adopted, which distinguishes itself from other existing one-dimensional (1D) transient (e.g. slug capturing and tracking) models by allowing a parametric investigation of the slug characteristics. Some of the important SIV aspects from the numerical study, such as the individual and combined effects of slug length and velocity, are expected from the laboratory tests. Model validation is attempted by comparing the numerical prediction against and the experimental results for the limiting SIV cases. To incorporate VIV effects, a phenomenological model based on wake

oscillators is first implemented in case of rigid structures under uniform flows and then applied for examining the significance of planar SIV and VIV for the flexible catenary riser subject to slug flows and perpendicular uniform currents to the riser curvature. More specifically, the objectives of the present thesis are:

- To develop a mathematical model of a catenary riser transporting slug gas-liquid flows, accounting for adequate slug-induced loads attributed to space-time varying internal flow mass, weight, centrifugal force, Coriolis force and pressure.
- To parameterise the slug flow by translational velocity, length, void fraction, pressure loss and slug characteristic frequency for individual slug unit and input them into the numerical model for exploring potential global riser responses.
- To carry out parametric investigations by using the developed model under various assigned flow conditions for identifying the individual effect of the key slug characteristics (slug unit length, translational velocity and frequency) on SIV responses.
- To conduct laboratory tests of a flexible catenary riser conveying slug gas-liquid flows to experimentally assess the significance of SIV for various designated flow conditions with obtaining insights into the slug flow-riser dynamics interaction.
- To compare numerical against experimental results of limiting cases for supporting the explanation of the observed SIV phenomena as well as justifying the prediction ability of the proposed mathematical model.
- To predict VIV characteristics using wake oscillators in case of a rigid cylinder in uniform flows and extend the semi-empirical approach to model hydrodynamic forces for the flexible catenary risers experiencing perpendicular flows.
- To numerically investigate the planar motion of the catenary riser subject to various combined internal-external flow conditions and explore the significance of SIV and VIV in VIV-SIV phenomena.

### 1.3 Outline of the Thesis

The thesis is structured as follows:

Chapter 2 presents a literature review on flow patterns, empirical/semi-theoretical gas-liquid flow maps of different flow directions. The literature on SIV is listed and discussed with respect to numerical and experimental investigations. Moreover, research studies of VIV within the scope of catenary risers are also reviewed.

Chapter 3 describes a numerical study conducted for fundamental planar dynamics of an inclined curved flexible riser carrying slug gas-liquid flows. A two-dimensional continuum model describing coupled horizontal and vertical motions of the curved riser subject to time-varying slug flow-induced loads is presented. The individual effect of slug characteristics including the slug unit length and the translational velocity on the slug flow properties and the resultant SIV behaviours of the riser are highlighted.

Chapter 4 focuses on a numerical study of a flexibly mounted rigid cylinder in uniform flows subject to cross-flow/in-line (CF/IL) VIV. A semi-empirical model based on wake oscillators is employed for obtaining hydrodynamic lift/drag forces exerted on the cylinder. Combined analytical and numerical results are presented and discussed, showing fundamental VIV characteristics. In addition, investigations are carried out by adding linear or nonlinear damping to assess their efficiency in VIV mitigation.

Chapter 5 exhibits a mathematical model of CF-only VIV aligning with planar SIV of the flexible catenary riser. The validity of the VIV model is justified by a good qualitative and quantitative agreement with the published experimental results for a straight cylinder. Dynamic behaviours of the catenary riser in VIV-only and combined VIV-SIV scenarios are compared.

Chapter 6 describes an experimental study on a flexible catenary pipe conveying gas-liquid flows. The details of the experimental apparatus, data acquisition and post-processed results are presented. Slug flows are captured under various flow conditions, causing SIV of the flexible pipe. The correlation between the slug flow characteristics such as travelling velocities, slug unit lengths, slug frequencies and SIV responses is investigated. Numerical simulations and laboratory tests are qualitatively and quantitative compared.

Chapter 8 summarises the key conclusions of the present thesis and provides suggestions for future research in the field.

### 1.4 Scope of the Thesis

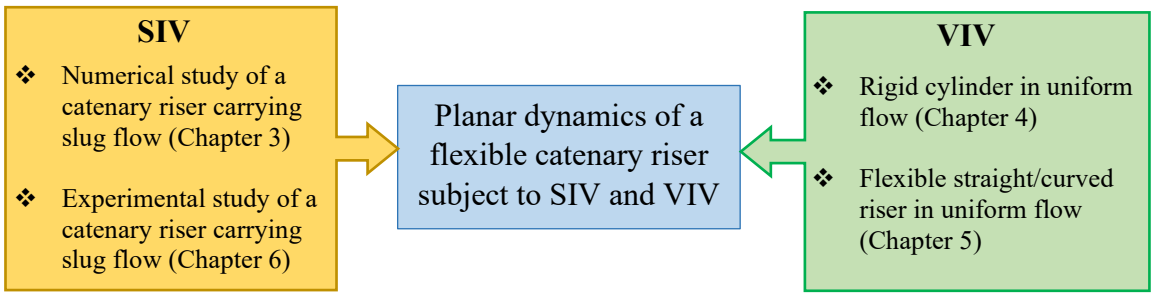


**Figure 1.3:** Illustration of the scope in the present research.

# Chapter 2. Literature Review

With new offshore oil and gas reservoirs being identified, an effective and economical way of production, such as subsea tieback development, becomes increasingly popular. However, the long-distance operation requires extra technical considerations since subsea production systems (Figure 2.1a) in far and harsh offshore fields are vulnerable to both the environmental factors and flow assurance issues. In particular, the multiphase hydrocarbon flow (Figure 2.1b) has come into sight owing to its possible appearance throughout the subsea facilities and the associated problems significantly concerning the front-end design, reliable analysis and efficient operation. Thus, investigations on the practical challenges, e.g. VIV and SIV as introduced in Chapter 1, could give insights into the complex fluid-structure interaction phenomena, and hence benefit the ongoing research and development in both academia and industry. Within the scope of the present work, this chapter provides a review of previous research related to gas-liquid flow characteristics, SIV and VIV. Three main sections are described in the following. Gas-liquid flow features and regime maps based on empirical and theoretical methods are first reviewed for various flow directions. Numerical SIV investigations in terms of slug flow models and experimental tests are summarized in the second section. Then, VIV investigations in the context of catenary risers are reviewed.

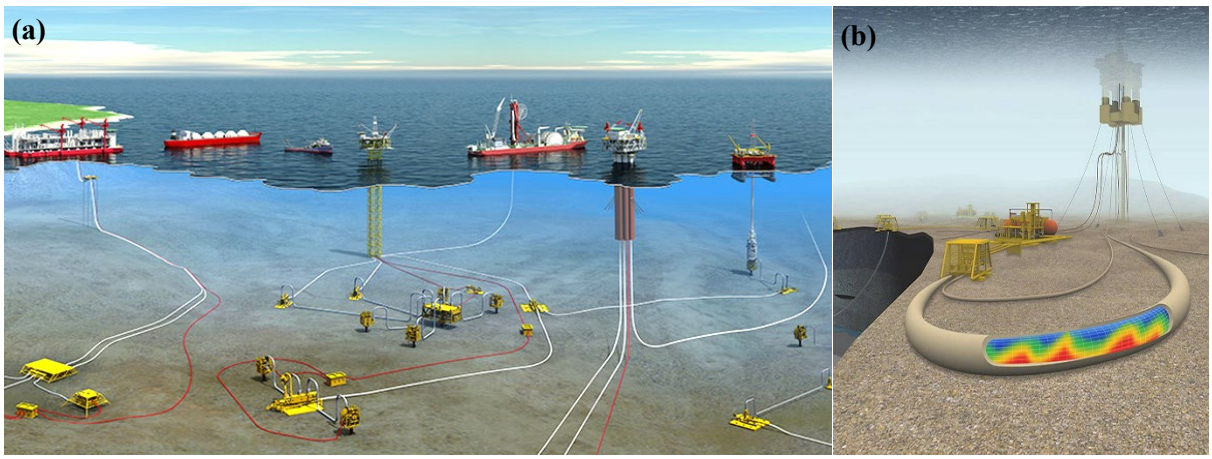


**Figure 2.1:** Illustration of (a) typical subsea oil and gas production systems (source: GENESIS) (b) conveying multiphase gas-liquid flow (source: SINTEF).

## 2.1 Gas-Liquid Flow Features and Maps

### *2.1.1 Common flow patterns in horizontal and vertical tubes*

It is known that gas-liquid flows may result in different flow patterns. Since variables of engineering significance such as the heat and mass transfer, momentum loss, pressure drop and

pipe vibration strongly depend on flow patterns, it is important to identify a flow regime for accurate measurement and determination of design parameters. Over past decades, many experimental works have been carried out in terms of the flow regime identification for which several methods have been developed. They can be generally classified into a direct observation and indirect determination approach (Rouhani and Sohal, 1983). For instance, observing the flow patterns directly through visual high-speed photography (Vince et al., 1980) or X-ray attenuation (Hewitt and Roberts, 1969) provides a simple but subjective way of determining flow patterns. In contrast, indirect approaches using flow signal characterization, such as pressure fluctuation (Matsui, 1984), electrical impedance (Barnea et al., 1980) and ultrasound method (Liang et al., 2016), have been regarded as relatively objective methodologies for flow pattern determination. In the context of a gas-liquid horizontal co-current flow, some major flow patterns in a tube are schematically illustrated in Figure. 2.2.

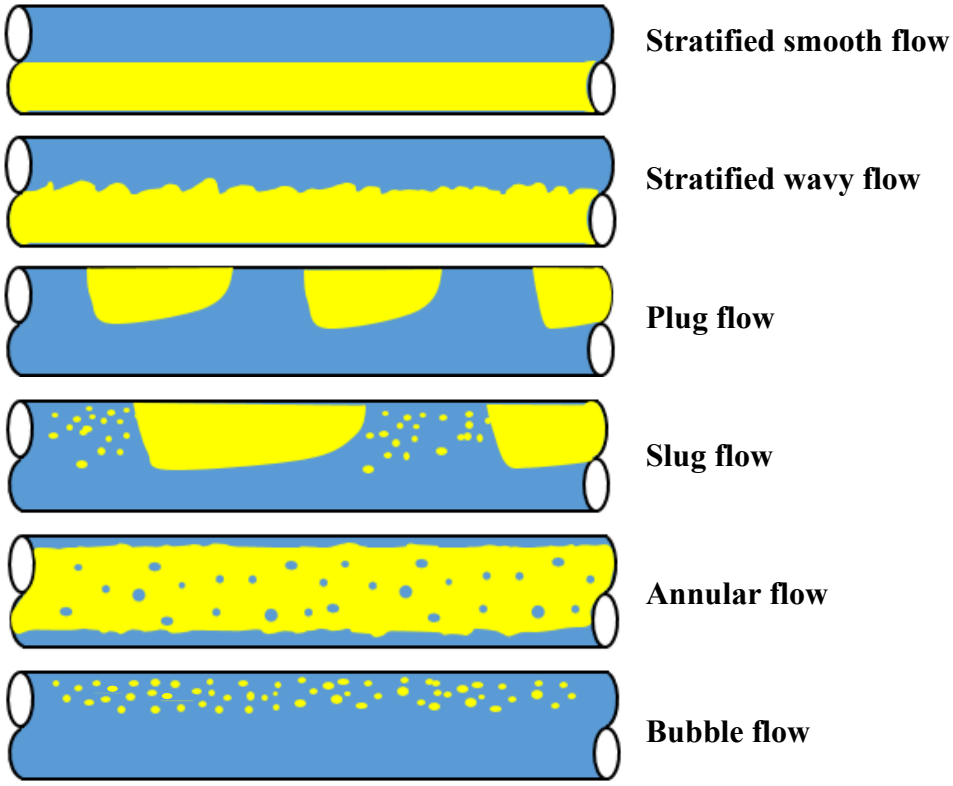


**Figure 2.2:** Gas-liquid flow patterns in horizontal pipes adapted from Rouhani and Sohal (1983).

The stratified smooth flow is formed by separated gas-liquid phases located at the top and bottom due to gravity effects. This type of flow is usually developed at relatively low liquid and gas flow rates and it can be evolved into the stratified wavy flow as the gas flow rate increases, where the smooth interface turns to be rippled and wavy. Instead, keeping the gas flow rate low, an intermittent flow pattern, known as the plug flow, will develop as the liquid

rate increases. For this flow pattern, liquid plugs free of gas bubble are separated by elongated gas pockets. By increasing the gas flow rate based on the plug flow, the liquid region will be aerated with small bubbles and a new regime termed slug flow develops. Compared with the plug flow, the slug flow shows stronger intermittency and larger gas bubbles. If the gas flow rate gets further increased, the annular flow will form with a thick film of liquid around the periphery of the channel walls with gas in the central core, where some liquid droplets may be entrained. As another type of dispersed flow, the bubble flow may take place when the liquid flow rate is relatively high alongside a low gas flow rate, in which the gas phase in the form of small bubbles are distributed in the continuous liquid phase.

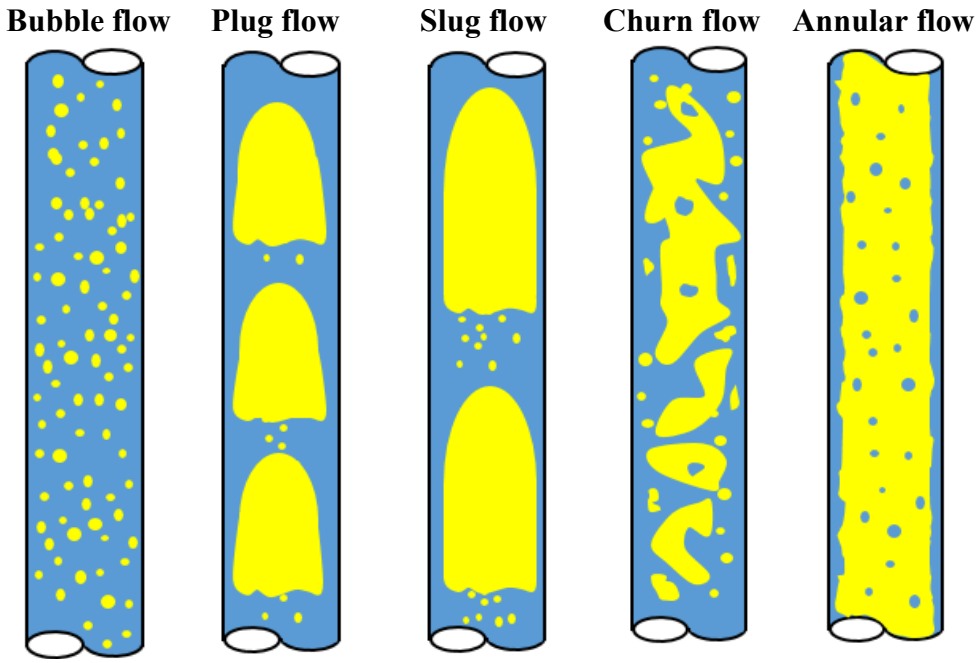


**Figure 2.3 :** Gas-liquid flow patterns in vertical pipes adapted from Rouhani and Sohal (1983).

On the other hand, some of the main vertical co-current flow regimes are depicted in Figure 2.3. It is noticed that several common flow regimes occur in both the vertical and horizontal channels including the bubble, plug, slug and annular flows, whereas the former exhibit more axisymmetrical patterns than the latter (see Figure 2.2). With a low gas flow rate and a moderate liquid flow rate, the bubble flow may take place. As the gas flow rate increases, the plug flow takes place when the small bubbles coalesce with constituting large bubbles. Further increasing the gas flow rate, the slug flow develops with larger bubbles, termed the Taylor bubbles. Each of these bubbles is shaped with spherical nose and relatively flat tail, almost occupying the whole cross-sectional area with the thin liquid film around the periphery

of the tube walls (Fernandes et al., 1983). Following the slug flow, one may observe the churn flow when the flow velocity is increased, where the relatively regular liquid slugs become chaotic. On the contrary, annular flow exists at a relatively large gas flow rate and a low liquid flow rate. If the gas flow rate is sufficiently high, some portion of the liquid in the form of small droplets will be entrained in the continuous gas core.

*2.1.2 Gas-liquid flow maps for different flow directions*

To predict and determine the types of flow patterns, flow maps may be used as a guide. Typically, flow maps are constructed as two-dimensional (2D) graphs with transition lines to classify and separate various flow regimes. These lines are not distinctive boundaries since the transitions between the neighbouring flow regimes take place gradually rather than a sudden change. Flow maps may be generally categorized into empirical and theoretical ones, where the former are plotted based on the experimental observations and the latter predict the transition criteria by involving mechanistic models accounting for fluid and structural properties.

Over the past decades, a large number of flow maps based on different fluid and pipe conditions have been developed. According to the existed literature, Baker (1954) proposed the first flow map for horizontal co-current pipe flows. It was established empirically by observing and summarizing different regimes including stratified, plug, slug, bubble, annular, wavy and dispersed flow patterns. The gas-liquid mass superficial velocities were combined with two dimensionless parameters, which account for gas-liquid densities, surface tensions and dynamic viscosities, to describe the system coordinates. In the ensuing years, empirical flow maps for horizontal co-current flow were modified or constructed by different researchers (Hoogendoorn and Buitelaar, 1961; Govier and Omer, 1962; Mandhane et al., 1974). By applying 5935 individual observations of flow patterns, Mandhane et al. (1974) constructed a flow pattern map for horizontal air-water flows. The gas-liquid superficial velocities ($u_{gs}$-$u_{ls}$) were employed as the coordinate system to determine the transition criteria. Through the comparison with three horizontal flow maps from Hoogendoorn and Buitelaar (1961), Baker (1954) and Govier and Omer (1962), the proposed map appeared to be better agreed with the air-water data than the others.

On the other hand, two-phase flows in other orientations, such as vertical or inclined upward flows, are of significant relevance to the offshore oil and gas production. One of the leading flow maps for vertical flows is the one presented by Hewitt and Roberts (1969). They experimentally determined air-water flow patterns in vertical tubes and constructed a flow map categorized by annular, churn, slug and bubble flow regimes by using the phase superficial

momentum fluxes as system coordinates. By using the volumetric ratios and the Froude number as the transition criteria, flow maps for various inclination angles from vertically downward to upward air-water flows were developed by Spedding and Nguyen (1980) for investigating potential orientation effects on the flow regime development. The flow regime maps for horizontal (0°), inclined (45°, 70°, –6.17° and –44.75°) and vertical (90°) flows are exemplified in Figure 2.4, where $u_{ls}$ and $u_{gs}$ represent liquid and gas superficial velocities. They remarked that the stratified flow regime vanishes and was replaced by the slug flow regime as the pipe orientation varies from the horizontal to the upward ones. Such observation was also revealed in the experimental investigations by Barnea et al. (1980) and Weisman and Kang (1981).

Flow regimes and their corresponding transitions highly depend on many parameters in terms of fluid properties (e.g. density, surface tension and viscosity), flow rates (e.g. velocity, velocity ratio) and structure properties (e.g. pipe inclination, diameter). Therefore, the maps purely based on experimental observations may be limited to a narrow band of flow and pipe conditions. However, for many engineering applications, the flow conditions may be out of the range of the existing data, while simple extrapolation of the empirical correlations may result in a high level of uncertainty and inaccuracy. Moreover, it may not be adequate to represent the transition boundaries between various flow regimes with only some simple and arbitrary variables, where the generality and accuracy may be restricted by the lack of physical basis in the selected coordinate systems.

Therefore, attempts and efforts were made to generalize maps for a wider range of flow conditions through the aid of theoretical models with dimensionless coordinate systems. Taitel and Dukler (1976) presented a semi-theoretical model to determine the regime transition criteria in horizontal and slightly-inclined gas-liquid flows. The map was developed with five different transition regions, including annular-dispersed, dispersed-bubble, stratified-wavy, stratified-smooth and intermittent flows, where the lines are theoretically derived from a mechanistic model. For different adjacent flow regimes, various groups of dimensionless variables were employed as coordinates. A good agreement is found in the comparison between their theoretical criteria and the empirical ones of Mandhane et al. (1974). The model was then utilized to explore the potential influences of several design variables including pipe diameters and fluid densities on the transition criteria. Further, such a theory-based approach was also applied to predict the flow regime transition for upward vertical gas-liquid flows (Taitel et al., 1980).

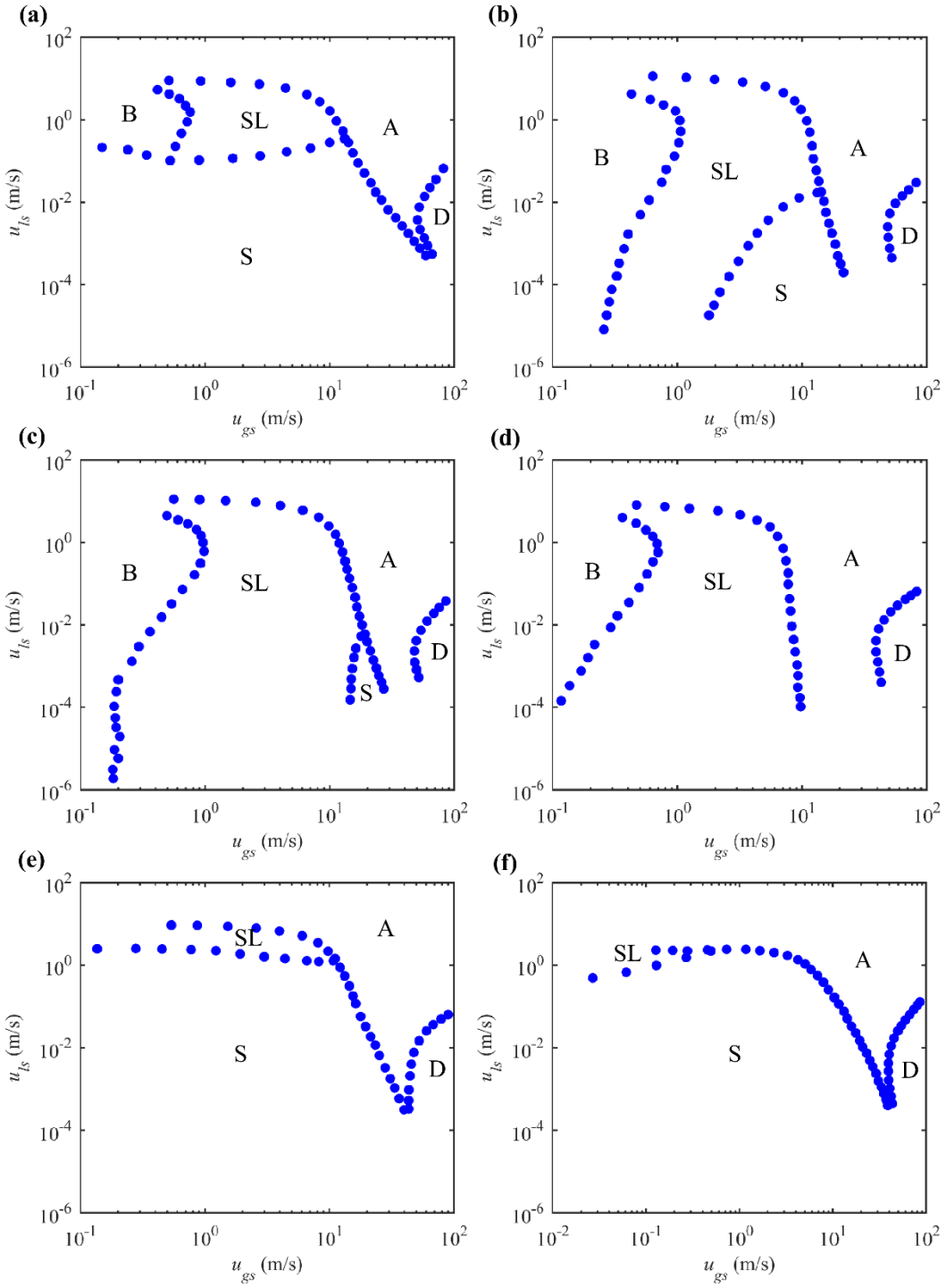


**Figure 2.4:** Flow pattern maps adapted from Spedding and Nguyen (1980) for (a) horizontal, (b) 45°, (c) 70°, (d) upward vertical, (e) -6.17° and (f) -44.75° flows: SL, DB, S, A, D represent slug, dispersed bubble, stratified, annular and droplet flow.

The attempts in developing gas-liquid flow maps have been continuously made by many researchers during the last few decades (Lin and Hanratty, 1987; Hand and Spedding, 1993; Furukawa and Fukano, 2001; Omebere-Iyari and Azzopardi, 2007; Zhuang et al., 2016). A

**Table 2.1:** Summary of experimental and theoretical studies characterizing gas-liquid flow regimes.

| References | Orientation | Phases | *d* (cm) | Coordinates | Method |
|---|---|---|---|---|---|
| | H | Natural gas-oil | 2.54-25.4 | $Q_g\,\rho_g/A$, $Q_l\,\rho_l/A$ with physical parameters | Experimental |
| Hoogendoorn (1959) | H | Air-Water/Oil | 2.4-14 | $Q_g/(Q_g+Q_l)$, $U_s$ | Experimental |
| Hoogendoorn and Buitelaar (1961) | H | Freon 11- water | 1.5 | $Q_g/(Q_g+Q_l)$, $U_s$ | Experimental |
| Govier and Omer (1962) | H | Air-Water | 2.54 | $Q_g\,\rho_g$, $Q_l\,\rho_l$ | Experimental |
| Duns Jr and Ros (1963) | V | Air-Oil | 8 | $u_{gs}(\rho_l/g\sigma)^{0.25}$, $u_{ls}(\rho_l/g\sigma)^{0.25}$ | Experimental |
| Eaton et al. (1967) | H | Natural gas-water | 5.08, 10.16 | Re, We | Experimental |
| Hewitt and Roberts (1969) | V | Air-water | 3.2 | $u_{ls}^2\rho_l$, $u_{gs}^2\rho_g$ | Experimental |
| Mandhane et al. (1974) | H | Air-Water | 1.27-16.5 | $u_{ls}$ , $u_{gs}$ | Experimental |
| Taitel and Dukler (1976) | H/I | Air-Water | 1.25-30 | Dimensionless parameters | Theoretical |
| Weisman et al. (1979) | H | Air-Water | 2.54 | $u_{ls}$ , $u_{gs}$ | Experimental |
| Spedding and Nguyen (1980) | V/I/H | Air-Water | 4.55 | $Q_l/Q_g$, $(U_s/(gd)^{0.5})^{0.5}$ | Experimental |
| Barnea et al. (1980) | H/I | Air-Water | 1.95, 2.55 | $u_{ls}$ , $u_{gs}$ | Experimental |
| Taitel et al. (1980) | V | Air-Water | 2.5, 5 | $u_{ls}$ , $u_{gs}$ | Theoretical |
| Weisman and Kang (1981) | V/I | Freon 113 | 2.5 | $u_{ls}$ , $u_{gs}$ | Experimental |
| Spedding and Chen (1981) | H | Air-Water | 4.55 | $u_{ls}$ , $u_{gs}$ | Theoretical |
| Mukherjee and Brill (1985) | V/I/H | Air-Kerosene | 5.08 | $u_{gs}(\rho_l/g\sigma)^{0.25}$, $u_{ls}(\rho_l/g\sigma)^{0.25}$ | Empirical correlation |
| Stanislav et al. (1986) | H/I | Air-Oil | 2.58 | $u_{ls}$ , $u_{gs}$ | Experimental |
| Lin and Hanratty (1987) | H | Air-Water | 2.54, 9.53 | $u_{ls}$ , $u_{gs}$ | Experimental |
| Alexeyev et al. (1991) | H | Helium Flow | 0.79 | $u_{ls}$ , $u_{gs}$ | Empirical correlation |
| Hasan and Kabir (1992) | V/I | Air-water | 12.7 | $u_{ls}$ , $u_{gs}$ | Theoretical |
| Hand and Spedding (1993) | H | Air-Water/Glycerine | 9.35 | $u_{ls}$ , $u_{gs}$ | Experiment |
| Filippov (1999) | H | Helium Flow | 0.79 | $u_{ls}$ , $u_{gs}$ | Empirical correlation |
| Furukawa and Fukano (2001) | V | Air-Water/glycerol | 1.92 | $u_{ls}$ , $u_{gs}$ | Experimental |
| Ghajar (2005) | H/I | Air-Water | 2.54 | $Q_g\,\rho_g$, $Q_l\,\rho_l$ | Experimental |
| Rozenblit et al. (2006) | V | Air- water | 2.5 | $u_{ls}$ , $u_{gs}$ | Experimental |
| Omebere-Iyari and Azzopardi (2007) | V | Nitrogen-Naphtha | 18.9 | $u_{ls}$ , $u_{gs}$ | Experimental |
| Zhuang et al. (2016) | H | R170 | 0.4 | We, $X_{tt}$ | Experimental |

Note: H, V, I denote horizontal, vertical and inclined flow orientations, respectively.

summary of experimental and theoretical studies characterizing the gas-liquid flow regimes is herein demonstrated chronologically in Table 2.1, reflecting the flow orientations, phase properties, pipe diameters, mapping coordinates and methodologies. It is noticeable in the table that a variety of coordinate systems have been applied for describing the flow maps. The common ones are based on $u_{gs}$-$u_{ls}$, gas-liquid volumetric flow rates ($Q_g$-$Q_l$) and their modified forms accounting for some physical properties such as gas-liquid densities ($\rho_g$-$\rho_l$), viscosities, surface tension ($\sigma$) and pipe inner diameter ($d$). Besides, dimensionless parameters were employed in several studies. For instance, the modified Weber number (We) and the Reynolds number (Re) were applied in Eaton et al. (1967), where the former mainly accounts for fluid density, velocity, characteristic length (e.g. $d$) and surface tension, whereas the latter comprises fluid velocity, characteristic length and kinematic viscosity. Also, Zhuang et al. (2016) used a modified We and Lockhart-Martinelli parameter ($X_{tt}$) as the mapping coordinates, where $X_{tt}$ is mainly defined by the combined effects of gas-liquid mass flow rates and densities. Although the existed maps have accommodated several aspects in terms of both fluid and pipe (see Table 2.1) and understanding of flow pattern transitions has been improved, there remains a challenge of constructing the generalized flow maps (Brennen and Brennen, 2005; Cheng et al., 2008). Nevertheless, the valuable information, such as the flow regime transition criteria, provided by the flow maps has contributed to the development in mathematical multiphase (e.g. gas-liquid) modelling (Danielson, 2012).

## 2.2 Slug Flow-Induced Vibrations

Over past decades, SIV has been recognized as a problematic phenomenon, especially concerning long flexible pipelines/risers in the oil and gas industry. This drives the momentum of research on SIV. Miwa et al. (2015) have recently provided a comprehensive review on the research progress related to the two-phase FIV in rigid pipes with small diameters. Significant vibrations in straight horizontal/vertical pipes with bends have been experimentally reported under slug flows, which cause an intermittent change in a mixture momentum flux and a resonance between the momentum/pressure fluctuations vs. the pipe natural frequencies. In the following sections, the literature for both numerical and experimental SIV investigations are reviewed. Numerical studies can be categorized by slug flow models, including the idealized and mechanistic models.

### *2.2.1 SIV investigation by idealized model*

By using a classic Euler's beam theory, Hara (1973) formulated the equation of transverse motion of a straight pipe transporting slug flows which were modelled as a series of piston gas-

liquid phases moving alternatively with a narrow-band characteristic frequency. Hara showed that, by using a pipe fundamental mode approximation, SIV is dominantly caused by a parametric resonance due to the space-time varying mass distributions, centrifugal and Coriolis forces. The parametric resonance was described through a derived Mathieu-type equation with periodically time-varying coefficients. By including the effects of gravity and fluid pressure fluctuation, Hara (1977) further compared and demonstrated a good agreement between theoretical and experimental results for a horizontal pipe conveying air-water slug flows. These preliminary works justify the potential use of a simple slug flow model for predicting SIV.

For flexible risers with larger diameters and longer lengths, Patel and Seyed (1989) theoretically described key features of internal flow-induced static and dynamic forces acting on the pipe, including the fluid weight, curvature-induced load, centrifugal and Coriolis effects associated with the flow momentum. They also modelled a steady-state slug flow through a sinusoidal function of fluid densities having a mean component and a space-time varying counterpart with a harmonic representing the slug frequency, which reads

$$\psi(t,s) = \psi_m + \psi_s \sin(k_s s + \theta_s) e^{i 2\pi f_s t}, \tag{2.1}$$

where $\psi$ is a slug shape function depending on time ($t$) and arc length coordinate ($s$) along the pipe length ($L$), $\psi_m$ and $\psi_s$ the mean and amplitude values. $k_s$, $f_s$, $\theta_s$ denote the slug wave number, characteristic frequency and arbitrary phase angle, respectively. By performing a frequency-domain dynamic analysis of an S-shaped riser, they remarked how SIV can amplify dynamic tensions at slug frequencies and modify the riser geometric stiffness. A time-domain simulation of a 510 m long lazy-wave riser subject to the combined effects of wave, vessel motion and slug flow was further conducted by Seyed and Patel (1992). The results showed amplified riser responses due to the slug flow and its predominant role over the environmental loading. This slug flow idealization has been applied by Pollio and Mossa (2009) to a catenary riser. Both constant and variable slug wavelength were considered, where the latter was modelled by further accounting for a relationship between the slug wavelength and pipe inclination permitting the variable slug frequency. The more irregular behaviour of riser axial stress was found in the unsteady case than the steady one. More recently, Meléndez and Julca (2019) applied a sinusoidal density function to model the slug flow in a catenary riser subject to external current flows without VIV. They demonstrated amplified riser top dynamic tensions depending on a mass flow rate and addressed an insignificant effect of Coriolis force associated with low fluid velocities.

Alternatively, slug flow may be modelled in a form of pulse train. This approach allows the representation of sudden mass variation between gas and liquid slug regions, which is a typical slug flow feature. Also, a wide range of volumetric liquid holdup can be designated for a slug unit. Bordalo and Morooka (2018) modelled the steady slug flows as a series of liquid plugs and gas pockets travelling with a single slug unit velocity according to a given flow rate. They introduced a mass distribution function depending on the slug velocity and unit length through the liquid and gas densities. Simulations were carried out for steel catenary and lazy-wave risers, showing slug induced impacts on riser displacements and bending stresses. They concluded that large oscillations may be generated when the slug frequency nearly resonates with one of the riser natural frequencies. Kim and Srinil (2018) have implemented such a slug unit cell as an initial input velocity and volumetric fraction at the pipe inlet for a 3D computational fluid dynamics (CFD) simulation of a subsea M-type jumper transporting slug flows. The effects of multiple bends on the flow pattern modification and flow-induced force fluctuation were highlighted. Based on this slug unit concept, Safrendyo and Srinil (2018) introduced a slug length randomness into the dynamic simulation of a catenary riser carrying slug flows. They highlighted a chaotic feature with multiple broad-band oscillation frequencies in the space-time varying dynamics of the catenary riser. More importantly, greater vibration amplitudes were found when accounting for the combined effects of SIV and VIV. This observation of amplified dynamic responses has also been reported by Bossio et al. (2014) who considered a horizontal pipeline. By using a steady-state plug model in the form of pulse train, Cabrera-Miranda and Paik (2019) investigated dynamic responses of a lazy-wave riser excited by slug flows and then conducted a limit state assessment. It was concluded that SIV is significant near the riser bottom, which subsequently introduces crucial fatigue damage. The pulse train function has been defined as

$$\psi(t,s) = \sum \psi_{Ns}(t,s), \tag{2.2}$$

$$\psi_{Ns}(t,s) = \begin{cases} 0, & \left|s - U_t t - N_s L_u\right| > L_s/2 \\ 1, & \left|s - U_t t - N_s L_u\right| \leq L_s/2 \end{cases}, \tag{2.3}$$

where $\psi$ accounts for slug translational velocity ($U_t$), slug number ($N_s$), slug unit length ($L_u$) and liquid slug length ($L_s$). Similar to Eq. (2.1), this idealized slug model is also space-time ($s$-$t$) dependent. Nevertheless, this idealized slug function can generate a series of square pulses that imitate the slug flow shapes with the sudden transition between the liquid slug and gas pocket regions. Moreover, this model enables the adjustment in the ratio of $L_s$ to $L_u$, whereas the sinusoidal function only allows $L_s$=0.5 $L_u$.

For a better illustration of the two slug models, Figure 2.5 exemplifies three gas-liquid slug units created by the sinusoidal (Eq. (2.1)) and pulse train (Eqs. (2.2) and(2.3)) functions, where the yellow and white areas denote the liquid and gas phases. As expected, the former (Figure 2.5a) results in sinusoidal slug shapes with $L_s$=0.5$L_u$, which also implicitly renders the liquid holdup of 0.5 in each slug unit. In contrast, the square slug shapes in case of $L_s$=0.5$L_u$, $L_s$=0.25$L_u$, $L_s$=0.75$L_u$ are produced by the latter (Figures 2.5b, c, d), corresponding to the liquid holdup of 0.5, 0.25, 0.75, respectively. Using the pulse train model, Dong and Shiri (2019) parametrically analysed SIV on a catenary riser in the touchdown zone with also including wave and seabed effects. The riser responses and stresses are evaluated in case of individual and combined effects from the slug flows and waves. They remarked the amplified responses and in turn the stresses owing to the coupled internal-external impacts.

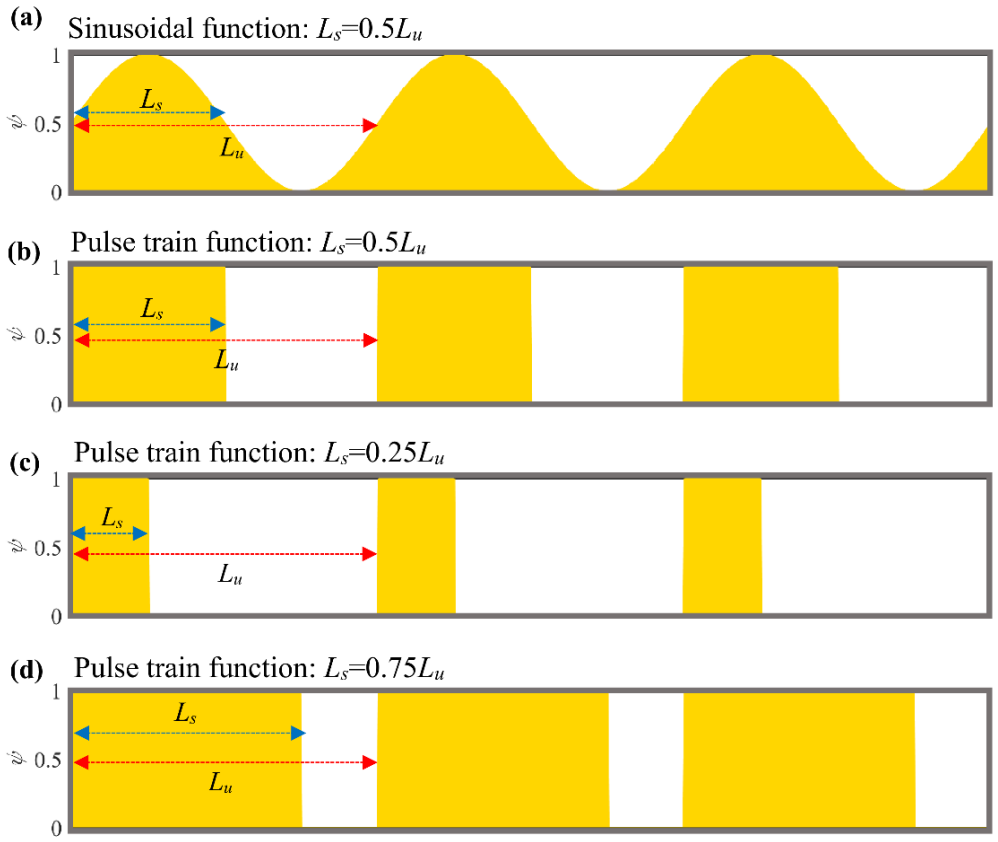


**Figure 2.5:** Illustration of slug flow shapes from (a) sinusoidal function and (b-d) pulse train function in case of $L_s$=0.5$L_u$, $L_s$=0.25$L_u$ and $L_s$=0.75$L_u$.

*2.2.2 SIV investigation by mechanistic model*

The above idealized fluid force models overlook the detailed slug flow features with variable internal pressure, phase velocities and fractions. To account for more realistic two-phase flows, theoretical models based on continuity, momentum and energy conservation equations should be implemented. Modelling of one-dimensional two-phase flows, averaged over a pipe cross

section, may be generally classified into three main categories: homogenous (Ouyang and Aziz, 2000; Monette and Pettigrew, 2004), drift-flux (Zuber and Findlay, 1965; Ishii, 1977) and two-fluid models (Ishii and Hibiki, 2010);

For a homogeneous model, a single set of the mass-momentum-energy conservation equations depend on the gas-liquid mixture as a pseudo-single phase. For drift-flux models, the conservation of momentum depends on the relative velocities of fluid phases whilst other conservations may be derived for individual fluids. As a more complex model, two-fluid models require the full conservations of each phase, realistically accounting for different physical fluid properties. Montoya-Hernández et al. (2014) used the homogeneous model to demonstrate that natural frequencies of a vertical riser transporting the upward gas, oil and water flows decrease with the increasing mixture flow velocity. This agrees with a general free vibration trend of a tensioned straight beam with internal flows which reduce the structural stiffness but increase the system mass (Paidoussis, 2014). If the conservation equations are assumed to be time-invariant, the considered two-fluid flows are steady; otherwise, they are transient, describing the space-time varying quantities.

For two-phase slug flow models, they can be mainly referred to three approaches: unit cell models (Taitel and Barnea, 1990; Cook and Behnia, 1997), slug tracking (Zheng et al., 1994; Nydal and Banerjee, 1996) and slug capturing (Issa and Kempf, 2003) models. For unit cell models, slug flow characteristics are periodic and time-invariant within slug units of the same length and velocity. These models are known as steady-state slug models, where the conservation of mass and momentum are described in a frame of reference moving at a slug translational velocity. As a transient approach, slug tracking models are formulated based on the concept of pickup process at the liquid slug front and shedding at the liquid slug tail, solving for flow parameters by conservation laws on every liquid slug and gas pocket. This object-orientated method requires an initial condition of pre-assigned slugs in the pipe by an initiation model, and then tracks each liquid slug individually as it propagates. For slug capturing models, the 1D two-fluid model is solved directly regardless of initial conditions with automatically capturing the formation, growth, or decay of slug flow.

Based on a unit cell model of Taitel and Barnea (1990), Chatjigeorgiou (2017) investigated the planar dynamics of a catenary riser transporting steady slug gas-oil flows and subject to a top-end harmonic excitation. Using a frequency domain approach, it is revealed that slug flows amplify axial-normal responses with increased dynamic tensions and curvatures.

The mechanistic model is formulated based on gas and liquid phase mass balances over the slug unit and momentum balances over the film zone, where the former result in

$$(U_t - U_b)\rho_g A\alpha_s = (U_t - U_g)\rho_l A\alpha_f, \tag{2.4}$$

$$(U_t - U_l)\rho_l AR_s = (U_t - U_f)\rho_l AR_f, \tag{2.5}$$

in which $U_b$ ($U_l$) denotes the gas (liquid) phase velocity in the liquid slug region, $U_g$ ($U_f$) the gas (liquid) phase velocity in the film zone, $R_s$ ($\alpha_s$) the liquid holdup (void fraction) in the liquid slug region, $R_f$ ($\alpha_f$) the liquid holdup (void fraction) in the film zone and $A$ the inner area of the pipe. The gas-liquid momentum balances read

$$\rho_g(U_t - U_g)\frac{\partial(U_t - U_g)}{\partial z_s} = -\frac{\partial P}{\partial z_s} + \frac{\tau_g S_g}{A_g} - \frac{\tau_i S_i}{A_g} + \rho_g g\sin\beta - \rho_g g\cos\beta\frac{\partial h_f}{\partial z_s}, \tag{2.6}$$

$$\rho_l(U_t - U_f)\frac{\partial(U_t - U_f)}{\partial z_s} = -\frac{\partial P}{\partial z_s} + \frac{\tau_f S_f}{A_f} - \frac{\tau_i S_i}{A_f} + \rho_l g\sin\beta - \rho_l g\cos\beta\frac{\partial h_f}{\partial z_s}, \tag{2.7}$$

where $z_s$ represents the local slug coordinate, $P$ the internal fluid pressure, $\tau_f$ ($\tau_g$) the liquid-wall (gas-wall) friction force, $\tau_i$ the gas-liquid interfacial force, $A_g$ ($A_f$) the cross-sectional (gas) liquid film area, $S_g$ ($S_f$) the associated wetted perimeter, $S_i$ the interfacial width, $\beta$ the pipe inclination and $h_f$ the film height. Further, by substituting Eqs. (2.4) and (2.5) into Eqs. (2.6) and (2.7), an equation describing $h_f$ can be determined, which consequently provides slug information over the slug film zone. Detailed results of this slug flow model can be found in Chapter 3.

For a floating free-hanging pipe transporting air-water flows, Vieiro et al. (2015) simulated the fluid-pipe coupling by using a two-fluid model and solving the transient fluid equations with a combined slug capturing-tracking approach (Nydal, 2012). They predicted a severe slugging phenomenon with space-time phase fraction variations and a slug severe cycle in good agreement with in-house experiments. Recently, based on a transient slug tracking approach, Ortega et al. (2018) studied a forced vibration of a catenary riser subject to regular waves and slug flows. External wave excitations influence the riser shapes which, in turn, affect the slug flow developments. Numerical results showed the increased static drifts caused by the slug flow and the amplified dynamic responses due to the interaction of external flow wave and internal slug flow loadings.

Table 2.2 summarizes some relevant studies related to SIV modelling and analysis of flexible pipes/risers, by distinguishing the slug modelling concepts, pipe geometries, two-phase parameters and observed features.

**Table 2.2:** Review of some relevant studies on SIV modelling and analysis with key observations.

| References | Slug Flow Model | Pipe Geometry | | | Multiphase Flow Properties | | | | | | External Excitation | Observed SIV features |
|---|---|---|---|---|---|---|---|---|---|---|---|---|
| | | Type | $L$ (m) | $D$ ($d$) mm | $u_{ls}$ (m/s) | $u_{gs}$ (m/s) | $\rho_l$ (kg/m$^3$) | $\rho_g$ (kg/m$^3$) | $U_t$ (m/s) | $L_w/d$ ($L_s/d$) | | |
| Hara (1977) | Pulse train | H | 2.2 | 30 (23.8) | 0.11-0.4 | 0.19-2.25 | 998 | 1.2 | 2.6-11 | 11.6-46.2 | - | • $f_n/f_s$ = 1 leads to resonant SIV.<br>• $f_n/f_s$ = 0.5 and 1.5 lead to parametric resonances. |
| Patel and Seyed (1989) | Sinusoidal | S | 3.071 | 9.2 (6) | - | - | 998 | 1.2 | 0.45 | 411.7 | - | • Slug flow modifies pressure and pipe tension.<br>• SIV resonance amplifies pipe response/stress. |
| Chatjigeorgiou (2017) | Steady state (Taitel and Barnea, 1990) | C | 2025 | 429 (385) | 0.4 | 2 | 790 | 0.675 | - | 20 | Top imposed excitation | • Slug flows amplify dynamic tension/curvature.<br>• Slug resonance affects structural dynamics. |
| Bordalo and Morooka (2018) | Pulse train | C | 3100 | 212 (165) | - | - | 1000 | 0.01 | 2.4–4 | 606.1 | - | • Large-amplitude SIV takes place when $f_n/f_s \approx 1$.<br>• SIV is dominated by weight force when pipe curvature and flow speed is small. |
| | | LW | 4560 | | - | - | 1000 | 0.01 | 2.1–2.8 | 842.4 | | |
| Liu and Wang (2018) | Steady state (Cook and Behnia, 1997) | H | 15, 20, 30 | 40 (30)<br>30 (25.4)<br>25 (20) | 0.8-1.2 | 2-20 | 998 | 1.2 | - | - | - | • $f_n$ increases with $u_{gs}$ when $u_{ls}$ is small.<br>• Divergent instability occurs at large $u_{gs}$. |
| Ortega et al. (2018) | Transient slug tracking (Nydal and Banerjee, 1996) | C | 445 | 275.5 (200.8) | 2.1 | 38.7 | 998 | 1.2 | - | - | Waves | • Slug flow leads to static or mean drifts.<br>• Slug flow induces irregular dynamics, coupling with wave-induced motions. |
| Wang et al. (2018) | Steady-state model (Zhang et al., 2003) | H | 3.81 | 63 (51.4) | 0.29 | 1.39 | 1000 | 1.2 | 1.5-4.5 | (9.7-68.1) | - | • Amplified SIV exists at higher liquid velocity and slug translational velocity.<br>• SIV amplitudes increase with slug unit lengths. |
| Safrendyo and Srinil (2018) | Pulse train | C | 2025 | 429 (385) | - | - | 790 | 0.675 | 2-10 | 20-50 | VIV | • Steady/random SIV amplify pipe responses.<br>• VIV-SIV coupling reveals complex behaviours. |
| Cabrera-Miranda and Paik (2019) | Pulse train | LW | 2641 | 458.4 (254.1) | - | - | 800 | 0 | 1-32 | 5197, 20787, 41575 | - | • Large-amplitude SIV occurs near riser bottom.<br>• SIV fatigue damage may be crucial. |
| Meléndez and Julca (2019) | Sinusoidal | C | 450 | 400 (360) | 0.98-3.94 | 0.39 | 998 | 100-400 | - | 6.7-29.2 | Currents | • Higher liquid mass flow rate induces greater top tension amplitudes.<br>• Coriolis force has negligible effects at small slug flow velocities. |
| Dong and Shiri (2019) | Pulse train | C | 2333 | 324 (283) | - | - | 600 | 100 | 10, 25 | 106, 176.7 | Waves | • Combined effects of SIV and waves are meaningful and greater than individual cases.<br>• Slug flow-induced inertia and momentum effects are important for riser analysis. |

Note: H, S, C, LW denote horizontal pipe, S-shaped, catenary and lazy-wave riser, respectively.

*2.2.3 Experimental investigations on SIV*

Laboratory experimental studies have also been carried out, providing some insightful observations and validating the analysis models. For flexible pipes with a bending rigidity, mostly a two-phase air-water FIV in a small-diameter tube with a short span has been tested. Considering a catenary riser with $L \approx 28.7$ m and $d \approx 0.32$ cm, Bordalo et al. (2008) carried out a series of tests to investigate gas-liquid flow-induced riser responses for a catenary configuration. Flow patterns including slug and annular flows are observed depending on various gas-liquid superficial velocities, in which the slug flow was found to generate greater vibrations than the annular flow owing to the various levels of intermittency. For a given liquid superficial velocity, they addressed the increased SIV and top tension with the air superficial velocity. The significant role of phase superficial velocities were also highlighted by Al-Hashimy et al. (2016), who carried out an experiment of a horizontal pipe ($L \approx 8$ m; $d \approx 6.8$ cm) transporting slug flows. For a given $u_{gs}$, amplified SIV with decreased oscillation frequencies was observed as $u_{ls}$ increases. For a straight horizontal pipe with $L \approx 0.8$-$1.5$ m and $d \approx 2$ cm, Ortiz-Vidal et al. (2017) measured the pipe dynamic responses subject to a wide range of two-phase flow regimes including bubble, dispersed and slug flows. They noticed that the pipe vibration increases with the increased mixture velocity and the peak oscillation frequency strongly depends on the void fraction as well as the flow pattern.

For a horizontal pipe ($L \approx 3.8$ m; $d \approx 5.1$ cm) transporting slug flows, the experimental-numerical studies conducted by Wang et al. (2018) revealed that the pipe vibration response is enhanced by the increasing slug unit velocity and the liquid slug length since these properties affect the rate of change of system stiffness, mass, damping and loading. For a continuous horizontal pipe with multiple supports ($L \approx 20$ m; $d \approx 3$ cm) and transporting unsteady slug flows, Liu and Wang (2018) experimentally and numerically examined the time-varying natural frequencies of the flexible pipe as a function of superficial velocities. They observed a critical gas velocity which may change qualitatively the trend of the average frequency depending on the liquid velocity, pipe stiffness and span length.

Recently, SIV in a catenary pipe has been experimentally observed in Zhu et al. (2018b) for unsteady slug flows ($L \approx 0.95$m; $d \approx 0.4$ cm), and Zhu et al. (2018a) for severe slugging, unsteady and steady slug flows ($L \approx 1.34$ m; $d \approx 0.8$ cm). They reported pipe planar responses whose frequencies are associated with the pressure fluctuation frequencies, suggesting a resonance. The measured vibration amplitudes depend on the slug characteristics including the gas-liquid lengths, flow rate ratios and superficial velocities, highlighting the pipe curvature

effect on the pipe-slug flow interaction behaviours. More recently, Mohmmed et al. (2019) experimentally investigated the effects of slug flow on vibrational behaviours of a horizontal pipe ($L \approx 8$ m; $d \approx 7.4$ cm) by measuring slug frequencies and the associated stresses. They revealed that the slug frequency increases with $u_{ls}$ but decreases with $u_{gs}$ and the slug induced stress is more significant near the inlet than the outlet.

## 2.3 Vortex-Induced Vibrations

Vortex induced vibration is a common phenomenon existing in many branches of engineering. For the offshore oil and gas industry, subsea production systems such as the cylindrical members of offshore platforms, free spanning pipelines and marine risers may experience VIV due to currents. The effects of this phenomenon have been comprehensively studied and published in the literature for both rigid (Sarpkaya, 2004) as well as long flexible (Wu et al., 2012) cylinders over past decades. Compared with the rigid cylinder, a flexible one is more complicated due to the intrinsic feature of having an infinite number of degrees of freedom associated with different natural frequencies and vibration modes. The complexity becomes more pronounced when a flexible curved body is considered. One of the practical examples is the steel catenary riser, which has been widely used and considered a promising offshore engineering solution in deepwater oil exploitation due to its commercial efficiency and technical simplicity. In contrast to conventional straight risers (e.g. top-tensioned risers), the VIV effects on a catenary riser may be different and complicated since the angle of the incident flow relative to the riser axis changes along the curved span, affecting the vortex wake behaviour (Miliou et al., 2003; Gallardo et al., 2014; Zhu et al., 2018c) in relation to the riser responses. This is also true when flow directions vary with respect to the curvature plane, which has already been demonstrated in some works on VIV of rigid curved cylinders (Assi et al., 2014; Seyed-Aghazadeh et al., 2015; Srinil et al., 2018a). In the following two sections, a selective review of experimental and numerical investigations on VIV of long flexible cylinders in catenary configurations is presented.

### *2.3.1 Experimental studies on VIV of catenary risers*

An experimental investigation of VIV on a catenary riser was carried out and reported by Halse et al. (1999), where the riser was tested accounting for individual and combined effects from waves and currents. By setting different relative angles between the catenary plane and the towing direction, VIV responses were analysed based on parallel (0°) and oblique (23°) flows to assess the effects of current directions. For a catenary riser subject to convex currents, Morooka and Tsukada (2013) experimentally investigated VIV responses of the riser under

various current velocities. Through the post-processed results both in time and frequency domains, they noticed that the riser dynamic behaviours are predominated by travelling waves, where the dominant mode and oscillation frequency could change with time depending on the different power-in regions of the riser. For a catenary riser subject to concave currents, Fan et al. (2015) observed that the riser can experience VIV under various current velocities. Results including time-varying strains at different locations and their associated oscillation frequency spectra are shown. They concluded that both CF and IL responses increase with current velocities alongside multi-frequency dynamic behaviours. Such correlation between current velocities and VIV responses of a catenary riser was also indicated in Domala and Sharma (2018), where the riser was tested under various boundary conditions, geometries and concave current with various velocities.

Considering a pure heave motion at the top of a steel catenary riser, Wang et al. (2015) reported the occurrence of out-of-plane VIV of the riser in still water. Based on various assigned heave amplitudes and periods, oscillation patterns including standing, travelling and end reflecting waves were noted. They highlighted the correlation between the Keulegan-Carpenter number and the time-varying features in VIV responses. A further research was carried out later in Wang et al. (2017), where the dominant roles of maximum Keulegan-Carpenter number and local riser velocity in the vessel motion-induced VIV were remarked. Such a type of VIV was also studied by Pesce et al. (2017), who conducted a series of tests to investigate vortex self-induced vibration of a catenary riser in still water by imposing vertical motions on the top. Out-of-plane motions were observed and attributed to the vortex-shedding phenomena led by the relative fluid-structure motions. Depending on the amplitudes and frequencies of the imposed forces, both single- and multi-modal riser responses corresponding to standing and travelling vibration patterns were revealed.

Recently, Chaplin and King (2018) carried out a series of test to investigate VIV responses of a catenary riser with various mass ratios, in which both concave and convex currents at various velocities were assigned. They noticed that the riser behaves differently when the flow direction varies. It was revealed that the dominant frequency increases linearly with the flow velocity for the concave current, whereas the convex current results in almost constant dominant frequencies independent of the flow velocities. More recently, VIV of a catenary pipe undergoing exponential sheared concave flows were experimentally investigated by Zhu et al. (2019b). Through observing the pipe responses and the associated wake vortex patterns, they concluded that the sheared flow leads to the multi-frequency VIV and the dominant frequency changes along the riser span. For an increased reduced velocity, an

upgraded mode order was recognized with a transition from standing-dominant to travelling-dominant wave oscillations, corresponding to a switch of wake vortex patterns.

*2.3.2 Numerical studies on VIV of catenary risers*

Dalheim (2000) conducted a CFD analysis on a steel catenary riser subject to VIV. Cross-flow response amplitudes, dominant modes and oscillation frequencies of the riser were predicted under different flow velocities and compared with both existed experimental tests (Halse et al., 1999) and numerical simulations by SHEAR7. It was found that VIV due to higher flow velocities tend to excite more significant multi-modal riser responses with greater amplitudes than the one at lower flow velocities.

Some of the experimental results from the model test (Halse et al., 1999) were later used by Lie et al. (2001) for a numerical investigation, where the programs of RIFLEX (Fylling et al., 1995) and VIVANA (Larsen et al., 2001) were jointly employed for a combined time-frequency domain VIV analysis of a catenary riser. Good qualitative agreements were realized between the experimental and numerical results. The effect of negative (concave to the catenary plane) and positive (convex to the catenary plane) flow directions on the peak oscillation frequencies was addressed and suspected to be associated with the local flow pattern around the inclined part. Such combined time-frequency domain approach was further used by Larsen and Passano (2006), where a numerical analysis of a catenary riser subject to flows perpendicular and parallel to the catenary plane was conducted to account for in-plane and out-of-plane VIV. Through examining the riser responses and the associated bending stresses, they observed local stress peaks at the touchdown point of the catenary riser.

Srinil et al. (2009) developed a semi-empirical model for investigating VIV of a catenary riser. In the numerical case study, a steady uniform current is assigned perpendicular to the curvature plane, where distributed van der pol wake oscillators were employed to model the hydrodynamic forces responsible for the IL and CF VIV. Maximum riser responses of uni-modal resonance were parametrically studied in terms of both structural and fluid-structural parameters. They highlighted the geometrical effects of the initial curvatures on the riser dynamics due to VIV. As an extended work, Srinil (2010) carried out a numerical study for multi-modal responses of a catenary riser owing to CF VIV. The semi-empirical model was further modified by taking the Reynolds number (Re) effect into account. The results demonstrate several VIV characteristics of long flexible cylinders such as multi-modal lock-in, switching, sharing and interaction, addressing the meaningful role of multimodal effects and geometric nonlinearities in VIV predictions.

A CFD approach was applied by Huang et al. (2010) to simulate a catenary riser undergoing VIV due to a uniform concave flow. The correlation between VIV responses and riser tension distribution was revealed and discussed. Through comparing the numerical results and field measurements, it was remarked that a flexible catenary riser could experience greater cross-flow oscillations than a top-tensioned riser. Recently, following their in-house experimental test (Morooka and Tsukada, 2013), Tsukada and Morooka (2016) numerically analysed the cross-flow VIV responses of the catenary riser subject to a uniform convex flow. To model the VIV hydrodynamic forces, a semi-empirical model based on the experimental data of rigid cylinders was implemented. The numerical results showed a good agreement with the experimental observations in terms of oscillation frequencies with capturing the multi-modal responses in travelling wave pattern. Table 2.3 summarizes the experimental and numerical studies of flexible catenary risers undergoing VIV, by distinguishing the flow conditions and riser specifications.

**Table 2.3:** Summary of experimental and numerical studies of flexible catenary risers subject to VIV.

| Studies | Flow velocity profile | Re | Flow direction | *D* (m) | Aspect ratio (*L*/*D*) | Other factor | Static top tension (N) |
|---|---|---|---|---|---|---|---|
| **Experimental studies** | | | | | | | |
| Halse et al. (1999) | U | - | CA, CV, OB (23°) | 0.023 | 1234.8 | Wave | 242 |
| Morooka and Tsukada (2013) | U | 400-600 | CV | 0.008 | 940 | - | 0.385 |
| Fan et al. (2015) | U | 8000-16000 | CA | 0.02 | 390 | Seabed effects | - |
| Chaplin and King (2018) | U | <70000 | CA, CV | 0.056 | 95.7 | - | ≈12.5/62.5 |
| Domala and Sharma (2018) | U | 700-5400 | CA | 0.014 | 321 | Topside floater motion | 67 |
| Zhu et al. (2019b) | S | 165-1015 | CA | 0.006 | 108.3 | - | - |
| **Numerical studies** | | | | | | | |
| Dalheim (2000) | U | 12075, 17020 | CA | 0.023 | 1234.8 | - | 242 |
| Lie et al. (2001) | U | 460-8280 | CA, CV | 0.023 | 1234.8 | - | 242 |
| Larsen and Passano (2006) | S | <343200 | CA,PP | 0.429 | 2062.9 | - | $7\times10^5$ |
| Srinil et al. (2009) | U | 32000-200000 | PP | - | 2581 | - | - |
| Srinil (2010) | U | <300000 | PP | - | 2581 | - | - |
| Huang et al. (2010) | U | 115500 | CA | 0.33 | 3300 | - | $\approx2.25\times10^5$ |
| Tsukada and Morooka (2016) | U | 400-600 | CV | 0.008 | 940 | - | 0.385 |

Note: CA, CV, PP, OB denote concave, convex, perpendicular, oblique flow directions, respectively.
U, S denote uniform and sheared flow profiles.

## 2.4 Summary

A literature review is performed in this chapter covering several aspects relevant to the present research work, including gas-liquid flow features, regime maps, SIV and VIV with respect to experimental and numerical studies. The investigation on two-phase flow maps provides the fundamental knowledge of flow regimes and transition criteria, which are strongly depending on several fluid-structure and operational parameters. Moreover, the maps can serve as a reference of initial conditions where the target flow may occur, i.e. slug flow for the present thesis. Modelling of SIV could be classified by structural geometries such as straight or curved ones, by slug flow modelling approaches such as the idealized or mechanistic models, by additional external excitations such as current or wave. It is realized that the state-of-art research reveals a lack of understanding in individual effects of slug characteristic parameters including slug unit length, travelling velocity and the resultant slug frequency on SIV phenomena. Thus, it shows the need in research for both numerical and experimental investigations of SIV, especially for a catenary configuration, which is evidently less-studied but leading to complex SIV due to the curved geometry. Moreover, although SIV and VIV are considered the main contributors to the fatigue of subsea risers, the studies on the combined internal and external excitations are rather limited in the literature. Within the scope of this thesis, VIV is considered and involved as an external excitation for identifying the potential role of SIV in the joint VIV-SIV. These attempts constitute the main contribution of the present research.

To accomplish this aim, a steady-state slug flow model is applied, accounting for the mass-momentum balances of gas-liquid phases as well as allowing the parametric studies of slug flow characteristics on SIV responses of the considered catenary riser. A semi-empirical model based on wake oscillators is then investigated first for a rigid body and implemented in combined VIV-SIV scenarios. Laboratory tests are conducted to achieve insights of SIV and verification of the proposed SIV numerical model.

# Chapter 3. Planar Dynamics of Catenary Riser Carrying Slug Flows

Flexible risers transporting hydrocarbon gas-liquid flows may be subject to internal dynamic fluctuations of multiphase densities, velocities and pressure changes. Previous studies have mostly focused on single-phase flows in oscillating pipes or multiphase flows in static pipes whereas understanding of multiphase flow effects on oscillating pipes with variable curvatures is still lacking. This chapter aims to numerically investigate fundamental planar dynamics of a long flexible catenary riser carrying slug gas-liquid flows and to analyse the mechanical effects of slug flow characteristics including slug unit length, translational velocity and fluctuation frequencies leading to resonances. A two-dimensional continuum model describing coupled horizontal and vertical motions of an inclined flexible/extensible curved riser subject to the space-time varying fluid weights, flow centrifugal momenta and Coriolis effects is presented. Steady slug flows are considered and modelled by accounting for the mass-momentum balances of gas-liquid phases within an elongated gas bubble (interfacing with the liquid film) and idealized slug unit cell comprising the slug liquid (containing small gas bubbles) parts. Several SIV features including the slug flow-induced transient drifts, mean and oscillatory displacements are highlighted. Parametric studies in terms of the slug unit length and the translational velocity are performed to investigate the individual effect of the slug unit length and the translational velocity on SIV response.

## 3.1 Mechanical Model of Curved Pipe Conveying Slug Flows

A planar dynamic model of an inclined curved bendable pipe conveying slug gas-liquid flows is displayed in Figure 3.1 where a fixed global Cartesian ($X$-$Y$) coordinate system is employed to describe the riser statics and dynamics. The slug flow along the pipe is schematically exemplified, which will be introduced in details in the following. The pipe is submerged in the water, subject to additional buoyancy and hydrostatic pressure. A local Lagrangian ($s$) coordinate system is introduced to track a series of slug flow units travelling upwardly from a fixed pipe bottom connection to a top stationary support. Standard pinned-pinned boundary conditions are considered, allowing only the end rotations of the long bendable pipe. In this study, the riser pipe is considered to move in two dimensions with coupled horizontal ($u$) and vertical ($v$) displacements from its planar ($\tilde{x}$, $\tilde{y}$) static equilibrium, subject to the gravity ($g$) and the longitudinal momentum of internal flows. This planar response scenario is plausible since recent SIV experiments of a catenary flexible pipe by Zhu et al. (2018b) revealed negligible out-of-plane vibrations, depending on the system flow rates.

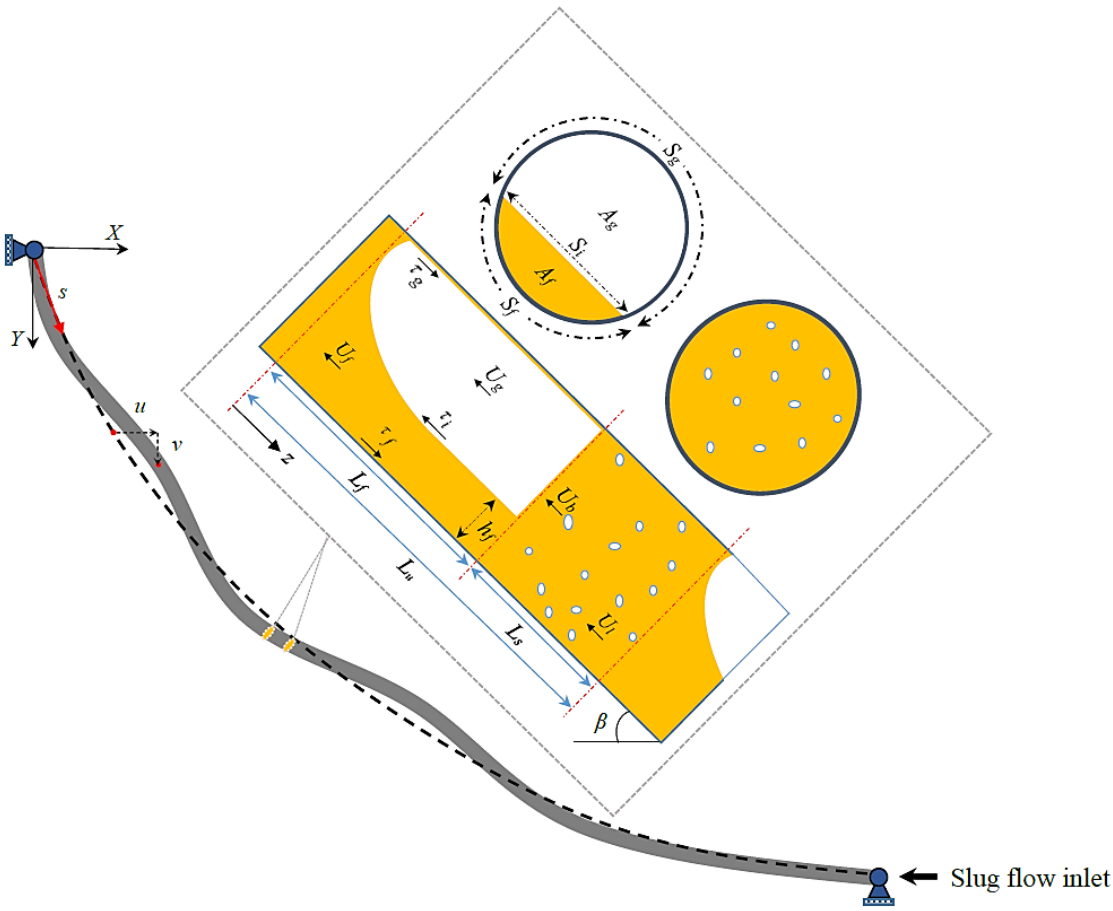


**Figure 3.1:** A planar dynamic model of an inclined curved flexible riser conveying slug gas-liquid flows.

To arrive at the system equations of motion governing the planar dynamics of an inclined bendable pipe transporting slug flows, some main assumptions and hypotheses are employed as follows.

- Materials of the pipe are linearly elastic, with spatially uniform properties including the pipe mass per unit length ($m_s$), outer ($D$) and inner ($d$) diameters with a smooth surface, pipe cross-sectional area ($A_r$), inner area ($A$), outer area ($A_o$), moment of inertia ($I$) and the Young's modulus ($E$). Hence, the bending ($EI$) and axial stiffness ($EA$) terms are constant. Owing to the longitudinal internal flow loading character and the inherent slenderness of the bendable pipe with a high aspect ($L/D$) ratio ($L/D \approx 10^2$-$10^3$), shear and torsional rigidities are disregarded based on the Euler-Bernoulli theory. Therefore, the pipe cross section under loading remains circular with a plane perpendicular to its longitudinal axis.
- Static configurations of the loaded pipe are established in two consecutive stages. In the first stage, the pipe forms into an inextensible sagged catenary due only to its own weight ($m_s g$) and buoyancy (in the case of a submerged pipe). For a specified top tension or pipe

length, a closed-form hyperbolic expression describing a catenary profile as a function of $s$ can be simply obtained (Srinil et al., 2009). In the second stage, such a catenary geometry is further subject to the weights of moving slug trains which, simultaneously, induce the flow momenta leading to the pipe oscillations. In this condition, the riser displacements ($u$, $v$) comprise static and dynamic components which are physically coupled. Once a steady-state response is achieved, the riser dynamics can be described by referring to this second static drift. Correspondingly, the slug flow-induced extensional static and dynamic strains can be evaluated through the differential infinitesimal arc lengths and the strain-displacement relations.

- Slug flows are assumed to be fully developed and non-homogeneous, travelling steadily as a series of slug units through the catenary pipe. As displayed in Figure 3.1, each slug unit comprises (i) a liquid-dominant phase containing very small gas bubbles (i.e. typically called a liquid slug) and (ii) a long non-uniform gas phase above a thin liquid film (i.e. an elongated bubble), travelling with a single translational unit velocity relative to the pipe ($U_t$). Slug properties including individual phase mass per unit length ($m_i$), density ($\rho_i$), local velocity ($U_i$) and internal fluid pressure ($P$) may be described through a conservation of mass and momentum within a control fluid volume where a subscript $i$ = 1 and 2 denotes the coexisting liquid and gas phase, respectively. Consequently, the pipe motions are subjected to these distributed parameters which vary in space and time following the specified and constant $U_t$.
- Slug flow-induced displacements with respect to a pipe diameter are assumed to be small, compared with the riser length such that the effects of geometric nonlinearities and multi-modal coupling with out-of-plane motions are negligible (Srinil et al., 2004). For steady flows, the catenary pipe is subject to the travelling and non-uniformly distributed parameters (mass inertia, weight, velocity, pressure) and the gas-liquid properties are assumed to be undisturbed by the pipe oscillations with small amplitudes.

In the literature, several riser mechanical models have been derived based on a Hamiltonian or Newtonian formulation (Chen, 1985; Lee and Chung, 2002; Paidoussis, 2014). By following Chucheepsakul et al. (2003) and Srinil et al. (2007), the variational principles are herein applied to account for the potential or strain energy due to the static tension, axial dynamic stretching and bending, the work done by the weight, pipe inertia, viscous damping and internal flow inertia accounting for the absolute flow velocity in the Cartesian coordinate system. Based on the above-mentioned assumptions and by describing the pinned-pinned pipe motions with respect to the self-weight-based static configuration ($\tilde{x}$, $\tilde{y}$), the linear partial-

differential equations of coupled horizontal and vertical motions of an inclined curved pipe conveying steady slug flows may be expressed in a dimensional form as

$$\left(m_t+\sum_{i=1}^{2}m_i\right)\ddot{u}+c\dot{u}+EIu^{iv}-\left[\left(T+2\nu(P_oA_o-PA)\right)u'+EA_r\left(\tilde{x}'^2u'+\tilde{x}'\tilde{y}'v'\right)\right]'+\sum_{i=1}^{2}\left[m_iU_i^2\left(\tilde{x}''+u''\right)+2m_iU_i\dot{u}'\right]=0, \quad (3.1)$$

$$\left(m_t+\sum_{i=1}^{2}m_i\right)\ddot{v}+c\dot{v}+EIv^{iv}-\left[\left(T+2\nu(P_oA_o-PA)\right)v'+EA_r\left(\tilde{x}'\tilde{y}'u'+\tilde{y}'^2v'\right)\right]'+\sum_{i=1}^{2}\left[m_iU_i^2\left(\tilde{y}''+v''\right)+2m_iU_i\dot{v}'\right]=\sum_{i=1}^{2}m_ig, \quad (3.2)$$

in which $T(s)$ is the initial pipe wall tension, $P(s,t)$ is the pressure induced by internal flows, varying due to the influence of wall/interfacial frictions and gravity (see Section 3.2, Eqs. (3.8) and (3.9)), and $c$ is the overall linear damping coefficient which may be identified in terms of a modal damping ratio $\xi$. In the case of a submerged pipe, we further account for the external hydrostatic pressure $P_o(s)$, the total mass $m_t = m_s + m_a$, in which $m_a$ is the still-water added mass equal to $\rho_o A_o$, with $\rho_o$ being the external water density, and the effect of Poisson's ratio ($\nu$) through the so-called apparent tension concept (Sparks, 1984). A dot (prime) denotes differentiation with respect to the time $t$ ($s$). It is worth noting that the added mass coupling between $X$ and $Y$ directions are not considered in the present model. For an improved model, the coupling effect due to the different incident flow directions relative to the structure on $m_a$ should be accounted for, which potentially modifies the total system mass and the consequent resonant response frequency. In the present study, this effect is assumed to be small compared to the total weight of steel pipe and internal fluid and hence not considered. Therefore, the same $m_a$ in $X$ and $Y$ directions are applied in the above equations of motion. This assumption has also been considered in Srinil (2010) and Zanganeh and Srinil (2016).

In this study, the internal flow-related terms may be approximated by accounting for a summation Σ of individual liquid and gas phase quantities, as in Monette and Pettigrew (2004), without a phase interaction which could be considered through a more rigorous transient two-fluid model (Issa and Kempf, 2003). Note that $U_i$ have a negative sign for upward flows (Païdoussis and Luu, 1985) because of taking the opposite direction to the $s$ coordinate, see Figure 3.1. Eqs (3.1) and (3.2) contain the internal flow-induced momenta forces due to the gyroscopic Coriolis ($m_iU_i$) effect depending on the angular velocity of the pipe element, and the centrifugal or centripetal $m_iU_i^2$ acceleration contributing to the pipe axial tension variation and depending on the pipe dynamic curvatures. Moreover, a static centrifugal effect related to the static curvatures ($\tilde{x}''$, $\tilde{y}''$) is accounted for. The space-time varying weight term in Eq. (3.2) is responsible for the gravity effects from the internal flow. This term has been neglected in Ma and Srinil (2018) who applied modal shapes as initial displacement conditions.

Due to lack of an analytical solution for such a gyroscopically conservative system with travelling and non-uniformly distributed parameters, Eqs. (3.1) and (3.2) are herein numerically solved by using a 2nd order finite difference discretization in space combined with a 4th order Runge-Kutta time integration as performed, e.g., in Cabrera-Miranda and Paik (2019). Convergence of numerical simulations is checked for which validation of the present riser model is shown in Table 3.1 based on a comparison of fundamental natural frequencies ($f_{n1}$). To obtain the natural frequency through the proposed numerical scheme, a free vibration simulation is carried out by applying the riser mode shape obtained from OrcaFlex (Orcina, 2016) as an initial displacement condition. The riser responses are analysed via Fast Fourier Transform (FFT) to capture $f_{n1}$ subject to an internal single-phase flow at different velocities.

**Table 3.1:** Validation of the present model and numerical simulations through comparison of natural frequencies of production riser with previously published results.

| $U_i$ (m/s) | $f_{n1}$ (rad/s) (accounting for bending/tension effects) | | | $f_{n1}$ (rad/s) (accounting for only tension effect) | | |
|---|---|---|---|---|---|---|
| | (a) M. (2007) | (b) This study | $\left\|\frac{a-b}{a}\right\|\times 100$ | (a) M. (2007) | (b) This study | $\left\|\frac{a-b}{a}\right\|\times 100$ |
| 0 | 0.3001 | 0.2992 | 0.30 | 0.2891 | 0.2891 | 0 |
| 5 | 0.2994 | 0.2985 | 0.30 | 0.2881 | 0.2882 | 0.03 |
| 10 | 0.2972 | 0.2962 | 0.34 | 0.2853 | 0.2857 | 0.14 |
| 15 | 0.2934 | 0.2923 | 0.37 | 0.2804 | 0.2813 | 0.32 |
| 20 | 0.2880 | 0.2874 | 0.21 | 0.2731 | 0.2736 | 0.18 |
| 25 | 0.2809 | 0.2799 | 0.36 | 0.2627 | 0.2652 | 0.95 |
| 30 | 0.2717 | 0.2711 | 0.22 | 0.2478 | 0.2517 | 1.57 |
| 35 | 0.2603 | 0.2592 | 0.42 | 0.2224 | 0.2279 | 2.47 |
| 40 | 0.2461 | 0.2446 | 0.61 | Unstable* | Unstable* | |
| 45 | 0.2282 | 0.2255 | 1.18 | | | |
| 50 | 0.2052 | 0.2021 | 1.51 | | | |
| 55 | 0.1738 | 0.1701 | 2.13 | | | |
| 60 | 0.1250 | 0.1215 | 2.80 | | | |
| 65 | Unstable** | Unstable** | | | | |

Note: Critical $U_i \approx 38$* and 64** m/s.

In the context of instability analysis of the pipe transporting a single-phase flow with increasing velocity $U_i$, a vertical fully-submerged production steel riser given by Moe and Chucheepsakul (1988) is considered whose $E = 2.07\times10^{11}$, $D = 0.26$, $d = 0.20$ m, $\rho_i = 998$ kg/m$^3$, $L = 300$ m, $\nu = 0.5$ and $T = 476.2$ kN. Good agreement with less than 3% differences can be seen in Table 3.1 based on the present finite difference simulation and finite element method in Monprapussorn et al. (2007). The fundamental mode experiences a divergence instability (i.e.

the total axial stiffness becomes negative as $U_i$ is increased) at the critical $U_i \approx 38$ m/s in the case of bending-neglected riser whereas its stability is maintained to a higher $U_i$ if the bending rigidity is accounted for. In the latter case, the critical $U_i \approx 64$ m/s. This validation enables us to apply the present model and numerical approach to the SIV analysis in Section 3.4 where results are based on a time step $\Delta t = 0.001$s and a pipe discretized segment $\Delta s = 5$m ensuring the converged simulations of transient and steady-state responses.

### 3.2 Mechanistic Model of Slug Gas-Liquid Flows

The concept of a slug unit cell, first introduced by Wallis (1969), is herein applied to a small pipe segment having a local inclination angle of $\beta$, as depicted in Figure 3.1. Each slug unit cell has a length of $L_u$ which is further subdivided into two main parts: a liquid slug zone of length $L_s$ and a liquid film zone of length $L_f$.

In the film zone which may be treated as a stratified flow regime, a non-uniformly elongated gas bubble is located at the upper part of the inclined pipe with a gas void fraction ($\alpha_f$) surrounded by a bottom thin liquid film with a certain holdup ($R_f$). Such a long gas bubble and liquid film travels with a local velocity of $U_g$ and $U_f$, respectively, and they are subject to either the gas-wall ($\tau_g$), liquid-wall ($\tau_f$) or gas-liquid interfacial ($\tau_i$) shear stresses. As for the liquid slug zone separating the two consecutive films, the bubbly liquid phase fills the whole cross section, travelling with an average velocity of $U_l$, subject to $\tau_f$ and having a much greater holdup ($R_s$) than the associated void fraction ($\alpha_s$) of the small dispersed gas bubbles propagating with an average axial velocity of $U_b$. A sign of actual velocities ($U_g$, $U_f$, $U_l$, $U_b$) is meaningful as it is negative in the upward flow direction opposite to the $s$ coordinate (Figure 3.1). Note that $U_l$ and $U_b$ are uniform within $L_s$ whereas $U_g$ and $U_f$ are spatially varied along $L_f$, depending on the film thickness or height ($h_f$).

#### *3.2.1 Governing equations*

To capture a spatial distribution of gas-liquid masses, velocities and pressure gradient which are the key input parameters for the inclined pipe model (Eqs. (3.1) and (3.2)), a 1D steady slug flow model derived by Taitel and Barnea (1990) is herein employed, by assuming the incompressible gas-liquid phases. This model was also considered by Chatjigeorgiou (2017) for a forced vibration problem of riser subject to a support motion. Based on the mass and momentum conservations of gas and liquid phases over a slug unit cell, the key unknown $h_f$ as function of the slug unit coordinate $z_s$ (from $z_s = 0$ to $z_s = L_f$) maybe determined through

$$\frac{dh_f}{dz_s}=\frac{\frac{\tau_f S_f}{A_f}-\frac{\tau_g S_g}{A_g}-\tau_i S_i\left(\frac{1}{A_f}+\frac{1}{A_g}\right)+(\rho_l-\rho_g)g\sin\beta}{\left[(\rho_l-\rho_g)g\cos\beta-\left\{\rho_l V_f\frac{(U_t-U_l)R_s}{R_f^2}+\rho_g V_g\frac{(U_t-U_b)(1-R_s)}{(1-R_f)^2}\right\}\frac{dR_f}{dh_f}\right]}, \tag{3.3}$$

where $\rho_g$ ($\rho_l$) is the gas (liquid) density, $V_g$ ($V_f$) the relative gas (liquid film) velocity, $A_g$ ($A_f$) the cross-sectional gas (liquid film) area, $S_g$ ($S_f$) the associated wetted perimeter, and $S_i$ the interfacial width. Depending on $U_g$, $U_f$ and $U_l$, one may assume that $\tau_f=f_f\rho_l U_f|U_f|/2$, $\tau_g=f_g\rho_g U_g|U_g|/2$ and $\tau_i=f_i\rho_g(U_g-U_f)|U_g-U_f|/2$ where $f_f$, $f_g$ and $f_i$ are the associated friction coefficients (Taitel and Dukler, 1976; Spedding and Hand, 1997). As displayed in Figure 3.1, the pipe cross section has the geometric properties $\phi=2\cos^{-1}(1-2h_f/d)$, $A_f=d^2(\phi-\sin\phi)/8$, $A_g=A-A_f$, $S_f=\phi d/2$, $S_i=d(2-2\cos\phi)^{1/2}/2$, and $S_g=\pi d-S_f$, where $\phi$ denotes the liquid film geometric angle. By specifying a translational velocity of the slug unit $U_t$, $V_f$ and $V_g$ are expressed as

$$V_f=U_t-U_f=(U_t-U_l)R_s/R_f, \tag{3.4}$$

$$V_g=U_t-U_g=(U_t-U_b)\alpha_s/\alpha_f, \tag{3.5}$$

in which a geometric relationship between $R_f$ ($\alpha_f=1-R_f$) and $h_f$ for a stratified film flow is defined by Taitel and Barnea (1990)

$$R_f=\frac{1}{\pi}\left[\pi-\cos^{-1}\left(\frac{2h_f}{d}-1\right)+\left(\frac{2h_f}{d}-1\right)\sqrt{1-\left(\frac{2h_f}{d}-1\right)^2}\right]. \tag{3.6}$$

Accordingly, $dR_f/dh_f=(4/\pi d)[1-(2h_f/d-1)^2]^{0.5}$ which can be then substituted into Eq. (3.3). In numerically integrating Eq. (3.3) for $h_f$, a certain criterion is imposed to determine a suitable film length ($L_f$) for a given liquid and gas flow rate. By following Taitel and Barnea (1990), the liquid mass balance over a slug unit entails

$$u_{ls}=U_l R_s+U_t(1-R_s)L_f/L_u-(U_t/L_u)\int_0^{L_f}\alpha_f dz_s, \tag{3.7}$$

where $u_{ls}$ is the superficial liquid velocity to be assigned along with the superficial gas velocity $u_{gs}$. For a constant $\rho_g$ and $\rho_l$, the volumetric flow rate through any cross section is constant such that the mixture velocity $U_s=u_{ls}+u_{gs}=U_l R_s+U_b\alpha_s$ for the liquid slug zone or $U_f R_f+U_g\alpha_f$ for the film zone. All Eqs. (3.4)-(3.7) are combined to evaluate the film zone features. As the liquid slug section may be regarded as a bubble flow, the associated properties may be estimated through the existing empirical correlations as described in Section 3.2. Ultimately, a pressure drop ($dP_u$) over a slug unit length may be evaluated through

$$dP_u = \rho_u L_u g \sin\beta + \frac{\tau_f \pi d}{A} L_s + \int_0^{L_f} \left( \frac{\tau_f S_f + \tau_g S_g}{A} \right) dz_s, \tag{3.8}$$

where $\rho_u = \alpha_u \rho_g + (1-\alpha_u)\rho_l$ is the average density and $\alpha_u$ is the average void fraction with $\alpha_u = (u_{gs} - U_b\alpha_s + U_t\alpha_s)/U_t = (-u_{ls} + U_l R_s + U_t\alpha_s)/U_t$ (Barnea, 1990). Note that $dP_u$ consists of three main components associated with the gravitational contribution, frictional effects in the liquid slug and film zones (Taitel and Barnea, 1990). As $\alpha_u$ is independent of the film height, bubble and slug lengths, the first term in Eq. (3.8) may be assessed independently of the slug structure.

*3.2.2 Slug flow variables and solution steps*

For each hydrodynamic slug unit, the present mechanistic model depends on several input and output variables. These may be classified into 5 groups (a-e) as follows.

a) Specified gas-liquid flow properties: $\rho_g$, $\rho_l$, $\nu_g$, $\nu_l$, $u_{gs}$, $u_{ls}$, $U_s$, $L_u$,
b) Specified pipe geometric variables: $\beta$, $d$, $A$,
c) Fluid variables identified through empirical or 'closure' functions: $R_s$ ($\alpha_s$), $U_b$, $U_t$, $U_l$, $f_g$, $f_f$, $f_i$, $U_d$, $U_0$, $U_\infty$, $\sigma$,
d) Empirical coefficients associated with functions in c): $C$, $B$, $C_{fg}$, $n_o$, $j_o$,
e) Numerically predicted variables: $\phi$, $A_g$, $A_f$, $S_g$, $S_f$, $S_i$, $h_f$, $L_f$, $\alpha_f$, $R_f$, $L_s$, $U_g$, $U_f$, $\alpha_u$, $\rho_u$, $dP_u$.

By assigning the inputs a) and b), the film zone hydrodynamics is first analysed to identify a spatial distribution of $h_f$, establishing a long and nonlinear gas bubble shape. The so-called closure relationships or empirical functions for $R_s$, $U_t$ and $U_b$ are required, rendering an empirical $\alpha_s$ and $U_l$ since $\alpha_s = 1 - R_s$ and $U_l = (U_s - U_b\alpha_s)/R_s$. Closure functions may be correlated with experimental data in the literature. For vertical tubes, Fernandes et al. (1983) suggested a constant $R_s = 0.75$ ($\alpha_s = 0.25$). However, $R_s$ should be variable for inclined pipes as, e.g., in Greskovich and Shrier (1971) who reported $0.5 < R_s < 1$. Due to a lack of $R_s$ correlation for such a larger-diameter inclined pipe as offshore riser, a widely used $R_s$ correlation of Gregory et al. (1978) with $R_s = 1/[1+(U_s/8.66)^{1.39}]$ is herein considered as it has been verified and applied to several mechanistic fluid models (Xiao et al., 1990; Petalas and Aziz, 1998; Zhang et al., 2003) .

As for $U_t$, the associated closure formula is typically a linear superimposition ($U_t = CU_s + U_d$) of the drift velocity ($U_d$) of the elongated bubble in stagnant liquid and the flow mixture contribution $U_s$ with a factor $C$ being the ratio of the maximum and mean velocities of the liquid slug (i.e. $C > 1$). For a good approximation, $C$=1.2 (2) for turbulent (laminar) flows are recommended in Taitel and Barnea (1990). Bendiksen (1984) proposed $U_d = 0.54(gd)^{0.5}\cos\beta + 0.35(gd)^{0.5}\sin\beta$, which is shown to be a good approximation for inclined pipes with $0^\circ \le \beta \le 90^\circ$

(Xiao et al., 1990; Kaya et al., 1999).

As for $U_b$, the corresponding closure may be defined in a similar manner to $U_t$ as $U_b = BU_s + U_0$, in which $B$ is the distribution parameter and $U_0$ is the average drift velocity of dispersed bubbles. By following Bendiksen (1984), $B(\beta)=B(0^\circ)+[B(90^\circ)- B(0^\circ)]\sin^2\beta$ may be used where $B$ is bounded between 1 (horizontal pipe) and 1.2 (vertical pipe). $U_0$ may be obtained through the relation $U_0 = U_\infty(1-\alpha_s)^{j_o}$, where the modification factor $j_o \approx 0$ (i.e. $U_0 \approx U_\infty$) for the liquid slug (Taitel and Barnea, 1990), and the bubble rising velocity $U_\infty = 1.54[\sigma g(\rho_l - \rho_g)/\rho_l^2]^{0.25}$ with $\sigma$ being the interfacial surface tension (Harmathy, 1960). For a laminar and steady flow with low $u_{gs}$ and $u_{ls}$, $\sigma$ may be small and the associated surface tension parameter $\sigma/[(\rho_l - \rho_g)(d/2)^2 g]$ may be assumed to be equal to 0.001 (Chatjigeorgiou, 2017). Note that $U_b$ is equal to the gas velocity in the liquid slug zone whereas $U_t > U_g$ in the film zone (Taitel and Barnea, 1990).

For a pipe with smooth inner surface, the Blasius correlation may be used: $f_f = C_{fg}(D_{hf}U_f/\nu_l)^n$ and $f_g = C_{fg}(D_{hg}U_g/\nu_g)^{n_o}$ in which $D_{hf} = 4A_f/S_f$ or $D_{hg} = 4A_g/(S_g + S_i)$ is the hydraulic diameter, $D_{hf}U_f/\nu_l$ or $D_{hg}U_g/\nu_g$ is the Reynolds number (Re), $C_{fg} = 16$ and $n_o = -1$ for laminar flow if Re < 2000, $C_{fg} = 0.046$ and $n_o = -0.2$ for turbulent flow if Re > 3000 (Taitel and Barnea, 1990), $\nu_l$ ($\nu_g$) the liquid (gas) kinematic viscosity. In the range 2000 < Re < 3000, a friction coefficient may be interpolated to avoid a discontinuity across the flow transition region (Zhang et al., 2003). For an inclined pipe with a stratified flow feature in the liquid film zone, it is assumed that $f_i \approx 0.014$ (Cohen and Hanratty, 1968). A random change in $f_i$ has been found to produce a negligible effect on the riser dynamics (Chatjigeorgiou, 2017). These coefficients have been widely used in both the mechanistic (Zhang et al., 2003) and transient (Bonizzi et al., 2009) models.

With the selected closures and empirical coefficients, the numerical solution starts by letting $R_f = R_s$ as an initial condition at $z_s = 0$ for each slug unit. This assumption is reasonable as a head section of the elongated bubble ($z_s = 0$) and a tail part of the liquid slug ($z = L_u$) of consecutive slug units share the same location (Figure 3.1). With $R_f = R_s$, Eq. (3.6) is solved for the initial $h_f = h_s$ which is then compared with the critical film height $h_c$ obtained from the zeroing denominator in Eq. (3.3). The $h_f$ value at $z_s = 0$ is assigned to be equal to the lower one of $h_s$ vs. $h_c$ (Taitel and Barnea, 1990). With the deduced $h_f$, $R_f$, $\alpha_f$, $U_f$, $U_g$, $A_g$, $A_f$, $S_g$, $S_l$ and $S_i$ are computed, respectively. Consequently, Eq. (3.3) is numerically and spatially integrated using a 4th order Runge-Kutta scheme and a small increment $\Delta z_s$ of 0.001 m, during which all related parameters are updated for every station to obtain the complete spatial $h_f$ profile. This process

is carried out until the mass balance condition in Eq. (3.7) is fulfilled so that $L_f$ , and subsequently $L_s$, is identified: $L_u = L_f + L_s$. The pressure drop is then evaluated through Eq. (3.8).

For a uniform inner cross section, $\Sigma m_i = (R_s\rho_l + \alpha_s\rho_g)A$ within a liquid slug part whereas $\Sigma m_i = (R_f\rho_l + \alpha_f\rho_g)A$ within a liquid film zone. Depending on a specified bottom or top end pressure, a cross-sectionally averaged or mean pressure variation $P_m(s)$ can be identified through the pressure drop calculation in Eq. (3.8). For a given $U_t$, element spacing $\Delta s$ and time step $\Delta t$, a function of the space-time varying slug flow properties ($m_i$, $U_i$, $P$), contributing to Eqs. (3.1) and (3.2), may be expressed as

$$\begin{aligned} m_i(s,t) &= m_i(s + U_t\Delta t, t + \Delta t), \\ U_i(s,t) &= U_i(s + U_t\Delta t, t + \Delta t), \\ P(s,t) &= P_m(s + U_t\Delta t)\left[1 + k\tilde{R}(s + U_t\Delta t, t + \Delta t)\right], \end{aligned} \tag{3.9}$$

where $k$ is the percentage of pressure fluctuation which is assumed to have a space-time varying profile similar to that of the liquid hold up (Hara, 1977) to account for their interdependence. Herein, the normalized holdup profile ($\tilde{R}$) with a maximum (minimum) amplitude of 1 (−1) is introduced so that the fluctuation occurs around $P_m$. In the following Section 3.3, the slug gas-liquid flow features depending on the system flow-pipe parameters are presented prior to the analysis of pipe planar SIV in Section 5.

### 3.3. Fundamental Pipe Properties and Slug Flow Characteristics

Prior to investigating the planar dynamics of catenary pipe transporting slug flows and the effects of slug flow-pipe parameters on SIV, it is first important to gain some fundamental insights into the pipe statics (geometric profile, pre-tension variation) and modal (natural frequencies, modes) properties, and the combined gas-liquid flow features ($h_f$, $u_L$, $u_G$, $R$, $P_m$) contributing to the mass, velocity and pressure variables in Eqs. (3.1) and (3.2). By way of examples applicable to a deep-water application, we consider a very long catenary riser pipe made of steel with $E$ = 207 GPa, $L$ = 2025 m, $d$ = 0.385 m and $D$ = 0.429 m ($L/D \approx 4720$). The variable-inclination riser is fully submerged in a 1000 m depth of quiescent sea waters. The pipe materials have an effective weight of 699 N/m and initial top tension of 1860 kN, transporting upwardly the combined oil ($\rho_l$ = 790 kg/m$^3$) and methane gas ($\rho_g$ = 0.675 kg/m$^3$) flows (Chatjigeorgiou, 2017). Based on the stability analysis of Bakis and Srinil (2019), this considered top-tensioned and pinned-pinned riser is free from a divergence instability due to an internal flow which would occur at a very high flow velocity of about 80 m/s.

A referenced static profile of a submerged catenary pipe subject to the combined effective weight and external hydrostatic pressure is displayed in Figure 3.2 including (a) $\tilde{x}$-$\tilde{y}$ coordinates,

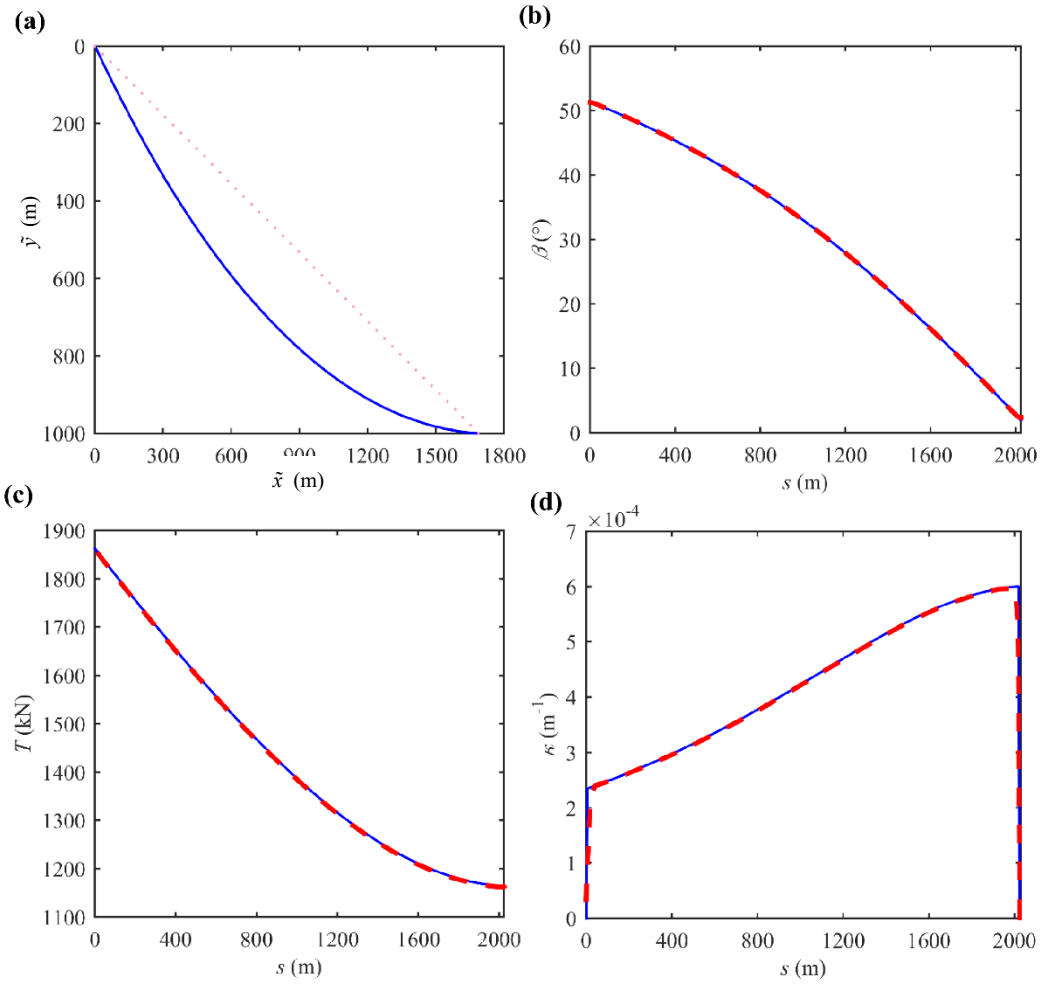


**Figure 3.2:** Properties associated with initial static profile of catenary riser: (a) $\tilde{x}$-$\tilde{y}$ coordinates, (b) local inclination angles, (c) pre-tensions, (d) curvatures: blue and red dashed lines denote the results of present study and OrcaFlex (Orcina, 2016).

(b) local inclination angles $\beta$ ($0 < \beta < 90^{o}$) measured clockwise from the $X$ axis, (c) pre-tensions and (d) curvatures along $s$ from the top ($\tilde{x} = \tilde{y} = s = 0$) to the bottom ($\tilde{x} = 1688$, $\tilde{y} = 1000$, $s = 2025$ m). Validation of the static profile is conducted by comparing the results (blue lines) against the ones (red dashed lines) obtained from OrcaFlex (Orcina, 2016). In Figure 3.2a, the maximum sagging measured perpendicularly from the inclined chord, per the chord span (dashed line), is about 0.11 at $s \approx 1096$ m (more than a half of $L$ at $s \approx 1012.5$ m). This signifies the pipe asymmetric geometry which would influence on the associated modal characteristics of SIV responses. In Figure 3.2b, the maximum $\beta \approx 51^{o}$ occurs at the top whereas the minimum $\beta \approx 2^{o}$ occurs at the bottom, the latter reflecting a nearly horizontal laid-down pipe. By averaging all nodal $\beta$ (with $\Delta s = 1$m), the mean $\beta \approx 30^{o}$ is coincidentally equal to the chord inclination ($\tan^{-1}(1000/1688)$). In Figure 3.2c, the variable pre-tension experiences a considerable reduction (37.4%) from the top (1860 kN) to the bottom (1164 kN), caused by the distributed gravity and static pressure loads. Such tension and asymmetric profile changes affect

the pipe stiffness properties. In Figure 3.2d, the pipe curvatures ($\kappa$) are small (order of $10^{-4}$), albeit nonlinearly varying. It is worth mentioning that the maximum (minimum) $\kappa$ is near the riser bottom (top) before the riser ends, which leads to a steep change in $\kappa$ close to $s$=0 m and $s$=2025m. This is due to the effect of bending stiffness (Sparks, 2007) and the assumption of pinned-pinned boundary condition, which yield the zero values of curvature at the riser boundaries. Additional travelling slug flow masses would further modify such initial geometry and tensions along the span due to the moving weight effect and the internal pressure drop change. Based on the finite element method of free vibrations (Safrendyo and Srinil, 2018), natural frequencies ($f_n$) of the submerged and empty pipe in Figure 3.2 are found to be in the range of 0.03-0.71 Hz for the first 40 planar modes, suggesting a tension-dominated flexible riser due to such closely spaced low frequencies (Srinil et al., 2009).

As for slug flows consisting of a series of slug unit trains, a fixed normalized unit length $L_u/d$ is herein considered so that the gas-liquid mass balances of all slug units travelling along the pipe span are consistent with the assumed steady-state flow model described in Section 3.1. As each slug unit propagates upwardly, part of the liquid film may move backwards with a negative $U_l$ relative to the gas-liquid interface. Nevertheless, the amount of this part is picked up by the following slug liquid. This enables a constant flow rate at a fixed cross section over the time of the slug unit passage (Taitel and Barnea, 1990). Based on the experimental gas-liquid flow maps of inclined pipes with $0^\circ < \beta < 90^\circ$ (Spedding and Nguyen, 1980), a volumetric flow rate is chosen such that $u_{ls}$ and $u_{gs}$ are associated with a slug flow regime whose likelihood of occurrence increases with $\beta$ (Spedding and Nguyen, 1980). The main slug unit outputs may be described as a function of $\beta$, $L_u/d$, $u_{gs}$ and $u_{ls}$, where the associated slug unit velocity $U_t$ depends on the mixture velocity $U_s = u_{ls} + u_{gs}$. For steady flows, a characteristic or primary slug frequency ($f_s$) may be approximated as $f_s \approx U_t/L_u$ (Hz), depending on the specified $L_u/d$. In the literature, the suggested $L_u/d$ values for subsea applications are variable, depending on several practical and operational factors as exemplified in Table 2.2. In this study, $L_u/d$ is assumed such that a unique real-valued numerical solution of the Taitel-Barnea model can be found.

By assigning $u_{ls}$ = 2 m/s, Table 3.2 presents case studies with specified $\beta$, $L_u/d$, $u_{gs}$, $U_t$, and the associated $f_s$. Note that $\beta$ is based on the maximum, minimum and averaged inclinations from Figure 3.2b. There are two cases of parametric ($L_u/d$, $U_t$) pairs yielding a comparable $f_s$: (80, 6) vs. (208, 16) and (63, 16) vs. (80, 20). These cases will be elaborated in Section 3.4 to verify whether there is a dependence of SIV on individual $L_u/d$ or $U_t$, regardless of $f_s$.

**Table 3.2:** Specified slug flow parameters for SIV case studies with $u_{ls}$ = 2 m/s.

| $\beta$ (°) | $L_u/d$ | $u_{gs}$ (m/s) | $U_t$ (m/s) | $f_s$ (Hz) |
|---|---|---|---|---|
| 30 | 63, 80, 120, 140, 208 | 2.0 | 6 | 0.25, 0.20*, 0.13, 0.11, 0.08 |
| 2, 15, 30, 51 | 80 | 4.5 | 9 | 0.29 |
| 30 | 80 | 7.0 | 12 | 0.39 |
| 30 | 63, 80, 120, 140, 208 | 10.3 | 16 | 0.66**, 0.52, 0.35, 0.30, 0.20* |
| 30 | 80 | 14.0 | 20 | 0.66** |

Note: * and ** denote cases with similar $f_s$.

**Table 3.3:** Slug flow profile properties in cases of varying (a) $U_t$, (b) $L_u/d$ and (c) $\beta$.

**(a)** $\beta$ = 30° and $L_u/d$ = 80

| $U_t$ (m/s) | $L_f$ (m) | $L_s$ (m) | $L_u$ (m) | $L_f/L_s$ | $L_f/L_u$ | $\alpha_{vol}$ |
|---|---|---|---|---|---|---|
| 6 | 8.96 | 21.84 | 30.8 | 0.41 | 0.29 | 0.393 |
| 9 | 14.74 | 16.06 | 30.8 | 0.92 | 0.48 | 0.579 |
| 12 | 17.8 | 13 | 30.8 | 1.37 | 0.58 | 0.676 |
| 16 | 20.2 | 10.6 | 30.8 | 1.90 | 0.66 | 0.749 |
| 20 | 21.7 | 9.1 | 30.8 | 2.38 | 0.70 | 0.797 |

**(b)** $\beta$ = 30° and $U_t$ = 16 m/s

| $L_u/d$ | $L_f$ (m) | $L_s$ (m) | $L_u$ (m) | $L_f/L_s$ | $L_f/L_u$ | $\alpha_{vol}$ |
|---|---|---|---|---|---|---|
| 63 | 16.73 | 7.37 | 24.1 | 2.27 | 0.69 | 0.749 |
| 80 | 20.2 | 10.6 | 30.8 | 1.91 | 0.66 | 0.749 |
| 120 | 27.79 | 18.41 | 46.2 | 1.51 | 0.60 | 0.749 |
| 140 | 31.45 | 22.45 | 53.9 | 1.4 | 0.58 | 0.749 |
| 208 | 43.49 | 36.56 | 80.05 | 1.18 | 0.54 | 0.749 |

**(c)** $U_t$ = 9 m/s and $L_u/d$ = 80

| $\beta$ (°) | $L_f$ (m) | $L_s$ (m) | $L_u$ (m) | $L_f/L_s$ | $L_f/L_u$ | $\alpha_{vol}$ |
|---|---|---|---|---|---|---|
| 2 | 22.61 | 8.19 | 30.8 | 2.76 | 0.73 | 0.598 |
| 15 | 16.86 | 13.94 | 30.8 | 1.21 | 0.55 | 0.591 |
| 30 | 14.74 | 16.06 | 30.8 | 0.92 | 0.48 | 0.579 |
| 51 | 12.84 | 17.96 | 30.8 | 0.71 | 0.42 | 0.560 |

The effect of varying $u_{gs}$ ($U_t$) on slug flow features is first analyzed. By considering $\beta$=30° and $L_u/d \approx 80$, and varying $u_{gs}$ = 2, 4.5, 7, 10.3 and 14.0 ($U_t \approx$ 6, 9, 12, 16 and 20) m/s, Figure 3.3 illustrates spatial profiles of slug flow properties in the liquid and gas zones including the normalized film thickness $h_f/d$ (Figure 3.3a), liquid holdup $R$ (Figure 3.3b), liquid velocity $u_{L,}$(Figure 3.3c) and gas velocity $u_G$ (Figure 3.3d), along $L_u/d$. Actual values of $L_u$, film length ($L_f$), liquid slug length ($L_s$) and $L_f/L_s$ are reported in Table 3.3a. Note that, in Figure 3.3 (and subsequent Figures 3.4-3.5), the flow direction is from left to right; $u_G = U_b$, $u_L = U_l$ and $h_f/d$ =1 (i.e. fully occupied with liquid) in the slug liquid zone whereas $u_G = U_g$ and $u_L = U_f$ in the film zone. As $u_{gs}$ is increased from 2 to 14 m/s, Figure 3.3a shows that $h_f/d$ decreases whereas $L_f/d$ ($L_s/d$) elongates (shrinks), rendering a wider, longer and more uniform gas bubble shape.

This is justified in Table 3.3a with the increasing $L_f/L_s$, $L_f/L_u$ and gas volumetric fraction per slug unit $\alpha_{vol}$. Correspondingly, $R_f$ decreases from the bubble nose to its tail as in Figure 3.3b. A spatial variation in $h_f/d$ and $R_f$ is more nonlinear in the lower $u_{gs}$ case entailing a greater liquid mass variation in the film zone. Hence, an assumption of a rectangular slug unit pulse employed in some previous studies (Table 2.2) might not be justified at a low $u_{gs}$. For the highest $u_{gs}$, the gas phase dominates the slug unit with the maximum $\alpha_{vol}$. The $u_L$ profile in Figure 3.3c experiences a transition from being positive at the bubble nose to negative at the tail for low $u_{gs}$ = 2.0, 4.5 and 7 m/s. Such a negative $u_L$ is influenced by low $U_t$ and $R_f$ (Eq. (3.4)), enabling the prevailing gravity effect. On the other hand, $u_G$ in Figure 3.3d is always positive because of the greater $\alpha_f$ (Eq. (3.5)): this is typical for the gas buoyancy feature.

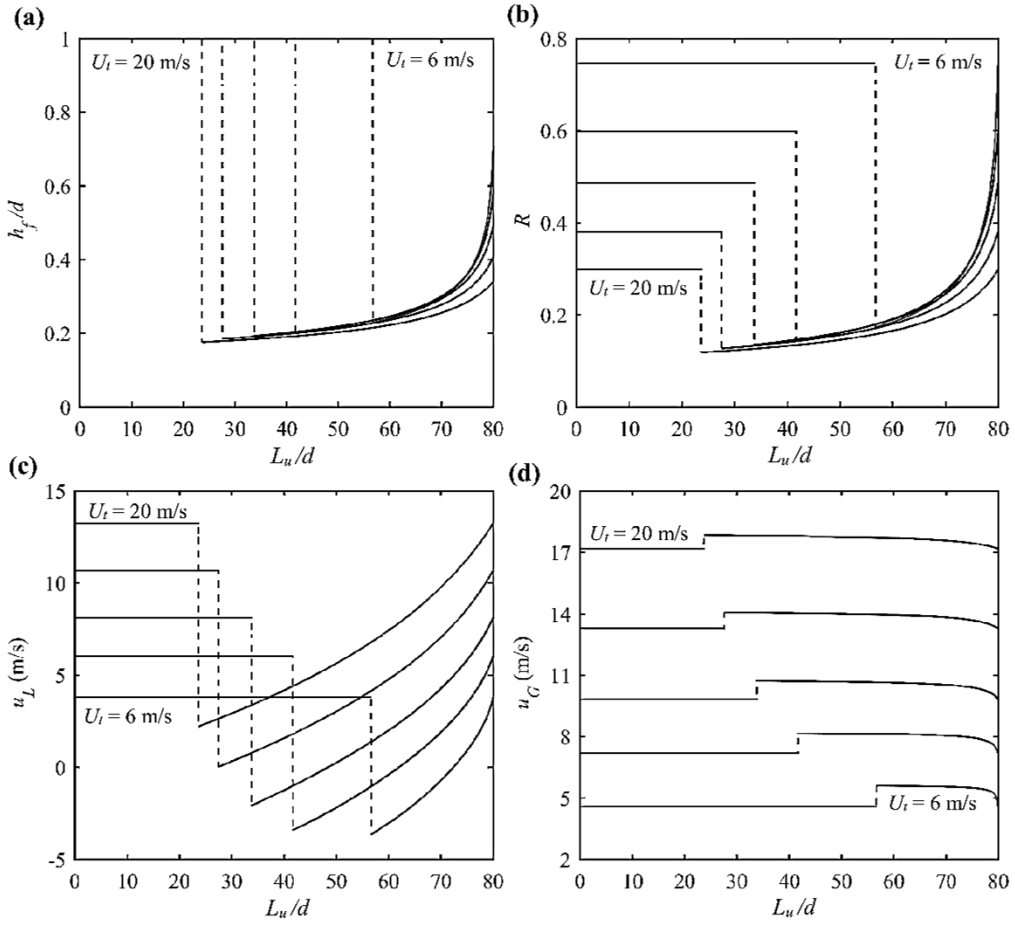


**Figure 3.3:** Influence of $U_t$ (6, 9, 12, 16, 20 m/s) on (a) $h_f/d$, (b) $R$, (c) $u_L$ and (d) $u_G$ for a slug unit with $L_u/d$ = 80, $u_{ls}$=2 m/s and $\beta$=30°.

Nevertheless, both $u_L$ and $u_G$ increase with $u_{gs}$, with the maximum $u_L$ ($u_G$) at the bubble nose (tail). In all cases, absolute values of $u_G > u_L$ and $u_G$ profiles are relatively uniform with a smaller percentage change along $L_u/d$. There is a discontinuity (vertical dashed lines) in the obtained outputs, clearly distinguishing the liquid slug from the film zones. This essentially

emphasizes a rapid change in slug flow properties which, in turn, would influence the pipe distributed mass and stiffness. Based on Figure 3.3 and Table 3.3a, the pipe SIV would be subject to a greater flow velocity effect in the case of higher $U_{gs}$ (i.e. $U_t$) and to a greater liquid mass (density) fluctuation in the case of lower $U_{gs}$.

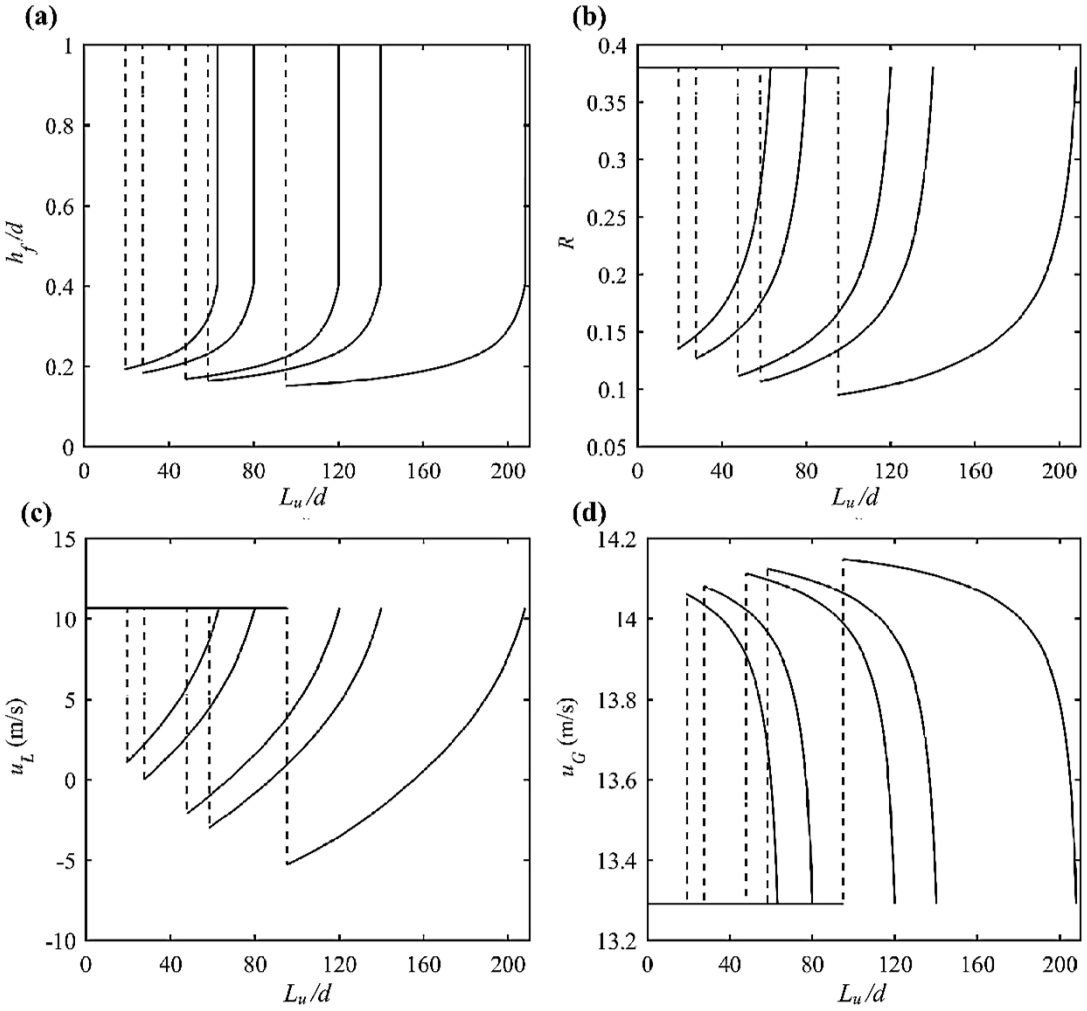


**Figure 3.4:** Influence of $L_u/d$ (63, 80, 120, 140, 208) on (a) $h_f/d$, (b) $R$, (c) $u_L$ and (d) $u_G$ for a slug unit with $u_{gs}$=10.3 m/s, $u_{ls}$=2 m/s and $\beta$=30°.

The effect of varying $L_u/d$ is next discussed through Figure 3.4 and Table 3.3b. By assigning $\beta$=30° and $u_{gs}$ = 10.3 ($U_t \approx 16$) m/s, variations of $h_f/d$ (Figure 3.4a), $R$ (Figure 3.4b), $u_L$, (Figure 3.4c) and $u_G$ (Figure 3.4d) are displayed in the case of increasing $L_u/d$ from 63 to 208. Both $L_f$ and $L_s$ are seen to increase such that a conservation of unit mass is satisfied for a fixed $u_{ls}$ and $u_{gs}$; i.e., $\alpha_{vol}$ = 0.749 is constant as justified in Table 3.3b. For this fixed $u_{gs}$, $L_f/L_s$ decreases as $L_u/d$ increases, contrary to the increasing $L_f/L_s$ trend in Table 3.3a. The variable ranges of $0.5 < L_f/L_u < 0.7$, $0.2 < h_f/d < 0.4$ and $0.1 < R < 0.38$ in the varying $L_u/d$ case are smaller than those ($0.25 < L_f/L_u < 0.7$, $0.2 < h_f/d < 0.7$ and $0.1 < R < 0.75$) in the varying $u_{gs}$ case in Figure 3.3. This implies a greater effect of varying $U_t$, than varying $L_u/d$, on the slug profile

modification. As $L_w/d$ is increased, $h_f/d$ and $R_f$ in the film zone decrease, the latter rendering the decreasing and eventually negative $u_L$ (Eq. (3.4)). On the contrary, $u_G$ slightly increases owing to the increasing $\alpha_f$ (Eq. (3.5)). Parameters within $L_s$ remain unchanged since $u_{ls}$ and $u_{gs}$ remain the same. The change in $L_u$ affects Eq. (3.7) for determining $L_f$ such that a greater $L_u$ would result in a lower $h_f$ and $R_f$ (Eq. (3.6)).

**Table 3.4:** Pressure drop components, bottom pressure and resulting pre-tension variations in cases of varying (a) $U_t$, (b) $L_w/d$ and (c) $\beta$.

**(a)** $\beta = 30°$ and $L_w/d = 80$

| $U_t$ (m/s) | $N_s$ | $dP_f$ (kPa) | $dP_s$ (kPa) | $dP_g$ (kPa) | $dP_u$ (kPa) | $P_b$ (kPa) | $P_{drop}$ (%) | $T_b$ (kN) | $T_{drop}$ (%) |
|---|---|---|---|---|---|---|---|---|---|
| 6 | 65 | 0.08 | 4.55 | 72.51 | 77.14 | 5174.5 | 98.04 | 802.19 | 56.77 |
| 9 | 65 | 0.39 | 7.68 | 50.30 | 58.37 | 3936.8 | 97.42 | 888.64 | 52.11 |
| 12 | 65 | 1.07 | 10.64 | 38.82 | 50.53 | 3420.2 | 97.04 | 924.72 | 50.16 |
| 16 | 65 | 2.62 | 14.19 | 30.14 | 46.95 | 3184.2 | 96.82 | 941.21 | 49.27 |
| 20 | 65 | 5.09 | 17.71 | 24.32 | 47.12 | 3212.7 | 96.85 | 939.21 | 49.38 |

**(b)** $\beta = 30°$ and $U_t = 16$ m/s

| $L_w/d$ | $N_s$ | $dP_f$ (kPa) | $dP_s$ (kPa) | $dP_g$ (kPa) | $dP_u$ (kPa) | $P_b$ (kPa) | $P_{drop}$ (%) | $T_b$ (kN) | $T_{drop}$ (%) |
|---|---|---|---|---|---|---|---|---|---|
| 63 | 84 | 2.60 | 9.87 | 23.53 | 36.00 | 3126.6 | 96.76 | 945.23 | 49.06 |
| 80 | 65 | 2.62 | 14.19 | 30.11 | 46.92 | 3184.2 | 96.82 | 941.21 | 49.27 |
| 120 | 43 | 2.62 | 24.65 | 45.12 | 72.39 | 3274.3 | 96.91 | 934.91 | 49.61 |
| 140 | 37 | 2.63 | 30.10 | 52.62 | 85.35 | 3306.9 | 96.94 | 932.64 | 49.74 |
| 208 | 25 | 2.65 | 48.94 | 78.24 | 129.83 | 3384.3 | 97.01 | 927.23 | 50.03 |

**(c)** $U_t = 9$ m/s and $L_w/d = 80$

| $\beta$ (°) | $N_s$ | $dP_f$ (kPa) | $dP_s$ (kPa) | $dP_g$ (kPa) | $dP_u$ (kPa) | $P_b$ (kPa) | $P_{drop}$ (%) | $T_b$ (kN) | $T_{drop}$ (%) |
|---|---|---|---|---|---|---|---|---|---|
| 2 | 65 | 2.31 | 4.17 | 3.36 | 9.84 | 748.4 | 86.46 | 1111.3 | 40.11 |
| 15 | 65 | 0.71 | 6.98 | 25.29 | 32.98 | 2269.8 | 95.54 | 1005.1 | 45.83 |
| 30 | 65 | 0.39 | 7.68 | 50.27 | 58.34 | 3936.8 | 97.43 | 888.6 | 52.11 |
| 51 | 65 | 0.25 | 7.81 | 81.72 | 89.78 | 6004.0 | 98.31 | 744.2 | 59.89 |

The slug flow features are also dependent on $\beta$ which affects some empirical input variables ($U_t$, $U_b$). Understanding of this $\beta$ effect is meaningful for a catenary pipe with variable inclinations. By specifying $u_{gs} = 4.5$ m/s and $L_w/d \approx 80$, variations of $h_f/d$ (Figure 3.5a), $R$ (Figure 3.5b), $u_L$, (Figure 3.5c) and $u_G$ (Figure 3.5d) are plotted for $\beta = 2°$, 15°, 30° and 51°, together with outputs in Table 3.3c. As $\beta$ is increased, Figure 3.5a shows that $L_f/d$ ($L_s/d$) is shortened (elongated), enabling the decreasing $L_f/L_s$, while $h_f/d$ is slightly reduced. Hence, the associated $R_f$ is reduced as shown in Figure 3.5b. These indicate that the gas bubble shape becomes shorter

and wider, increasingly occupying the cross section as the pipe is more inclined towards a vertical 90° where a so-called Taylor bubble would be developed (Fernandes et al., 1983). At higher $\beta$, $u_G$ becomes faster due to the buoyancy effect (Figure 3.5d) whereas $u_L$ becomes slower (Figure 3.5c) due to the gravity effect. For such a low $u_{ls}$ = 2 m/s and $u_{gs}$ = 4.5 m/s, $u_L$ < 0 appears at a relatively large $\beta$, suggesting a falling liquid film near the tail region. Because of the fixed $u_{gs}$ and $L_u/d$, $\alpha_{vol}$ slightly decreases as $\beta$ is increased. This implies that for a system with variable inclination under the steady-state slug flows, the changes in the gas-liquid velocities predominate over a volumetric mass variation.

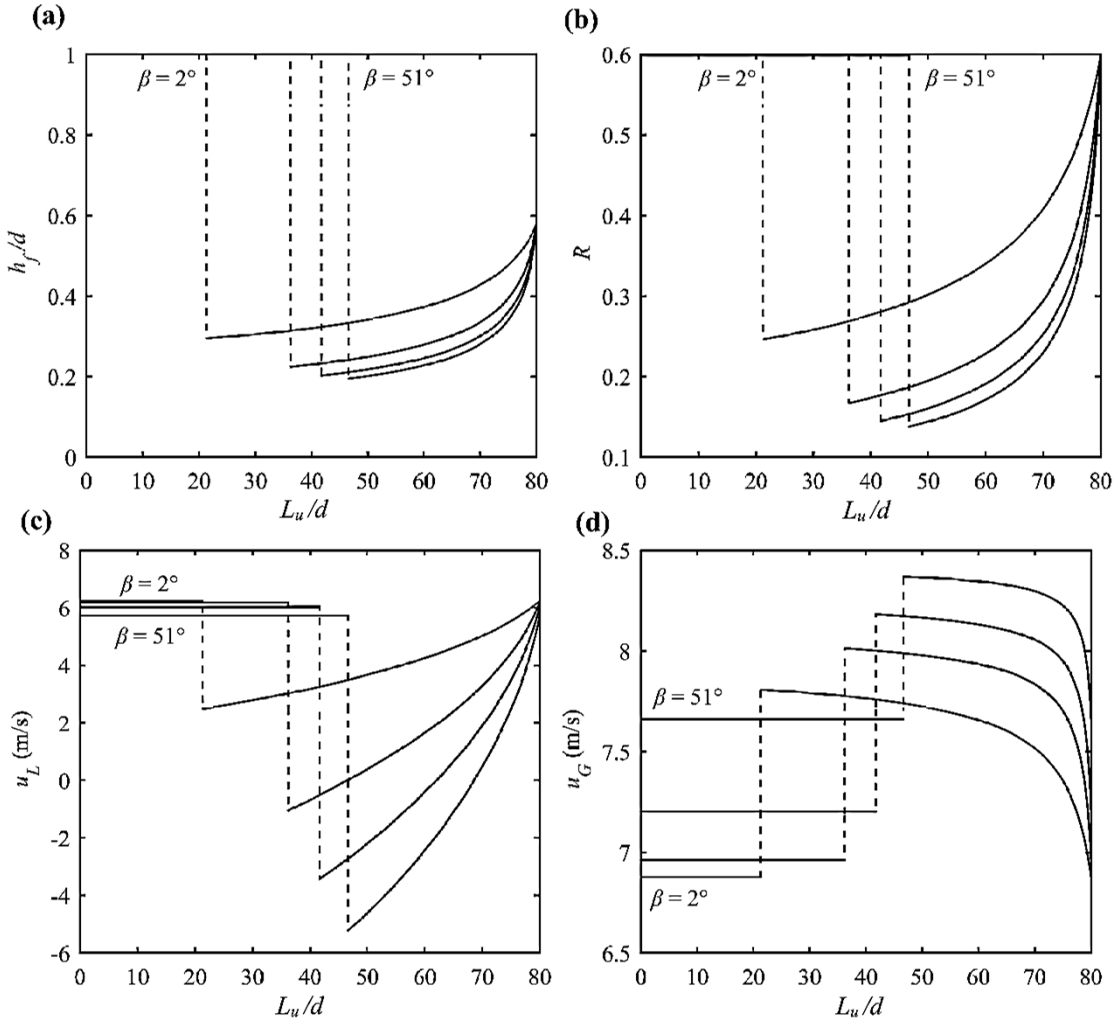


**Figure 3.5:** Influence of $\beta$ (2˚, 15˚, 30˚, 51˚) on (a) $h_f/d$, (b) $R$, (c) $u_L$ and (d) $u_G$ for a slug unit with $u_{gs}$=4.5 m/s, $u_{ls}$=2 m/s and $L_u/d$=80.

For a fixed $\beta$ = 30°, Tables 3.3a and 3.3b also show the slug outputs for the two parametric pairs ($u_{gs}$, $L_u/d$) having a comparable $f_s$ (Table 3.3), whose slug profiles have been displayed as part of Figures 3.3 and 3.4. For the first pair (2, 80) vs. (10.3, 208), there is a considerable difference in both $L_f/L_s$ (0.41 vs. 1.19) and $\alpha_{vol}$ (0.393 vs. 0.749), apart from the noticeable different ranges of $u_L$ and $u_G$ in Figures 3.3 and 3.4. As for the second pair (14, 80) vs. (10.3,

63), $L_f/L_s$ (2.38 vs. 2.27) and $\alpha_{vol}$ (0.797 vs. 0.749) are comparable, as are $u_L$ and $u_G$. These results suggest that the pipe SIV, especially for the first parametric pair case, could be somewhat different despite having a similarly potential resonance with the comparable $f_s$. This point will be discussed again in Section 3.4.

Once a fully-developed slug flow profile is established as in Figures 3.3-3.5, it is then feasible to estimate the total internal pressure variation for each slug unit ($dP_u$). By accounting for all the travelling slug units fully occupying the pipe span, the resulting mean-valued tension in the pipe wall $T_m = T\text{-}2\nu P_m A$, where $P_m$ is the mean pressure spatially varied due to slug flows along the pipe. From Eq. (3.8), $dP_u$ consists of the gravitational effect ($dP_g$), the frictional effect in the slug liquid zone ($dP_s$) and the frictional effect in the film zone ($dP_f$). By assuming that the top outlet mean pressure ($P_t$) is equivalent to the atmospheric pressure of 101.3 kPa as in Ortega et al. (2018), Table 3.4 summarizes $dP_g$, $dP_s$, $dP_f$, $dP_u$, the number of full slug units occupying the pipe ($N_s \approx L/L_u$) over a constant slugging period ($1/f_s$), the bottom mean pressure ($P_b$), the percentage of the mean pressure drop from the bottom to the top [$P_{\text{drop}} = (P_b - P_t)\times 100/P_b$], the resulting $T_m$ at the bottom ($T_b$), and the percent reduction of $T_m$ ($T_{\text{drop}}$) from the top ($T_m$ = 1855.5 kN) to $T_b$. Results in the cases of varying (Table 3.4a) $U_t$, (Table 3.4b) $L_u/d$ and (Table 3.4c) $\beta$, including the cases of $U_t$-$L_u/d$ pairs for a fixed $f_s$, are presented.

As $U_t$ is increased for a given $L_u/d$ = 80 and $\beta$ = 30°, Table 3.4a shows that $dP_g$ decreases while both $dP_s$ and $dP_f$ ($dP_s > dP_f$) increase. A reduction in $dP_g$ is due to an increment of $\alpha_u$, hence, a reduction in $\rho_u$ in Eq. (3.8) (i.e. having less liquid and more $\alpha_{vol}$) as $u_{gs}$ is increased. On the contrary, $dP_s$ increases due to the increasing liquid slug velocity (Figure 3.3c) where a squared value amplifies the shear stress $\tau_f$ notwithstanding the decreasing $L_s$ (Table 3.3a). Likewise, $dP_f$ increases due to the increasing $L_f$ (Table 3.3a) and amplification of $\tau_f$ and $\tau_g$ as a result of increasing gas-liquid velocities (Figures 3.3c and 3.3d). By summing up all the pressure drop components ($dP_u$) and accumulating that along the pipe, $dP_u$ and $P_b$ decrease as $u_{gs}$ is increased, mostly following the $dP_g$ trend. Note that, at $u_{gs}$ = 10.3 and 14 m/s, $dP_u$ and $P_b$ in both cases are comparable with a similar $P_{\text{drop}}$ and $T_{\text{drop}}$, regardless of the increasing (decreasing) trend of $dP_f$ and $dP_s$ ($dP_g$). For a constant $N_s$, the lowest $u_{gs}$ case experiences the maximum $T_{\text{drop}} \approx 57\%$.

As $L_u/d$ is increased for a given $u_{gs}$ = 10.3 m/s and $\beta$ = 30°, Table 3.4b shows that both $dP_g$ and $dP_s$ ($dP_s > dP_f$) increase, contributing to the increasing $dP_u$. The increment of $dP_g$ is due to the increasing $L_u$ since $\alpha_{vol}$ is constant (Table 3.3b) whereas the increment of $dP_s$ is due to the increasing $L_s$ since the liquid slug velocity associated with the fixed $u_{gs}$ is unchanged.

Because of a constant $\alpha_{vol}$, $dP_f$ is nearly unaltered as $L_u/d$ is varied. The minimum $P_b$ is associated with the lowest $L_u/d$ case having the highest $N_s$ whereas the minimum $T_b$ is associated with the greatest $L_u/d$ case. Nevertheless, both Tables 3.4a (varying $u_{gs}$) and 3.4b (varying $L_u/d$) reveal similar values of nearly 97% of $P_{\text{drop}}$ and 50% of $T_{\text{drop}}$ in comparison with 37% of the $T$ reduction in Figure 3.2c. This slug-induced tension variation would influence the pipe axial stiffness, associated natural frequencies and modal properties, which, in turn, could modify the pipe resonant SIV during the slug transportation.

For a given $u_{gs}$ = 4.5 m/s and $L_u/d \approx 80$, Table 3.4c shows that both $dP_g$ and $dP_s$ increase, contributing to the increasing $dP_u$, as $\beta$ is increased. This is similar to the increasing $L_u/d$ case in Table 3.3b, but due to a different reason. Since $u_{gs}$ and $L_u/d$ are constant and $\alpha_{vol}$ is nearly unchanged (Table 3.3c), the increasing $dP_g$ is now due to the inclination effect (i.e. increasing $\sin\beta$ in Eq. (3.8)). The increasing $dP_s$ is due to the increasing $L_s$. On the other hand, despite the increasing $L_f$, $dP_f$ tends to decrease as the pipe is more inclined. This is attributed to the increasing gas-liquid velocities moving in the opposite directions within the liquid film (Figures 3.5c vs. 3.5d), enabling the sign differences of the associated shear stress terms and, hence, the ensuing reduction of integrated values in Eq. (3.8). It is also interesting to remark for the pipe with highest $\beta$ = 51° that $P_b$ is maximum while $T_b$ is minimum, the latter softening the pipe stiffness (Srinil et al., 2003), potentially increasing the pipe sagging displacement and hence reducing the pipe natural frequencies.

In accordance with Table 3.3, Table 3.4 also compares the pressure change components, resulting $P_b$ and $T_b$, $P_{\text{drop}}$ and $T_{\text{drop}}$, for the two parametric pairs ($u_{gs}$, $L_u/d$) having a comparable $f_s$ (Table 3.2). It is seen that the first pair (2, 80) vs. (10.3, 208) experiences a greater difference in both $P_b$ (5174.5 vs. 3384.3 kPa) and $T_b$ (802.19 vs. 927.23 kN) than the other pair (14, 80) vs. (10.3, 63) with comparable $P_b$ (3212.7 vs. 3126.6 kPa) and $T_b$ (939.21 vs. 945.23 kN). These are due to the greater differences in $L_f$, $L_s$, $L_u$, $\alpha_{vol}$, the associated liquid-gas velocities (Figures 3.3 and 3.4) and the resulting shear stresses in the former case.

Overall variations in the key input flow-pipe parameters and the associated output characteristics will influence the planar static (drifts) and dynamic responses (amplitudes, modes, oscillation frequencies, resonances) of the slug-transported pipe. These are analysed and discussed in the following.

### 3.4. Mechanisms of Curved Flexible Pipe Transporting Slug Flows

Mechanisms of a long inclined curved bendable pipe transporting steady slug flows are now investigated based on the slug flow-pipe properties in Section 3.3. In this study, multiple slug

unit trains travelling along the pipe have the same features according to the steady-state flow assumption. As the mean pipe inclination and the chord angle are both about 30°, the slug flow profile with $\beta = 30^o$ is specified, unless stated otherwise, as a representative slug unit cell. From Eq. (3.9), a small local fluctuation amplitude ($k$) of the internal pressure about a mean value is taken as 5%, following recent experimental and numerical works of Ortega (2015) who reported $k \approx 5.5\%$. Experimental results in the case of steady SIV in catenary pipe in Zhu et al. (2018a) also suggested $k \approx 5.8\%$. Attention is placed on investigating the effect of varying $U_t$ and $L_u/d$ primarily governing $f_s = U_t/L_u$. The slug flow properties (Figures 3.3-3.5), pressure and tension variations (Tables 3.2-3.4) are incorporated as the space-time varying inputs into the pipe model through the slug flow-induced momentum and gravity loading terms. In the following, key features of slug flow-induced fluctuation frequencies, transient drifts, steady mean displacements, SIV and bending/axial dynamic stresses are presented and discussed.

*3.4.1 Slug flow-induced fluctuation frequencies*

With $L_u/d = 80$ and $U_t = 16$ m/s, the space-time varying profiles of the four main properties of slug flows are illustrated in Figure 3.6, including (a) $R$, (b) $u_L$, (c) $u_G$ and (d) $P$, within the first 20 s and 200 m of the pipe's bottom part starting from the inlet ($1825 < s < 2025$ m). For this $L_u/d = 80$ and $U_t = 16$ m/s, it takes about 126s (i.e. the transient period) for the pipe to be fully occupied by about 65 slug units. Note that, for a demonstration purpose, the incremental profiles in Figure 3.6 are plotted for every second, despite the actual $\Delta t = 0.001$ s, with the flow direction being from right to left as in Figure 3.1. Based on Figure 3.6, time histories of input variables at a specific pipe location can be recorded, showing a certain periodicity. The associated fluctuation frequencies may be approximated using the Fast Fourier Transform (FFT). Despite having different profiles of $R$, $u_L$, $u_L$ and $P$, their frequency contents are the same based on the unique space-time variation.

In the case of varying $U_t = 6$, 9, 16 and 20 m/s, Figure 3.7 illustrates FFT plots in which the peaks have a normalized spectral density amplitude of unity. It can be seen that, in consistent with results in Table 3.2, the dominant slug frequency increases as $U_t$ is consecutively increased, confirming that $f_s = 0.20$, 0.29, 0.52 and 0.66 Hz according to the relation $f_s = U_t/L_u$. In addition to $f_s$, several secondary peaks with smaller amplitudes can be remarked whose frequencies are approximately about $(N+1)f_s$, where $N$=1, 2, 3. Such a multi-harmonic feature is typical for a square-like wave, which can be can be represented as an infinite sum of sinusoidal waves (Brigham, 1988). Similar $f_s$ behaviour has also been reported in Safrendyo and Srinil (2018), where a rectangular pulse train model of slug flows was considered. Within the displayed 3 Hz

range, the minimum (maximum) $U_t$ =6 m/s (20 m/s) case experiences the highest (lowest) number of 15 (4) frequency contents in Figure 3.7.

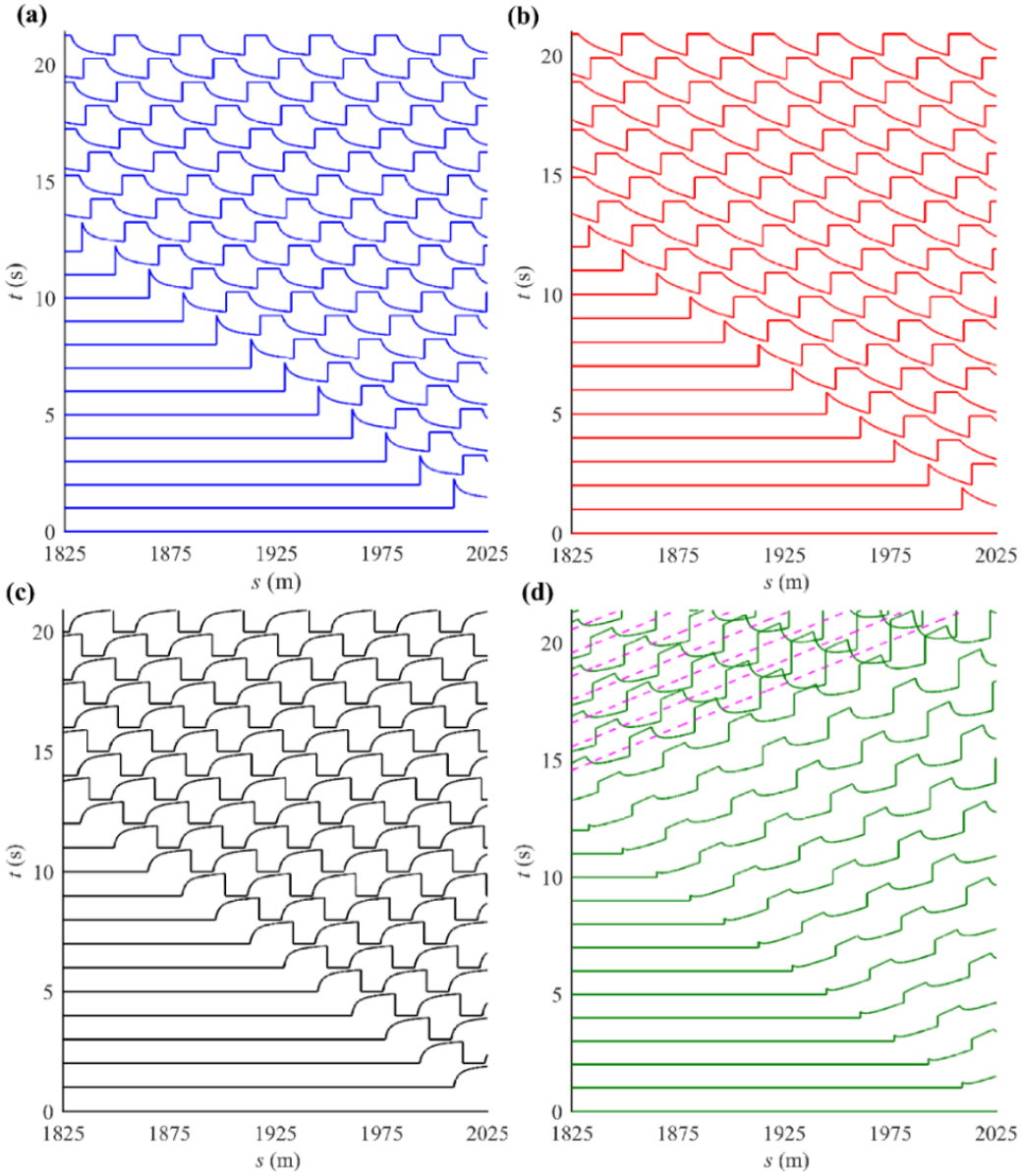


**Figure 3.6:** Illustration of space-time varying profiles (a) $R$, (b) $u_L$, (c) $u_G$ and (d) $P$ based on $L_u/d$ = 80, $U_t$ =16 m/s. Dashed lines in (d) denote $P_m$.

By assigning $U_t$ = 16 m/s, Figure 3.8 displays FFT plots in the case of varying $L_u/d$ = 63, 120, 140 and 208, confirming $f_s$ values reported in Table 3.2. As expected from $f_s = U_t/L_u$ and in contrast to the varying $U_t$ case, the minimum (maximum) $L_u/d$ = 63 (208) case experiences the lowest (highest) number of 4 (14) frequency contents within the displayed 3 Hz range. For a fixed $U_t$ = 9 m/s and $L_u/d$ = 80, FFT plots in the case of varying $\beta$ = 2°, 15°, 30° and 51° are shown in Figure 3.9. Their frequency contents in all $\beta$ cases appear to be similar with identical $f_s$ = 0.29 Hz. There are 9 secondary peaks with very small moderations of amplitudes and frequencies.

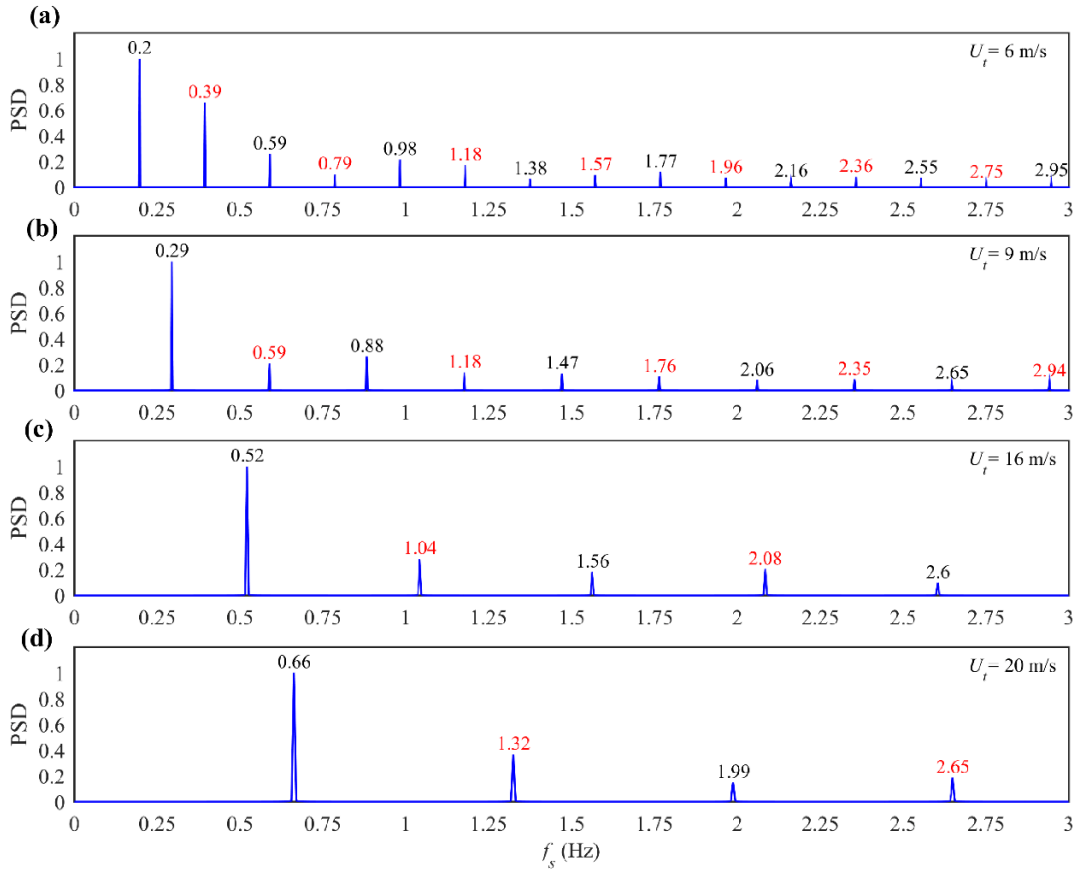


**Figure 3.7:** Frequency spectra of slug fluctuations based on $L_u/d$= 80 and varying $U_t$.

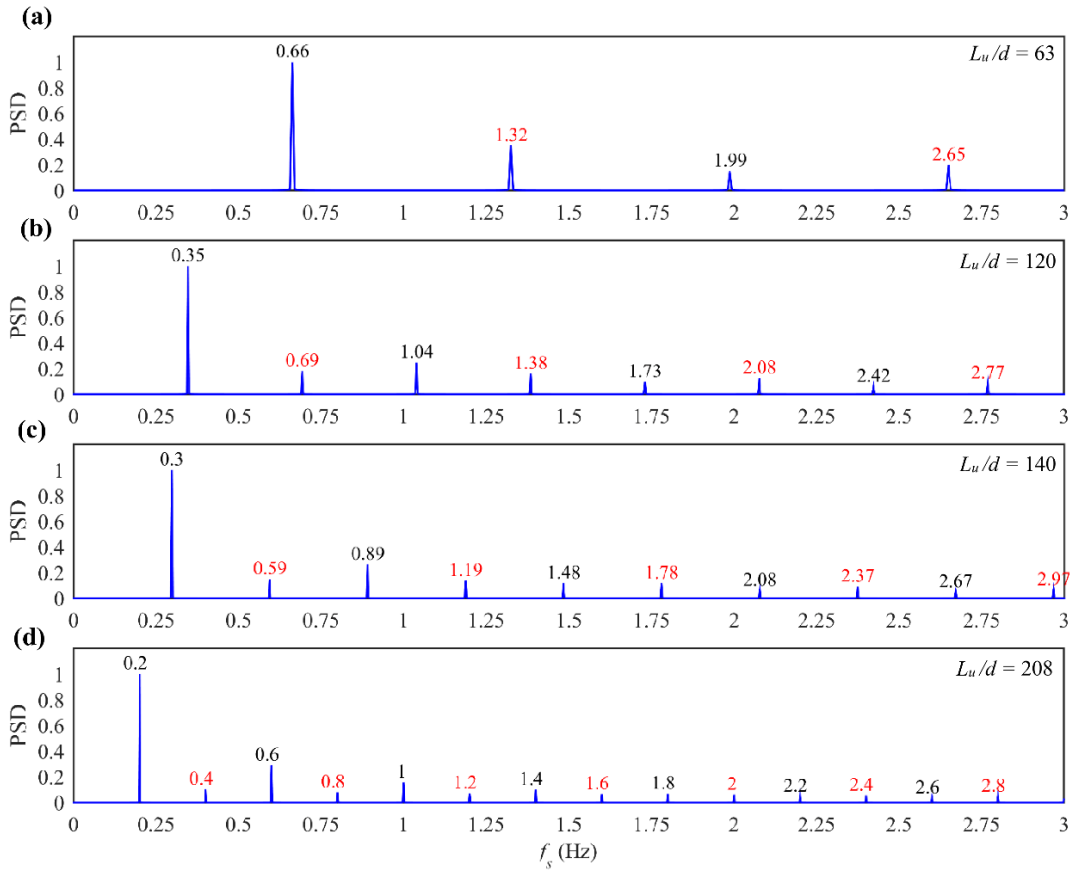


**Figure 3.8:** Frequency spectra of slug fluctuations based on $U_t$ = 16 m/s and varying $L_u/d$.

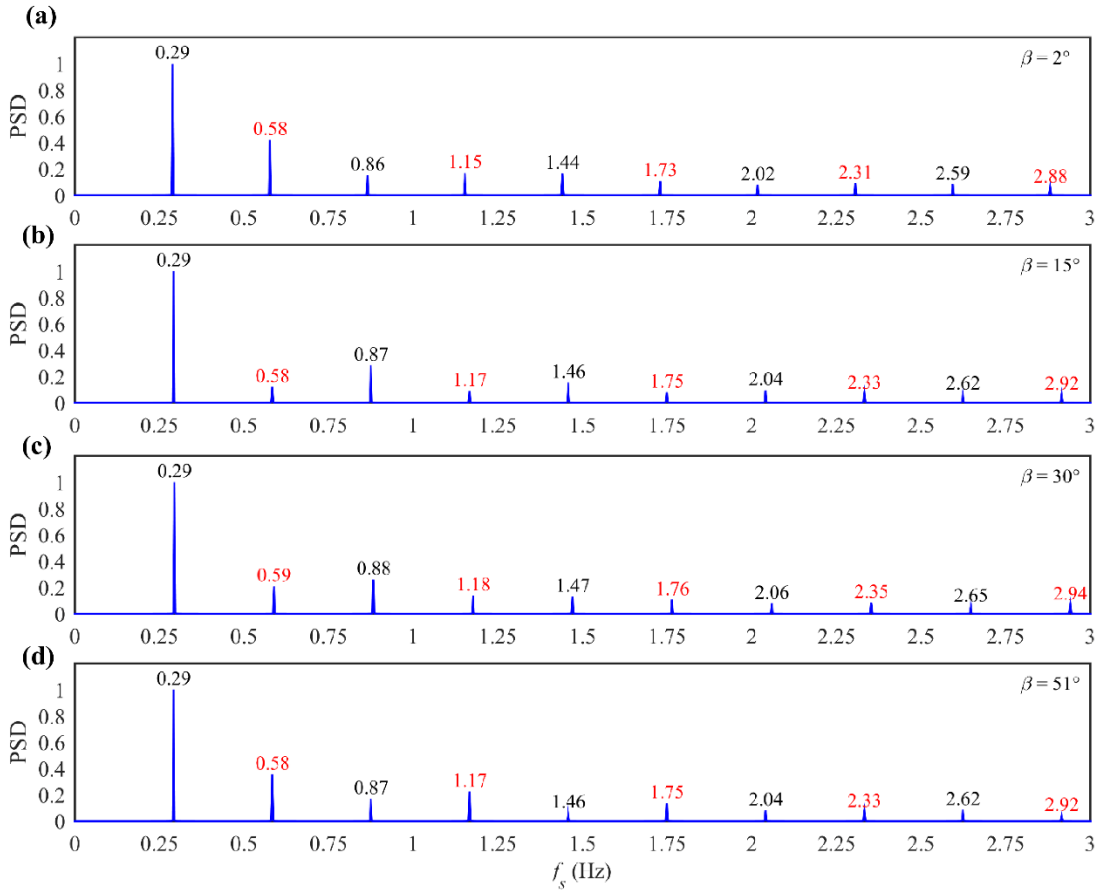


**Figure 3.9:** Frequency spectra of slug fluctuations based on $U_t = 9$ m/s and $L_u/d = 80$ with varying $\beta$.

Overall, based on the observed fluctuation frequencies, it is expected that the pipe SIV in the lower $U_t$ or greater $L_u/d$ case might be subject to a greater number of excited vibrational modes. These will be examined in Sections 3.4.3 and 3.4.4, by also accounting for other key factors related to the pipe initial static profile, fluid propagating masses, velocities and pressure drop changes.

### *3.4.2 Slug flow-induced transient drifts*

Figure 3.10 displays the space-time variations of pipe responses in $u$ and $v$ directions, capturing the slug flow-induced initial transient (quasi-static) and steady-state (dynamic) stages, in the case of varying $U_t$ (Figures 3.10a, b), $L_u/d$ (Figures 3.10c, d) and $\beta$ (Figures 3.10e, f).

As slug flows gradually propagate into the pipe and fully occupy it, Figure 3.10 reveals that, during $t < 250$ s, the pipe experiences a considerable excursion or transient drift in all directions and parametric cases. Such $u$ and $v$ drift profiles are asymmetric with respect to the middle span, having an inflection point around $s/L \approx 0.6$ which exhibits a sign change in the pipe curvatures between the bottom and top parts. This feature agrees with an observation in Chatjigeorgiou (2017). The $u$ drifts in the lower part are negative and nearly zero because of a

small local pipe inclination (nearly horizontal) whereas those in the upper more-inclined part are positive with greater values. On the other hand, *v* drifts in the lower part are positive because of the dominant gravity effect in the *Y* direction whereas they are negative in the upper part through an inflection point. These features, which are triggered by a sudden entrance of fluctuating slug flows unbalancing the space-time varying liquid holdups in conjunction with the variable initial tensions and geometric profiles (Figure 3.2), make the lower and upper parts bend outward (i.e. far away from the curvature centre) and inward about an inflection point, respectively. Similar large excursions of a catenary riser owing to the instantaneous passage of slug flows have been reported by Ortega (2015) and Meléndez and Julca (2019).

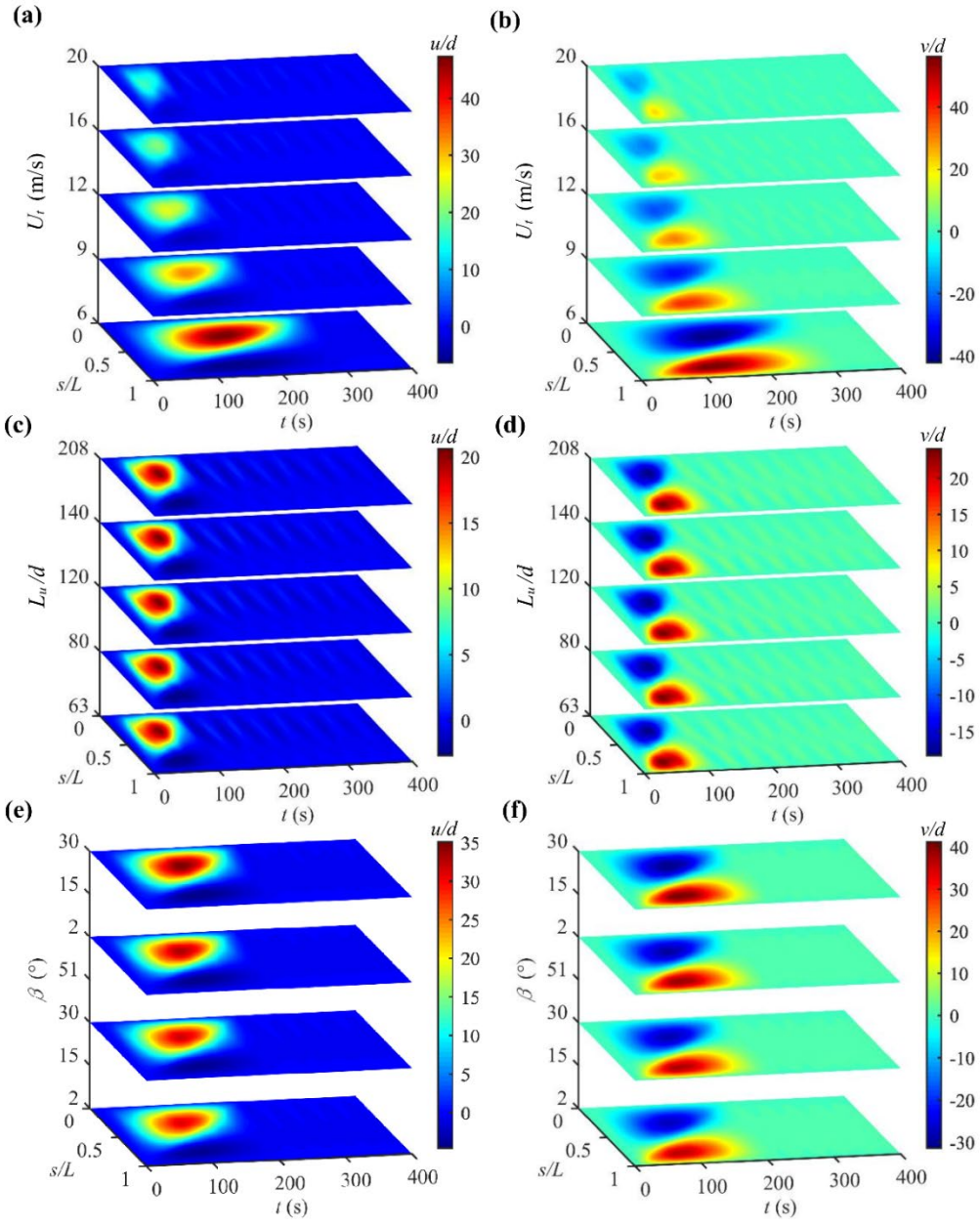


**Figure 3.10:** Space-time varying (a, c, e) *u/d* and (b, d, f) *v/d* during initial transient slug initiation and subsequent steady state in the case of varying (a, b) $U_t$, (c, d) $L_u/d$ and (e, f) $\beta$.

**Table 3.5:** Maximum amplified mean drifts during transient and steady states in cases of varying (a) $U_t$, (b) $L_u/d$ and (c) $\beta$.

**(a)** $\beta = 30^0$ and $L_u/d = 80$

| $U_t$ (m/s) | Transient | | Steady | |
|---|---|---|---|---|
| | Max $u_m/d$ | Max $v_m/d$ | Max $u_m/d$ | Max $v_m/d$ |
| 6 | 47.31 | 56.16 | 0.68 | 1.62 |
| 9 | 33.11 | 38.80 | 0.50 | 1.13 |
| 12 | 25.46 | 30.76 | 0.37 | 0.90 |
| 16 | 20.57 | 24.01 | 0.26 | 0.68 |
| 20 | 16.80 | 21.69 | 0.24 | 0.55 |

**(b)** $\beta = 30^0$ and $U_t = 16$ m/s

| $L_u/d$ | Transient | | Steady | |
|---|---|---|---|---|
| | Max $u_m/d$ | Max $v_m/d$ | Max $u_m/d$ | Max $v_m/d$ |
| 63 | 20.55 | 23.97 | 0.32 | 0.66 |
| 80 | 20.57 | 24.01 | 0.26 | 0.68 |
| 120 | 20.58 | 24.02 | 0.29 | 0.68 |
| 140 | 20.58 | 24.01 | 0.29 | 0.68 |
| 208 | 20.62 | 24.04 | 0.29 | 0.68 |

**(c)** $U_t = 9$ m/s and $L_u/d = 80$

| $\beta$ (°) | Transient | | Steady | |
|---|---|---|---|---|
| | Max $u_m/d$ | Max $v_m/d$ | Max $u_m/d$ | Max $v_m/d$ |
| 2 | 30.97 | 36.15 | 0.48 | 1.08 |
| 15 | 31.83 | 37.19 | 0.48 | 1.10 |
| 30 | 33.11 | 38.78 | 0.50 | 1.13 |
| 51 | 35.08 | 41.16 | 0.50 | 1.19 |

In association with Figure 3.10, Table 3.5 compares the maximum $u$ and $v$ drifts ($u_m$, $v_m$) occurring at $s/L \approx 0.3$ and 0.8, respectively, in all cases. These nearly quarter-span locations and the associated drift profiles are reminiscent of the fundamental planar mode of a catenary pipe (Srinil, 2010). With increasing $U_t$, it is seen in Figures 3.10a and 3.10b that the excursion duration decreases as $U_t$ is increased from 6 to 20 m/s. This is expected since slug flows with a higher $U_t$ requires less time to reach the pipe outlet. For instance, the pipe conveying slug flows at $U_t = 6$ and 16 m/s switches to the perfectly steady states after $t \approx 337$ and 126 s, respectively. However, the maximum (minimum) transient effect is observed at the lowest (highest) $U_t$, attaining the maximum (minimum) $u$ drift of about 47$d$ (17$d$) and $v$ drift of about 56$d$ (22$d$). Such considerable drifts are caused by the greater $R$ or lower $\alpha_{\text{vol}}$ (Table 3.3a), giving rise to a greater gravity effect which is further imbalanced between the two asymmetric pipe parts. In the case of varying $L_u/d$, results in Figures 3.10c and 3.10d reveal similar behaviours of planar drifts and excursion durations, with maximum $u$ drift of about 20$d$ and $v$ drift of about 24$d$. This

is expected since the transient duration depends on $U_t$ being fixed as 16 m/s whereas the maximum drifts are proportional to $\alpha_{vol}$ which is nearly unchanged as about 0.75 (Table 3.3b). These rules may also be applied to the case of varying $\beta$ as shown in Figures 3.10e and 3.10f. Although the excitation durations are comparable in all cases with the same $U_t$, the maximum $u$ and $v$ transient drifts increase with $\beta$. By comparing the cases of $\beta$ =51° and 2°, the former experiences the $u$ drift of about 35$d$ and the $v$ drift of about 41$d$, being slightly greater than 31$d$ and 36$d$ in the latter case, respectively. Again, a small increment of maximum transient drifts with increasing $\beta$ is attributed to the associated decreasing $\alpha_{vol}$ as in Table 3.3c.

*3.4.3 Slug flow-induced mean displacements*

Once the pipe is fully occupied by the slug flows, the transient responses decay and eventually die out due to the system damping. Consequently, a steady-state SIV response takes place after $t$ > 300s and the pipe experiences an oscillation around a new stabilized static equilibrium or mean displacement profile. Figure 3.11 illustrates contour plots of the space-time varying responses in case of varying $U_t$ for 2990 < $t$ < 3000s. Some interesting features are noticed. Due to the effect of gravity and flow momenta, the total $u$ and $v$ responses – inclusive of mean and oscillatory components – decrease as $U_t$ is increased. For the low $U_t$ = 6 and 9 m/s, contour plots appear to contain considerable mean components with some moderate oscillations along the pipe. For the intermediate $U_t$ = 16 m/s, larger moderating oscillations become visible. Both mean and oscillation components decrease at the high $U_t$ = 20 m/s. Figure 3.12 depicts the mean $u$ and $v$ displacement envelopes associated with the case of varying $U_t$ (Figures 3.12a, b), $L_u/d$ (Figures 3.12c, d), $\beta$ (Figures 3.12e, f) and for the two parametric pairs (Figures 3.12g, h). In addition, Table 3.5 compares the maximum $u$ and $v$ mean values whereas Table 3.6 compares the associated top and bottom mean tensions accounting for the additional axial mean stretching during the steady-state response.

Different from the transient excursions reported in Section 3.4.2, the plots in Figure 3.12 reveal that the pipe is quasi-statically forced to bend outward in both $u$ and $v$ directions, exhibiting a new asymmetric and larger-sagged catenary profile with maximum displacements being less than 2$d$ and locating near $s/L \approx 0.5$ for $u$ and 0.6 for $v$. In the case of varying $U_t$ (Figures 3.12a, b), mean values decrease from 0.68$d$ ($u$) and 1.62$d$ ($v$) to 0.24$d$ ($u$) and 0.55$d$ ($v$) as $U_t$ is increased from 6 to 20 m/s, respectively. Again, such difference is attributed to the associated $\alpha_{vol}$ (Table 3.3a) and $T_e$ (Table 3.4a) entailing the different slug weight effects. In the case of varying $L_u/d$ (Figures 3.12c, d), the mean displacement profiles and their maximum values are slightly varied (about 0.3 for $u$ and 0.7 for $v$) because of a small variation in $\alpha_{vol}$

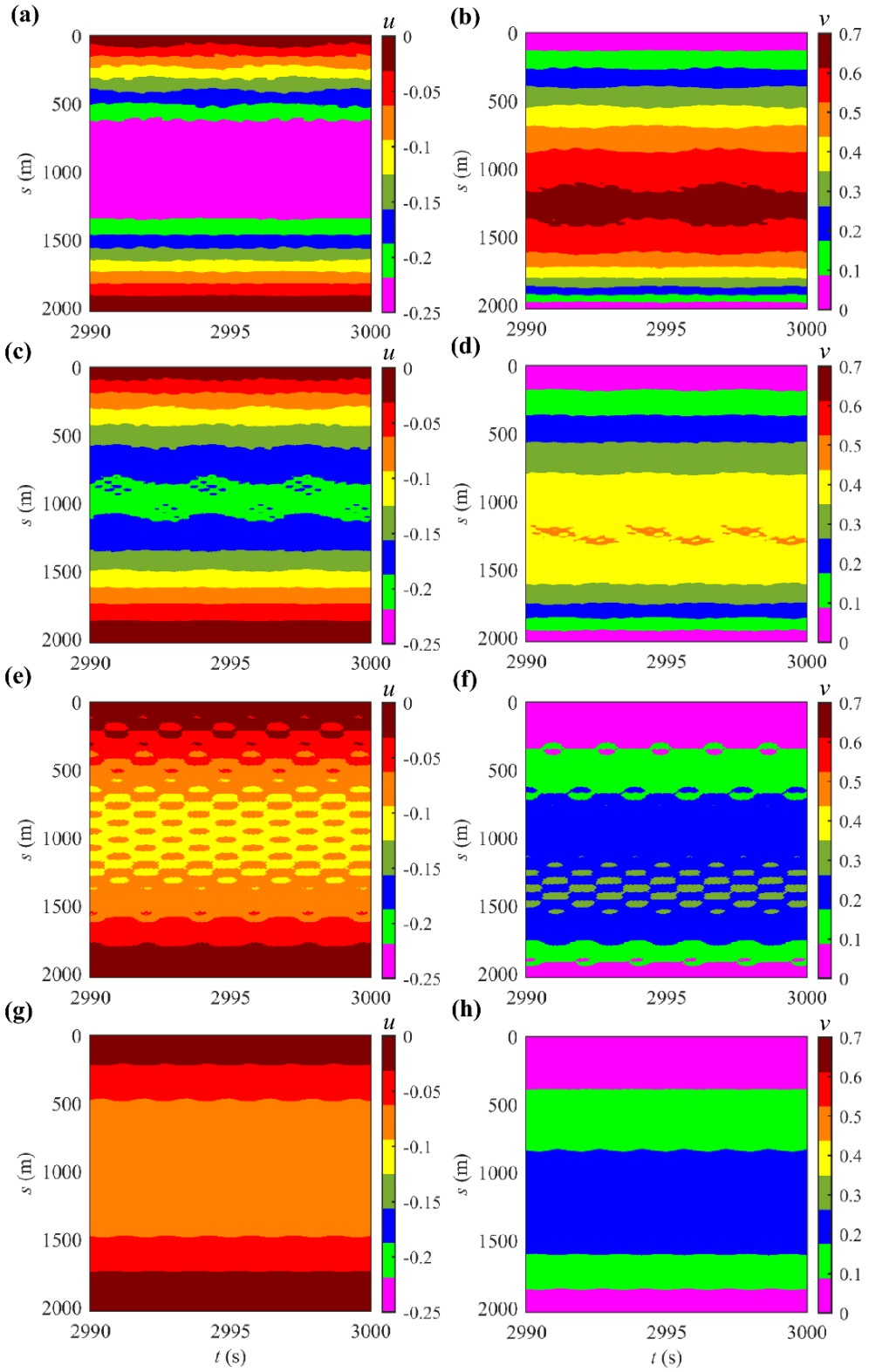


**Figure 3.11:** Space-time varying (a, c, e, g) $u$ and (b, d, f, h) $v$ inclusive of mean drifts during steady-state SIV for $L_u/d$= 80 at (a, b) $U_t$ = 6 m/s, (c, d) 9 m/s, (e, f) 16 m/s and (g, h) 20 m/s.

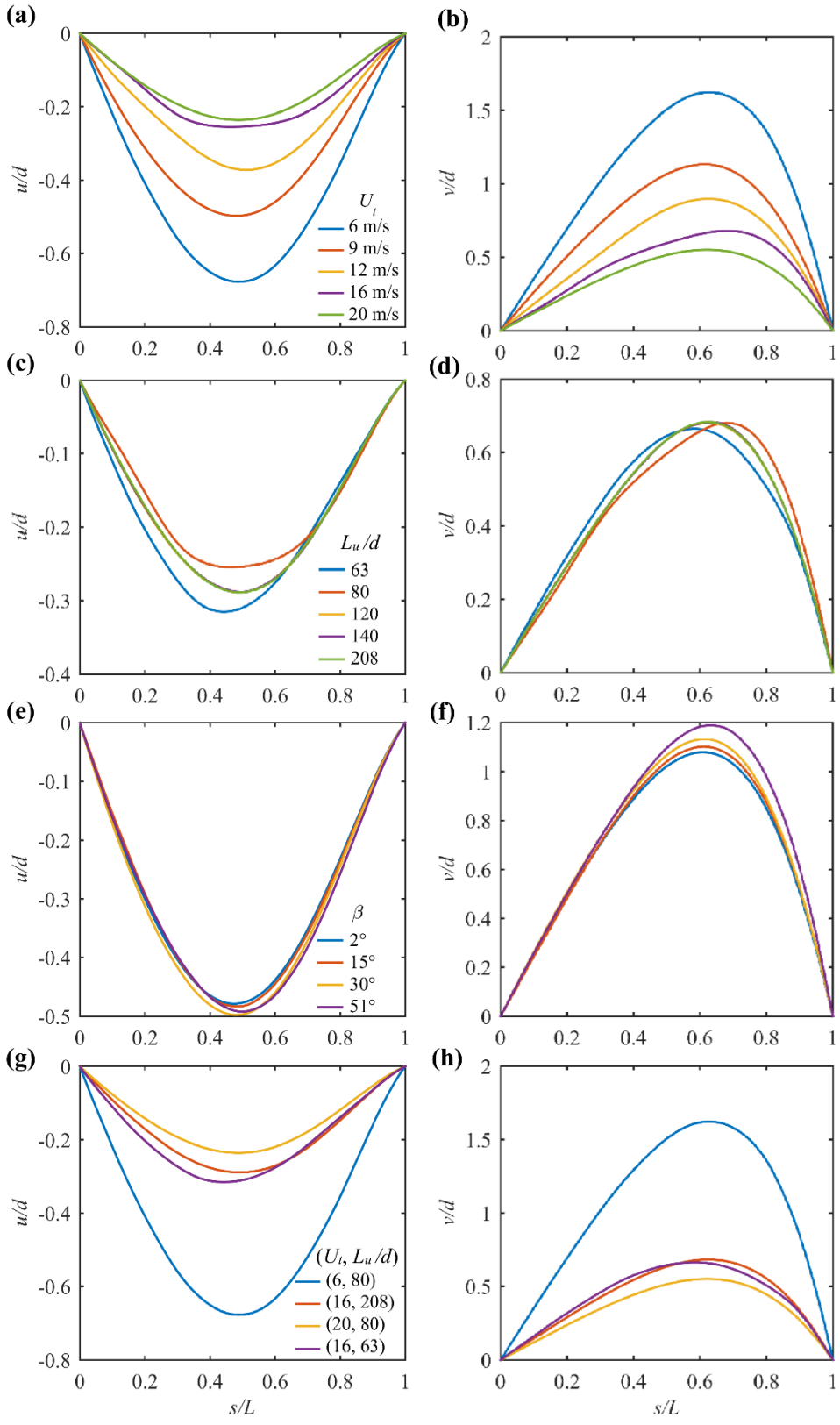


**Figure 3.12:** Spatial profiles of mean drifts in (a, c, e, g) $X$ and (b, d, f, h) $Y$ directions in the case of varying (a, b) $U_t$, (c, d) $L_u/d$, (e, f) $\beta$ and (g, h) $f_s$.

(Table 3.3b) and $T_e$ (Table 3.4b). In the case of varying $\beta$ (Figures 3.12e, f), the mean displacements generally and slightly increase with $\beta$ due to the decreasing $\alpha_{vol}$ (Table 3.3c) and

$T_e$ (Table 3.4c). In comparison with the initial pre-tension results in Figure 3.2 and Table 3.4, the overall end tensions in Table 3.6 are further increased due to the mean displacement amplifications subject to the steady static weights of the moving slugs. In the case of the two parametric pairs (Figures 3.12g, h), the prevailing effects from $\alpha_{vol}$ (Table 3.3) and $T_e$ (Table 3.4) are revealed regardless of $f_s$, in which the case (6, 80) shows distinctively larger mean displacements than the other three cases. Overall, such modifications in the mean displacement profiles and associated tensions affect geometrically the pipe restoring forces and natural frequencies. These, in turn, influence the SIV features as discussed in the following.

**Table 3.6:** Modified mean tensions associated with pipe equilibrium reconfigurations during steady SIV

| $U_t$ (m/s) | $T_m$ (kN) | | $L_u/d$ | $T_m$ (kN) | | $\beta$ (°) | $T_m$ (kN) | |
|---|---|---|---|---|---|---|---|---|
| | Top | Bottom | | Top | Bottom | | Top | Bottom |
| 6 | 3310 | 1712 | 63 | 2460 | 1324 | 2 | 2821 | 1715 |
| 9 | 2865 | 1520 | 80 | 2460 | 1320 | 15 | 2837 | 1619 |
| 12 | 2635 | 1412 | 120 | 2460 | 1314 | 30 | 2865 | 1520 |
| 16 | 2461 | 1320 | 140 | 2460 | 1312 | 51 | 2911 | 1040 |
| 20 | 2345 | 1246 | 208 | 2460 | 1306 | | | |

*3.4.4 Slug flow-induced planar vibrations*

By removing the mean components from the total steady-state responses (e.g. Figure 3.11), Figure 3.13 displays the space-time variations of coexisting $u$ (a, c, e, g) and $v$ (b, d, f, h) oscillations (units in mm) with various $U_t$ for a given $L_u/d$ = 80, within 2990 < $t$ < 3000 s . The associated spanwise FFT plots along the pipe are shown in Figure 3.14 for the 3 Hz range of pipe oscillation frequencies ($f_o$) versus the slug fluctuations in Figure 3.7. Recall that $f_s$ increases as $U_t$ is increased or $L_u/d$ is decreased. At low $U_t$ = 6 (Figures 3.13a, b) and 9 (Figures 3.13c, d) m/s, high modulations of response amplitudes are evidently captured. Accordingly, FFT plots reveal multiple harmonics in which the dominant $f_o$ (with a highest normalized spectral density) is about 0.20 Hz (Figures 3.14a, b) for $U_t$ = 6 m/s and 0.29 Hz (Figure 3.14c, d) for $U_t$ = 9 m/s. These dominant frequencies are the same as the reported $f_s$ (Figure 3.7a, b) caused by the travelling slug excitations. Higher frequency contents with smaller amplitudes come into play in both $U_t$ cases, implying the increased likelihood of dynamic stresses and fatigue-related issue. Nevertheless, as $U_t$ becomes higher at 16 (Figures 3.13e, f) and 20 (Figure 3.13g, h) m/s, overall $u$ and $v$ responses exhibit a periodic, unimodal and standing-wave feature with distinctive positions of minimum, zero (at nodes) and maximum amplitudes. The associated FFT plots reveal a single harmonic peak whose $f_o$ is increased, due to increasing $U_t$, to 0.52 (Figures 3.14e, f) and 0.66 (Figures 3.14g, h) Hz, being the same as $f_s$ in Figures 3.7c

and d, respectively. In such a high $U_t$ range, higher frequencies of the slug fluctuation play a negligible role. Hence, results in Figures 3.13 and 3.14 highlight the effect of increasing $U_t$ leading to a transition from being multimodal to unimodal SIV.

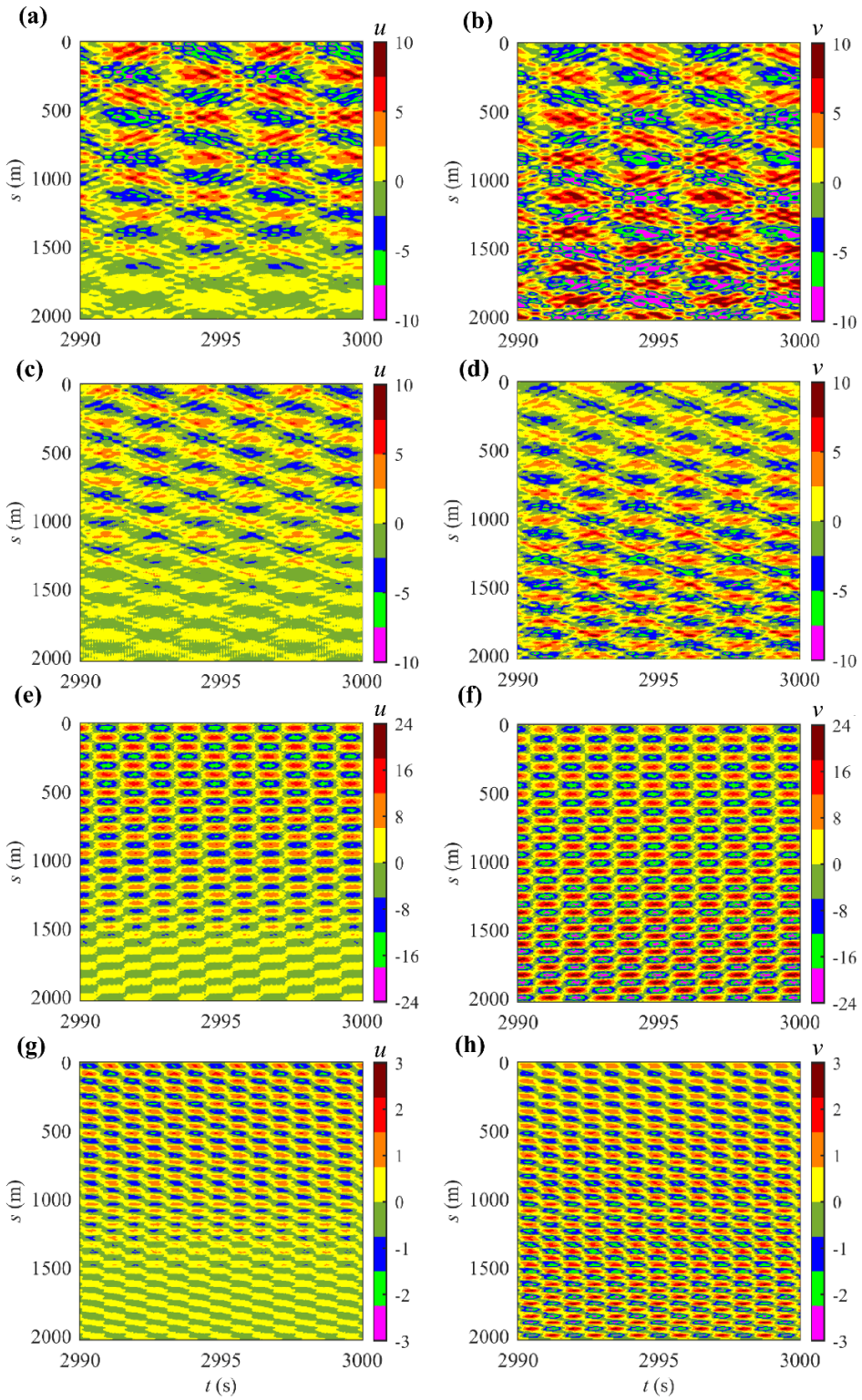


**Figure 3.13:** Space-time varying (a, c, e, g) $u$ and (b, d, f, h) $v$ in mm exclusive of mean drifts during steady-state SIV for $L_u/d$= 80 at (a, b) $U_t$ = 6 m/s, (c, d) 9 m/s, (e, f) 16 m/s, (g, h) 20 m/s.

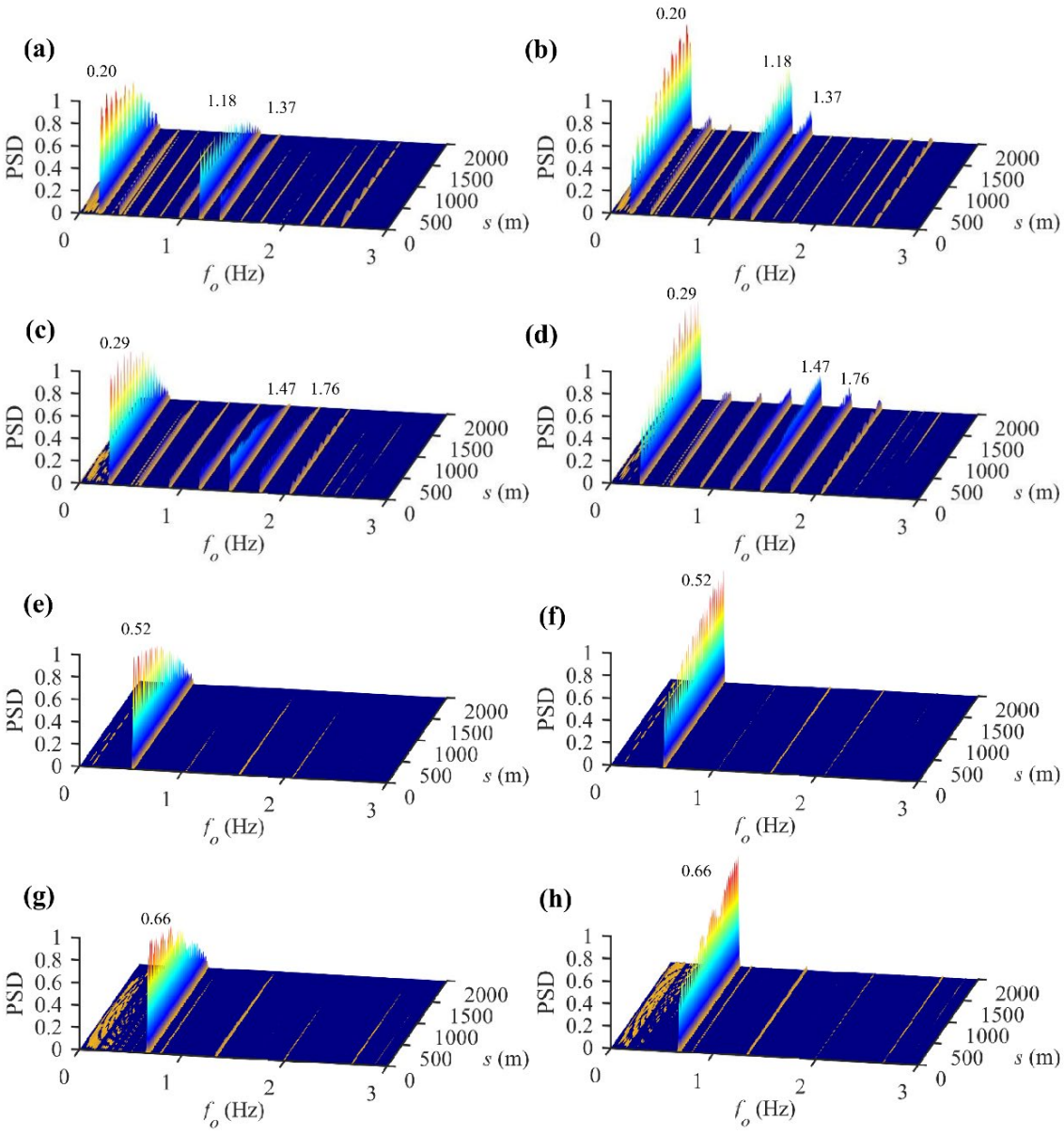


**Figure 3.14:.** Spatial profiles of oscillation frequencies associated with responses in Figure 3.13.

It can be observed that the slug flow-induced responses are closely correlated with $U_t$, which directly determines the slug flow-induced modal loads such as centrifugal and Coriolis forces as shown in Eqs. (3.1) and (3.2). Also, the gravity force mainly attributed to the liquid slug plays an important role in exciting the catenary riser due to the large inner area. These forces altogether lead the riser to vibrate at $f_s$ depending on the flow conditions. The observed transition from being multimodal to unimodal SIV can be a result of the travelling speed of the modal loads. The riser may be less affected by the slug flow-induced forces at high $U_t$ than the cases at relatively low $U_t$, which allows the riser to fully respond to the gravity and momentum forces. Such a similar trend was also reported in Huse Knudsen et al. (2016), where VIV responses of a riser were found to be more modulated at lower slug flow travelling velocities. Also, the slug frequency contents can be responsible for this mode transition. Figure 3.14 shows

that the dominant $f_o$ is excited by the primary $f_s$ (Figure 3.7) at different $U_t$. Nevertheless, the cases of low $U_t$ present more intensive distribution of $f_s$. For instance, 15 vs. 4 frequency peaks up to 3 Hz can be captured at $U_t$ = 6 vs. 20 m/s in Figure 3.7, respectively. Meanwhile, a low $U_t$ can result in a low primary $f_s$, which drives the riser to be dominated by the SIV at a low mode. This, in turn, may strengthen the effects of modal loads when a slowly oscillating riser is subject to a slowly travelling slug flow. Consequently, it is expected that the riser tends to experience multimodal oscillation at relatively low $U_t$ owing to the large number of multiple input $f_s$ as well as the enhanced effect of modal loads owing to an adequate reaction time. Besides, the liquid mass should be considered alongside $U_t$ since the modal loads depend on the combination of them. It can be seen from Table 3.3a that $R_s$ decreases with $U_t$. This trend implies that the modal loads on the riser may become smaller with $U_t$, consequently leading to more regular SIV responses. It is also worth noting that a linearized viscous damping is employed in the present study to highlight the correlation between slug characteristics and SIV. Also, the damping coefficient $c$ is calculated based on $f_{n1}$ of the catenary riser since SIV of a catenary pipe has been experimentally observed to follow a dominant 1$^{st}$ mode oscillation in some studies (Zhu et al., 2018a; Zhu et al., 2018b). Hydrodynamic damping due to the fluid drag is later incorporated in Chapter 5 for the combined VIV and SIV cases. The higher order modes observed in Figures 3.14a, b and c, d may potentially be suppressed due to the large damping effect from fluid drag.

The effect of varying $L_w/d$ is next discussed. In the case of high $U_t$ = 16 m/s, contour plots of coexisting $u$ and $v$ oscillations (units in mm) are displayed in Figures 3.15a, b for $L_w/d$ = 120 and in Figures 3.15c, d for $L_w/d$ = 208. The associated FFT plots are shown in Figures 3.16a-d. In comparison with Figures 3.13e, f and Figures 3.14e, f with the same $U_t$ = 16 m/s but lower $L_w/d$ = 80, the main standing-wave feature is maintained in Figure 3.14a-d with a greater $L_w/d$. With decreasing $f_s$, a lower vibration mode is excited with the dominant $f_o \approx$ 0.35 Hz for $L_w/d$ = 120 and 0.2 Hz for $L_w/d$ = 208. These results signify the unimodal SIV feature at high $U_t$, regardless of $L_w/d$. By comparing Figures 3.13a, b with Figures 3.15c, d, their $u$ and $v$ contour plots are clearly distinctive, despite being subject to the same $f_s$. These results further emphasize a different role played by individual $U_t$ or $L_w/d$. The case with higher $L_w/d$ = 208 and faster $U_t$ = 16 entails greater $u$ and $v$ responses potentially due to a greater flow momentum effect.

In the case of lower $U_t$ = 6 m/s, contour plots of $u$ and $v$ oscillations are displayed in Figures 3.15e, f for $L_w/d$ = 120 and Figures 3.15g, h for $L_w/d$ = 208. The associated FFT plots are shown in Figures 3.16e to h. These results should be compared with those in Figures 3.13a, b and Figures 3.14a, b with the same $U_t$ = 6 m/s but lower $L_w/d$ = 80. In the case of $L_w/d$ = 120,

the modulation feature is still visible in Figures 3.15e, f showing two dominant lower/higher modes intermittently switching among themselves over time. This mode-switching occurrence is justified by FFT plots with two outstanding and comparable $f_o$ peaks at 0.13 and 1.31 Hz.

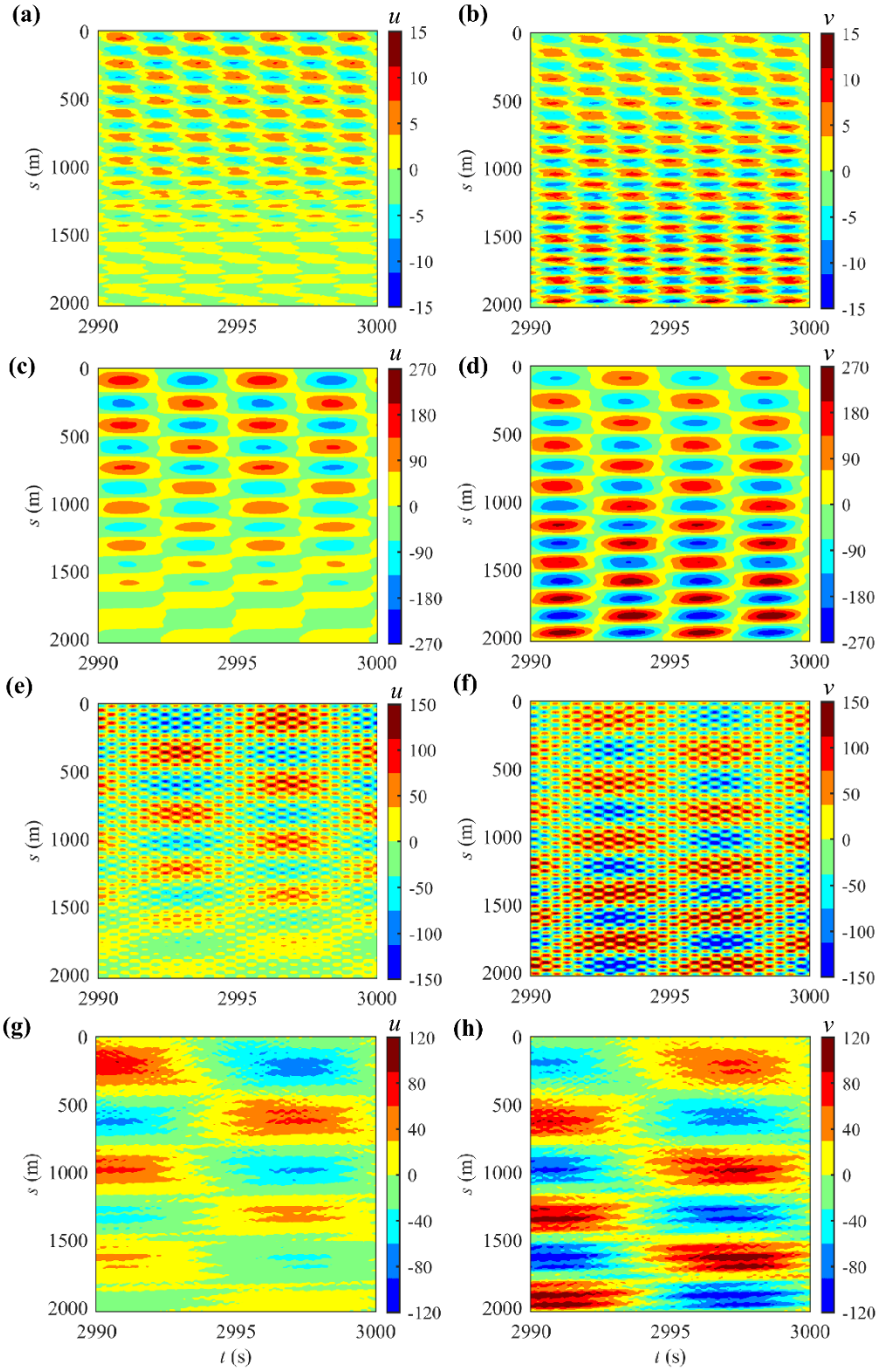


**Figure 3.15:** Space-time varying (a, c, e, g) $u$ and (b, d, f, h) $v$ in mm exclusive of mean drifts during steady-state SIV for (a, b & e, f) $L_u/d$ = 120, (c, d & g, h) $L_u/d$ = 208 at (a, b & c, d) $U_t$ = 16 m/s and (e, f & g, h) $U_t$ = 6 m/s.

Figure 17 exemplifies $u$ (a, c) and $v$ (b, d) spatial modal profiles inclusive of mean displacements at different time instants where the lower (a, b) or higher (c, d) mode prevails the riser dynamics with large drifts and variable curvatures along the span. Some local modulations are observed (see the red dotted circles in Figure 3.17b), suggesting a multi-modal interaction between higher/lower modes during SIV. Nevertheless, as $L_w/d$ is further increased to 208, contour plots of $u$ (Figure 3.15g) and $v$ (Figure 3.15h) responses, together with FFT (Figures 3.16g, h), appear to become unimodal as in the higher $U_t$ range. This feature now suggests a greater effect of increasing $L_w/d$ with respect to a multi-to-single modal transition in a low $U_t$ range.

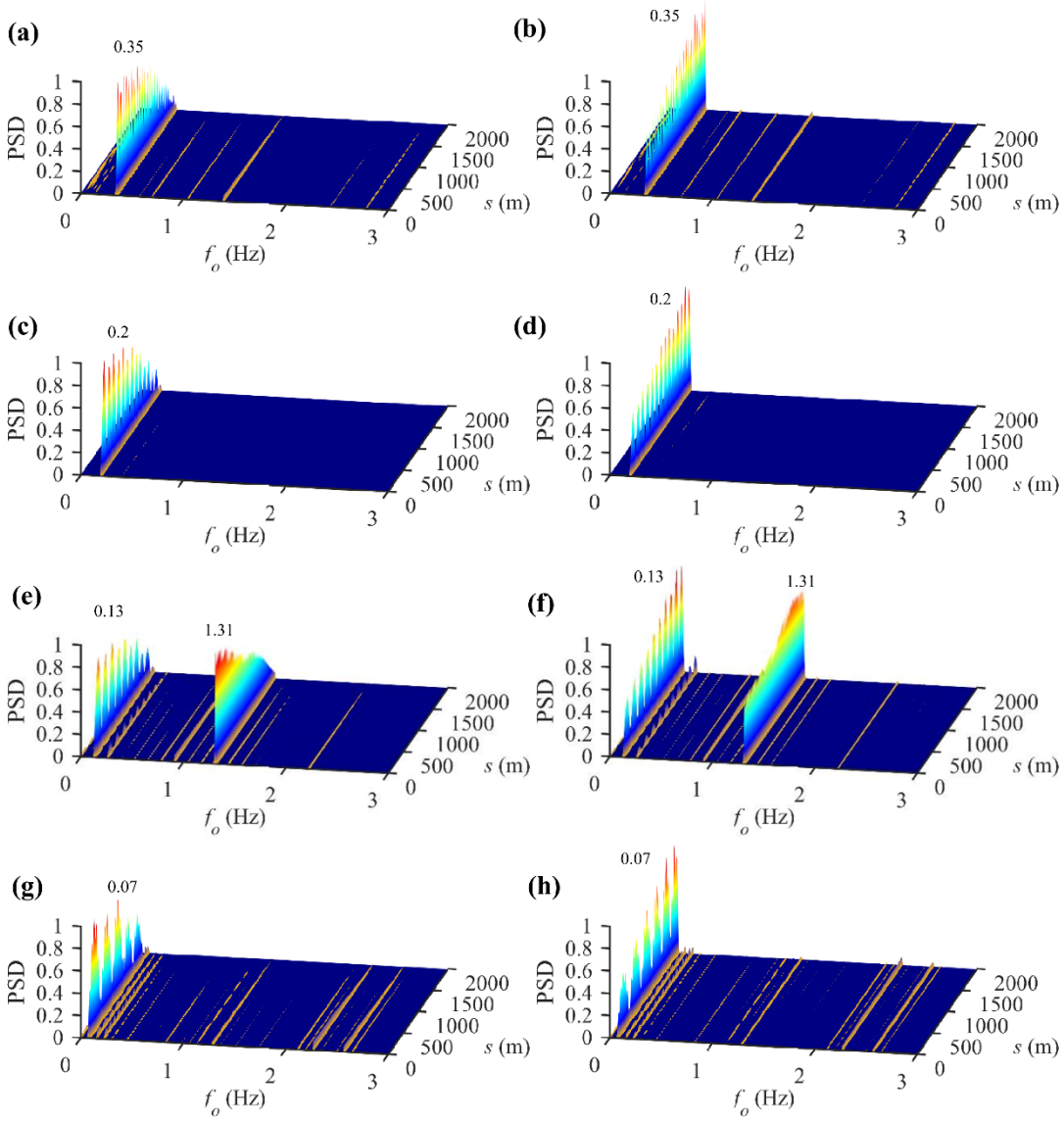


**Figure 3.16:** Spatial profiles of oscillation frequencies associated with responses in Figure 3.15.

Some selected phase plane trajectories associated with the spatially maximum root-mean-squared (RMS) $u$ and $v$ oscillations are displayed in Figure 3.18 for (a, b) $L_w/d = 80$ and $U_t = 6$ m/s, (c, d) $L_w/d = 80$ and $U_t = 16$ m/s, (e, f) $L_w/d = 208$ and $U_t = 16$ m/s, and (g, h) $L_w/d = 120$ and $U_t = 6$ m/s. In the low $L_w/d$ and low $U_t$ case (a, b), trajectories appear rather complicated, modulated and non-repetitive for each cycle due to the multi-harmonic effect. In the low $L_w/d$ but higher $U_t$ case (c, d), trajectories become dominated by a single harmonic, yet exhibiting a peculiar closed-loop pattern with a high level of repetitive cycles. In the high $L_w/d$ and high $U_t$ case (e, f), a nearly perfect circular trajectory associated with a single harmonic, unimodal and periodic motion takes place. Finally, in the intermediate $L_w/d$ and low $U_t$ case (g, h) exhibiting a two-dominant mode response (Figures 3.15e, f, 3.16e, f and 3.17), trajectories reveal a switching pattern between outer and inner closed-loop orbits with some modulations as a result of modal transition.

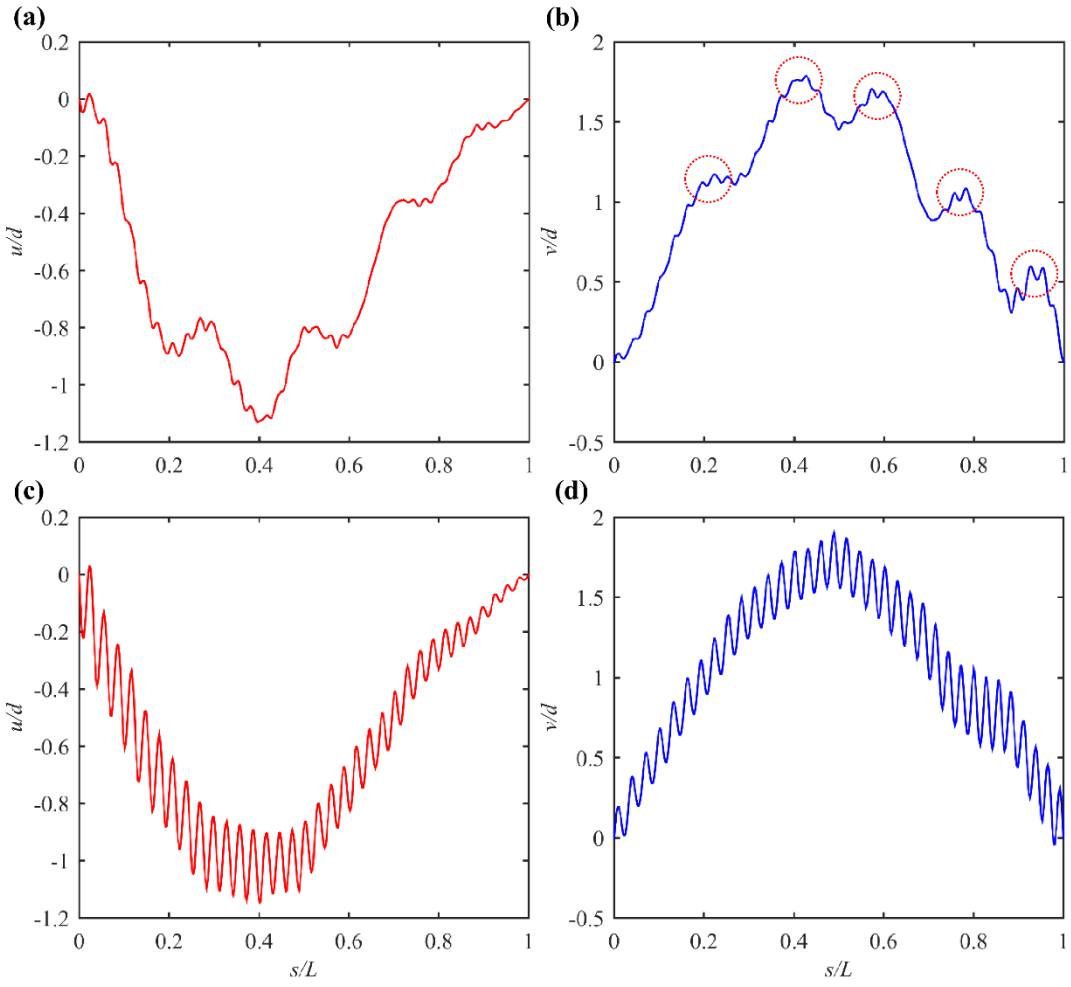


**Figure 3.17:.** Illustrative spatial modal profiles in (a, c) $X$ and (b, d) $Y$ directions for $L_w/d = 120$ at $U_t = 6$ m/s dominated by lower (a, b) and higher (c, d) modes.

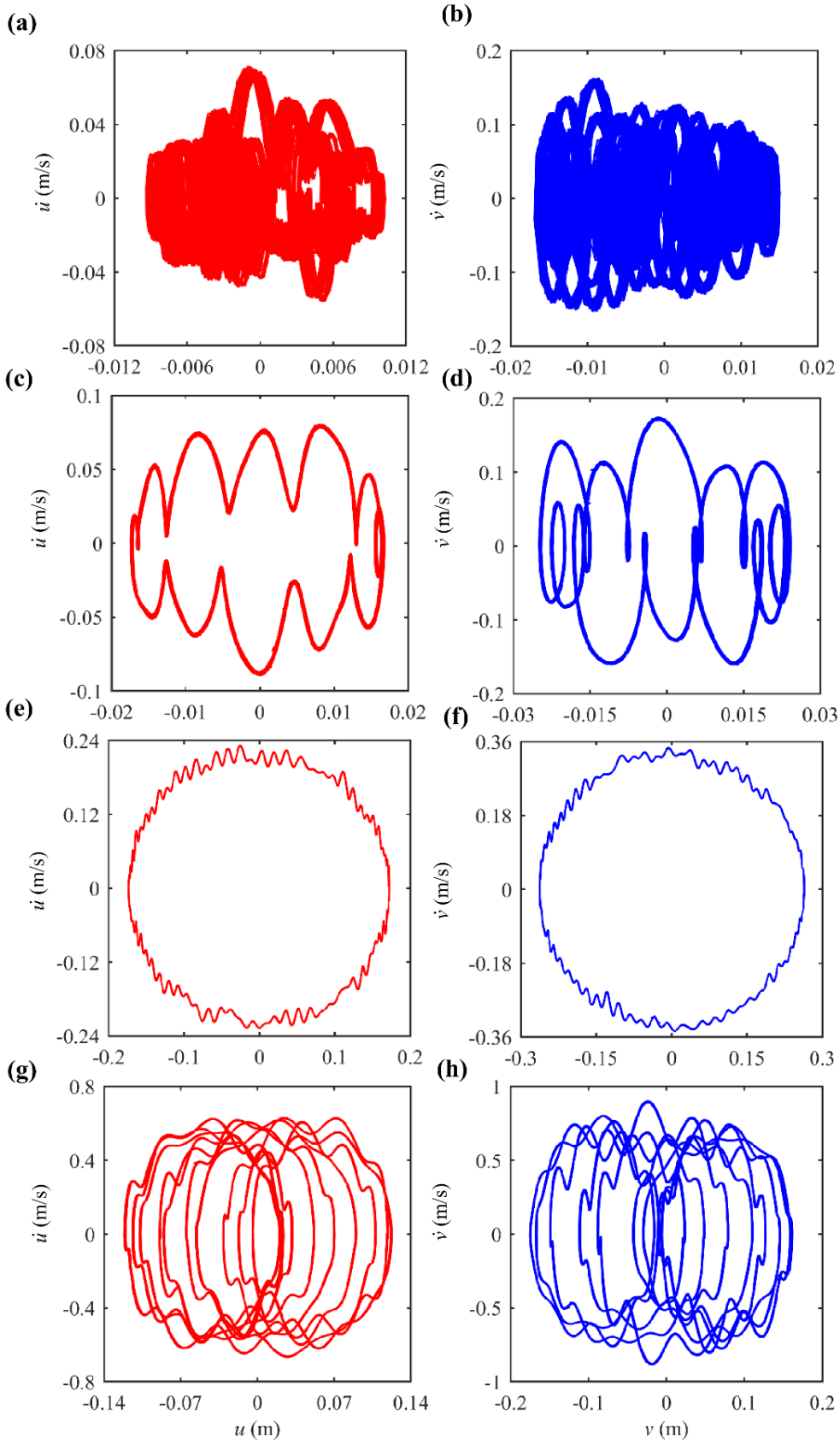


**Figure 3.18:** Phase plane trajectories associated with spatially maximum (a, c, e, g) $u_{rms}$ and (b, d, f, h) $v_{rms}$ for (a, b) $L_u/d$ = 80 and $U_t$ = 6 m/s; (c, d) $L_u/d$ = 80 and $U_t$ = 16 m/s; (e, f) $L_u/d$ = 208 and $U_t$ = 16 m/s, (g, h) $L_u/d$= 120 and $U_t$ = 6 m/s.

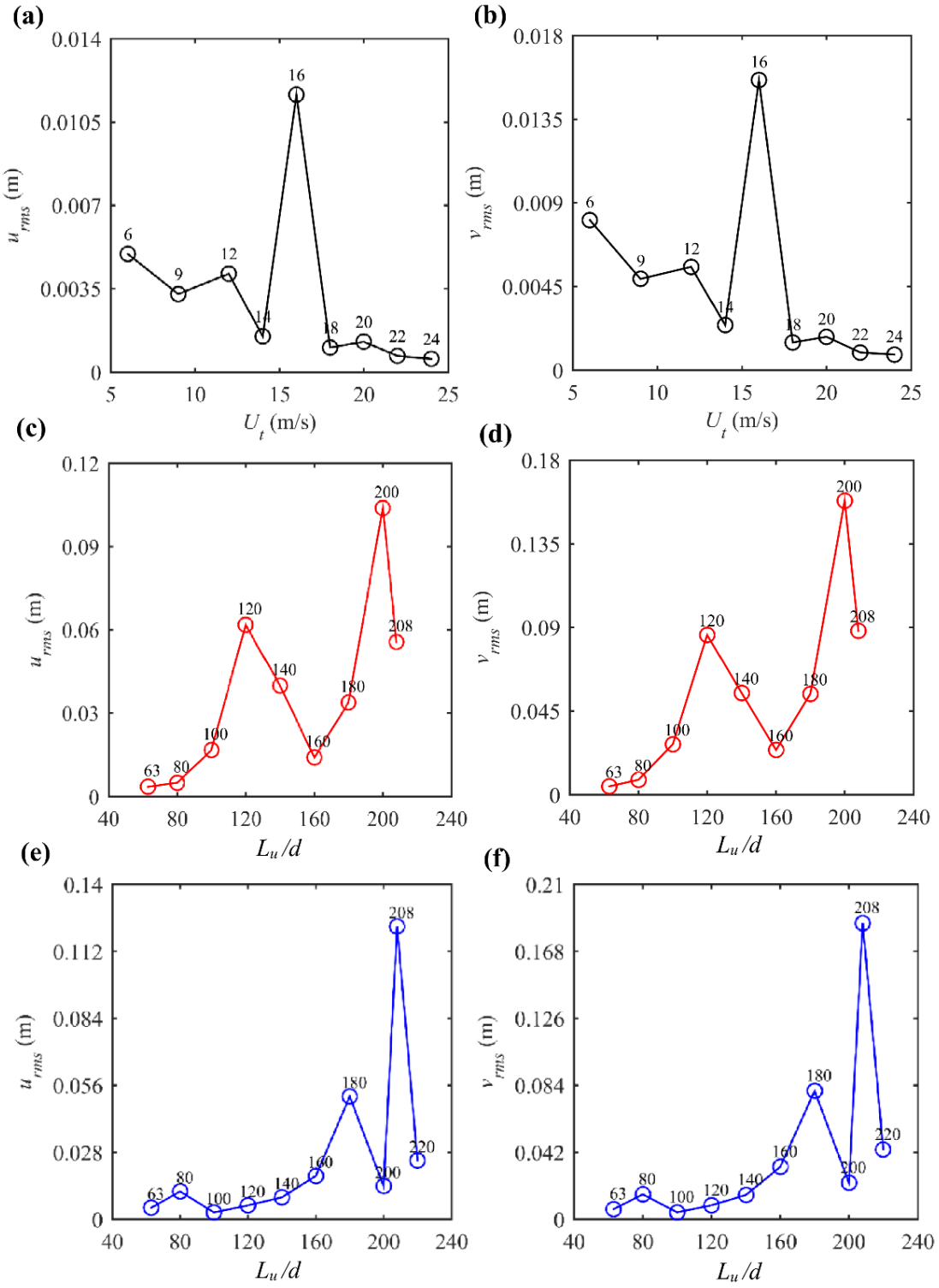


**Figure 3.19:** Variations of spatially maximum (a, c, e) $u_{rms}$ and (b, d, f) $v_{rms}$ in the case of (a, b) varying $U_t$ for $L_u/d$ = 80, (c, d) varying $L_u/d$ for $U_t$ = 6 m/s and (e, f) varying $L_u/d$ for $U_t$ = 16 m/s.

In summary, SIV features are found to be dependent on the individual effect of $L_u/d$ and $U_t$, rather than $f_s$. In order to determine the trends and most critical responses, Figure 3.19 plots the spatially maximum values of the root-mean-squared $u$ and $v$ amplitudes ($u_{rms}$, $v_{rms}$) in the case of varying $U_t$ for a fixed (a, b) $L_u/d$ = 80 and in the case of varying $L_u/d$ for a fixed (c, d) $U_t$ = 6 m/s and (e, f) 16 m/s. It is found that the peak $u$ and $v$ responses occur when $L_u/d$ = 80 and $U_t$ = 16 m/s (Figures 3.19a, b), $L_u/d$ = 120 and 200 for $U_t$ = 6 m/s (Figures 3.19c, d), and $L_u/d$ = 80, 108 and 208 for $U_t$ = 16 m/s (Figures 3.19e, f). Such multi-peak occurrences as $U_t$ or $L_u/d$ is varied suggest a dynamic resonance condition between the travelling slug flows and the pipe's dominant oscillation frequencies. Apart from the peak responses, it is also interesting to see generally decreasing and increasing trends with $U_t$ and $L_u$. By varying $U_t$ from 6 m/s to 24 m/s, SIV in terms of the root-mean-squared amplitude seem to be less pronounced. This may be associated with the aforementioned $U_t$ effects in terms of slug frequency distribution, mode transition and riser-slug flow responding time, causing less influential modal loads including centrifugal and gravity forces. On the other hand, the generally increased responses with $L_u$ may also be explained through the modal load concept, where a longer $L_u$ leads to more unbalanced modal loads and in turn enhances the riser responses. By contrast, it is reasonable to see that the slug flow with a short $L_u$ would affect the riser in a more averaged way than the long ones. This trend was also remarked in a numerical study by Thorsen et al. (2019) and experimentally observed by Zhu et al. (2019a). Overall, the case of $L_u/d$ = 208 and $U_t$ = 16 m/s appears to be the worst scenario producing largest $u$ and $v$ amplitudes for the present parametric case studies.

*3.4.5 Slug flow-induced bending and axial stresses*

It is of practical importance to examine bending and axial stresses caused by SIV. For the space-time varying maximum bending stresses in $X$ and $Y$ directions, $\sigma_u \approx \pm DEu''/2$ and $\sigma_v \approx \pm DEv''/2$, respectively, where + (−) denotes the tensile (compressive) stress depending on modal curvatures ($u''$, $v''$). Correspondingly, the space-time varying axial stress can be evaluated through $\sigma_a \approx E(\tilde{x}'u' + \tilde{y}'v')$ where the terms in the parenthesis are the extensional dynamic strain proportional to the pipe displacement gradients (Srinil et al., 2007). The total steady-state stresses ($\sigma_t$) can be finally computed based on the summation of static, dynamic bending and axial stresses. In the following, stress values are reported in MPa.

Figure 3.20 presents contour plots of $\sigma_u$ and $\sigma_v$ inclusive of mean and oscillatory components along the pipe span and time ($2980 < t < 3000$ s) by comparing the four chosen cases of (a, b) $L_u/d$ = 80 and $U_t$ = 6 m/s, (c, d) $L_u/d$ = 120 and $U_t$ = 6 m/s, (e, f) $L_u/d$ = 80 and $U_t$ = 16 m/s, and (g, h) $L_u/d$ = 208 and $U_t$ = 16 m/s. Note that the first and fourth cases are based

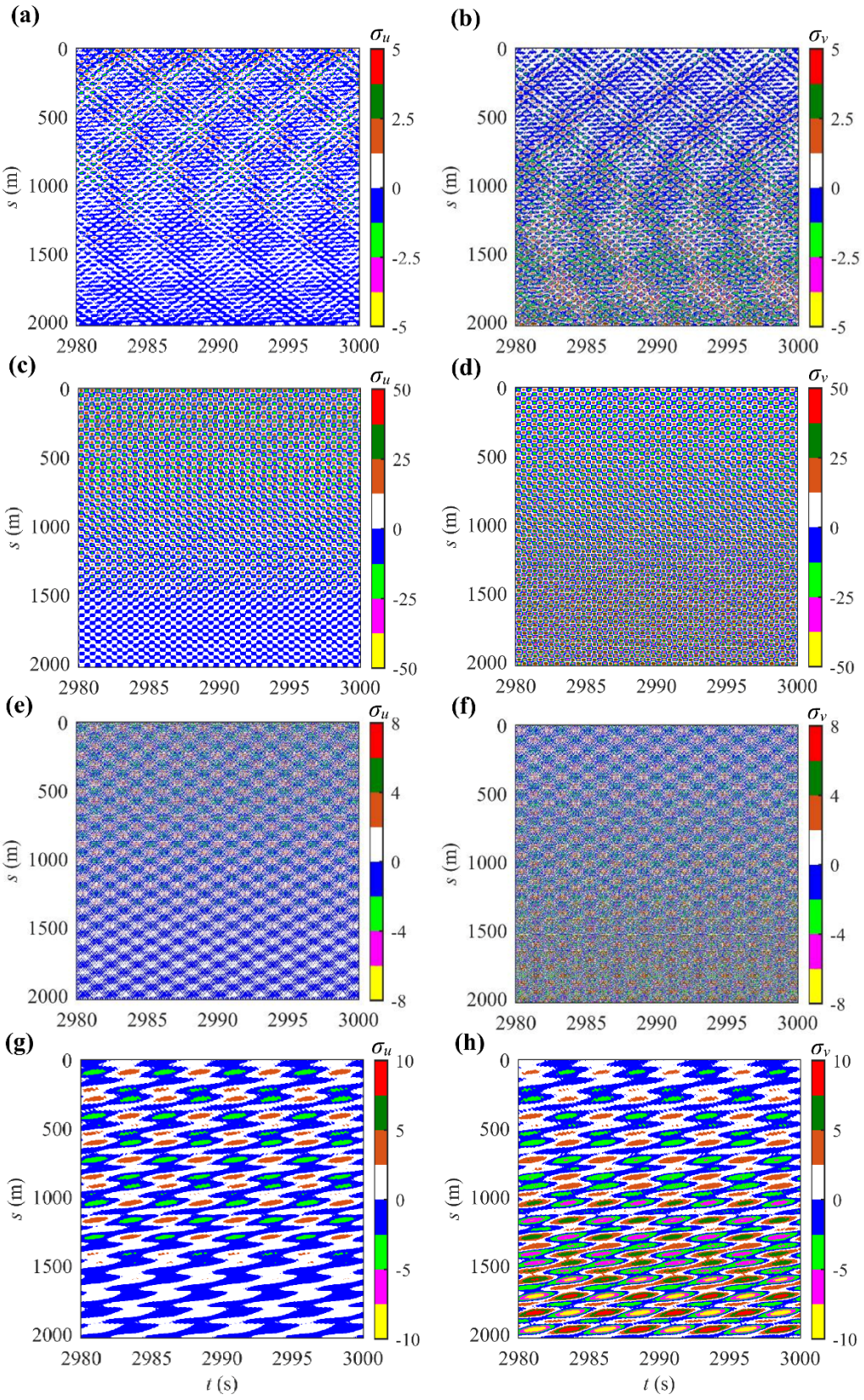


**Figure 3.20:** Space-time varying (a, c, e, g) $\sigma_u$ and (b, d, f, h) $\sigma_v$ inclusive of mean components: a, b (c, d) for $L_u/d$ = 80 (120) at $U_t$ = 6 m/s; e, f (g, h) for $L_u/d$ = 80 (208) at $U_t$ = 16 m/s.

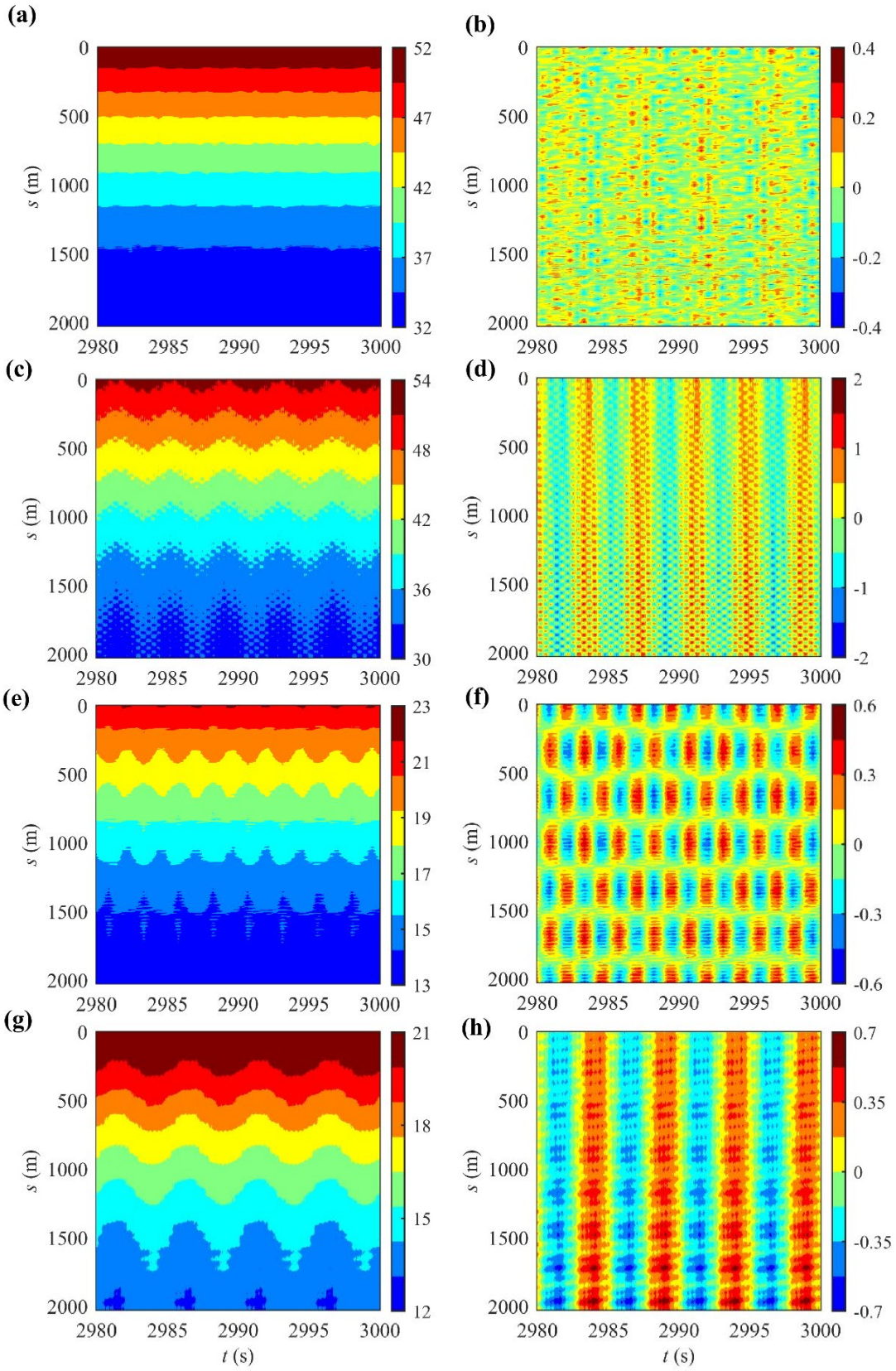


**Figure 3.21:** Space-time varying $\sigma_a$ (a, c, e, g) with and (b, d, f, h) exclusive of mean components: a, b (c, d) for $L_u/d$ = 80 (120) at $U_t$ = 6 m/s; e, f (g, h) for $L_u/d$ = 80 (208) at $U_t$ = 16 m/s.

on the same $f_s$ = 0.20 Hz. For $\sigma_a$ evaluations, the effects of mean components are certainly meaningful as noted in Zanganeh and Srinil (2016). For the above chosen cases, contour plots of $\sigma_a$ are displayed in Figure 3.21 by comparing between the total (mean and oscillatory) $\sigma_a$ (Figures 3.21a, c, e, g) and mean-free $\sigma_a$ (Figures 3.21b, d, f, h). For the cases of $f_s \approx$ 0.20 Hz, contour plots of $\sigma_t$ are shown in Figure 3.22 in both $X$ and $Y$ directions. Table 3.7 summarizes the spatially and temporally maximum (+) and minimum (−) $\sigma_u$ and $\sigma_v$ associated with Figure 3.20 and $\sigma_a$ ($\sigma_t$) associated with Figure 3.21 (Figure 3.22). In all cases, maximum and minimum bending stresses occur in the $v$ direction associated with the vertical moving gravity, and they are below the typical yield strengths of about 200-500 MPa for a standard steel pipe (e.g. API 5L) used in oil and gas applications.

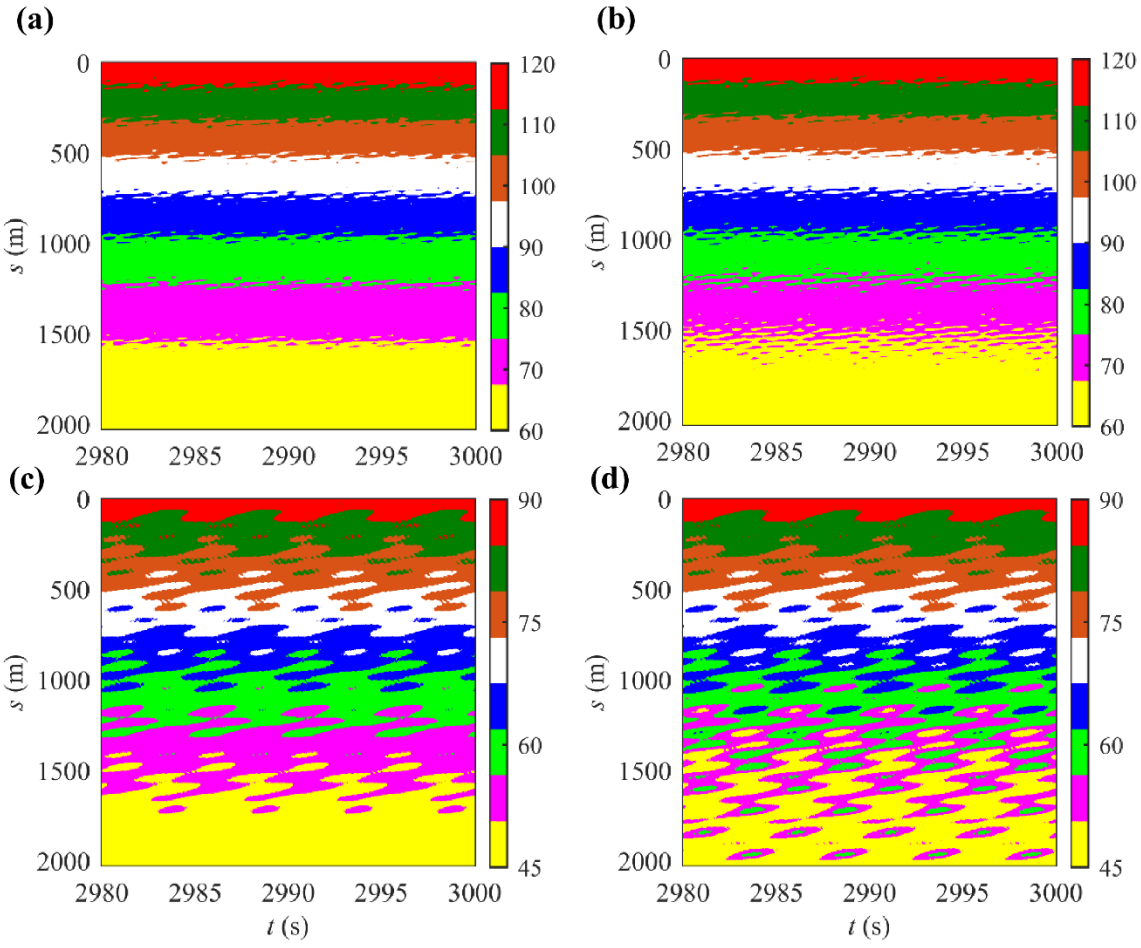


**Figure 3.22:** Space-time varying $\sigma_t$ in (a, c) $X$ and (b, d) $Y$ directions for (a, b) $L_u/d$ = 80 and $U_t$ = 6 m/s and (c, d) $L_u/d$ = 208 at $U_t$ = 16 m/s.

For a low $U_t$ = 6 m/s and $L_u/d$ = 80, high oscillatory modulations in $\sigma_u$ (Figure 3.20a), $\sigma_v$ (Figure 3.20b) and $\sigma_a$ (Figure 3.21b) contours are clearly observed, as in the displacement plots (Figures 3.13a, b), accompanied by large mean stresses (Figure 3.21a) associated with large mean displacements (Figures 3.12a, b). By increasing either $L_u/d$ to 120 (Figures 3.20c, d) or

$U_t$ to 16 m/s (Figure 3.20e, f), overall $\sigma_u$ and $\sigma_v$ contours reveal standing-wave patterns, as in the associated displacements, whose values are positively and negatively amplified in Table 3.7, with the worst scenario being associated with the former case. This highlights the important effect of increasing slug unit length on the pipe SIV bending stresses. Nevertheless, the variation of $U_t$ plays a greater role than that of $L_u/d$ in evaluating mean $\sigma_a$ as shown in Figures 3.21e vs. Figures 3.21c.

**Table 3.7:** Maximum/minimum bending, axial and total stresses in MPa corresponding to (a) Figure 3.20, (b) Figure 3.21 and (c) Figure 3.22, respectively.

**(a)**

| $U_t$ (m/s) | $L_u/d$ | $\sigma_u$ | | $\sigma_v$ | |
|---|---|---|---|---|---|
| | | **Max** | **Min** | **Max** | **Min** |
| 6 | 80 | 3.34 | -2.89 | 4.92 | -5.68 |
| 6 | 120 | 31.68 | -30.57 | 49.51 | -49.15 |
| 16 | 80 | 5.42 | -6.00 | 8.64 | -8.59 |
| 16 | 208 | 4.51 | -4.38 | 10.70 | -11.55 |

**(b)**

| $U_t$ (m/s) | $L_u/d$ | $\sigma_a$ (mean & oscillation parts) | | $\sigma_a$ (oscillation part) | |
|---|---|---|---|---|---|
| | | **Max** | **Min** | **Max** | **Min** |
| 6 | 80 | 52.08 | 32.01 | 0.42 | -0.43 |
| 6 | 120 | 53.62 | 30.75 | 1.96 | -1.96 |
| 16 | 80 | 22.06 | 12.86 | 0.64 | -0.63 |
| 16 | 208 | 21.94 | 12.76 | 0.73 | -0.74 |

**(c)**

| $U_t$ (m/s) | $L_u/d$ | $\sigma_t$ ($u$ direction) | | $\sigma_t$ ($v$ direction) | |
|---|---|---|---|---|---|
| | | **Max** | **Min** | **Max** | **Min** |
| 6 | 80 | 119.51 | 60.51 | 119.20 | 55.48 |
| 16 | 208 | 89.58 | 45.31 | 89.22 | 34.68 |

As reported in Table 3.7, the mean $\sigma_a$ values are considerably decreased with $U_t$ = 16 m/s and $L_u/d$ = 80 due to the decreased mean displacements (Figure 3.12). The trend of oscillatory $\sigma_a$ behaves similarly to that of the total $\sigma_u$ and $\sigma_v$ according to the same excited vibration modes. By comparing the case of $U_t$ = 6 m/s and $L_u/d$ = 80 vs. $U_t$ = 16 m/s and $L_u/d$ = 208, both having similar $f_s$, the latter exhibit greater $\sigma_u$, $\sigma_v$ and oscillatory $\sigma_a$ and whereas the former exhibits larger mean $\sigma_a$. These emphasize the individual role played by $L_u/d$ or $U_t$, regardless of $f_s$. Comparisons in Figure 3.22 and Table 3.7 also suggest the worst $\sigma_t$ scenario (i.e. tensile type) associated with the case subject to the maximum slug gravity weight effect under $U_t$ = 6 *m*/s

and $L_u/d = 80$. Nevertheless, since $\sigma_t$ decreases from the riser top to bottom, the case with higher $U_t$ = 16 m/s and $L_u/d$ = 208 may pose a critical challenge associated with the diminishing $\sigma_t$ leading to a greater likelihood dynamic buckling with a negative $\sigma_t$.

### 3.5. Summary

In this chapter, slug gas-liquid flow-induced planar vibrations in a long curved inclined flexible riser have been numerically investigated to understand the mechanical effects of slug flow characteristics including the slug unit length, translational velocity and fluctuation frequencies. A mechanistic slug flow model has been applied to arrive at the system phase fractions, local velocities and pressure changes of steady slug gas-liquid flows travelling upwardly through the flexible cylindrical pipe. Coupled horizontal and vertical motions of the bendable/extensible curved riser with pinned-pinned end conditions are subject to the space-time varying fluid weights and flow momenta associated with the uniformly travelling slug units. Depending on the pipe diameter and inclination, phase fractions, superficial velocities and internal pressure changes, parametric studies have been performed in the case of varying slug unit length, translational velocity and excitation frequency.

Overall, several key slug flow features and resonant SIV mechanisms have been observed. For a given pipe inclination, a greater liquid mass or density fluctuation occurs in the case of lower gas superficial velocity. For the riser system with variable inclinations, the changes in the gas-liquid flow velocities predominate over a volumetric mass variation. The liquid mass distribution is primarily responsible for the pressure drop and associated pipe wall tension change which, in turn, modifies the riser axial extensibility, static equilibrium reconfiguration and SIV resonance condition. An intrinsic excursion in global riser displacements is noticed during the initial transient slug initiation leading to a pipe flexing into a new double-curvature configuration. After this short-period excursion, the flexible riser reconfigures itself into a new static equilibrium owing to the combined effects of slug gravitational weight and flow momentum. For steady-state SIV, riser responses comprise the amplified mean and oscillatory components which are dynamically coupled as a result of the space-time varying gravity (mostly due to the liquid holdup with a higher fluid density) and the gas-liquid flow (centrifugal and Coriolis) momenta depending on the combined two-phase masses and velocities. Depending on the slug flow conditions, multi-modal vibration of the flexible riser is revealed and attributed to the multiple harmonic components in slug characteristic frequencies. By varying $U_t$, a transition from a multi-mode SIV (low $U_t$) to a single-mode SIV (high $U_t$) is realized. By increasing $L_u/d$, the single-mode SIV response could appear in the low $U_t$ range. Planar SIV seems not solely governed by characteristic slug excitation frequency but affected

by an individual effect of $U_t$ and $L_w/d$. In some cases, multiple resonant SIV may take place at a certain $L_w/d$-$U_t$ combination, where the oscillation mode switches intermittently between distinct lower/higher ones. Space-time varying bending, axial and total stresses associated with SIV have been examined to verify the material strength and identify a potential dynamic buckling occurrence. Both mean and oscillatory stress components have been evaluated. By comparing the two parametric ($L_w/d$-$U_t$) cases having an identical slug frequency, greater oscillatory bending and axial stresses occur in the case of higher $U_t$ and $L_w/d$, whereas greater mean stress components occur in the lower $U_t$ case. This emphasizes how $U_t$ or $L_w/d$ individually plays a meaningful role in riser SIV and the associated stress assessment.

# Chapter 4. Two-Dimensional VIV of Rigid Cylinders

Several SIV aspects have been observed and discussed in Chapter 3. To understand combined SIV and VIV phenomena, fundamental characteristics of the external counterpart is first investigated. In this chapter, a phenomenological model based on wake oscillators is applied and implemented for an elastically mounted rigid cylinder in uniform flows subject to cross-flow/in-line VIV. The dynamical system described by coupled nonlinear cylinder-wake oscillators is solved by a numerical-analytical approach. Extended investigations on 2-DOF VIV suppression are carried out by adding damping terms in the transverse direction, which represent closed-loop linear and nonlinear velocity feedback controllers. Approximated analytical expressions are derived by using the harmonic balance to explicitly capture the system nonlinear dynamic features and the resonant responses. Several important VIV features such as a lock-in range, amplitude jump, two-to-one resonant frequency and figure-of-eight trajectory are revealed and captured by this semi-empirical model. In addition, parametric investigations are carried out to evaluate the linear versus nonlinear controller performance in VIV mitigation.

## 4.1 Nonlinear Fluid-Structure Dynamic Model

A structurally active controller can be represented by a mechanical device (e.g. an electromagnetic actuator) installed inside the cylinder to avoid disturbing the external flow fields (Baz and Ro, 1991). This concept is intrinsically different from the active flow control strategy whose aim is to disrupt or interfere with the vortex formations. Because of the 2D nonlinear coupling of CF ($\tilde{Y}$) and IL ($\tilde{X}$) motions, the actuator can be activated in either $\tilde{Y}$ or $\tilde{X}$ direction with a control gain function imparting an adaptive damping force proportional to the cylinder velocity. This improvement of damping performance by the time-varying feedback control force proves to be the most reliable scheme for the active control (Inman, 2006).

Attention is placed on the two degrees of freedom (2-DOF) VIV suppression in the main critical lock-in region. The transverse $\tilde{Y}$ controller is implemented due to its larger response than the associated in-line motion. The $\tilde{X}$ controller can be considered in the pure in-line VIV range at lower reduced velocities. Both linear control (LC) and nonlinear control (NC) are employed and compared in order to justify (i) whether the former is sufficient for suppressing the VIV fluid-structure interactions with system nonlinearities, (ii) whether the latter should be accounted for due to potential higher-order nonlinear effects, and (iii) whether both strategies can be efficiently used for the coupled 2-DOF VIV mitigation of circular cylinders with

different mass ratios and power requirements.

Figure 4.1a displays a schematic idealisation of a flexibly mounted rigid circular cylinder placed in uniform flow of velocity $U_o$. The cylinder consists of a spring-mass-damping and $Y$ controller with 2-DOF of oscillations. A block diagram of the active control strategy is also displayed in Figure 4.1b. The nonlinear ordinary-differential equations of coupled $\tilde{X}$-$\tilde{Y}$ cylinder motions, which are subjected to in-line ($F_x^*$) and cross-flow ($F_y^*$) VIV excitations and control ($F_{yc}^*$) force per unit length, may be expressed as

$$\left(m_s + m_a\right)\ddot{\tilde{X}} + \left(c_s + c_f\right)\dot{\tilde{X}} + K\left(\tilde{X} + \alpha_x^*\tilde{X}^3 + \beta_x^*\tilde{X}\tilde{Y}^2\right) = F_x^*, \tag{4.1}$$

$$\left(m_s + m_a\right)\ddot{\tilde{Y}} + \left(c_s + c_f\right)\dot{\tilde{Y}} + K\left(\tilde{Y} + \alpha_y^*\tilde{Y}^3 + \beta_y^*\tilde{Y}\tilde{X}^2\right) = F_y^* - F_{yc}^*, \tag{4.2}$$

where an overdot denotes differentiation with respect to the dimensional time $t$. $m_s$ is the structural mass, $m_a$ the fluid added mass, $m_a = C_a\rho_o\pi D^2/4$, with $C_a$ being the added mass coefficient assumed to be unity for a circular cylinder (Sarpkaya, 2004), $\rho_o$ the fluid density, $D$ the cylinder diameter, $K$ the linear elastic stiffness coefficient, $c_s$ and $c_f$ the structural viscous and fluid-added damping coefficient, respectively.

It is worth noting that in practice $K$, $c_s$ and $c_f$ may be dissimilar between $\tilde{X}$ and $\tilde{Y}$ directions (Srinil et al., 2013); however, they are herein assumed to be equal in both directions to maintain the symmetry of cylinder properties. Following Facchinetti et al. (2004), $c_f$ may be fixed and defined as $c_f = \gamma\omega_n\rho_o D^2$ in which $\omega_n$ is the angular natural frequency of the cylinder in still water and $\gamma$ is the stall parameter (Skop and Balasubramanian, 1997) providing a self-limiting response in the absence of $c_s$. Note also that, from a phenomenological modelling viewpoint, $m_a$ and $c_f$ in Eqs. (4.1) and (4.2) are assumed to be associated with the oscillating cylinder in still water whereas their nonlinear dynamic counterparts subject to VIV are captured through the wake oscillator model (Zanganeh and Srinil, 2014). Separating $m_a$ and $c_f$ from the total force expressions allows one to normalize Eqs. (4.1) and (4.2) into general dimensionless forms. The geometrically nonlinear stiffness terms with the associated parameters ($\alpha_x^*$, $\beta_x^*$ $\alpha_y^*$, $\beta_y^*$) govern the physical stretching and the two-dimensional displacement coupling observed experimentally (Srinil et al., 2013). These cubic-type Duffing terms (Kovacic and Brennan, 2011) are accounted for since they enable the model to capture the key hysteresis effect with a response jump in the large-amplitude dual resonant VIV for a low-mass cylinder (Srinil and Zanganeh, 2012).

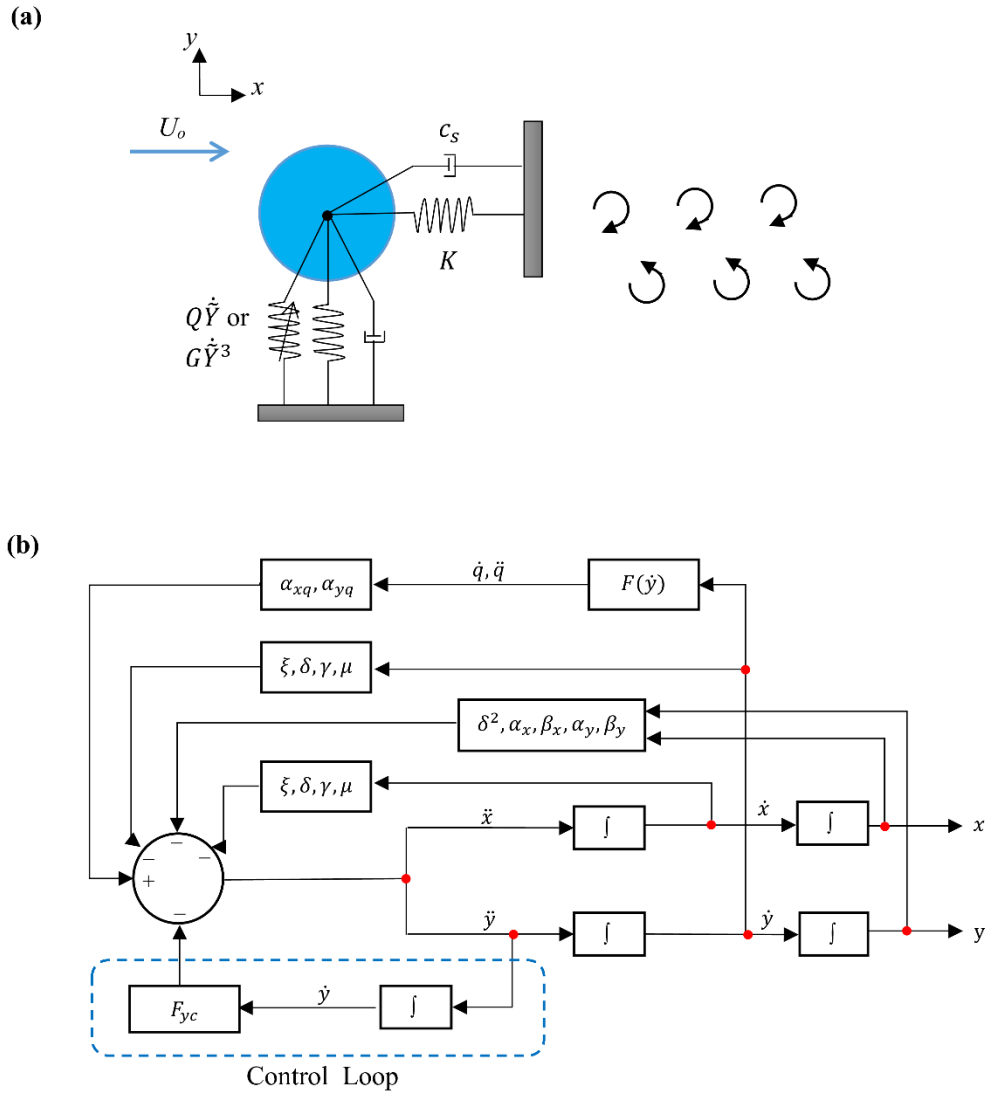


**Figure 4.1:** (a) An active velocity feedback control model of an elastically mounted circular cylinder undergoing 2D VIV; (b) a block diagram of active control strategy.

The LC force can be expressed as $F_{yc}^{*}=Q\dot{Y}$ whereas the NC one reads $F_{yc}^{*}=G\dot{Y}^3$, with a positive control gain ($Q$, $G$) to be assigned and varied (Nayfeh, 1993). The cubic-type NC is considered since the cylinder nonlinearities (Eqs. (4.1) and (4.2)) and the Rayleigh wake oscillator (Eq. (4.5)) are theoretically of cubic type. As for the hydrodynamic excitation forces associated with the 2-DOF VIV of a rigid cylinder, there are a few phenomenological models available in the literature. Herein, the fluid physics-based model – which has been derived from the vortex strength principle and requires a single variable describing the fluid displacement circulation $q$ – is considered. In-depth details can be found in Bai and Qin (2014) where the time-varying in-line and cross-flow fluid forces read $F_x^{*}(t)=-\rho_o C_{D0} D^4 \dot{q}\ddot{q}/(32\pi^3 \mathrm{St}^3 U_o)$ and $F_y^{*}(t)= C_{L0}\rho_o U_o D^2 \dot{q}/(8\pi \mathrm{St})$. These force functions contain empirical quantities, namely the Strouhal number (St), the unsteady lift ($C_{L0}$) and drag ($C_{D0}$) force coefficients of the stationary cylinder. Note that the effect of static mean drag force and its amplification due to VIV

(Zanganeh and Srinil, 2016) is herein neglected since attention is placed on the active control of the system fluctuating dynamics, rather than the statics.

By introducing the dimensionless time $\tau = t\omega_{st}$ in which $\omega_{st}$ is the angular vortex shedding frequency, and the normalized displacements $x = \tilde{X}/D$ and $y = \tilde{Y}/D$, the nonlinearly coupled equations of cylinder IL and CF motions can be expressed, in dimensionless forms, as

$$\ddot{x} + (2\xi\delta + \gamma/\mu)\dot{x} + \delta^2(x + \alpha_x x^3 + \beta_x xy^2) = -2\alpha_{xq}\dot{q}\ddot{q}, \tag{4.3}$$

$$\ddot{y} + (2\xi\delta + \gamma/\mu)\dot{y} + \delta^2(y + \alpha_y y^3 + \beta_y yx^2) = \alpha_{yq}\dot{q} - F_{yc}, \tag{4.4}$$

in which an overdot now denotes differentiation with respect to the dimensionless time $\tau$. For LC (NC), $F_{yc} = \beta_K\dot{y}$ ($F_{yc} = \gamma_G\dot{y}^3$). Dimensionless parameters include the damping ratio $\xi = c_s/(2m\omega_n)$, frequency ratio $\delta = \omega_n/\omega_{st}$, geometric coefficients ($\alpha_x$ $\beta_x$ $\alpha_y$ $\beta_y$), force coefficients $\alpha_{xq} = C_{D0}/(32\pi^2\ \mathrm{St}^2\mu)$ and $\alpha_{yq} = C_{L0}/(16\pi^2\mathrm{St}^2\mu)$, control gain $\beta_K = Q/m\omega_{st}$ and $\gamma_G = GD^2\omega_{st}/m$, with $\mu = m/\rho_o D^2$ and $m = m_s + m_a$. The nominal reduced velocity parameter $V_r$ can be related to $\delta$ through $\delta = 1/(\mathrm{St}V_r)$ since $V_r = 2\pi U_o/\omega_n D$. For parametric studies in Section 4.3, $V_r$ is varied through $\delta$ in Eqs. (4.3) and (4.4). It is important to note that the quadratic nonlinear coupling term as a function of fluid $\dot{q}\ddot{q}$ appears in Eq. (4.3) whereas the typical linear coupling term $\dot{q}$ appears in Eq. (4.4). Such quadratic term in the in-line equation is responsible for the appearance of a figure-of-eight $\tilde{X}$-$\tilde{Y}$ trajectory (Srinil and Zanganeh, 2012) associated with a dual 2:1 resonance (Dahl et al., 2006; Srinil et al., 2013). To describe the fluid displacement circulation $q$, a single Rayleigh (Hartlen and Currie, 1970) wake oscillator may be written as Bai and Qin (2014)

$$\ddot{q} - \varepsilon_y\left(1 - 3\lambda\dot{q}^2\right)\dot{q} + q = \Lambda_y\ddot{y}, \tag{4.5}$$

in which $\varepsilon_y$, $\Lambda_y$ and $\lambda$ are the system empirical wake coefficients which can be specified or tuned by calibrating with experimental data, see Section 4.3.1. They can also be functions of system properties such as the mass ratio ($m^* = m/(\rho\pi D^2/4)$) (Srinil, 2010; Srinil et al., 2013) and Re (Srinil, 2011). The form in Eq. (4.5) with the cylinder velocity coupling term $\Lambda_y\dot{y}$ is different from the van der Pol equation (Gabbai and Benaroya, 2005) typically employed in the literature with the wake damping $\varepsilon_y(1-q^2)\dot{q}$ and acceleration coupling $\Lambda_y\ddot{y}$ terms (Facchinetti et al., 2004). Nevertheless, through a variable transformation by letting $\dot{q} = p$, the van der Pol oscillator of $p$ can be rewritten (Nayfeh, 1993). For efficient numerical computations and convenience in the analytical formulation, only Eq. (4.5) is considered for the 2-DOF VIV, instead of using double van der Pol oscillators previously considered by Srinil and Zanganeh (2012).

Overall, the nonlinearly coupled Eqs. (4.3)-(4.5) contain several empirical parameters.

Through a number of parametric and sensitivity studies whose selected results will be presented in Section 4.3.3, we assign $\lambda = 0.2$, $\gamma = 0.5$, St = 0.19, $C_{D0} = 0.2$ and $C_{L0} = 0.3$, as in Bai and Qin (2014), and $\alpha_x = \beta_x = \alpha_y = \beta_y = 0.4$. Some of these parameters may be treated as random variables (Low and Srinil, 2016) due to variations in different sets of experimental data. Some values (St, $C_{D0}$, $C_{L0}$) are suitable for a cylinder with a smooth surface and subject to a sub-critical flow with $\mathrm{Re} < 2\times10^5$ (Blevins, 1990). Empirical wake-oscillator coefficients ($\varepsilon_y$, $\Lambda_y$) will be deduced in Section 4.3.1. For numerical integrations, a 4$^{th}$ order Runge-Kutta scheme can be used with initial conditions of $x=y=\dot{x}=\dot{y}=\dot{q}=0$ and $q = 2$, and with a fixed dimensionless time step of 0.01 providing a convergence of steady-state simulation results. Note that the present prediction model does not account for the Re dependence of response amplitudes as highlighted by Govardhan and Williamson (2006). With new and substantial experimental data of 2-DOF VIV in a wide range of system parameters, the Re effect could be further incorporated into the model, e.g., through the empirical wake coefficients which regulate the self-limiting ($\varepsilon_y$) and fluid-cylinder coupling ($\Lambda_y$) terms in Eq. (4.5). The dependence of wake coefficients on Re has been highlighted by Srinil (2010) for the CF VIV prediction of long flexible cylinders.

### 4.2 Analytical Prediction of VIV Responses

To gain insights into the 2D VIV responses and explicitly capture the nonlinear coupling of key physical parameters, analytical expressions are derived which can complement numerical integration results. To capture the most influential effects of system nonlinearities, the first-order harmonic balance approach is applied. Due to the natural occurrence of a periodic 2:1 resonance of the cylinder $\tilde{X}$-$\tilde{Y}$ response in a wide range of $V_r$ (Dahl et al., 2010; Srinil et al., 2013), it is reasonable to assume a periodic solution of cross-flow response ($y$) and vortex wake circulation ($q$) with a dimensionless resonant oscillation frequency ($\omega$) as in Facchinetti et al. (2004) whereas the cylinder in-line motion ($x$) can be treated as a harmonic motion at $2\omega$. Accordingly, the approximated motions for $x$, $y$ and $q$ may be expressed as

$$x = x_0 \sin\left(2\omega\tau + \theta_{xy}\right), \tag{4.6}$$

$$y = y_0 \sin(\omega\tau), \tag{4.7}$$

$$q = q_0 \sin\left(\omega\tau + \theta_{qy}\right), \tag{4.8}$$

in which $x_0$, $y_0$ and $q_0$ are the dimensionless oscillation amplitudes and $\theta_{xy}$ ($\theta_{qy}$) is the associated $x$-$y$ ($q$-$y$) phase relationship. The LC system is first considered. By substituting Eqs.(4.6)-(4.8) into Eqs.(4.3)-(4.5) with $F_{yc}=\beta_K\dot{y}$, expanding and balancing the trigonometric terms in the forms of $\sin(2\omega t+\theta_{xy})$, $\cos(2\omega t+\theta_{xy})$, $\sin(\omega t)$, $\cos(\omega t)$, $\sin(\omega t+\theta_{qy})$ and $\cos(\omega t+\theta_{qy})$, and neglecting the

higher harmonic terms, the associated expressions can be obtained, respectively, as

$$-4\omega^2 x_0 + \delta^2\left(x_0 + \alpha_x \frac{3x_0^{\,3}}{4} + \beta_x \frac{x_0 y_0^{\,2}}{2}\right) = \alpha_{xq} q_0^{\,2}\omega^3 \cos\left(2\theta_{qy} - \theta_{xy}\right), \tag{4.9}$$

$$2\left(2\xi\delta + \frac{\gamma}{\mu}\right)\omega x_0 = \alpha_{xq} q_0^{\,2}\omega^3 \sin\left(2\theta_{qy} - \theta_{xy}\right), \tag{4.10}$$

$$-\omega^2 y_0 + \delta^2\left(y_0 + \alpha_y \frac{3y_0^{\,3}}{4} + \beta_y \frac{x_0^{\,2} y_0}{2}\right) = -\alpha_{yq}\omega q_0 \sin\left(\theta_{qy}\right), \tag{4.11}$$

$$\left(2\xi\delta + \frac{\gamma}{\mu}\right)\omega y_0 + \left(\beta_K \omega y_0\right) = \alpha_{yq}\omega q_0 \cos\left(\theta_{qy}\right), \tag{4.12}$$

$$q_0\left(1-\omega^2\right) = \Lambda_y \omega y_0 \sin\left(\theta_{qy}\right), \tag{4.13}$$

$$\frac{3}{4}\varepsilon_y \lambda q_0^{\,3}\omega^3 - \varepsilon\omega q_0 = \Lambda_y \omega y_0 \cos\left(\theta_{qy}\right). \tag{4.14}$$

The pair of Eqs. (4.9) and (4.10), Eqs. (4.11) and (4.12), and Eqs. (4.13) and (4.14) are derived from Eq. (4.3), (4.4) and (4.5), respectively. By dividing Eq. (4.10) with Eq. (4.9) and summing the squares of them, Eqs. (4.15) and (4.16) can be obtained, respectively. Similarly, the combination of Eqs. (4.11) and (4.12) gives rise to the first expression in Eq. (4.17) and to Eq. (4.18), whereas the combination of Eqs. (4.13) and (4.14) entails the second expression in Eq.(4.17) and Eq. (4.19), respectively. These are written as follows.

$$\tan\left(2\theta_{qy} - \theta_{xy}\right) = \frac{2(2\xi\delta + \gamma/\mu)\omega}{-4\omega^2 + \delta^2\left(1 + \alpha_x \frac{3x_0^{\,2}}{4} + \beta_x \frac{y_0^{\,2}}{2}\right)}, \tag{4.15}$$

$$\left(\alpha_{xq} q_0^{\,2}\omega^3\right)^2 = \left[2\left(2\xi\delta + \frac{\gamma}{\mu}\right)\omega x_0\right]^2 + \left[-4\omega^2 x_0 + \delta^2\left(x_0 + \alpha_x \frac{3x_0^{\,3}}{4} + \beta_x \frac{x_0 y_0^{\,2}}{2}\right)\right]^2, \tag{4.16}$$

$$\tan\left(\theta_{qy}\right) = \frac{\omega^2 - \delta^2\left(1 + \alpha_y \frac{3y_0^{\,2}}{4} + \beta_y \frac{x_0^{\,2}}{2}\right)}{\left(2\xi\delta + \frac{\gamma}{\mu}\right)\omega + \left(\beta_K \omega\right)} = \frac{\left(1-\omega^2\right)}{\frac{3}{4}\varepsilon_y \lambda q_0^{\,2}\omega^3 - \varepsilon_y \omega}, \tag{4.17}$$

$$\left(\alpha_{yq}\omega q_0\right)^2 = \left[\left(2\xi\delta + \frac{\gamma}{\mu}\right)\omega y_0 + \left(\beta_K \omega y_0\right)\right]^2 + \left[-\omega^2 y_0 + \delta^2\left(y_0 + \alpha_y \frac{3y_0^{\,3}}{4} + \beta_y \frac{x_0^{\,2} y_0}{2}\right)\right]^2, \tag{4.18}$$

$$\frac{y_0}{q_0} = \frac{\sqrt{\left(1-\omega^2\right)^2 + \left(\varepsilon_y \omega - \frac{3}{4}\varepsilon_y \lambda q_0^{\,2}\omega^3\right)^2}}{\Lambda_y \omega}. \tag{4.19}$$

Due to the nonlinear $x$-$y$ displacement coupling term ($xy^2$) in Eq. (4.3), the associated mean drift effect ($D_t$) is generated which can be expressed in dimensionless form as

$$D_t = \frac{-\delta^2 \beta_x x_0 {y_0}^2 \sin(\theta_{xy})}{4}. \tag{4.20}$$

This drift effect is dependent on the cylinder properties including amplitudes ($x_0$, $y_0$), frequency ratio ($\delta$), stiffness ($\beta_x$) and phase difference ($\theta_{xy}$) associated with the figure-of-eight orbital $\tilde{X}$-$\tilde{Y}$ motion. From Eq. (4.20), the zero or maximum $|D_t|$ occurs when $\theta_{xy} = n\pi$ ($n$=0, 1, 2…) or $(n+1)\pi/2$ ($n$=0, 2,…), respectively, with a negative (positive) $D_t$ suggesting an in-line downstream (upstream) drift. This $D_t$ value should be recognized when performing numerical simulations and experiments (Srinil et al. 2013).

Equations (4.17) and (4.18) can be further rearranged as

$$\frac{\left(2\xi\delta + \frac{\gamma}{\mu} + \beta_K\right)\left(1-\omega^2\right)}{\varepsilon_y - \frac{3}{4}\varepsilon\lambda {q_0}^2\omega^2} = -\omega^2 + \delta^2\left(1 + \alpha_y \frac{3{y_0}^2}{4} + \beta_y \frac{{x_0}^2}{2}\right), \tag{4.21}$$

$$\left(\alpha_{yq}\omega\frac{q_0}{y_0}\right)^2 = \left[\left(2\xi\delta + \frac{\gamma}{\mu}\right)\omega + \left(\beta_K\omega\right)\right]^2 + \left[-\omega^2 + \delta^2\left(1 + \alpha_y \frac{3{y_0}^2}{4} + \beta_y \frac{{x_0}^2}{2}\right)\right]^2. \tag{4.22}$$

Then, by combining Eqs. (4.21) and (4.22), we obtain

$$\left(\alpha_{yq}\omega\frac{q_0}{y_0}\right)^2 = \left[\left(2\xi\delta + \frac{\gamma}{\mu}\right)\omega + \left(\beta_K\omega\right)\right]^2 + \left[\frac{\left(2\xi\delta + \frac{\gamma}{\mu} + \beta_K\right)\left(1-\omega^2\right)}{\varepsilon_y - \frac{3}{4}\varepsilon_y\lambda {q_0}^2\omega^2}\right]^2. \tag{4.23}$$

By substituting Eq. (4.19) for $q_0/y_0$ into Eq. (4.23), and analytically solving the resulting equation, the closed-form expression for the two possible values of $q_0$ reads

$$q_0 = \sqrt{\frac{4\varepsilon\omega + 2(1 \pm \sqrt{1 - 4{a_1}^2{a_2}^2})/a_2}{3\varepsilon_y\lambda\omega^3}}, \tag{4.24}$$

$$a_1 = 1-\omega^2, \qquad a_2 = \frac{2\xi\delta + \gamma/\mu + \beta_K}{\alpha_{yq}\Lambda_y\omega}. \tag{4.25}$$

It can be appreciated that the vortex force amplitude $q_0$ is controlled through $a_2$ with a series of damping terms. Once a positive real value of $q_0$ is obtained from Eq. (4.24), that of $y_0$ can be determined via Eq. (4.19). To derive a closed-form expression for $x_0$, Eq. (4.16) can be further rearranged as a sixth-order polynomial equation governing $x_0$. From numerical simulation checks, it is found that the ${x_0}^6$ term is negligible (< 0.02) since generally $x_0 < 0.5$; hence, by

considering the resulting equation accounting for the next highest order of $x_0^4$, the unique solution for $x_0$ can be derived as

$$x_0 = \sqrt{\frac{2\sqrt{\frac{a_3^2}{4} + \frac{a_3 a_4^2}{2} + \frac{a_4^4}{4} + 2a_6 a_5 a_4} - a_4^2 - a_3}{4a_4 a_5}}, \tag{4.26}$$

$$a_3 = 4\omega^2\left(2\xi\delta + \frac{\gamma}{\mu}\right)^2, \quad a_4 = -4\omega^2 + \delta^2 + \beta_x \frac{y_0^2\delta^2}{2}, \quad a_5 = \alpha_x \frac{3\delta^2}{4}, \quad a_6 = \left(\alpha_{xq} q_0^2 \omega^3\right)^2. \tag{4.27}$$

Depending on the system parameters and empirical coefficients, it can be appreciated that both $y_0$ (Eq. (4.19)) and $x_0$ (Eq. (4.26)) are nonlinear functions of $q_0$, and the reduction of $x_0$ is dependent on the suppressed $y_0$ due to their nonlinear coupling. Subsequently, the system phase differences $\theta_{qy}$ and $\theta_{xy}$ can be obtained through Eqs. (4.17) and (4.15), respectively.

For NC system, by substituting Eqs. (4.6)-(4.8) into Eqs. (4.3)-(4.5) with $F_{yc}=\gamma_G \dot{y}^3$ and applying the harmonic balance, Eqs. (4.9)-(4.22) from the LC system can be used with $\gamma_G(3\omega^3 y_0^3)/4$ replacing $\beta_K \omega y_0$ in Eqs. (4.12) and (4.18), $\gamma_G(3\omega^3 y_0^2)/4$ replacing $\beta_K \omega$ in Eqs. (4.17), (4.22) and (4.23), and $\gamma_G(3\omega^2 y_0^2)/4$ replacing Eq. (4.21). By combining the resulting Eqs. (4.21) and (4.22) with the above substitutions, the following expression reads

$$\left(\alpha_{yq}\omega q_0\right)^2 = \left[\left(2\xi\delta + \frac{\gamma}{\mu}\right)\omega y_0 + \gamma_G \frac{3\omega^3 y_0^3}{4}\right]^2 + \left\{\frac{\left[\left(2\xi\delta + \frac{\gamma}{\mu}\right)y_0 + \gamma_G \frac{3\omega^2 y_0^3}{4}\right]\left(1-\omega^2\right)}{\varepsilon_y - \frac{3}{4}\varepsilon_y \lambda q_0^2 \omega^2}\right\}^2. \tag{4.28}$$

Accordingly, due to the presence of nonlinear amplitudes ($y_0^2$, $y_0^3$), it is unfeasible to further derive analytical expressions. Nevertheless, for a specific $V_r$ and $\omega$, Eqs. (4.16), (4.19) and (4.28) can be simultaneously solved for the key unknown $q_0$, $y_0$ and $x_0$. Both $\theta_{qy}$ and $\theta_{xy}$ can then be obtained from Eqs. (4.17) and (4.15), respectively.

Next, by imposing the ideal perfect resonance or lock-in condition with $\omega = \delta = 1$ for which $V_r = 1/\mathrm{St}$ (Facchinetti et al., 2004), the linearly controlled vortex force and $Y$ response, based on Eqs. (4.23) and (4.24), can be predicted, respectively, by

$$q_M = 2\sqrt{\frac{[\varepsilon_y + \alpha_{yq}\Lambda_y \omega/(2\xi + \gamma/\mu + \beta_K)]}{3\varepsilon_y \lambda}} \tag{4.29}$$

$$y_M = \frac{2\alpha_{yq}}{(2\xi + \gamma/\mu + \beta_K)}\sqrt{\left[1 + \frac{\Lambda_y}{\varepsilon_y}\frac{\alpha_{yq}}{(2\xi + \gamma/\mu + \beta_K)}\right]\frac{1}{3\lambda}}. \tag{4.30}$$

Correspondingly, with Eqs. (4.26) and (4.27), the linearly controlled $x$ response reads

$$x_M = \sqrt{\frac{2\sqrt{\frac{a_7^2}{4}+\frac{a_7 a_8^2}{2}+\frac{a_8^4}{4}+2a_{10}a_9a_8}-a_8^2-a_7}{4a_8a_9}}, \tag{4.31}$$

$$a_7 = 4\left(2\xi+\frac{\gamma}{\mu}\right)^2, \quad a_8 = \beta_x\frac{y_M^2}{2}-3, \quad a_9 = \frac{3}{4}\alpha_x, \quad a_{10} = 16\alpha_{xq}^2\left[1+\frac{\alpha_{yq}\Lambda_y}{\left(2\xi+\frac{\gamma}{\mu}+\beta_K\right)\varepsilon_y}\right]^2. \tag{4.32}$$

In the NC case, based on Eqs. (4.16), (4.19) and (4.28), the nonlinearly controlled force and displacement amplitudes with $\omega = \delta = 1$ can be simultaneously solved through

$$q_M = \frac{1}{\alpha_{yq}}\left[\left(2\xi+\frac{\gamma}{\mu}\right)y_M+\gamma_G\frac{3y_M^3}{4}\right], \tag{4.33}$$

$$y_M = \frac{1}{\Lambda_y}\left(\frac{3}{4}\varepsilon_y\lambda q_M^3-\varepsilon_y q_M\right), \tag{4.34}$$

$$\left(\alpha_{xq}q_M^2\right)^2 = \left[2\left(2\xi+\frac{\gamma}{\mu}\right)x_M\right]^2+\left[-4x_M+\left(x_0+\alpha_x\frac{3x_M^3}{4}+\beta_x\frac{x_M y_M^2}{2}\right)\right]^2. \tag{4.35}$$

Above LC (Eqs. (4.29)-(4.31)) and NC (Eqs. (4.33)-(4.35)) systems can be helpful for parametrically investigating the effect of system parameters without performing numerical integrations, as demonstrated in Section 4.3.3. It is also noticed that, for this particular frequency ratio case ($\omega = \delta = 1$), the geometrically nonlinear $\alpha_y$ and $\beta_y$ terms do not affect the controlled responses since $(1-\omega^2) = 0$ whereas the associated $\alpha_x$ and $\beta_x$ terms do. In the following, the parametric studies are presented and discussed.

## 4.3 Parametric Investigation and Discussion

Several aspects in LC and NC of the 2-DOF VIV of circular cylinders with geometric and hydrodynamic nonlinearities are discussed through the cases of varying reduced velocities ($0<V_r<14$). For the cylinder with a given $m^*$ and $\xi$, the control gains $\beta_K$ and $\gamma_G$ are specified such that their terms have the same order of magnitude as other damping ($\xi$, $\gamma$) effects, see Eqs. (4.25) and (4.28). Accordingly, it is deduced that $\beta_K$ and $\gamma_G$ should be of the order of unity.

### *4.3.1 Model calibration and validation*

Because the three nonlinearly coupled Eqs. (4.3)-(4.5) are used for the first time as a 2-DOF VIV prediction model, being the extended version of the linear cylinder model proposed by Bai and Qin (2014) and being different from other models with typical four equations (Srinil and

Zanganeh, 2012), a model calibration is required to determine appropriate empirical coefficients ($\varepsilon_y$, $\Lambda_y$). This can be achieved by validating the obtained analytical and numerical results with experimental data. In this study, $\varepsilon_y$ and $\Lambda_y$ are tuned such that the dynamic model captures the main lock-in range, maximum cross-flow ($A_y/D$) and in-line ($A_x/D$) amplitudes associated with the upper branch, and possible response jump due to the nonlinear hysteresis effect.

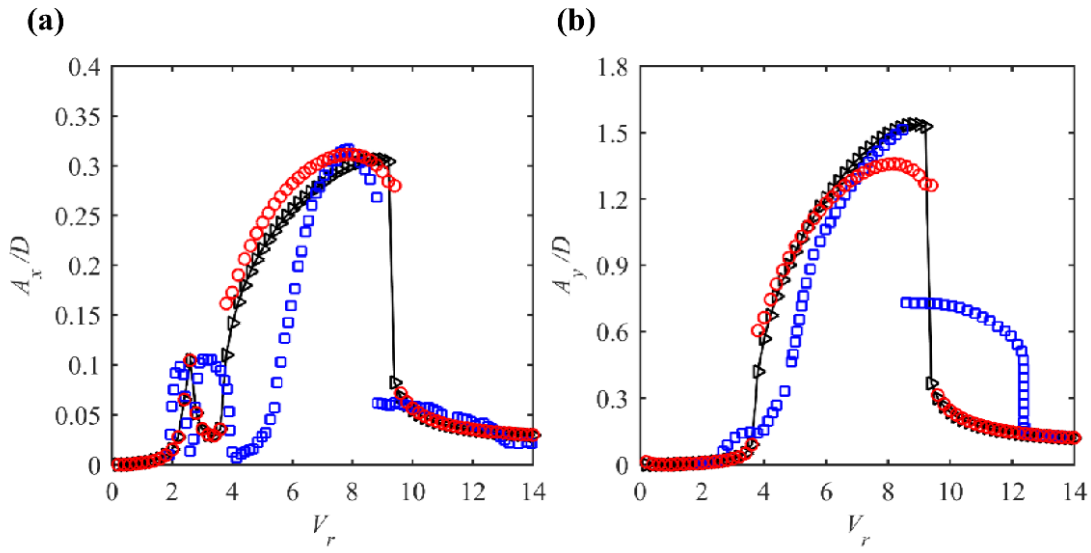


**Figure 4.2:** Comparisons of response amplitudes in the absence of control with numerical (triangles), analytical (circles) and experimental (squares) results for cylinder with $m^*$ = 2.6 and $\xi$ = 0.00361.

Accordingly, the low mass-damping 2-DOF cylinder ($m^*$ = 2.6, $\xi$ = 0.00361) tested by Jauvtis and Williamson (2004) is considered. Comparisons of analytical (circles), numerical (triangles) and experimental (squares) results are displayed in Figure 4.2 where $A_x/D$ (Figure 4.2a) and $A_y/D$ (Figure 4.2b) responses are plotted versus $V_r$. The tuning trials are carried out with a criterion such that the predicted maximum cross-flow and in-line amplitudes in the upper branches, as well as the associated lock-in ranges, are matched satisfactorily with the associated experimental results. This is deemed suitable as attention is placed on the most critical response and excitation range for a given $m^*$ and $\xi$ (Srinil and Zanganeh, 2012). The most satisfactory calibration is found in Figure 4.2 with a single set of $\varepsilon_y$ = 0.058 and $\Lambda_y$ = 12: the model predicts the first pure in-line VIV ($1.5< V_r <3$), the self-limiting maximum amplitudes ($A_y/D \approx 1.5$ and $A_x/D \approx 0.3$) in the main lock-in range ($4< V_r <10$), and the response jump at $V_r \approx 9$. Greater differences in maximum $A_y/D$ between analytical and numerical results are also noticed in Figure 4.2b due to the omitted higher-order harmonic contributions in the analytical solution (Eqs. (4.6)-(4.8)). Nevertheless, such discrepancies are reduced for smaller $A_x/D$ as shown in Figure 4.2a. The effect of high-order harmonics would become negligible for the controlled

system with decreased responses. To also capture the maximum $A_y/D$ in the lower branch ($V_r$ >8), another set of $\varepsilon_y$ and $\Lambda_y$ may be introduced. In this study, we use the above unique set across the $V_r$ range. If tuning with different and large set of experimental data is required, an optimization algorithm could also be employed for optimal calibration (Bódai and Srinil, 2015; Kurushina et al., 2018). Herein, we use $\varepsilon_y = 0.058$ and $\Lambda_y = 12$ across the $V_r$ range.

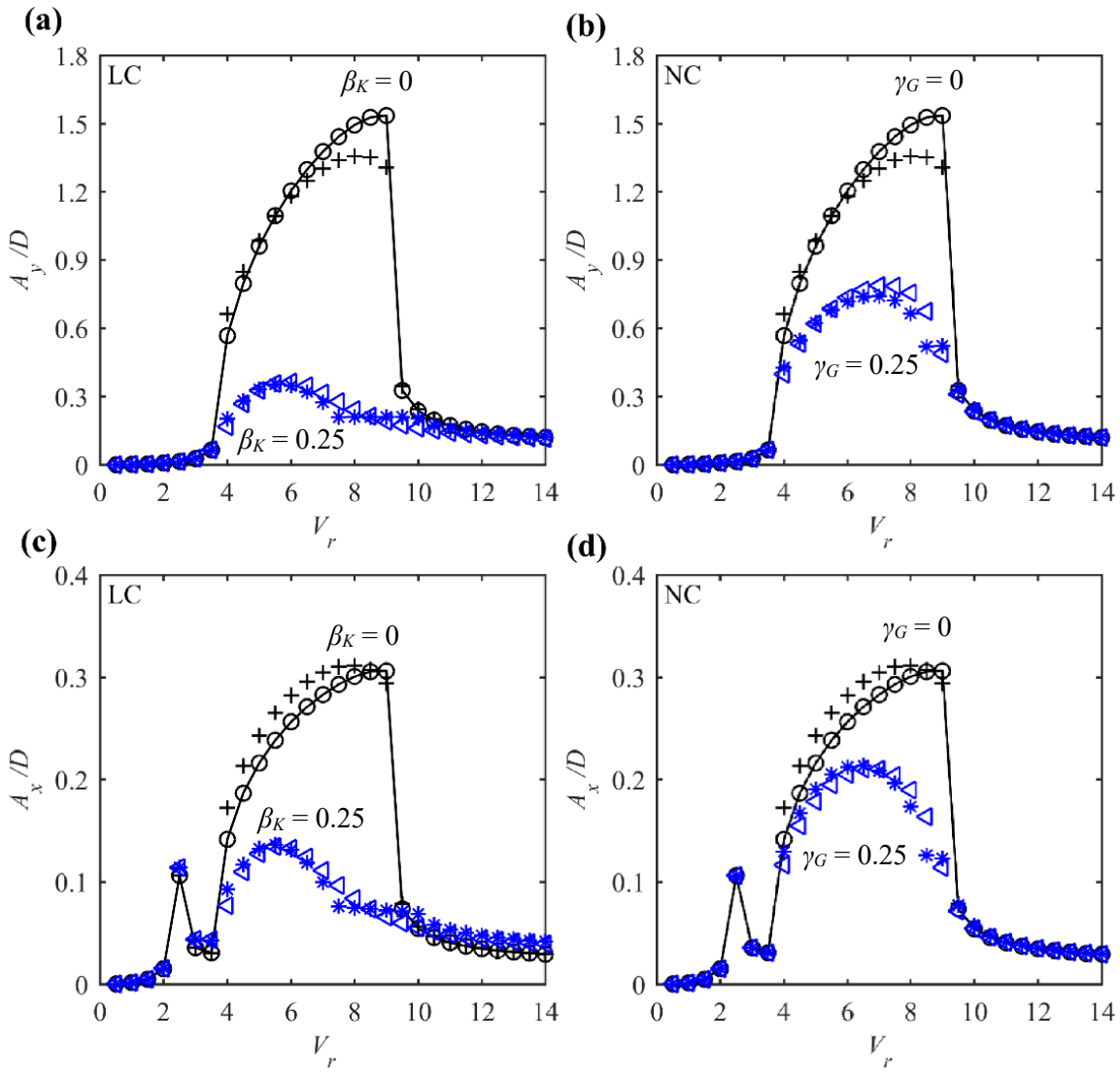


**Figure 4.3:** Comparisons of non-controlled and controlled amplitudes for cylinder with $m^* = 2.6$ and $\xi = 0.00361$: lines with circles (crosses) and triangles (stars) denote numerical (analytical) results.

Since the proposed model can predict the 2-DOF VIV in the absence of control, both LC and NC are now considered. By triggering the active $\tilde{Y}$ control with $\beta_K = \gamma_G = 0.25$ versus the uncontrolled case ($\beta_K = \gamma_G = 0$), analytical and numerical $\tilde{X}$-$\tilde{Y}$ responses are compared in Figures 4.3a and 4.3c (LC) and in Figures 4.3b and 4.3d (NC). It can be seen that both $A_x/D$ and $A_y/D$ are reduced with increasing $\beta_K$ and $\gamma_G$. The response jumps also disappear. Such suppression improves the overall analytical-numerical comparisons enabling almost identical results due to

the diminishing effects of high-order harmonics and nonlinearities. With the same control gain ($\beta_K = \gamma_G$), the LC system (Figures 4.3a and 4.3b) entails a greater reduction in both $\tilde{X}$ and $\tilde{Y}$ responses. This trend is similar to the CFD study of Mehmood et al. (2014) who considered, however, a 1-DOF VIV active control of a much higher $m^* = 149.10$ and very low Re = 106. They showed a greater $A_y/D$ suppression by LC. Our focus is placed on the low-mass ($m^* < 6$) cylinder undergoing 2-DOF VIV whose problems are found in a wide range of offshore applications. It should also be noted that the first IL VIV peak is unaffected by either LC (Figure 4.3c) or NC (Figure 4.3d) due to the negligible $A_y/D$ within that region. Instead, an inline control could be applied for $1.5 < V_r < 3$. Based on the results in Figures 4.2 and 4.3, $\varepsilon_y = 0.058$ and $\Lambda_y = 12$ are used in the following studies.

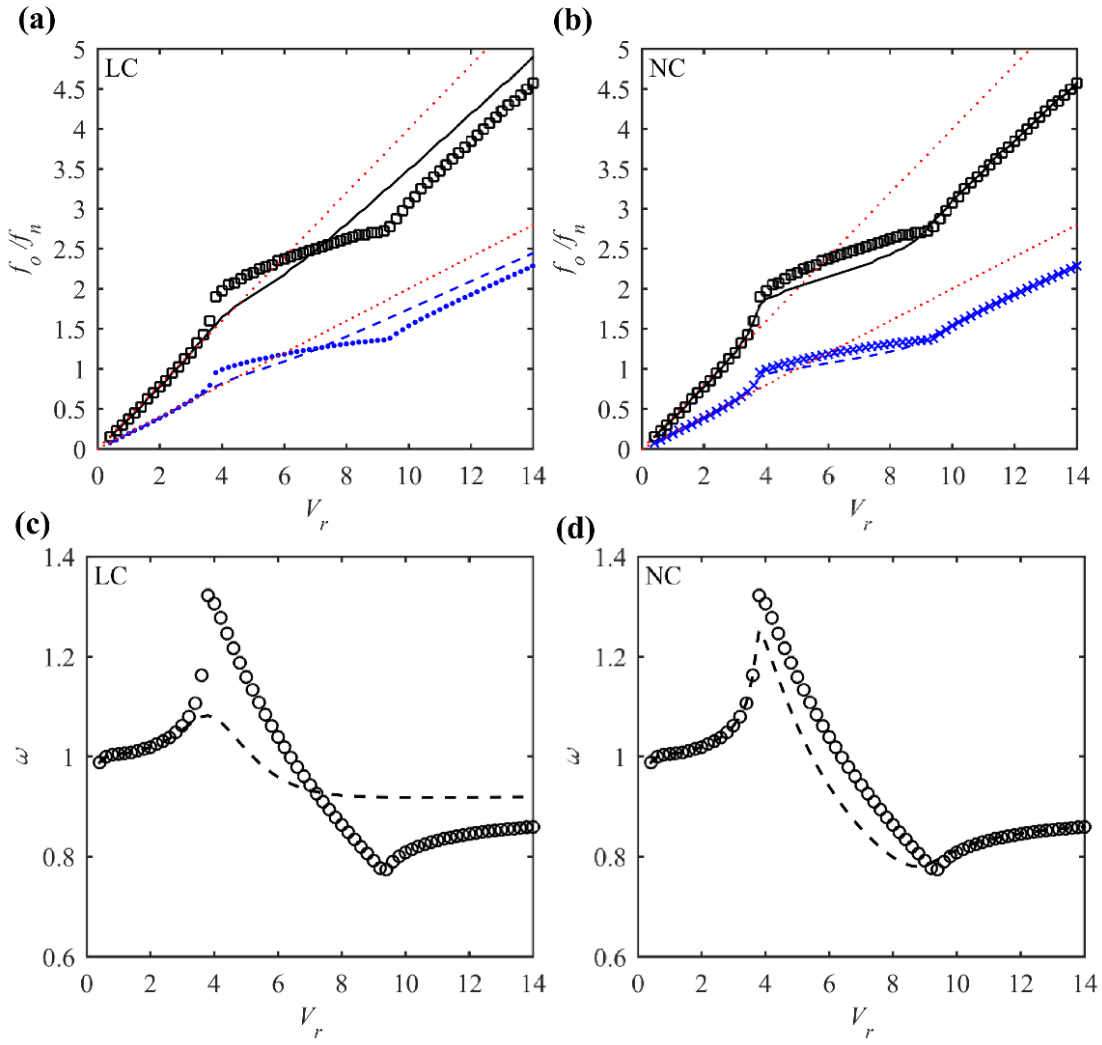


**Figure 4.4:** Comparison of oscillation frequency ratios (a, b) and resonant frequencies (c, d) for cylinder with $m^* = 2.6$, $\xi = 0.00361$ and $\beta_K = \gamma_G = 0.5$: lines (symbols) denote controlled (non-controlled) results. Higher $x$ and lower $y$ frequencies are shown in (a, b) with Strouhal rule (dotted lines).

*4.3.2 Frequencies, motion trajectories, phases and static drifts*

With $m^*$ = 2.6 and $\xi$ = 0.00361, Figure 4.4 presents the cylinder $\tilde{X}$-$\tilde{Y}$ oscillation frequencies normalized with respect to the natural frequency ($f_o/f_n$) as well as the resonant frequency normalized with the vortex-shedding frequency ($\omega$), see Eqs. (4.6)-(4.8), based on LC (Figures 4.4a and 4.4c) and NC (Figures 4.4b and 4.4d) with $\beta_K = \gamma_G = 0.5$. Controlled vs. non-controlled frequencies are plotted with lines and symbols, respectively, with higher $f_0/f_n$ values in Figures 4.4a and 4.4b corresponding to $\tilde{X}$ responses. It can be seen that, in general, LC has a greater effect on $f_0/f_n$ and $\omega$ than NC, especially with respect to the upper ($4< V_r <9$) and lower ($V_r > 9$) branches. With linear control, the $f_o/f_n$ (Figure 4.4a) and $\omega$ (Figure 4.4c) trends remarkably deviate from those without a control. The $f_o/f_n$ plots for the controlled $\tilde{X}$-$\tilde{Y}$ responses exhibit qualitatively similar features to the Strouhal-based dotted lines whose slopes represent the estimation of the vortex-shedding frequency for a stationary cylinder in CL (St = 0.2) and IL (St=0.4) directions. Accordingly, $\omega$ become close to the unity, suggesting the desynchronization state (Facchinetti et al., 2004). As a result, the associated responses are more reduced, see Figures 4.3a vs. 4.3b ($A_y/D$) and Figures 4.3c vs. 4.3d ($A_x/D$). With a higher gain, both LC and NC would entail a greater departure of $f_0/f_n$ and $\omega$, and subsequently greater $\tilde{X}$-$\tilde{Y}$ amplitude reductions. Nevertheless, the controlled $\tilde{X}$-$\tilde{Y}$ frequencies in Figures 4.4a and 4.4b still maintain their dual-resonant 2:1 frequency ratios across the $V_r$ range, regardless of the control scheme.

With $\beta_K = \gamma_G = 0.5$ and $V_r = 7$, the phase plane plots of $x$, $y$ and $q$ variables are exemplified in Figure 4.5 for LC (Figures 4.5a, 4.5c and 4.5e) and NC (Figures. 4.5b, 4.5d and 4.5f). By turning on the control actuator (the dots in Figure 4.5) after initial transient oscillations, limit cycles of periodic motions are stabilized for overall controlled responses. These plots justify the assumption made in Section 4.2 for which a primary harmonic motion with $\omega$ ($y$, $q$) and $2\omega$ ($x$) is postulated in Eqs. (4.6)-(4.8). To further visualize dual resonances in the presence of control, Figure 4.6 compares $\tilde{X}$-$\tilde{Y}$ motion trajectories in the case of $V_r$ = 7 (Figures 4.6a and 4.6b) and $V_r$ = 4 (Figures 46c and 6d). It can be seen that, when LC (Figures 4.6a and 4.6c) or NC (Figures 4.6b and 4.6d) is activated, the figure-of-eight appearances are still maintained with appreciable repeatability in the last ten cycles shown, and with the two lobs pointing downstream (positive $x$) or upstream. Results in Figures 4.5 and 4.6 justify the negligible effect of higher harmonics in the controlled responses.

Apart from the controlled $\tilde{X}$-$\tilde{Y}$ amplitudes, frequencies and trajectories, it is also of interest to evaluate the associated phase differences $\theta_{xy}$ and $\theta_{qy}$, the latter implying the fluid-cylinder

energy transfer (Zanganeh and Srinil, 2014). With $\beta_K = \gamma_G = 0.5$, numerical results (circles) of $\theta_{xy}$ and $\theta_{qy}$ are plotted in Figures 4.7a and 4.7c for LC and in Figures 4.7b and 4.7d for NC, respectively. Experimental $\theta_{xy}$ data (squares) of Jauvtis and Williamson (2004) and numerical ($\theta_{xy}$, $\theta_{qy}$) results (solid lines) in the absence of control are also overlapped in Figures 4.7a-4.7d.

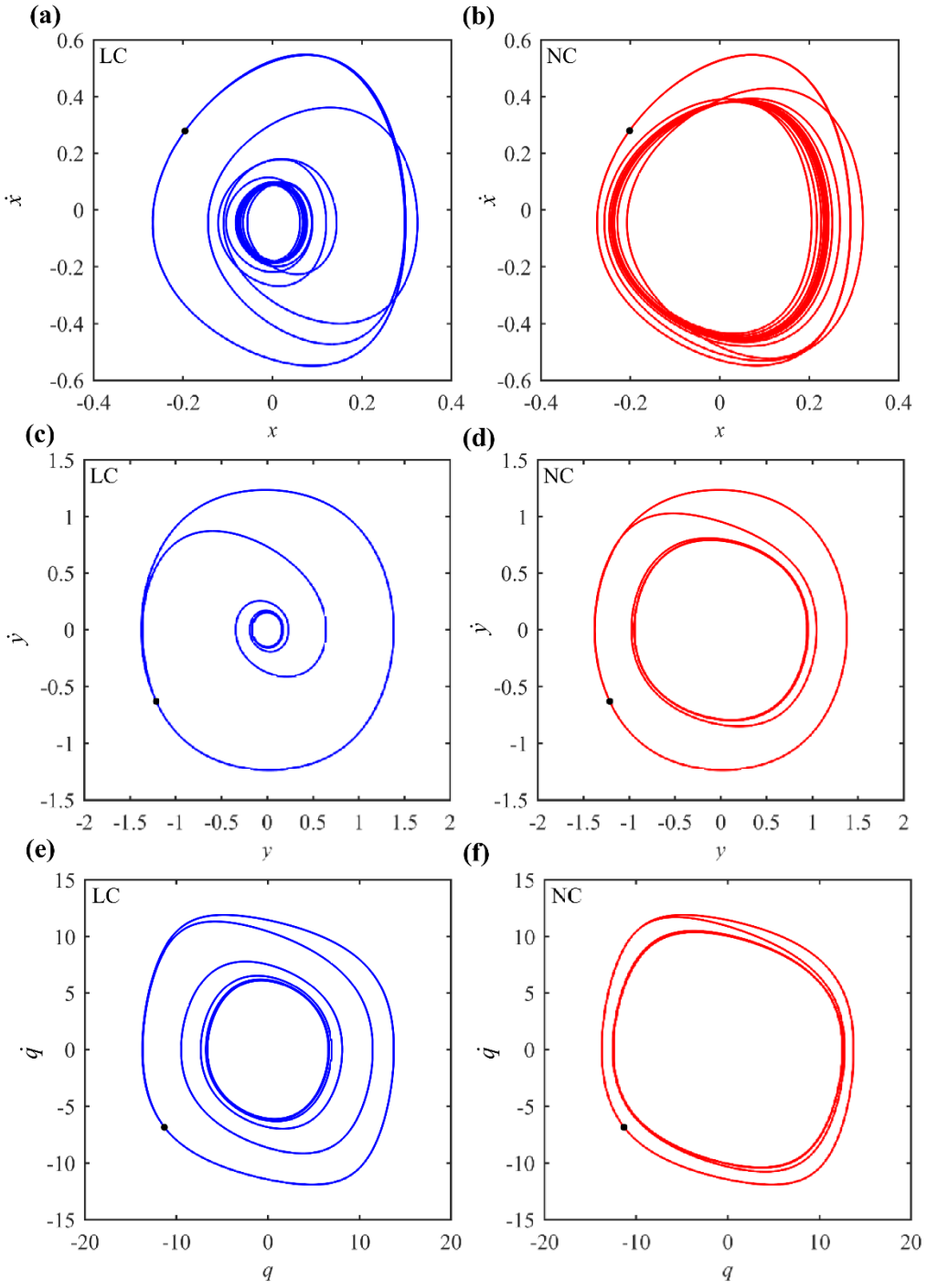


**Figure 4.5:** Phase plane portraits for cylinder with $m^* = 2.6$, $\xi = 0.00361$, $\beta_K = \gamma_G = 0.5$ and $V_r = 7$: a dot represents the moment of control activation.

With varying $V_r$, numerical and experimental results reveal similarly the referenced $\pi/2 < \theta_{xy} < 2\pi$ and $\pi/4 < \theta_{qy} < \pi$ within the main excitation range of $4 < V_r < 14$ covering initial, upper and lower branches, and the observed jump in the phase responses at $8 < V_r < 10$. The $\theta_{xy}$ range suggests a transition from the clockwise figure-eight trajectories ($\pi/2 < \theta_{xy} < 3\pi/2$) to the anti-clockwise ones ($3\pi/2 < \theta_{xy} < 2\pi$) with increasing $V_r$ whereas the $\theta_{qy}$ range suggests the fluid excitation (as opposed to the damping) leading to VIV responses. With LC, a jump disappears from Figure 4.7c, and the $\theta_{qy}$ phase change is clearly observed for $V_r > 9$ which gives rise to $\pi/4 < \theta_{qy} < 3\pi/4$. With NC, the jump also disappears from Figure 4.7d although $\theta_{qy}$ values are less affected. In both control cases, the figure-of-eight patterns maintain their clockwise or anti-clockwise shapes since $\theta_{xy}$ values in both Figures 4.7a and 4.7b slightly change. This is in agreement with the results in Figure 4.6.

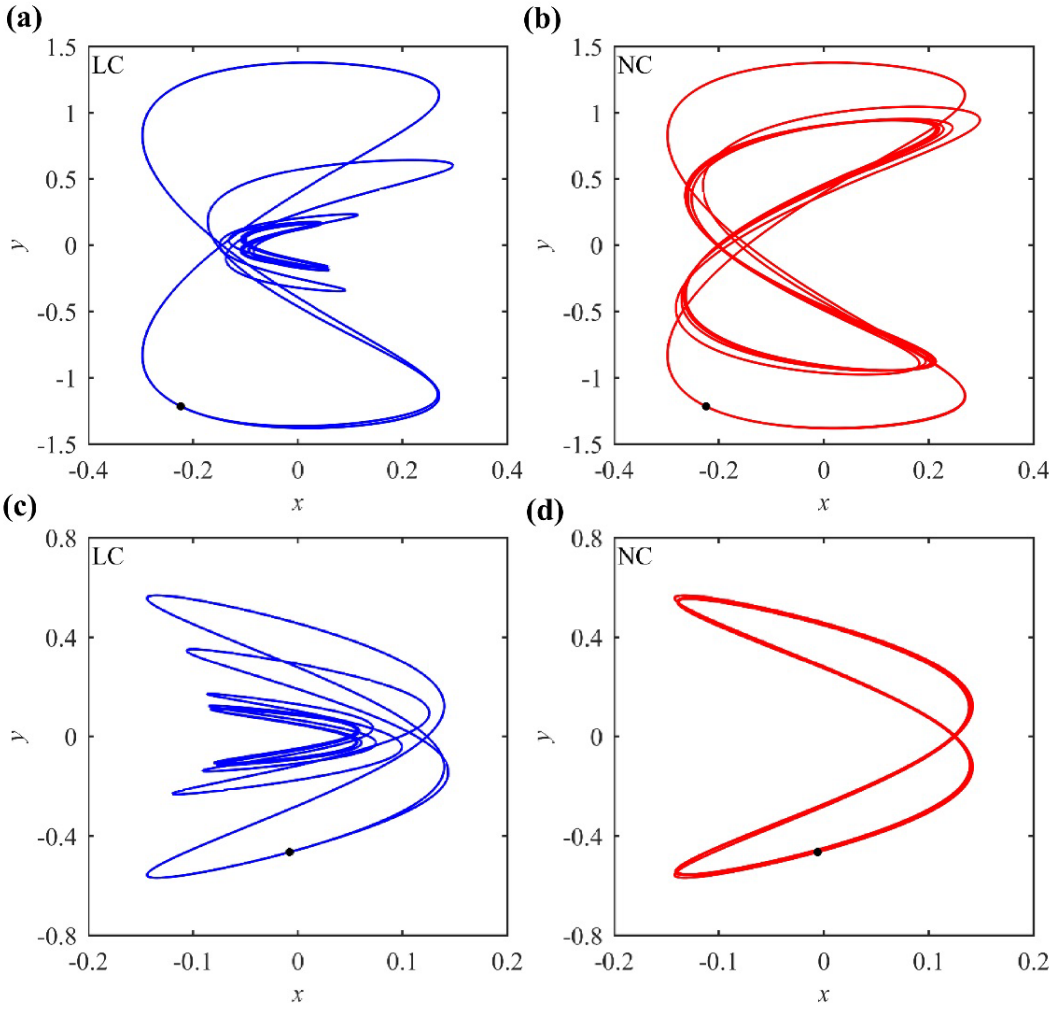


**Figure 4.6:** Two-dimensional $\tilde{X}$-$\tilde{Y}$ motion trajectories at $V_r = 7$ (a, b) and $V_r = 4$ (c, d) for cylinder with $m^* = 2.6$, $\xi = 0.00361$ and $\beta_K = \gamma_G = 0.5$: a dot represents the moment of control activation.

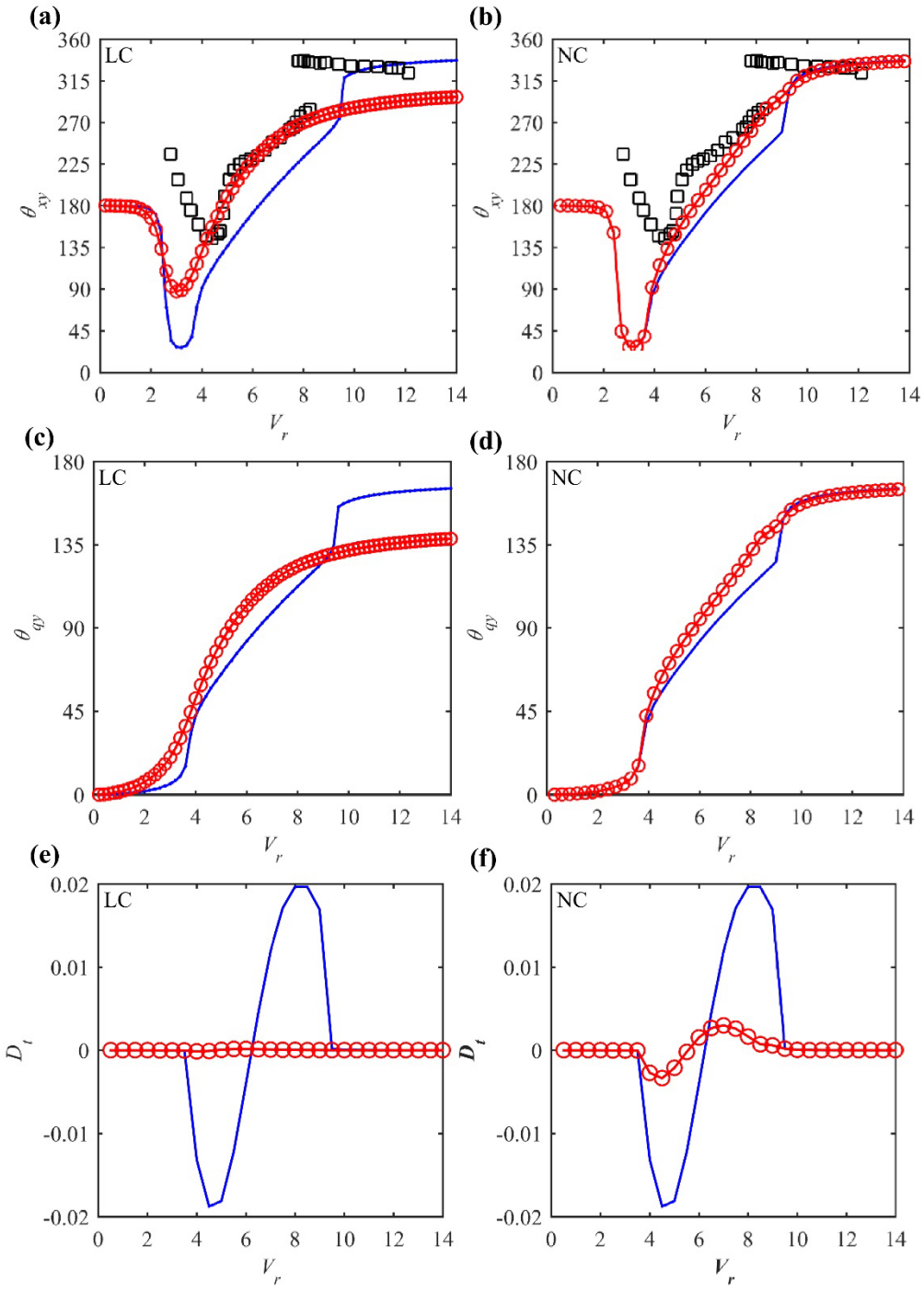


**Figure 4.7:** Comparisons of phase relationships (a-d) and mean drift effect (e, f) for cylinder with $m^* = 2.6$, $\xi = 0.00361$ and $\beta_K = \gamma_G = 0.5$: lines (circles) denote non-controlled (controlled) results; squares denote experimental free-vibration data.

The capability of suppressing the static drift due to the geometric nonlinear coupling is illustrated in Figure 4.7e (LC) and Figure 4.7f (NC) with $\beta_K = \gamma_G = 0.5$. The drift, which changes its sign following $\theta_{xy}$ in Eq. (4.20) (Figures 4.7a and 4.7b), is almost totally eliminated with LC. This observation is hopeful since passive VIV control devices such as strakes generally have a limitation in the mitigation of in-line force including its amplified mean component. The active cylinder control might provide an alternative strategy to suppress the mean drag effect.

*4.3.3 Influence of control gain, geometrically nonlinear coupling and mass ratio*

With $m^*$ = 1.2 and $\xi$ = 0.00361, the controller performance in the reduction of 2-DOF amplitudes is now displayed in Figure 4.8 by varying $\beta_K$ or $\gamma_G$ from 0 to 0.1, 0.2, 0.3, 0.4 and 0.8. For LC, amplitudes are suppressed with increasing $\beta_K$, leading to a large reduction up to about 88% and 70% for maximum $A_y/D$ (Figure 4.8a) and $A_x/D$ (Figure 4.8c), respectively. Likewise, the NC demonstrates the controlling effect on the 2-DOF VIV with about 58% ($A_y/D$) and 39% ($A_x/D$) maximum amplitude reductions (Figures 4.8b and 8d). However, the lock-in region does not shift since the mass ratio $m^*$ is fixed. Similar qualitative behaviours can be found through a 1-DOF wake oscillator model of Dai et al. (2015) where the control gain of a time-delay feedback controller was increased, yielding the decreased $A_y/D$. As previously discussed, the response suppression is attributed to the added damping effect with increasing gain. To achieve greater control performance, both $A_y/D$ and $A_x/D$ can be further reduced with increasing $\beta_K$ and $\gamma_G$.

The variation of control gain was also employed by Baz and Ro (1991) where a 1-DOF direct velocity feedback control was shown to suppress VIV. According to their experiments, the controller would achieve a maximum gain and amplitude reduction. This is also demonstrated in Figures 4.8a-4.8d where the increases in $\beta_K$ and $\gamma_G$ lead to the minimum reduced responses. The histogram plots in Figures 4.8e (LC) and 4.8f (NC) illustrate the maximum amplitude reduction percentage ($R_m$) of both CF (left blue bar) and IL (right yellow bar) responses when increasing consecutively the gain with each 0.1 increment (i.e. from 0 to 0.1, from 0.1 to 0.2 and so on). It can be observed that both $\tilde{X}$-$\tilde{Y}$ responses and both LC/NC demonstrate a gradual decreasing $R_m$ as each gain increment is applied. This confirms the existence of maximum gain value, and, thus, the maximum amplitude reduction capability for each controller. The feedback closed-loop control will reach a maximum efficiency once the control gain is sufficiently large (Inman, 2006).

The effect of geometric displacement coupling is now highlighted in Figure 4.9 where $\alpha_y$ governing $y^3$ in Eq. (4.4) is varied for a given cylinder ($m^*$ = 1.2, $\xi$ = 0.00361) and control gain ($\beta_K = \gamma_G$ = 0.1). Contour plots of the suppressed 2-DOF amplitudes with varying $\alpha_y$ and $V_r$ are displayed in Figures 4.9a and 4.9c for LC and in Figures 4.9b and 4.9d for NC. It can be seen how the increased cylinder nonlinearities affect the main lock-in responses which exhibit the right-bending features and widening resonance ranges due to the enhanced cubic nonlinearities in both $A_y/D$ (Figures 4.9a and 4.9b) and $A_x/D$ (Figures 4.9c and 4.9d) plots. Owing to the intrinsic $\tilde{X}$-$\tilde{Y}$ coupling, maximum $A_y/D$ are slightly increased while maximum $A_x/D$ are more

decreased as $\alpha_y$ is increased for both LC/NC. As for other geometric nonlinear terms ($\beta_y$, $\alpha_x$, $\beta_x$), they have a lesser effect on the controlled responses due to the smaller contributions from the $x$-based ($yx^2$, $x^3$, $xy^2$) terms.

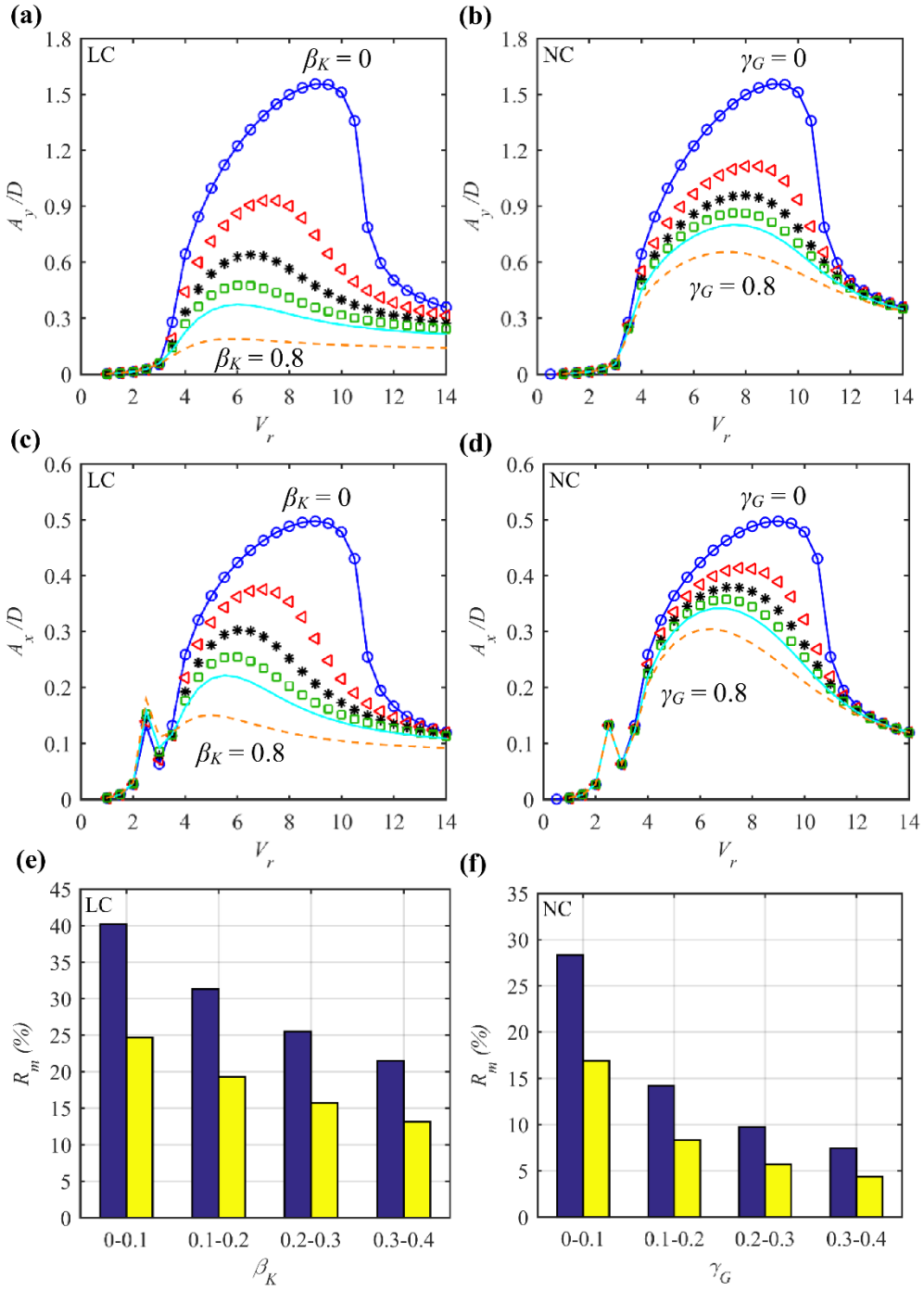


**Figure 4.8:** Influence of control gain on response amplitudes (a-d) and maximum amplitude reduction percentage $R_m$ (e, f) for cylinder with $m^* = 1.2$, $\xi = 0.00361$, $\beta_K$ and $\gamma_G$ being increased from 0 to 0.1, 0.2, 0.3, 0.4 and 0.8, respectively.

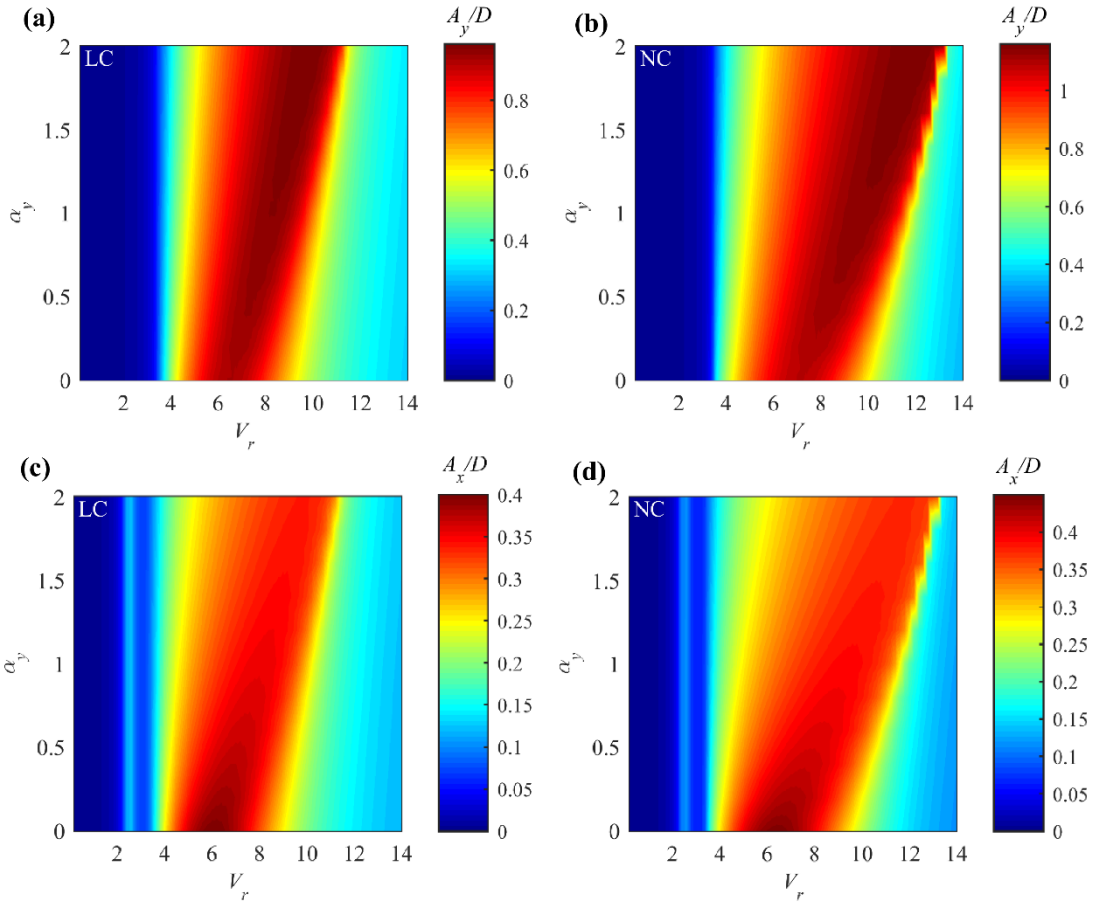


**Figure 4.9:** Influence of geometrically nonlinear coefficient ($\alpha_y$) on controlled amplitudes for cylinder with $m^* = 1.2$, $\xi = 0.00361$ and $\beta_K = \gamma_G = 0.1$.

With $\beta_K = \gamma_G = 0.1$, contour plots of the suppressed 2-DOF amplitudes ($A_y/D$, $A_x/D$) with varying $m^*$ and $V_r$ are displayed in Figure 4.10. Apart from the fact that the first resonance in-line VIV region is not affected by any $\tilde{Y}$-controllers, Figure 4.10 shows how the controlled cylinder with lower $m^*$ has greater $\tilde{X}$-$\tilde{Y}$ responses and lock-in ranges regardless of LC or NC. This is expected from the $m^*$ effect viewpoint. The effect of $m^*$ on the controlled responses ($y_M$, $x_M$) is further highlighted in Figure 4.11 with the advantage of analytical expressions in Section 4.2 which has been derived for the referenced resonant lock-in condition ($\omega = \delta = 1$). Two gain values with $\beta_K = \gamma_G = 0.25$ (triangles) and 0.50 (solid lines) are considered for both LC (Figures 4.11a and 4.11c) and NC (Figures 4.11b and 4.11d) versus the no-control (squares) case ($\beta_K = \gamma_G = 0$). In general, both linearly and nonlinearly controlled 2-DOF responses exhibit similar trends of decreasing responses with increasing gain and $m^*$. The amplitude reduction function appears to be more non-linear in a lower mass ratio range ($m^*<6$). This could emphasize, through an active control study, the effect of 2-DOF VIV on the low-mass cylinder. Nevertheless, due to the limiting control performance, the amplitude reduction capability is reduced from $\beta_K = \gamma_G = 0$ to 0.25 and from $\beta_K = \gamma_G = 0.25$ to 0.5.

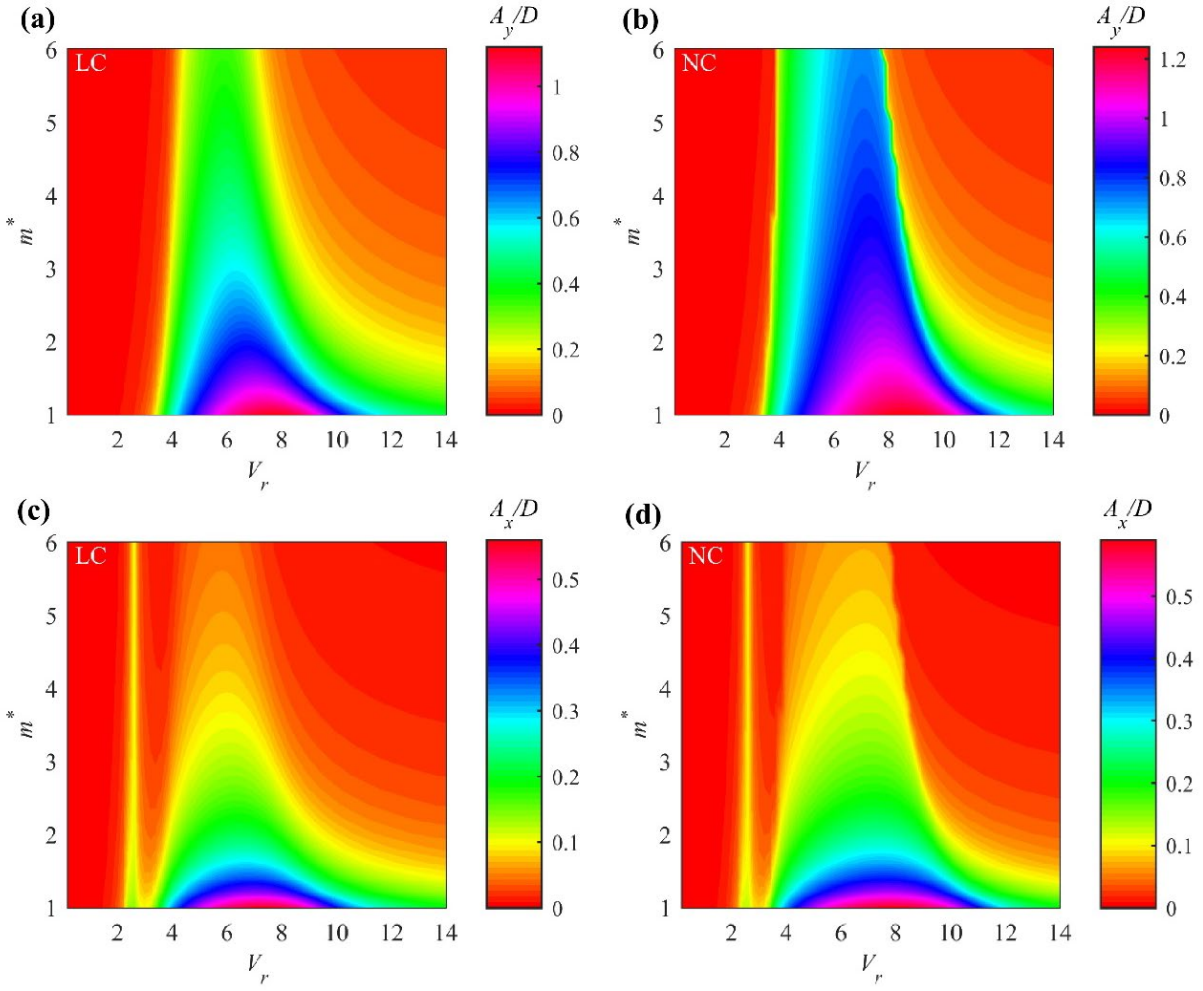


**Figure 4.10:** Influence of $m^*$ on controlled amplitudes for cylinder with $\xi = 0.00361$ and $\beta_K = \gamma_G = 0.1$.

*4.3.4 Comparison of power requirement*

Finally, it is of practical importance to examine the power requirement for each controller since the control performance is also dependent on the forces exerted from the controllers, besides the capability of amplitude reduction. Based on the numerically obtained steady-state responses, the dimensionless averaged power $P_w$ for linear ($\beta_K$) and nonlinear ($\gamma_G$) $\tilde{Y}$ control may be evaluated, respectively, from Mehmood et al. (2014)

$$P_w = \lim_{T\to\infty} \frac{1}{T} \int_0^T \beta_K \dot{y}^2(\tau) d\tau \quad \text{or} \quad P_w = \lim_{T\to\infty} \frac{1}{T} \int_0^T \gamma_G \dot{y}^4(\tau) d\tau \,. \tag{4.36}$$

This can be evaluated for a particular period of time ($T$) and herein it is equal to 100 cycles of periods. The power demand would be particularly useful, e.g., for sizing the control actuators to handle the power requirement. Since the force is applied in the $\tilde{Y}$ direction, the power is dependent on the cylinder $\tilde{Y}$, rather than $\tilde{X}$, velocity.

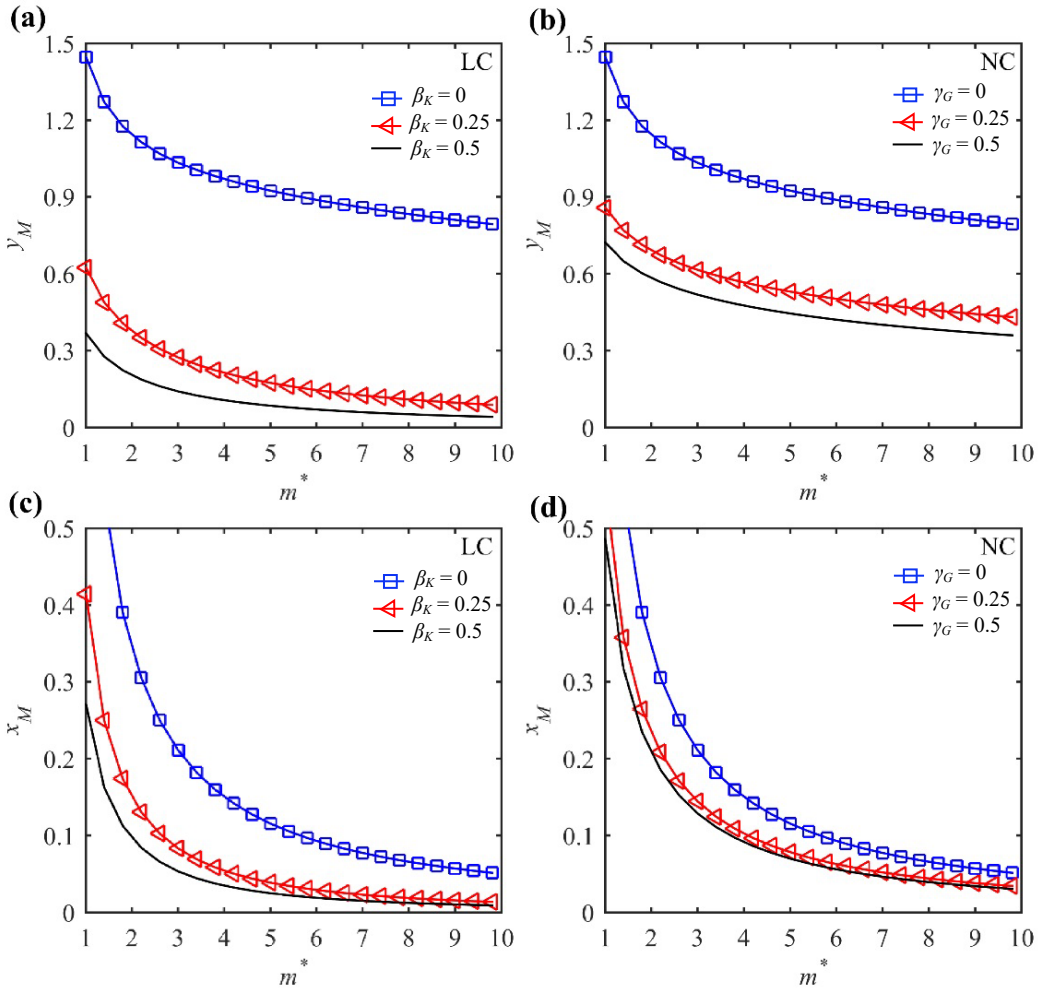


**Figure 4.11:** Comparisons of response amplitudes at ideal perfect lock-in condition with varying $m^*$ for cylinder with $\xi = 0.00361$, $\beta_K$ and $\gamma_G$ being increased from 0 to 0.25, 0.5, respectively.

Depending on the level of targeted controlled amplitudes, Figure 4.12 illustrates a comparisons of $P_w$ based on LC (dots) versus NC (lines) for the cylinder with $m^* = 6.9$ and $\xi = 0.00361$ (Figure 4.12a), $m^* = 2.6$ and $\xi = 0.00361$ (Figure 4.12b) and the limiting case of $m^* = 1$ and $\xi = 0$ (Figure 4.12c). It can be seen that both LC and NC generally require comparable $P_w$ for both high (Figure 4.12a) and low (Figure 4.12b) $m^*$ as well as in both high ($A_y/D > 0.9$) and low ($(A_y/D < 0.9$) amplitude ranges, with the maximum $P_w$ occurs at the targeted $A_y/D \approx 0.9$. Based solely on the maximum amplitude reduction, the LC appears to be superior to NC. However, for the neutrally-buoyant cylinder (Figure 4.12c), the NC system is seen to require a lower $P_w$ (about 5%) within the lower amplitude range as zoomed in Figure 4.12d. This 2-DOF control observation is similar to the CFD control results of Mehmood et al. (2014) who suggested a better NC performance when the targeted $A_y/D < 0.2$ for a very high $m^* = 149.1$ of the 1-DOF circular cylinder.

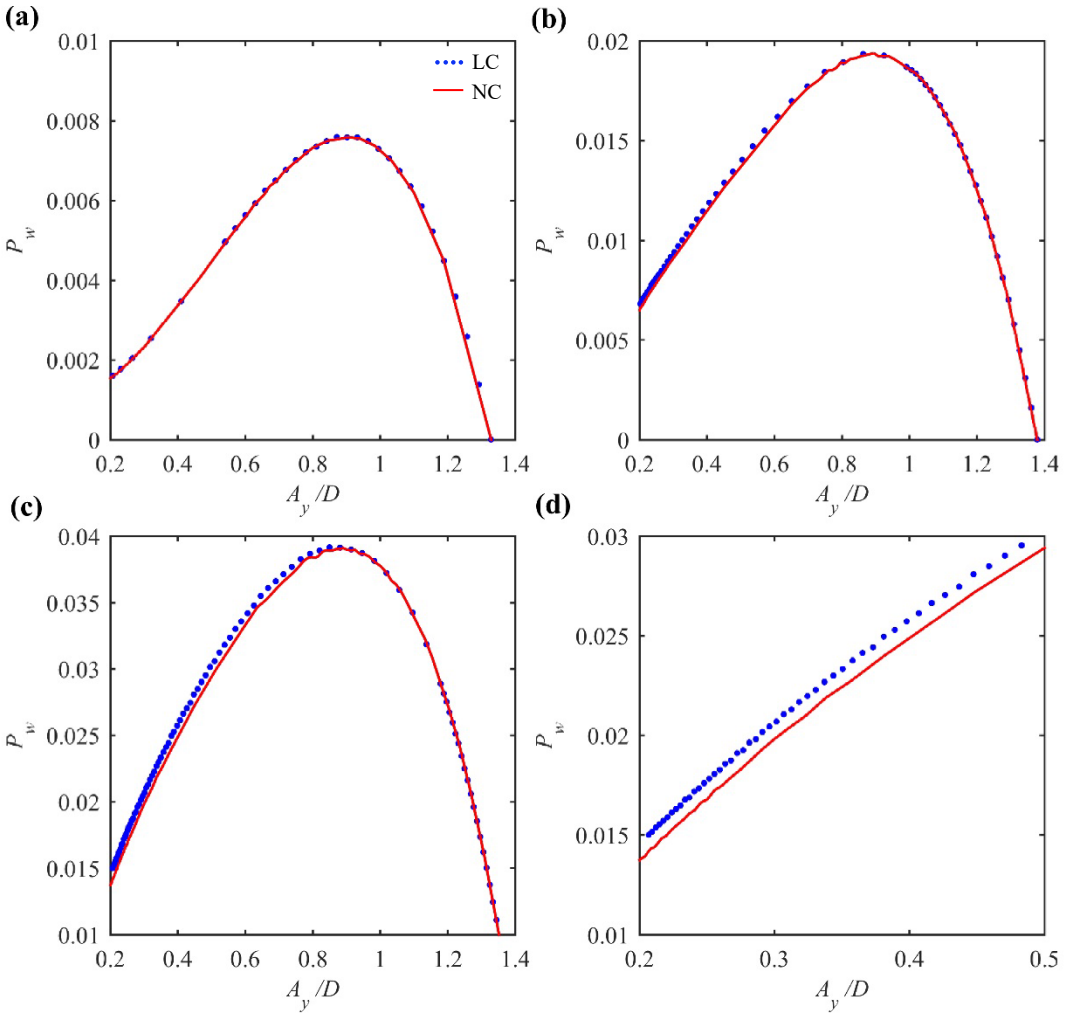


**Figure 4.12:** Comparisons of averaged power requirement with the targeted reduced amplitudes with LC (dots) vs NC (lines): (a) $m^* = 2.6$ and $\xi = 0.00361$, (b) $m^* = 6.9$ and $\xi = 0.00361$, (c) $m^* = 1$ and $\xi = 0$; (d) showing the zoomed results in (c).

## 4.4 Summary

Investigation into the two-dimensionally coupled VIV of a flexibly mounted circular cylinder in uniform flows has been presented. In addition, the effectiveness of active linear and nonlinear controls by using the cylinder transverse velocity feedback for the VIV suppression is evaluated. The reduced-order nonlinear dynamic model simulating the structure-vortex strength interaction is based on the use of coupled cylinder-wake oscillators which capture basic VIV phenomena. Model empirical coefficients have been calibrated with free-vibration experimental data and then applied to the parametric studies with active controls. Combined analytical and numerical results are presented and discussed. At lock-in oscillation frequencies, some analytical expressions for response amplitudes have been derived to explicitly describe the resonant dynamics.

The phenomenological model is found capable of capturing several VIV characteristics

such as a lock-in range, amplitude jump, two-to-one resonant frequency and figure-of-eight trajectory. Typical VIV responses including response amplitudes, oscillation frequencies, phase relationships, orbital motions are presented and assessed in a wide range of reduced velocities. Moreover, the effects of control gain, mass ratio and geometric nonlinear displacement have also been explored. Parametric results reveal that linear and nonlinear controllers can be implemented for mitigating the coupled cross-flow/in-line VIV and the associated static drifts. For the limiting case of neutrally-buoyant cylinder with negligible structural damping, the nonlinear control requires lower power in the targeted small-amplitude range. This chapter has shown the capability of the semi-empirical model in predicting VIV, which serves as a preliminary study for the following investigations on combined SIV and VIV of a curved flexible riser in Chapter 5.

# Chapter 5. Catenary Riser Responses Subject to Combined VIV and SIV

During oil and gas development, the subsea riser carrying multiphase product flows may experience current simultaneously, which could result in a challenging operation condition because of the combined external-internal effects. In this chapter, catenary riser responses subject to combined VIV and SIV are investigated. Based on Chapter 3, the slug-conveying riser model is applied for modelling SIV. By using distributed van der Pol wake-oscillators, the low-order model in Chapter 4 is extended to CF-only VIV aligning with the planar SIV of the flexible catenary riser under a perpendicular uniform flow. Validation of the semi-empirical VIV model is conducted by comparing with published experimental results of a flexible riser. As typical VIV features of flexible risers under increased current velocities, a transition from low- to high-mode dominated multimode responses accompanied by standing to travelling oscillation wave patterns is captured through a modal analysis. By considering different current velocities, riser responses are assessed in case of VIV-only and VIV-SIV scenarios with respect to response displacement, resonant frequency, dominant mode and mode distribution, dynamic and total stresses. The results reveal the prevailing role of VIV in the combined external-internal excitations as well as the significant effects from slug flows on VIV, highlighting amplified and rich structural dynamics led by VIV-SIV.

## 5.1 Mechanical Model and Governing Equations

Investigation into the planar dynamics of a catenary pipe owing to both SIV and VIV is carried out. The slug-conveying riser model introduced in Chapter 3 is considered for SIV. On the other hand, a phenomenological model based on wake oscillators has revealed its abilities in predicting 2D VIV of an elastically mounted rigid cylinder in Chapter 4. Herein, distributed wake oscillators are applied for modelling the hydrodynamic forces along the flexible pipe. Based on the same assumptions, a planar dynamic model of an inclined curved bendable pipe subject to combined effects from SIV and VIV is displayed in Figure 5.1, where a steady uniform flow (in $Z$) perpendicular to the curvature plane ($X$-$Y$) is introduced while slug flows are transported upwardly. For a curved cylinder, a perpendicular flow was experimentally observed leading to more significant VIV responses than concave/convex flows (Srinil et al., 2018a). Also, it is worth noting that the CF-only VIV is considered in the present study to focus on the planar pipe dynamics for investigating the coupled internal and external FIV. Following Chapter 3, the linear partial differential equations describing planar motion of a curved pipe conveying steady slug flows are presented by accounting for VIV effects, which may be formulated as

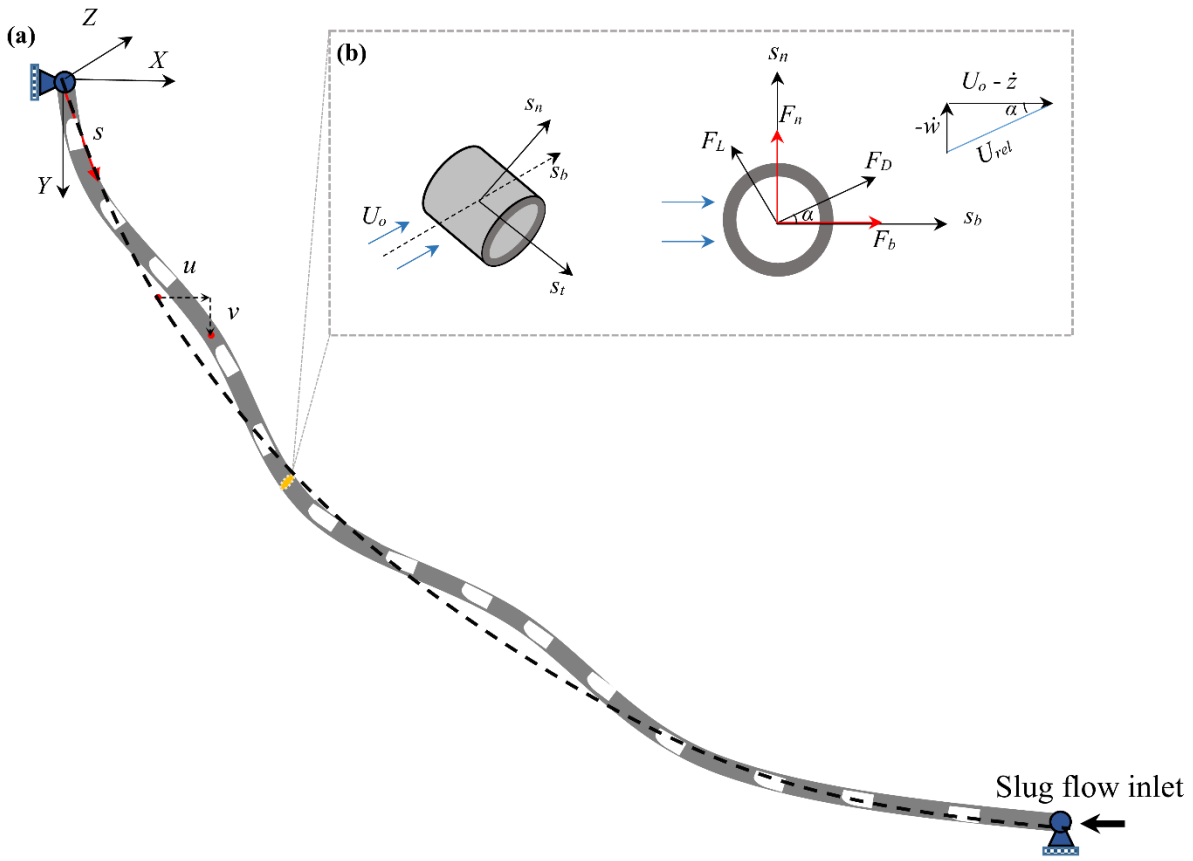


**Figure 5.1:** (a) A planar dynamic model of an inclined curved flexible riser conveying slug gas-liquid flows and undergoing VIV with (b) illustration of hydrodynamic forces for a cross section.

$$\left(m_t+\sum_{i=1}^{2}m_i\right)\ddot{u}+c\dot{u}+EIu^{iv}-\left[\left(T+2\nu(P_oA_o-PA)\right)u'+EA_r\left(\tilde{x}'^2u'+\tilde{x}'\tilde{y}'v'\right)\right]'+\sum_{i=1}^{2}\left[m_iU_i^2\left(\tilde{x}''+u''\right)+2m_iU_i\dot{u}'\right]=F_X, \quad (5.1)$$

$$\left(m_t+\sum_{i=1}^{2}m_i\right)\ddot{v}+c\dot{v}+EIv^{iv}-\left[\left(T+2\nu(P_oA_o-PA)v'\right)+EA_r\left(\tilde{x}'\tilde{y}'u'+\tilde{y}'^2v'\right)\right]'+\sum_{i=1}^{2}\left[m_iU_i^2\left(\tilde{y}''+v''\right)+2m_iU_i\dot{v}'\right]=\sum_{i=1}^{2}m_ig+F_Y, \quad (5.2)$$

where $F_X$ and $F_Y$ denote the horizontal and vertical components of the lift force, inducing CF VIV (Srinil, 2010). Note that although the present study considers CF-only VIV, both lift ($F_L$) and drag ($F_D$) forces are introduced herein for the sake of better interpretation. Unlike a stationary pipe, where $F_L$ ($F_D$) is aligned with the associated CF (IL) directions directly, the relative motions between an oscillating pipe and a steady uniform flow with a velocity of $U_o$ lead to apparent $F_L$ and $F_D$ in arbitrary directions, depending on the fluid and structure velocities. Figure 5.1b displays the cross-sectional force components based on a local coordinate system, where $s_t$, $s_n$ and $s_b$ denote tangential, normal, and bi-normal directions, respectively. Note that $w$ and $z$ denote the pipe motion in $s_n$ and $s_b$, leading to respective relative velocities of $-\dot{w}$ and $U_o - \dot{z}$. Consequently, a dynamic angle of attack ($\alpha$) may be recognized, which directs instant

$F_D$ and $F_L$ to be parallel and perpendicular to the direction of the relative velocity ($U_{rel}$). Therefore, the projected 2D fluid forces ($F_b$ and $F_n$) in $s_b$ and $s_n$ can be expressed as

$$F_b = F_D \cos\alpha - F_L \sin\alpha, \tag{5.3}$$

$$F_n = F_D \sin\alpha + F_L \cos\alpha, \tag{5.4}$$

in which

$$F_D = \frac{1}{2}\rho_o D U^2_{rel}\left(\overline{C}_D + C_D\right), \tag{5.5}$$

$$F_L = \frac{1}{2}\rho_o D U^2_{rel} C_L, \tag{5.6}$$

$$U_{rel} = U_o\sqrt{\left(1-\frac{\dot{z}}{U_o}\right)^2 + \left(\frac{\dot{w}}{U_o}\right)^2}, \tag{5.7}$$

$$\sin\alpha = \frac{-\dot{w}}{U_{rel}}, \tag{5.8}$$

$$\cos\alpha = \frac{U_o - \dot{z}}{U_{rel}}. \tag{5.9}$$

$\overline{C}_D$, $C_D$ and $C_L$ represent mean drag, fluctuating drag and lift force coefficients, respectively. Since the pipe is only subject to CF-only VIV in the present study, fluid forces are then employed by neglecting effects from IL motion while keeping $\overline{C}_D$ remained, which accounts for the fluid-added damping. Thus, $F_D$, $U_{rel}$, and cos $\alpha$ may be reduced to

$$F_D = \frac{1}{2}\rho_o D U^2_{rel}\overline{C}_D, \tag{5.10}$$

$$U_{rel} = \sqrt{U_o^2 + \dot{w}^2}, \tag{5.11}$$

$$\cos\alpha = \frac{U_o}{U_{rel}}. \tag{5.12}$$

By substituting Eqs. (5.6), (5.8), (5.10)-(5.12) into Eq. (5.4), $F_n$ reads

$$\begin{aligned} F_n &= \frac{1}{2}\rho_o D U^2_{rel}\overline{C}_D \sin\alpha + \frac{1}{2}\rho_o D U^2_{rel} C_L \cos\alpha \\ &= -\frac{1}{2}\rho_o D U_{rel}\overline{C}_D \dot{w} + \frac{1}{2}\rho_o D U_{rel} U_o C_L. \end{aligned} \tag{5.13}$$

To model $F_n$, wake oscillators can be used (Facchinetti et al., 2004; Srinil, 2010; Zanganeh and Srinil, 2016). In Chapter 4, a Rayleigh-type wake oscillator proposed by Bai and Qin (2014) is applied for 2-DOF VIV prediction of a rigid body. This model can be easily transformed into a van der Pol-type oscillator with an acceleration coupling term (Facchinetti et al., 2004), which is typically employed in the literature. For convenience, a van der Pol wake-

oscillator is now considered by introducing a wake variable of $q_n$=2$C_L$/$C_{L0}$ (Facchinetti et al., 2004), where $C_{L0}$ is the associated lift coefficient of a stationary cylinder. Furthermore, $q_n$ (in $s_n$) may be projected into $X$ and $Y$ directions (Srinil, 2010) through the local inclination angle ($\beta$), yielding $q_x$= $q_n$sin$\beta$ and $q_y$= $q_n$cos$\beta$, which are governed by the following projected wake oscillators as

$$\frac{\ddot{q}_x}{\sin\beta}+\varepsilon_x\omega_{st}\frac{q_x{}^2\dot{q}_x}{\sin\beta^3}-\varepsilon_x\omega_{st}\frac{\dot{q}_x}{\sin\beta}+\omega_{st}{}^2\frac{q_x}{\sin\beta}=\frac{\Lambda_x}{D}\frac{\ddot{u}}{\sin\beta}, \tag{5.14}$$

$$\frac{\ddot{q}_y}{\cos\beta}+\varepsilon_x\omega_{st}\frac{q_y{}^2\dot{q}_y}{\cos\beta^3}-\varepsilon_y\omega_{st}\frac{\dot{q}_y}{\cos\beta}+\omega_{st}{}^2\frac{q_y}{\cos\beta}=\frac{\Lambda_y}{D}\frac{\ddot{v}}{\cos\beta}, \tag{5.15}$$

where $\omega_{st}$= 2π$\mathrm{St}U_o/D$ denotes the vortex shedding frequency. $\varepsilon_x$, $\Lambda_x$, $\varepsilon_y$, $\Lambda_y$ are empirical parameters, which can be determined by calibrating the model based on experimental data. Herein, the wake coefficients of $\Lambda_x$=$\Lambda_y$=12, $\varepsilon_x$=0.3 and a variable $\varepsilon_y$ depending on Re as suggested in Srinil et al. (2018b) are employed, which reads

$$\frac{\Lambda_y}{\varepsilon_y}=\left[\frac{4\mathrm{S_G}+16\pi^2\mathrm{St}^2\gamma}{C_{L0}}\right]\left[\left(\left(\frac{2\mathrm{S_G}+8\pi^2\mathrm{St}^2\gamma}{C_{L0}}\right)\left(1-1.12\alpha_{md}+0.3\alpha_{md}{}^2\right)\log\left(0.41\,\mathrm{Re}^{0.36}\right)\right)^2-1\right], \tag{5.16}$$

where $\mathrm{S_G}$= $8\pi^2\mathrm{St}^2\mu\xi$ is the so-called Skop-Griffin parameter (Skop and Balasubramanian, 1997), and $\alpha_{md}$=($m^*$+$C_a$)$\xi$, where $C_a$=1. To obtain the hydrodynamic forces required by Eqs. (5.1) and (5.2), $F_n$ (Eq. (5.13)) and the associated $U_{rel}$ (Eq. (5.11)) are projected corresponding to wake oscillators (Eqs. (5.14) and (5.15)), where $\dot{w}$ in $U_{rel}$ is projected into $X$ and $Y$ by $\dot{u}$= $\dot{w}$sin$\beta$ and $\dot{v}$= $\dot{w}$cos$\beta$, respectively. Thus, $F_X$ and $F_Y$ yield

$$F_X=-\frac{1}{2}\rho_o D U_{rel.x}\bar{C}_D\dot{u}+\frac{1}{4}\rho_o D U_{rel.x}U_o C_{L0}q_x, \tag{5.17}$$

$$F_Y=-\frac{1}{2}\rho_o D U_{rel.y}\bar{C}_D\dot{v}+\frac{1}{4}\rho_o D U_{rel.y}U_o C_{L0}q_y, \tag{5.18}$$

where

$$U_{rel.x}=\sqrt{U_o{}^2+\left(\frac{\dot{u}}{\sin(\beta)}\right)^2}, \tag{5.19}$$

$$U_{rel.y}=\sqrt{U_o{}^2+\left(\frac{\dot{v}}{\cos(\beta)}\right)^2}. \tag{5.20}$$

The first term Eqs. (5.17) and (5.18) accounts for the fluid-added damping forces through both fluid ($U_o$) and structure ($\dot{u}$, $\dot{v}$) velocities (Srinil et al., 2018b), whereas the second term represents the time-space varying hydrodynamic forces coupled with the distributed wake oscillators (Eqs. (5.14) and (5.15)) through the wake variables ($q_x$, $q_y$) along the pipe. It is worth

mentioning that the form of $F_X$ and $F_Y$ are different from those in Srinil (2010) since $U_{rel}$ is considered herein. The values of force coefficients are variable, affected by several factors, e.g. surface roughness and Re. Following Blevins (1990), $\bar{C}_D$ =1.2 and $C_{L0}$=0.3 are applied in the present study, which may be reasonable for the considered sub-critical flow in the following numerical cases (see Sections 5.2 and 5.3).

In general, the partial differential Eqs. (5.1) and (5.2) coupled with spatially distributed Eqs. (5.14) and (5.15) may be used to investigate the planar dynamics of a flexible pipe conveying slug flows and undergoing CF VIV simultaneously. By specifying initial conditions $u$=$v$=$\dot{u}$=$\dot{v}$=0 for the pipe at the static equilibrium and $q_x$=$q_y$=2 ($\dot{q}_x$=$\dot{q}_y$=0) for wake variables, the system of equations can be numerically solved by using the same approach as introduced in Chapter 3, where a combination of 2nd order finite difference in space and 4th order Runge-Kutta for time integration has been applied.

## 5.2 Validation of VIV Model for Flexible Risers

Prior to investigating the combined internal and external effects on a catenary pipe, it is important to validate the VIV prediction model for a flexible body. According to Chapter 2, available VIV tests of a catenary riser under perpendicular flow are rather limited in the literature. Herein, a straight flexible body is considered for VIV model validation. For a pipe subject to pure VIV, numerical and experimental results are compared based on a laboratory test conducted by Song et al. (2011), where a long horizontal flexible pipe of $E$=210 GPa, $L$=28.04 m, $d$=0.015 m, $D$=0.016 m, $m$*=1 was considered with various pre-tensions ($T$ = 600N, 700N 800N) under uniform flows of $U_o$ ranging from 0.18 to 0.6 m/s in a subcritical flow regime. For a horizontal flexible cylinder subject to CF VIV, $\tilde{x}'$=1, $\tilde{y}'$=0 and $\beta$=0° are assigned to Eq. (5.2) and (5.15) without effects of slug flows, i.e. neglecting internal fluid inertia, gravity, momenta and pressure. They are numerically solved based on a time step $\Delta t$ = 0.001s and spatial discretized segment $\Delta s$ =0.2 m, which enables the convergence of steady-state results.

Figure 5.2 demonstrates the numerical-experimental comparison of maximum ($v_{max}$) and spatially maximum RMS CF responses ($v_{rms}$) vs. $U_o$. As for $v_{max}$ (Figures 5.2a, c, e), qualitative and quantitative agreements are found in all pre-tensions cases (600, 700, 800N), although discrepancies between the numerical and experimental results are realized at relatively large $U_o$ ($U_o$ > 0.5m/s). Similar to the experimental results, $v_{max}$ generally shows an increasing trend alongside zigzag variations with varying $U_o$. Such fluctuation in $v_{max}$ vs. $U_o$ is also highlighted in Zanganeh and Srinil (2016), suggesting a lock-in and lock-out conditions during transitions between different dominant modes (Chaplin et al., 2005; Srinil, 2010). On the other hand,

comparisons of $v_{rms}$ between the numerical simulations and the tests with respect to various pre-tensions are also presented in Figures 5.2b, d, f, where the former generally exhibit slightly overestimated values compared to the latter. This may be attributed to the neglected IL motion and uncertainties such as damping effects. Nevertheless, the predicted VIV results demonstrate reasonable matches with the experimental results with capturing the maximum/RMS responses.

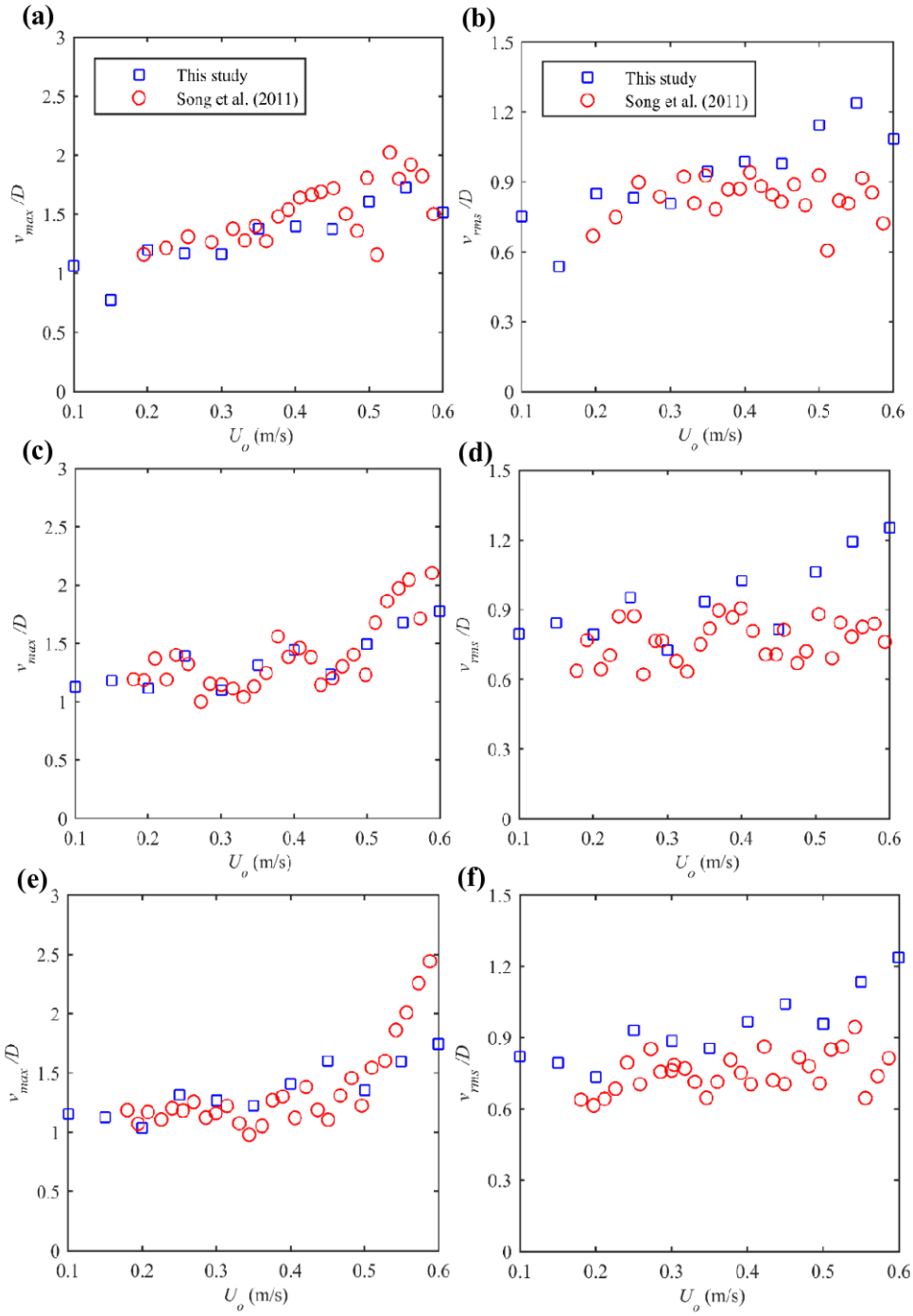


**Figure 5.2:** Comparison of numerical (blue squares) and experimental (red circles) results of (a, c, e) maximum and (b, d, f) RMS amplitudes at varying $U_o$ in case of (a, b) $T$ = 600 N, (c, d) 700 N and (e, f) 800 N.

To further validate the VIV model, a linear modal decomposition approach proposed by Lie and Kaasen (2006) and then adopted in both numerical and experimental studies (Song et al., 2011; Zanganeh and Srinil, 2016) is followed for identifying the modal components of current CF-VIV responses. By assuming approximately linear pipe oscillation with small amplitudes, the current space-time varying riser displacements can be decoupled into space and time as

$$v(Y_i,t)=\sum_{n=1}^{N}W_n(t)\phi_n(Y_i), \tag{5.21}$$

where $W_n$ and $\phi_n$ represent modal weights and shapes corresponding to different order $n$ = 1, 2, … $N$, $N$ the highest mode considered in the analysis, $Y_j$ the spanwise coordinates according to each spatial node $j$ = 1,2, …$J$ ($0 \le Y_j \le L$). For a pinned-pinned straight cylinder with uniform tension, $n$th mode shapes can be described by a sinusoidal function as

$$\phi_n\left(Y_j\right)=\sin\frac{n\pi Y_j}{L} \tag{5.22}$$

Further, Eq. (5.21) can be expressed in a matrix form accounting for all locations along the span, which reads

$$\tilde{v}=\Theta\tilde{W}, \tag{5.23}$$

Where the $J \times N$ matrix of mode shapes arrives at $\Theta$= [$\Phi_1$, $\Phi_2$, … $\Phi_N$] with the vector $\Phi_n$=[$\phi_n(Y_1)$, $\phi_n(Y_2)$,… $\phi_n(Y_J)$]$^T$, the weight vector $\tilde{W}$=[$W_1(t)$, $W_2(t)$,… $W_N(t)$]$^T$, the response vector $\tilde{v}$=[$v(Y_1,t)$, $v(Y_2,t)$,… $v(Y_J,t)$]$^T$. For $N < J$, Eq. (5.23) is solved by the method of least-squares for time-varying weights corresponding to the considered modes.

In association with the responses in Figure 5.2, RMS values of time-varying modal weights (normalized by the maxima) vs. various $U_o$ alongside numerical-experimental comparisons of dominant modes are exhibited in Figures 5.3a, c, e and b, d, f, separately. Comparing the mode distributions under different pre-tension conditions (Figures 5.3a, c, e), they demonstrate similar patterns of modal participation showing that higher-order modes exist at larger $U_o$. Meanwhile, the band of modes participated in the pipe responses gets wider as $U_o$ increases, suggesting more pronounced multi-modal VIV at greater $U_o$. These phenomena are in a qualitative agreement with the experimental results (see Figure 9 in Song et al. (2011)). Moreover, it is seen in Figures 5.3b, d, f that the order of the dominant mode increases with $U_o$, which justifies the general trend in Figures 5.3a, c, e and show fairly good comparisons with those from the experiment although the numerical results slightly overestimate the mode order at higher $U_o$. In Figures 5.4a-c, the theoretical and experimental results regarding variations of the dominant $f_o$ at different $U_o$ are compared in terms of three pre-tension conditions. Good

numerical-experimental matches are observed in all considered cases, showing the increasing dominant $f_o$ with $U_o$, which almost follow the Strouhal rule in CF direction.

Overall, the current model for CF-VIV prediction is validated by showing reasonable abilities in capturing several important aspects of VIV both qualitatively and quantitatively. This allows the further application of this model for the following investigation of combined effects from SIV and VIV on a flexible catenary pipe.

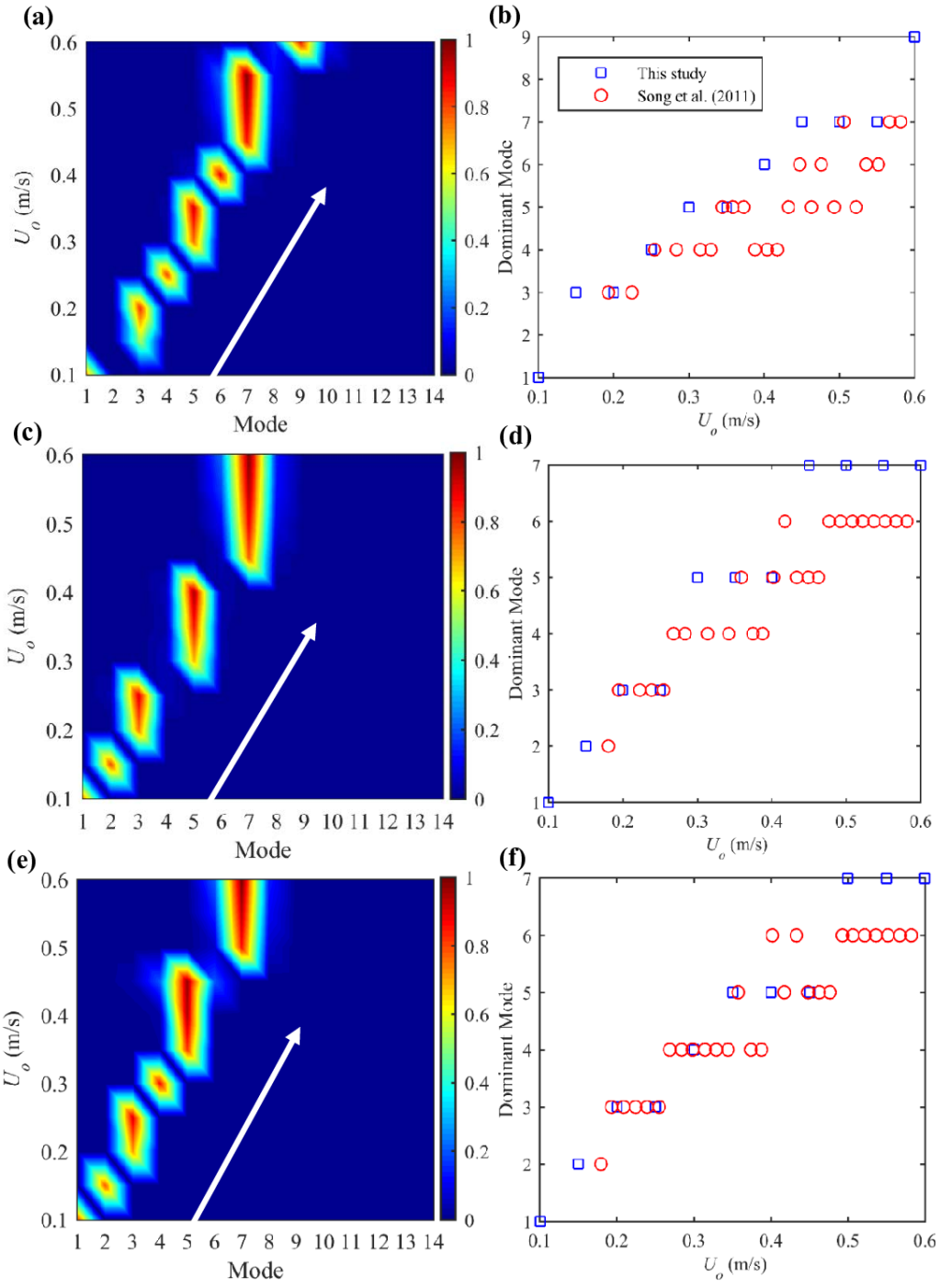


**Figure 5.3:** (a, c, e) Modal distribution and (b, d, f) comparison of numerical (blue squares) and experimental (red circles) results of dominant modes at varying $U_o$ in case of (a, b) $T$ = 600 N, (c, d) 700 N and (e, f) 800 N.

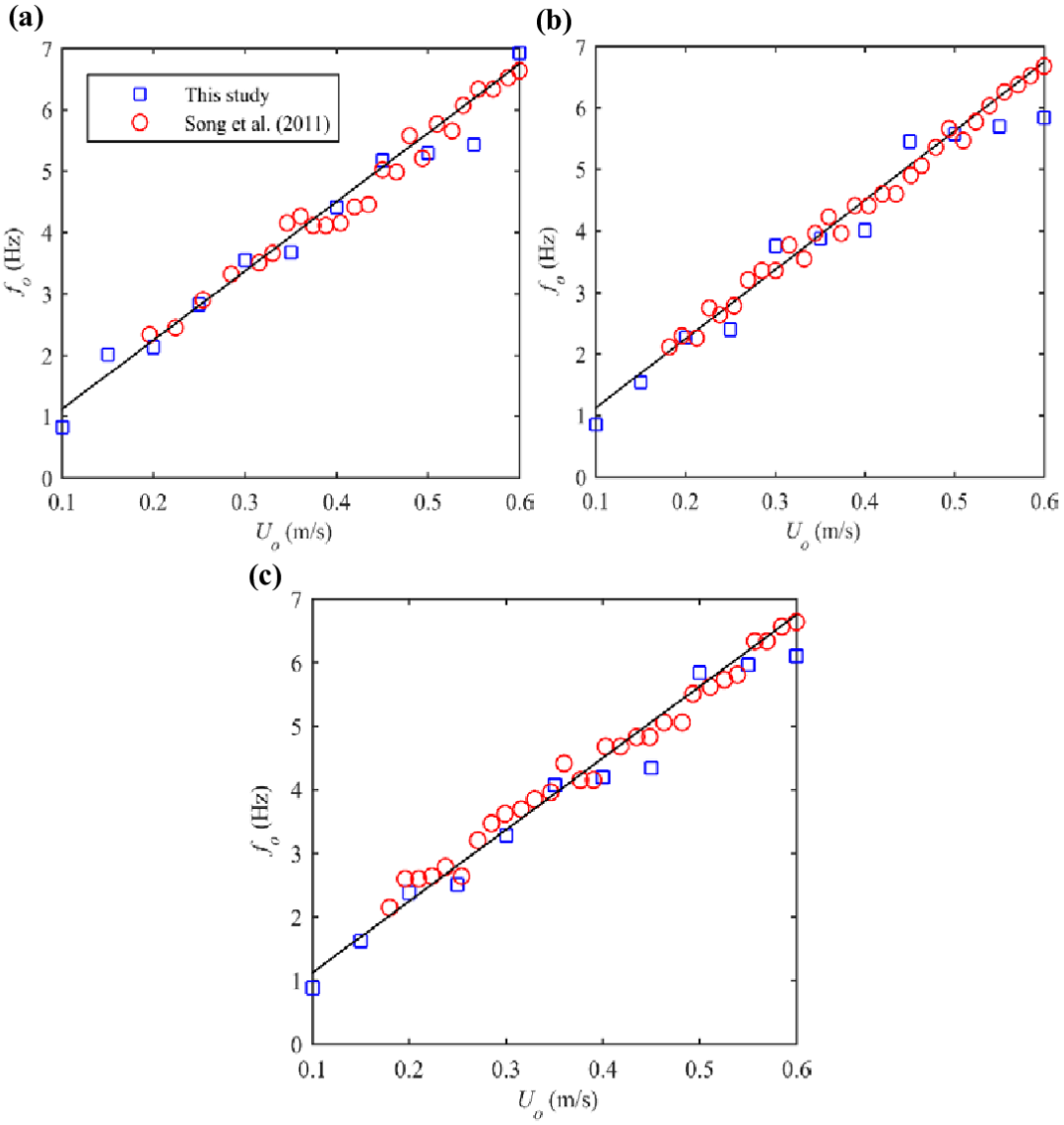


**Figure 5.4:** Comparison of numerical and experimental results with dominant frequency at varying $U_o$ in case of (a) $T$ = 600 N, (b) 700 N and (c) 800 N: black line represents the Strouhal rule.

## 5.3 Numerical Results and Discussion

*5.3.1 Dynamics responses under various current velocities: VIV vs. VIV-SIV*

To investigate combined effects of external-internal excitations on a catenary riser as displayed in Figure 5.1, the dynamical system of a curved pipe conveying slug flows as presented in Chapter 3 is herein considered alongside VIV effects due to various flow velocities. For each $U_o$, the slug flows of $U_t$ = 6 m/s ($u_{ls}$=2 m/s, $u_{gs}$=2 m/s) and 16 m/s ($u_{ls}$=2 m/s, $u_{gs}$=10.3 m/s) for a fixed $L_u/d$=80 are assigned. Also, numerical simulations are carried out for VIV-only and VIV-SIV scenarios to identify the individual effect of SIV on the riser dynamics among combined FIV. To achieve that, Eqs. (5.1), (5.2), (5.14) and (5.15) with and without the effect of slug flows are numerically solved.

By removing the mean components from the total steady-state responses, Figure 5.5 demonstrates comparison of $u_{max}$, $v_{max}$ (Figures 5.5a, b) and $u_{rms}$, $v_{rms}$ (Figures 5.5c, d) for $U_o$= 0.1m/s - 0.8 m/s among VIV-only, VIV-SIV ($L_u/d$=80, $U_t$ = 6 m/s) and VIV-SIV ($L_u/d$=80, $U_t$ = 16 m/s). In general, the VIV-SIV cases have shown comparable maximum and RMS amplitudes to the ones of VIV, though some differences are recognized at several $U_o$. Similar to the results of a straight pipe, the feature of zigzag trend with $U_o$ also appears in the catenary riser. Also, the responses in $Y$ are larger than those in $X$, where the former seems to increase with $U_o$ for the three scenarios. Such correlation between $U_o$ and VIV responses of a catenary riser has been observed in several experimental studies (Fan et al., 2015; Domala and Sharma, 2018).

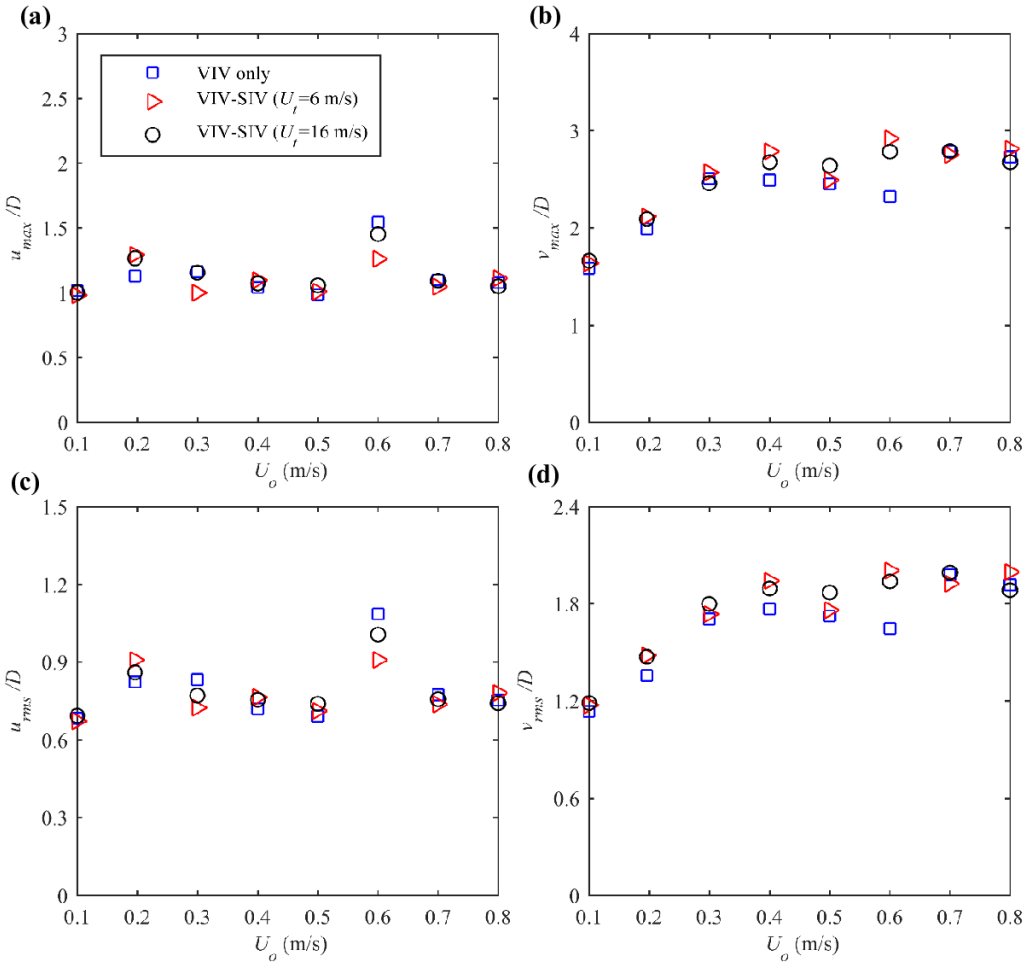


**Figure 5.5:** Comparison of (a, b) maximum and (c, d,) RMS amplitudes of (a, c) $u$ and (b, d) $v$ at varying $U_o$ in case of VIV-only (blue squares), VIV-SIV for $L_u/d$=80, $U_t$ = 6 m/s (red triangles) and VIV-SIV for $L_u/d$=80, $U_t$ = 16 m/s (black circles).

Further comparison among the three cases are conducted in terms of mode components. To obtain the riser mode shapes, OrcaFlex (Orcina, 2016) is utilized. By setting the catenary riser geometry (static configuration), mass per unit length, structural properties (bending and

axial stiffness) and environmental condition (still water) in OrcaFlex (Orcina, 2016), a modal analysis yielding undamped natural modes (up to 30$^{th}$) is carried out with 405 spatial sections ($\Delta s$=5 m). The mode shapes (5$^{th}$, 10$^{th}$, 15$^{th}$, 20$^{th}$, 25$^{th}$, 30$^{th}$) in $X$ and $Y$, i.e. $\phi_u$ (solid line) and $\phi_v$ (dashed line), are exemplified in Figure 5.6. Then, by following the modal decomposition

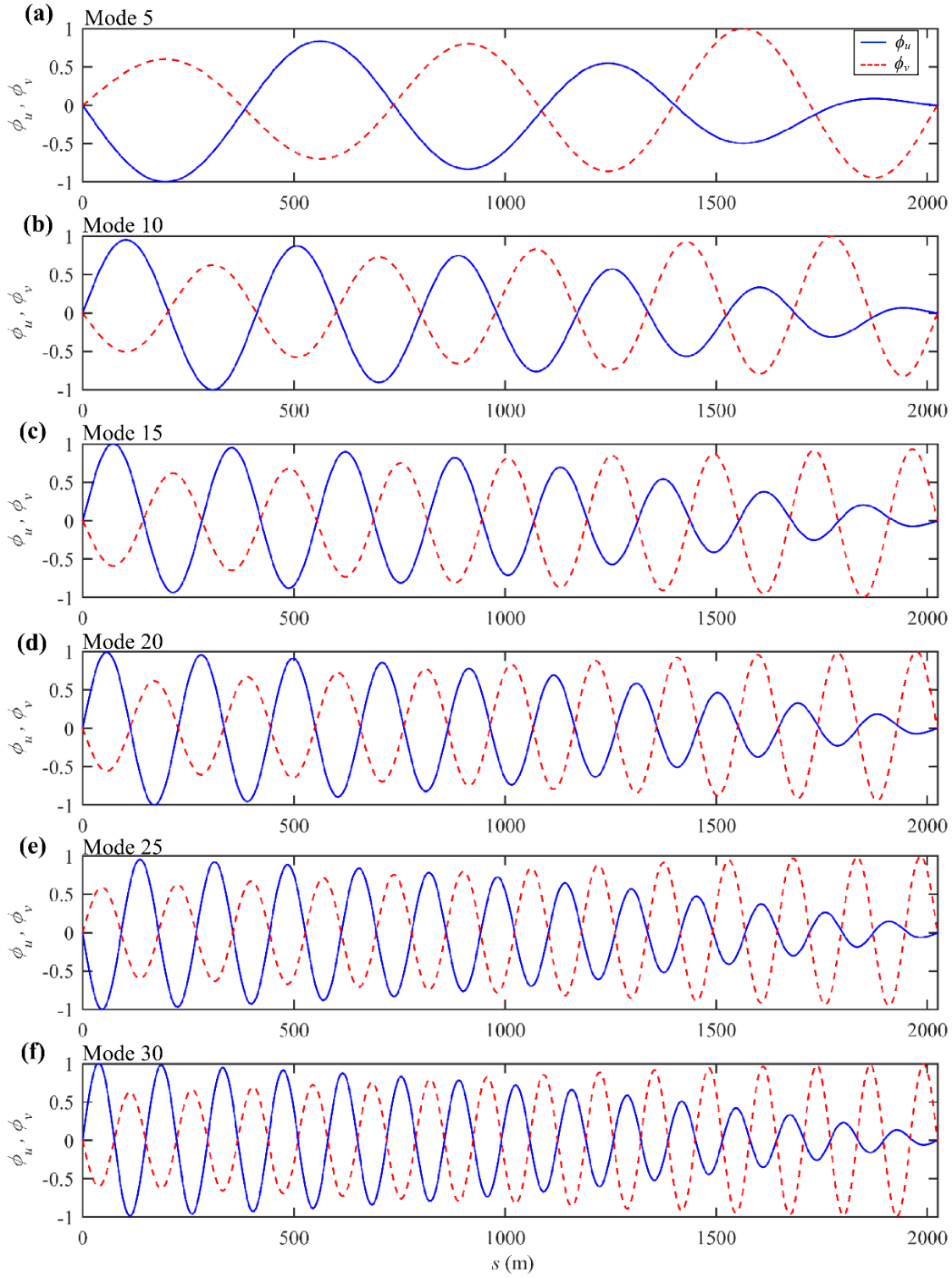


**Figure 5.6:** Illustration of normalized riser mode shapes for mode (a) 5, (b) 10, (c) 15, (d) 20, (e) 25, (f) 30: solid (dashed) lines denote the shapes in $X$ ($Y$), respectively.

method as presented in Section 5.2, a modal analysis of the above VIV and SIV-VIV responses can be conducted.

Associated with the responses in Figure 5.5, mode distributions against $U_o$ are illustrated in case of the VIV-only (Figures 5.7a, b), VIV-SIV of $U_t$ = 6 m/s (Figures 5.7c, d) and VIV-SIV of 16 m/s (Figures 5.7e, f) for both $X$ (Figures 5.7a, c, e) and $Y$ (Figures 5.7b, d, f) responses, in which the modal contribution is calculated by the RMS values of time-varying modal weights (normalized by the maxima) with highlighting the dominant mode (in red markers) for each $U_o$. Thus, the magnitude of the modal weight can also represent the weight ratio of the secondary modes to the associated dominant one. For a clear demonstration, any mode with weight ratio below 0.1 is not included in Figure 5.7. As for the VIV-only scenario, it is obvious to see that the riser vibration is dominated by a higher order of vibration mode at a greater $U_o$, ranging from 2$^{nd}$ to 23$^{rd}$ modes. Meanwhile, the number of participated modes in both $u$ and $v$ gets larger as $U_o$ increases. For instance, there is only one significant mode (2$^{nd}$) excited by VIV at $U_o$=0.1 m/s, whereas the riser responses contains six different modes (20$^{th}$ - 25$^{th}$) at $U_o$=0.8 m/s. Besides, the weights of the secondary modes are more comparable to the dominant one, i.e. higher weight ratio, at relatively high $U_o$, which indicates strong multi-mode effects in VIV. The pronounced multi-mode VIV behaviours of a catenary riser with increased $U_o$ were also experimentally observed by Halse et al. (1999) and numerically captured by Dalheim (2000). Such a feature of modal distributions vs. various $U_o$ can also be seen in VIV-SIV scenarios (Figures 5.7c, d and 5.7e, f). Nevertheless, compared with the VIV-only case, two VIV-SIV cases exhibit more significant modal contents in riser responses.

For VIV-SIV of $U_t$ = 6 m/s, the dominant modes get upgraded at several $U_o$, especially for the relatively high ones. For example, VIV of the riser is predominated by the 23$^{rd}$ mode at 0.8 m/s, while the 26$^{th}$ mode prevails when slug flow is introduced inside the riser. Moreover, multi-mode effects are more significant in the VIV-SIV than the VIV-only case, resulting in a greater number of secondary modes alongside more comparable modal weights to the dominant one. For instance, VIV at $U_o$ = 0.5 m/s (Figures 5.7a, b) contains three different modes (14$^{th}$-16$^{th}$) and the weight ratio of the secondary mode is about 0.5, whereas there are eight modes (15$^{th}$-22$^{nd}$) excited by the combined external-internal excitations (Figures 5.7c, d) with the weight ratio of the secondary mode being about 0.9. Similarly, the aforementioned features can also be observed in VIV-SIV of $U_t$ = 16 m/s although its mode-switching as well as multi-mode behaviours seem not as strong as the ones at $U_t$ = 6 m/s. For example, at $U_o$=0.3 m/s, the VIV-only case demonstrates a lower dominant vibration mode (7$^{th}$) accompanied by a smaller range

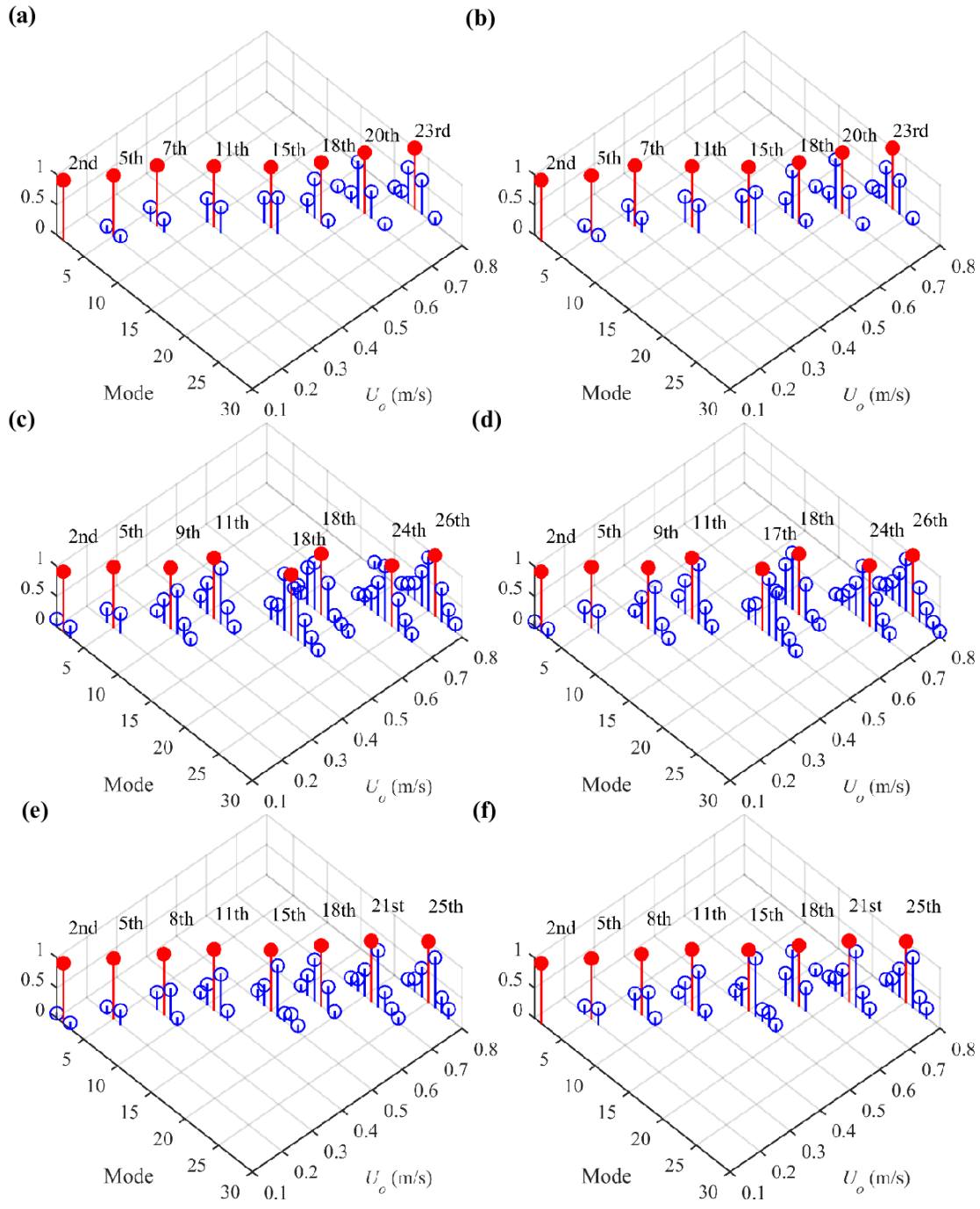


**Figure 5.7:** Modal distribution in (a, c, e) *u* and (b, d, f) *v* at varying $U_o$ in case of (a, b) VIV-only, (c, d) VIV-SIV for $L_u/d$=80, $U_t$ = 6 m/s and (e, f) VIV-SIV for $L_u/d$=80, $U_t$ = 16 m/s: red and blue markers represent dominant and secondary modes, respectively.

of secondary ones ($6^{th}$-$8^{th}$) than both the VIV-SIV cases. The slug flow at $U_t$ = 6 m/s results in more pronounced VIV with $7^{th}$-$12^{th}$ vibration modes, dominated by the $9^{th}$ mode. In contrast, a lower dominant mode ($8^{th}$) accompanied by a relatively narrower band ($7^{th}$-$10^{th}$) participate in the VIV-SIV case at $U_t$ = 16 m/s. The VIV-SIV cases at $U_t$ = 6 m/s generally result in more pronounced multi-modal riser vibration with higher dominant mode than the ones at $U_t$ = 16 m/s. This is contrary to the trend of the modal loads that higher $U_t$ potentially leads to larger

centrifugal force and hence enhanced dynamics. The ratio of the magnitude of centrifugal force at $U_t$ = 16 m/s to the one at $U_t$ = 6 m/s yields about 3.3. Nevertheless, it is worth mentioning that the ratio of internal fluid mass to the riser mass (per unit length) is 25.4 % and 10.5% for $U_t$ = 6 m/s and $U_t$ = 16 m/s, respectively. The change of eigenfrequency in the present study is dominated by the increased system mass. Hence, it is reasonable to see more SIV effects at $U_t$ = 6 m/s than $U_t$ = 16 m/s. The different levels of riser dynamics can also be observed in Figure 5.5, where the cases at $U_t$ = 6 m/s result in larger riser response than the ones at $U_t$ = 16 m/s, e.g. $v_{rms}$ at $U_o$= 0.6 m/s. Apart from the aforementioned effect of internal fluid mass, this may be due to the relationship between the slug flow frequency and the vortex shedding frequency. It can be evaluated that the primary slug flow frequency (about 0.19 Hz) of the VIV-SIV case at $U_t$ = 6 m/s is closer to the vortex shedding frequency (about 0.28 Hz) than the one from VIV-SIV case at $U_t$ = 16 m/s (about 0.52 Hz). Such a relationship may be responsible for the higher $v_{rms}$ at $U_o$= 0.6 m/s, where a stronger resonance between SIV and VIV occurs. Besides, based on the discussion on the modal load concept in Chapter 3, the modal loads travelling at $U_t$ = 16 m/s may be too fast so that the riser cannot fully respond to them. In contrast, it may be reasonable to observe the enhanced riser responses at $U_t$ = 6 m/s, where the mass effect dominates over the velocity effect.

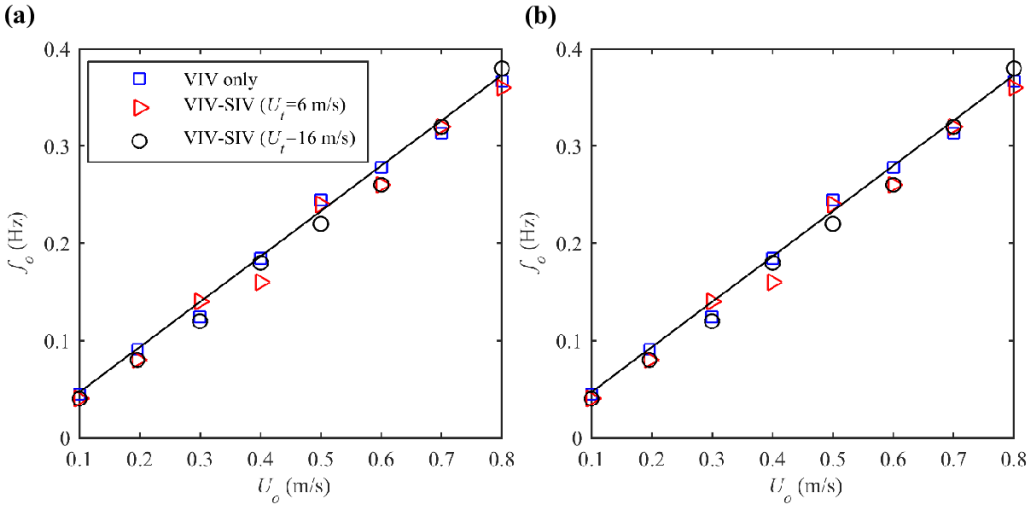


**Figure 5.8:** Comparison of dominant $f_o$ for (a) $u$ and (b) $v$ at varying $U_o$ in case of VIV-only (blue squares), VIV-SIV for $L_u/d$=80, $U_t$ = 6 m/s (red triangles) and VIV-SIV for $L_u/d$=80, $U_t$ = 16 m/s (black circles): black line represents the Strouhal rule.

In Figure 5.8, comparisons of the dominant oscillation frequency ($f_o$) for the three scenarios are shown at various $U_o$. In general, it can be seen that $f_o$ of the considered cases increase with $U_o$ linearly and follows the Strouhal rule for both $u$ (Figure 5.8a) and $v$ (Figure 5.8b). However, comparison of $f_o$ varies at different $U_o$. It is observed that the VIV-only case exhibits evidently higher $f_o$ than the VIV-SIV cases at $U_o$= 0.2 and 0.6 m/s, while this is not the

case for the other $U_o$, e.g. $U_o$= 0.3, 0.7 and 0.8 m/s, where at least one of the VIV-SIV cases results in higher $f_o$ than the one of VIV-only case. The differences of $f_o$ may be fundamentally related to the slug-induced changes in the structural stiffness, influencing the mode-switching and multi-mode behaviours in the riser responses.

*5.3.2 Influence of SIV in VIV-SIV at low and high current velocities*

Figure 5.9 displays contour plots of the variations of coexisting $u$ (a, c, e) and $v$ (b, d, f) steady-state oscillation (units in m) at a given $U_o$=0.2 m/s for (a, b) VIV-only, (c, d) VIV-SIV of $U_t$ =

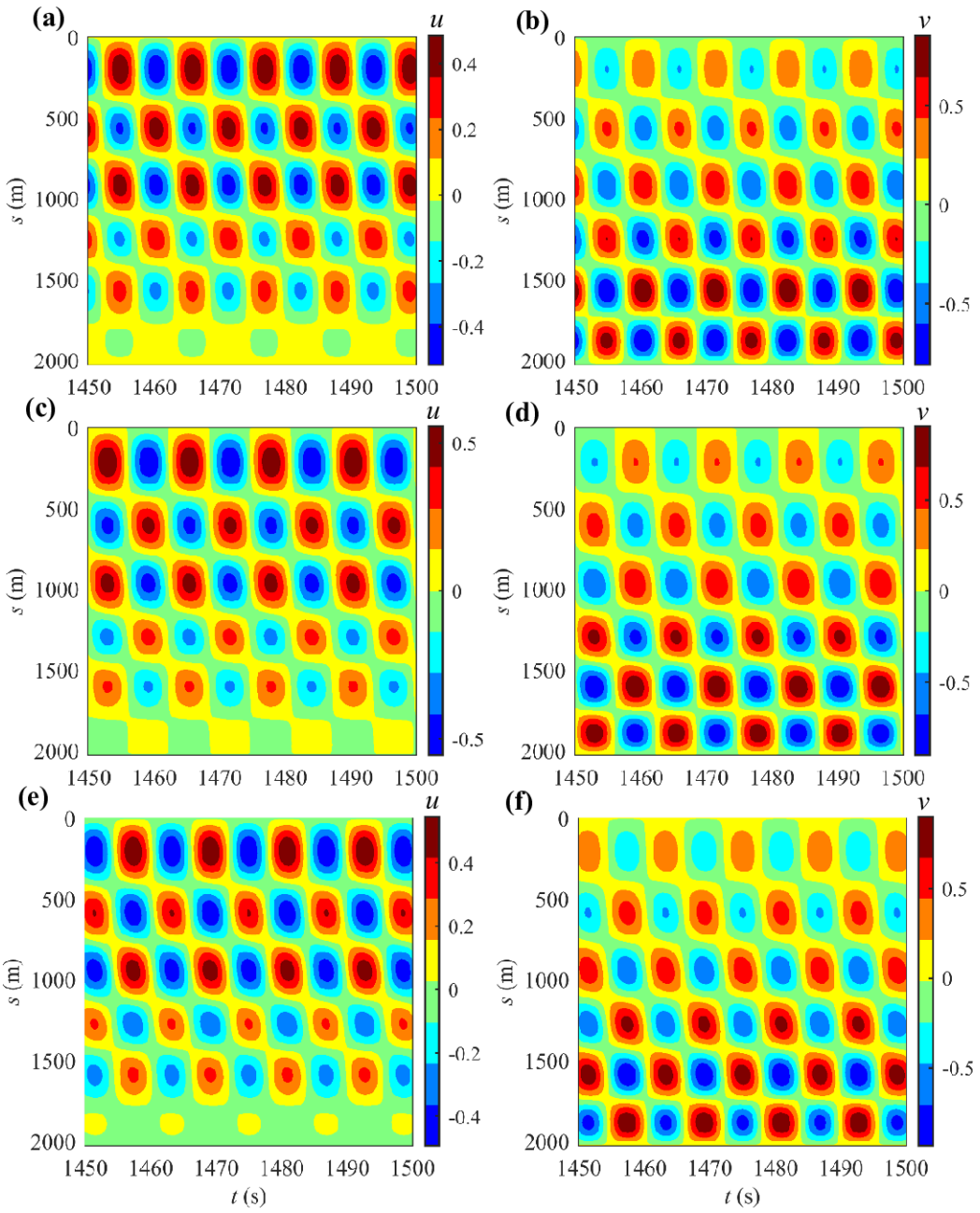


**Figure 5.9:** Space-time varying (a, c, e) $u$ and (b, d, f) $v$ exclusive of mean at $U_o$ = 0.2 m/s, for (a, b) VIV-only, (c, d) VIV-SIV: $L_u/d$ = 80 at $U_t$ = 6 m/s and (e, f) VIV-SIV: $L_u/d$ = 80 at $U_t$ = 16 m/s.

6 m/s and (e, f) VIV-SIV of $U_t$ = 16 m/s, within 1450s < $t$ <1500s. The associated spatial frequency spectra against normalized PSD are plotted in Figure 5.10 up to 1 Hz. By the comparisons between (Figures 5.9a, b) VIV-only and (Figures 5.9c-f) VIV-SIV cases, it can be observed that the overall oscillation patterns of the three cases are similarly governed by standing waves, suggesting the dominant role of VIV in the combined external-internal excitations. Nevertheless, the planar displacements are slightly increased owing to the participation of slug flows. For instance, maximum $u$ and $v$ of the VIV-only case are 0.516 m and 0.854 m, whereas they are amplified to 0.557 m and 0.906 m (0.55 m and 0.937 m) after the slug flow at $U_t$ = 6 m/s (16 m/s) is incorporated. Inspecting FFT plots, both VIV-only and VIV-SIV cases exhibit single-frequency responses with a slight involvement of higher 3rd harmonics. As presented in Chapter 3, slug flows are able to excite riser responses at dominant $f_s$ with high modulations. However, this is not the case for the combined VIV-SIV scenario.

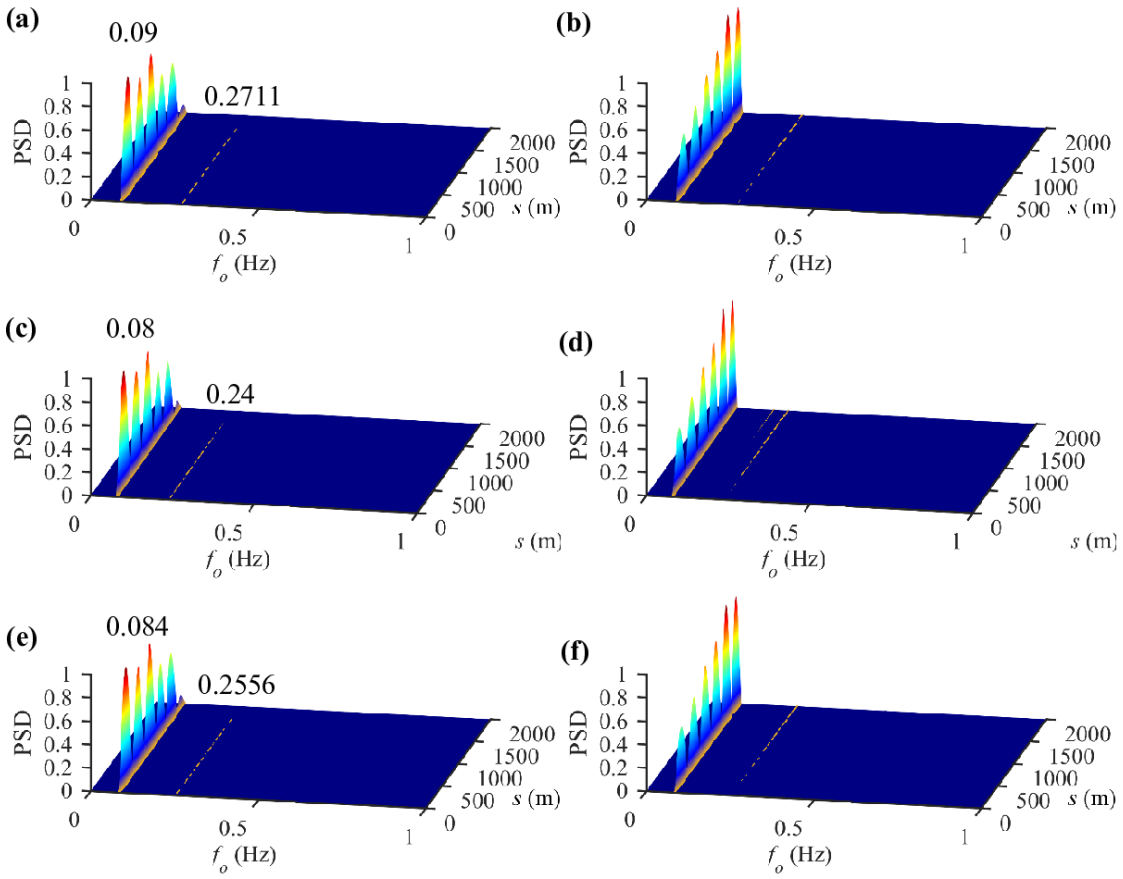


**Figure 5.10:** Spatial profiles of oscillation frequencies associated with responses in Figure 5.8.

In Figures 5.10c-f, it is evident to see the prevailing VIV effects without showing the frequency contents from SIV, i.e. $f_s$ = 0.2 Hz (0.52 Hz) for $U_t$ = 6 m/s (16 m/s) as reported in Table 3.2. This observation has justified the dominant VIV oscillation in Figure 5.9. The negligible participation of SIV in the frequency domain is expected since it is not comparable

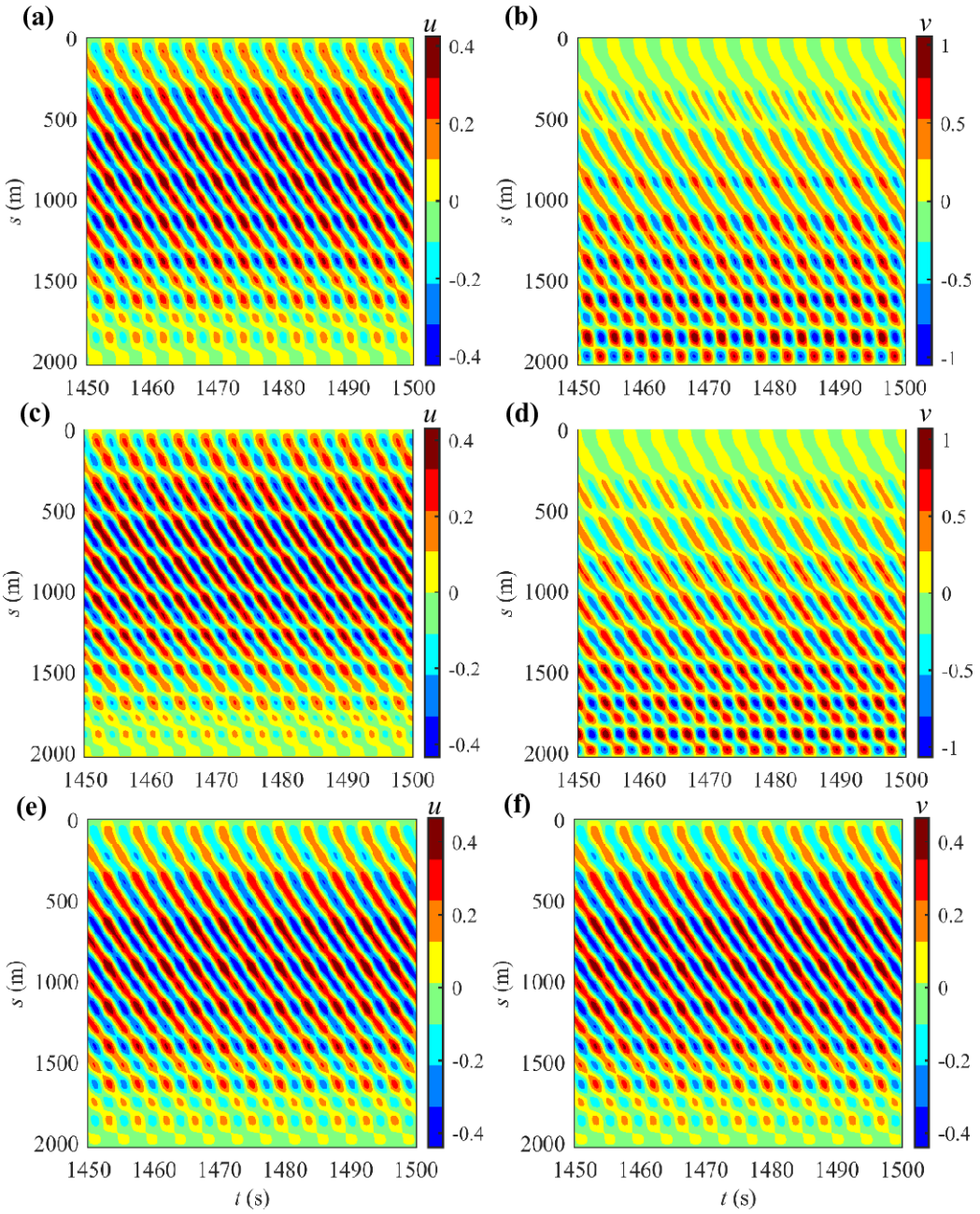


**Figure 5.11:** Space-time varying (a, c, e) $u$ and (b, d, f) $v$ exclusive of mean at $U_o = 0.5$ m/s for (a, b) VIV-only, (c, d) VIV-SIV: $L_u/d = 80$ at $U_t = 6$ m/s and (e, f) VIV-SIV: $L_u/d = 80$ at $U_t = 16$ m/s.

with VIV with respect to the order of magnitudes. Further, comparing Figures 5.10a, b with Figures 5.10c-f, the dominant $f_o$ of VIV-SIV cases are generally lower than those of the VIV-only case ($f_o$=0.09Hz). This is expected since slug-induced tension variation would influence the pipe axial stiffness and consequently the associated natural frequencies as discussed in Chapter 3. Besides, it is worth noting that the dominant $f_o = 0.08$ Hz at $U_t = 6$ m/s is slightly smaller than the one of $f_o = 0.084$ Hz at $U_t = 16$ m/s. This may be attributed to a larger tension drop by lower $U_t$ (Table 3.4). Although SIV is not comparable to the VIV in this case, slug

flows seem to result in softening stiffness, which may account for the slightly amplified maximum amplitudes as displayed in Figure 5.9.

In case of relatively high $U_o$=0.5 m/s, contour plots of coexisting $u$ and $v$ oscillations (units in m) are exhibited in Figure 5.11 in case of (a, b) VIV-only, (c, d) VIV-SIV at $U_t$ = 6 m/s ($u_{ls}$=2 m/s, $u_{gs}$=2 m/s) and (e, f) VIV-SIV at $U_t$ = 16 m/s ($u_{ls}$=2 m/s, $u_{gs}$=10.3 m/s). The associated spanwise FFT plots are shown in Figure 5.12. In comparison with Figures 5.9a and 5.9b, the VIV-only case presented in Figures 5.11a and 5.11b is now governed by travelling waves with greater maximum responses (up to 1.052 m). These observations are in consistent with experimental results of Zhu et al., (2019), where VIV response patterns of a curved flexible free-hanging riser become more travelling with larger amplitudes as the flow velocity inceases.

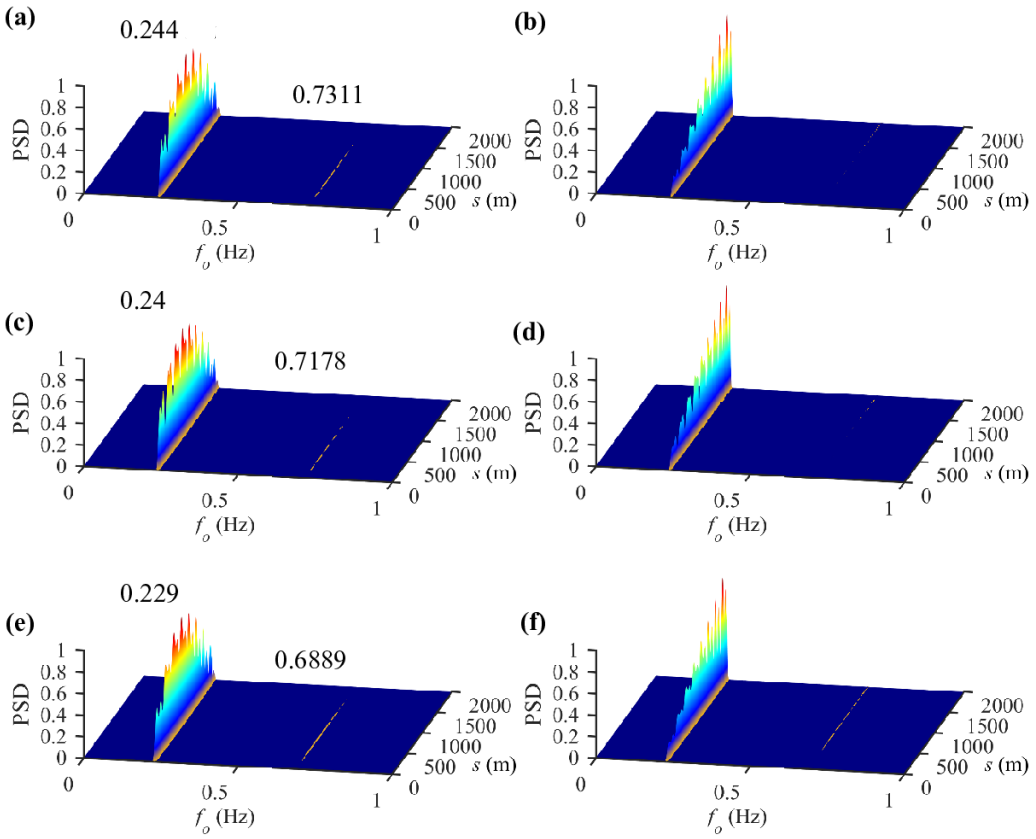


**Figure 5.12:** Spatial profiles of oscillation frequencies associated with responses in Figure 5.10.

By involving slug flows, the main travelling-wave feature is maintained in Figures 5.11c, d and 5.11e, f with slightly higher maximum $u$ and $v$ than the pure VIV case (Figures 5.11a, b), implying the dominant effects of VIV over SIV as discussed above. This is further justified by the response frequencies as presented in Figure 5.12, where VIV prevail in the combined FIV cases without the occurrence of SIV frequency contents. Besides, it is noticeable that overall responses are dominated by a single harmonic peak, with lower $f_o$ for VIV-SIV cases (Figures

5.12c, d and 5.12e, f). However, in contrast to the cases at lower $U_o$=0.2 m/s, $f_o$ of $U_t$=16 at $U_o$=0.5 m/s is now lower than the one of $U_t$ = 6m/s.

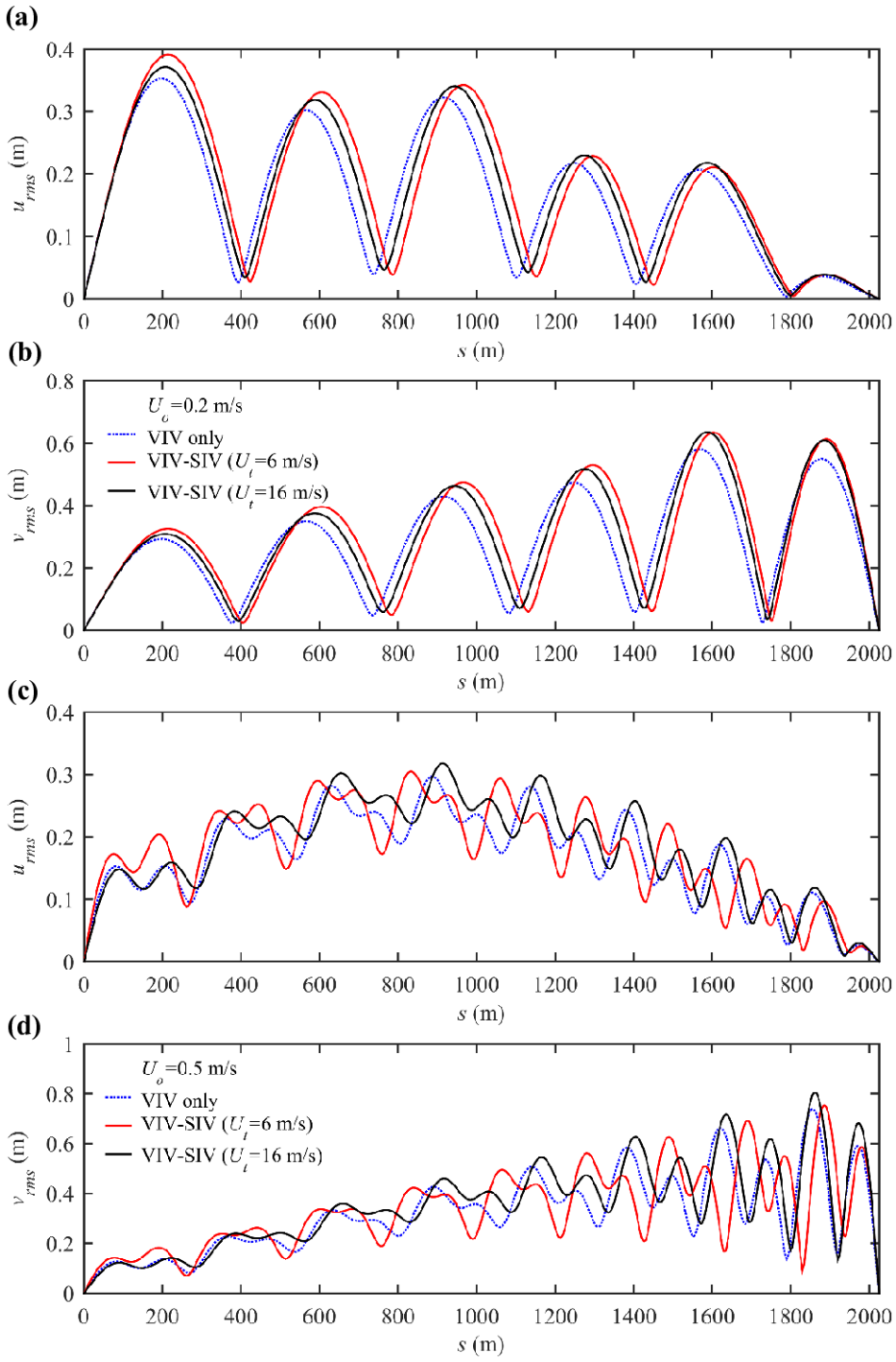


**Figure 5.13:** Spatial distribution of (a, c) $u_{rms}$ and (b, d) $v_{rms}$ in case of (a, b) $U_o$ = 0.2 m/s and (c, d) $U_o$ = 0.5 m/s.

Taking a closer look into the responses with and without slug flows, comparisons of spatial RMS responses are depicted in Figure 5.13. In the case of $U_o$ = 0.2 m/s (Figures 5.13a, b), six peaks are clearly observed spatially along the riser span, suggesting a predominant 5$^{th}$

mode across all the scenarios. These evident single-mode-dominant profiles justify the observed standing-waves responses in Figure 5.9 as well as the modal analysis as shown in Figure 5.7. Greater amplitudes are found in the spatial distribution of RMS responses of VIV-SIV cases than ones of the pure VIV case, which is consistent with the amplified displacements as shown in Figure 5.9. On the other hand, the spatial RMS responses in case of $U_o$=0.5 m/s are displayed in Figures 5.13c, d. More complex distributions appear in this case with multiple large peaks containing secondary small peaks along the riser span, which may reflect the significant participation of multiple modes in riser responses at higher $U_o$ (Figure 5.7) and hence explain the travelling-wave oscillation as seen in Figure 5.11. Such a correlation between single-/multi-mode responses and standing-/travelling-wave oscillation patterns have been reported in Tognarelli et al. (2004) and Gao et al. (2017). Comparing with the RMS profiles in Figures 5.13c, d, the slug-free case shows relatively lower values than the VIV-SIV cases, which again may be due to the stiffness-softening effects from slug flows.

Moreover, it is worth emphasizing the differences between the VIV-SIV cases at $U_t$= 16m/s and 6 m/s, in which the former follows the pure VIV case with respect to the RMS profile and the latter, however, exhibits additional peaks along the span. This suggests a resonance dominated by a higher mode as confirmed in Figures 5.7c, d, implying the potential increase in fatigue damage. Such change of dominant mode could be owing to a weaker stiffness caused by the appearance of slug flow. The observed riser responses are closely related to the modal loads, i.e. gravity, centrifugal and Coriolis forces. The loading terms in Eqs. (5.1) and (5.2) can be evaluated to determine the governing effect on the transition of responses from the VIV-only to VIV+SIV cases. For $U_o$=0.2 m/s, the ratio of the magnitude of centrifugal to Coriolis term is 14.97% (34.65%) at $U_t$= 6 (16 m/s), whereas the ratio becomes 6.32% (16.66%) at $U_t$= 6 (16 m/s) for $U_o$=0.5 m/s. It is noted that the centrifugal term is generally smaller than the Coriolis effect. The Coriolis effect plays the role of damping force for a non-conservative system. Nevertheless, for the present gyroscopically conservative system with a pinned-pinned boundary condition, the Coriolis force mainly results in the change of the mode shapes, where the classical normal modes from harmonic free vibrations do not exist (Chen, 1985). Also, this effect is usually regarded to be negligible (Huse Knudsen et al., 2016; Bordalo and Morooka, 2018; Meléndez and Julca, 2019), especially for relatively low $U_o$. On the other hand, the dynamic centrifugal term is equivalent to a compressive force contributing to the reduction of axial tension variation. Therefore, the transition of the dominant mode is partially attributed to this force. Also, the internal fluid mass contributes to an increase in the system mass, together with the reduced stiffness, causing altered eigenfrequencies. Hence, the centrifugal force is

considered prevailing over the Coriolis force in the present study. Consequently, a transition from lower to higher mode VIV takes place when the natural frequency is decreased, explaining the higher predominant $f_o$ of $U_t$=6 m/s in this case than the one of $U_t$=16 m/s as seen in Figure 5.12. In contrast, the slug flow at higher $U_t$ = 16m/s, which leads to a relatively smaller change of system stiffness, does not influence the order of VIV. Besides, compared with higher $U_o$, there are no mode-switching phenomena for $U_o$ = 0.2 m/s regardless of $U_t$. This may be due to the stranding- vs. travelling-wave behaviours, where a single-mode oscillation is more robust than multi-mode oscillation (Chaplin et al, 2005). Similar mode changing phenomena is also reported in a numerical study from Yang et al. (2018), in which VIV mode order of a flexible riser is found increased due to the decreased natural frequencies by an internal single-phase flow.

*5.3.3 Stress evaluation: VIV vs. VIV-SIV*

Evaluation of stresses based on the above results is meaningful for failure assessment and provides a further visualization of individual effects of VIV and SIV in the combined FIV system. Following the same procedure of stress calculation in Section 3.4.5, bending stresses ($\sigma_u$ and $\sigma_v$) in $X$ and $Y$ directions, axial stress ($\sigma_a$), and total steady-state stresses ($\sigma_t$) are computed.

Corresponding to Figure 5.9, Figure 5.14 displays the contour plots of space-time $\sigma_u$ (Figures 5.14a, c, e) and $\sigma_v$ (Figures 5.14b, d, f) exclusive of mean components in case of (a, b) VIV-only, (c, d) VIV-SIV of $U_t$ = 6 m/s and (e, f) VIV-SIV of $U_t$ = 16 m/s for a given $U_o$=0.2 m/s. It is evident to see the similar patterns of $\sigma_u$ and $\sigma_v$ to those of $u$ and $v$ (Figure 5.9), showing variations in standing waves. Comparing the case (Figures 5.14a, b) without and (Figures 5.14c-f) with slug flows, high modulations exist in VIV-SIV cases with significantly larger values (in MPa) than those of the pure VIV case. Such a discrepancy highlights the effects of SIV in magnifying bending stresses, causing additional curvatures in space due to the uneven slug-induced gravity and momentum forces.

Although SIV is insignificant in the context of response displacements and frequencies, it comes into play in bending stresses due to the involvement of high-order derivatives in stress calculations. These additional spatial curvatures together with the amplified displacements due to the softening stiffness are responsible for the largely amplified $\sigma_u$ and $\sigma_v$ in the VIV-SIV cases. On the other hand, bending stresses are also evaluated for higher $U_o$=0.5 m/s and shown in Figure 5.15. It is observed that travelling waves predominate in $\sigma_u$ and $\sigma_v$ in accordance with Figure 5.11, leading to moving maximum and minimum stresses along the pipe, i.e. no clear

nodes in variations of $\sigma_u$ and $\sigma_v$. Such widely distributed stresses may signify potential critical damage all over the span. Besides, it is worth noting that $\sigma_u$ and $\sigma_v$ at higher $U_o$ present

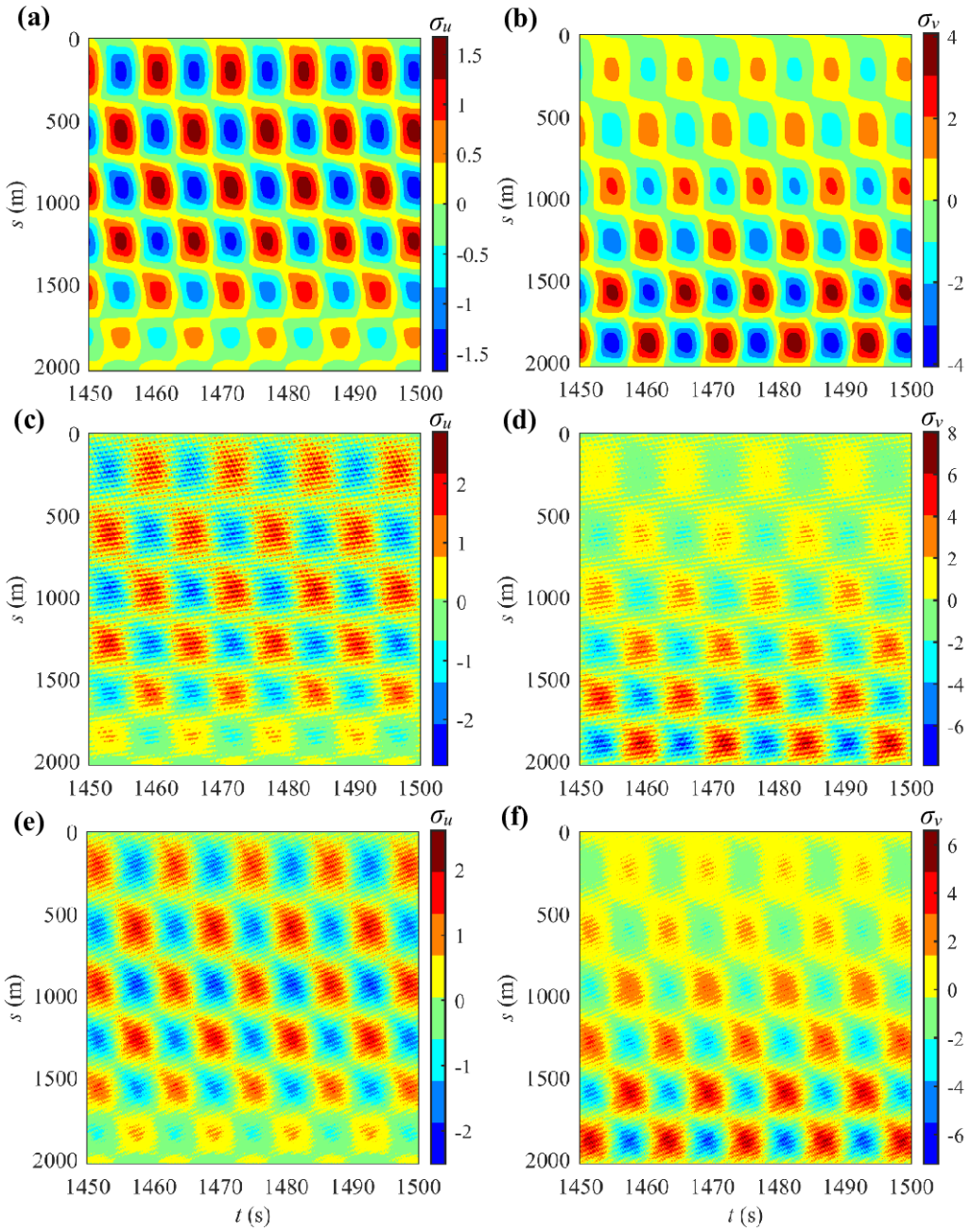


**Figure 5.14:** Space-time varying (a, c, e) $\sigma_u$ and (b, d, f) $\sigma_v$ exclusive of mean components at $U_o$ = 0.2 m/s for (a, b) VIV-only, (c, d) VIV-SIV: $L_u/d$ = 80 at $U_t$ = 6 m/s and (e, f) VIV-SIV: $L_u/d$ = 80 at $U_t$ = 16 m/s.

nodes in variations of $\sigma_u$ and $\sigma_v$. Such widely distributed stresses may signify potential critical damage all over the span. Besides, it is worth noting that $\sigma_u$ and $\sigma_v$ at higher $U_o$ present considerably larger values than those of lower $U_o$ (Figure 5.14), which is associated with the high vs. low modal oscillations because of large vs. small curvatures. Further, by the comparisons between VIV-SIV cases at $U_o$=0.2 m/s (Figures 5.14c-f) and $U_o$=0.5 m/s (Figures

5.15c-f), the latter demonstrates less modulated stresses than the former. This may be due to the greater fluid-added damping effects associated with the higher $U_o$ so that the SIV effect is further damped. Overall, amplified $\sigma_u$ and $\sigma_v$ are revealed in case of VIV-SIV compared with the pure VIV case, which are fundamentally related to the aforementioned stiffness-softening effects. This effect is more pronounced in the mode-switched case (Figures 5.15c, d), resulting in higher-modal VIV and hence the worst $\sigma_u$ and $\sigma_v$.

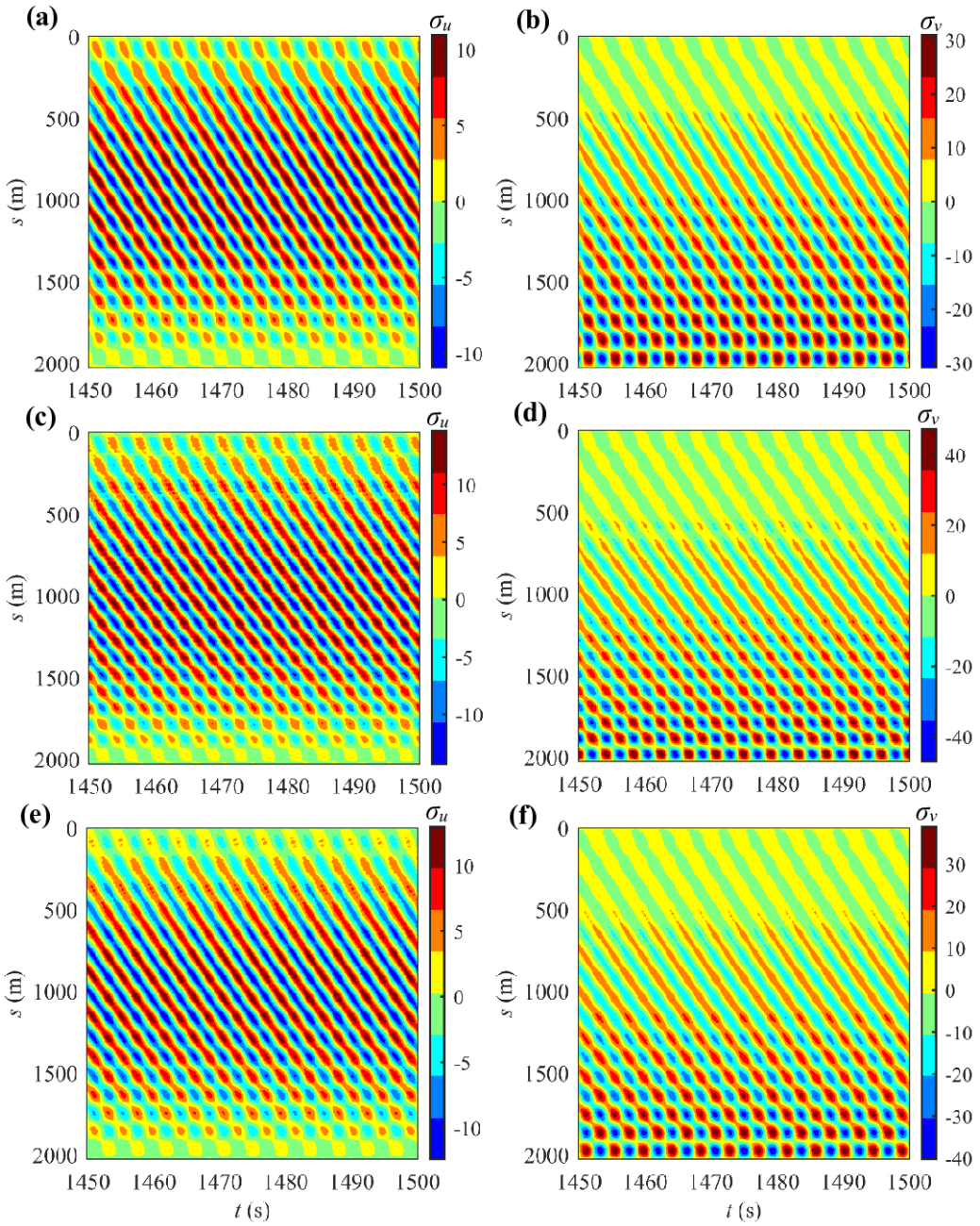


**Figure 5.15:** Space-time varying (a, c, e) $\sigma_u$ and (b, d, f) $\sigma_v$ exclusive of mean components at $U_o$ = 0.5 m/s, for (a, b) VIV-only, (c, d) VIV-SIV: $L_u/d$ = 80 at $U_t$ = 6 m/s and (e, f) VIV-SIV: $L_u/d$ = 80 at $U_t$ = 16 m/s.

Variations of $\sigma_u$ and $\sigma_v$ are further discussed by spatial distributions of RMS values along the span as depicted in Figure 5.16. In case of low $U_o$=0.2 m/s, it is seen that the stresses generally follow the trend of $u$ and $v$ as plotted in Figures 5.16a, b, while obvious increases are

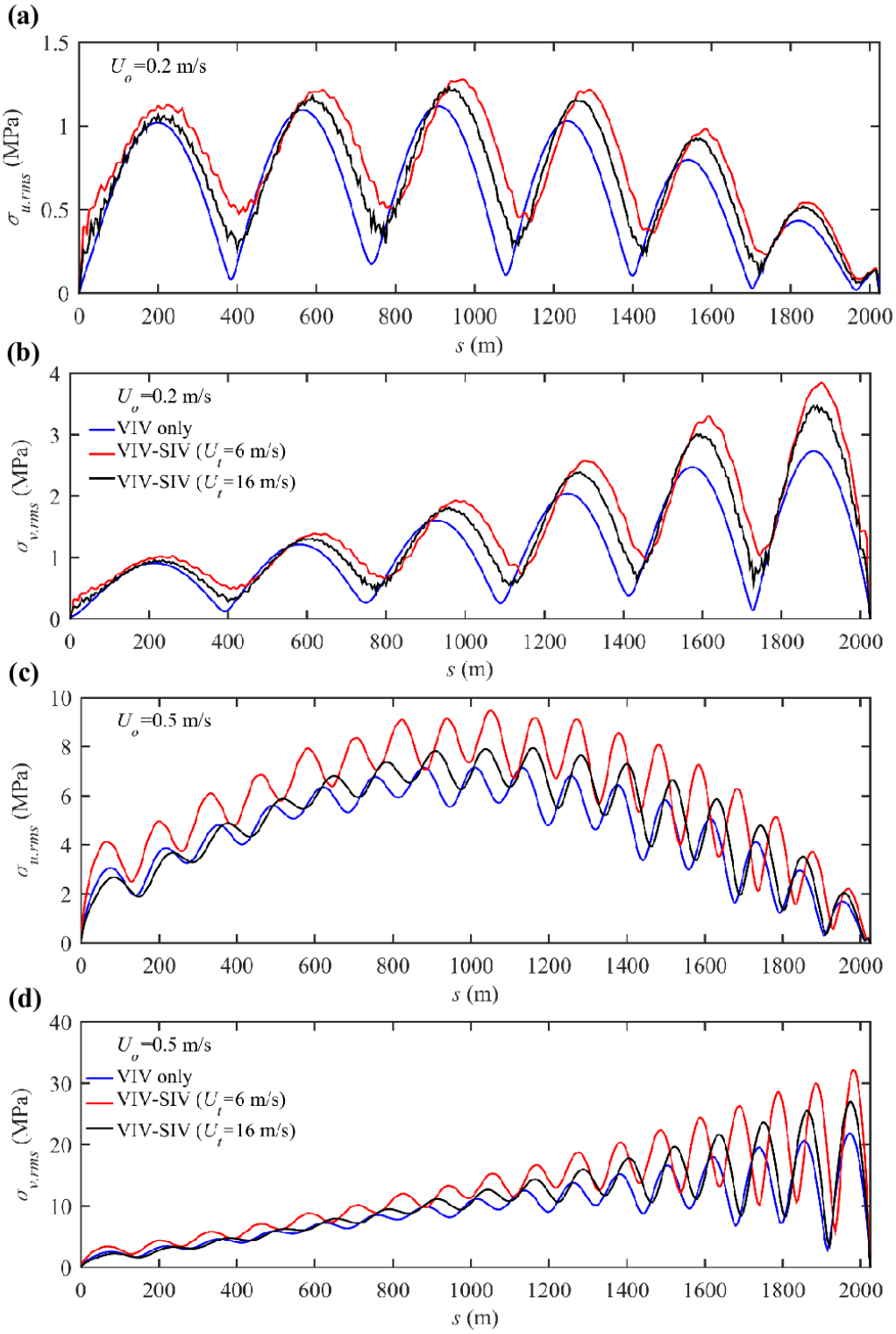


**Figure 5.16:** Spatial distribution of (a, c) $\sigma_{u.rms}$ and (b, d) $\sigma_{v.rms}$ in case of (a, b) $U_o$ = 0.2 m/s and (c, d) $U_o$ = 0.5 m/s.

observed in the spatial RMS values of slug-flow-involved cases than the those of the slug-free case. Plus, strong local fluctuations are noticeable in VIV-SIV cases, justifying the modulated space-time stress variations in Figure 5.14. In contrast, there are no clear modulated RMS profiles in case of $U_o$=0.5 m/s (Figures 5.16c, d), which confirms the observation of similar patterns across Figure 5.15. Although comparable RMS displacements are revealed in Figures 5.13c, d, VIV-SIV of $U_t$=6 m/s results in distinctively larger RMS bending stresses than the other two (see Figures 5.16c, d), highlighting the significant role of slug flows in upgrading mode orders of VIV at higher $U_o$.

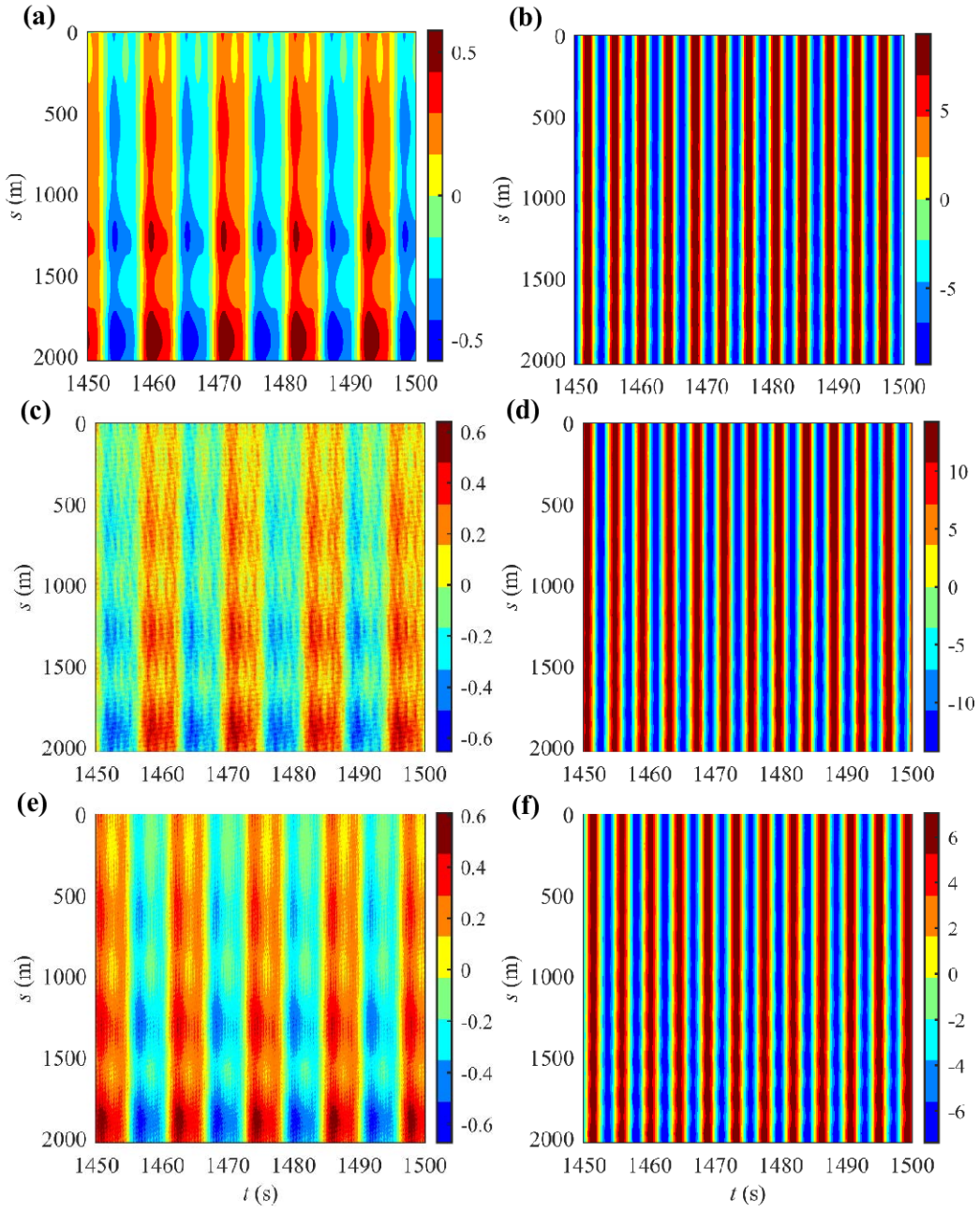


**Figure 5.17:** Space-time varying $\sigma_a$ exclusive of mean components at (a, c, e) $U_o$ = 0.2 and (b, d, f) 0.5 m/s, for (a, b) VIV-only, (c, d) VIV-SIV: $L_u/d$ = 80 at $U_t$ = 6 m/s and (e, f) VIV-SIV: $L_u/d$ = 80 at $U_t$ = 16 m/s.

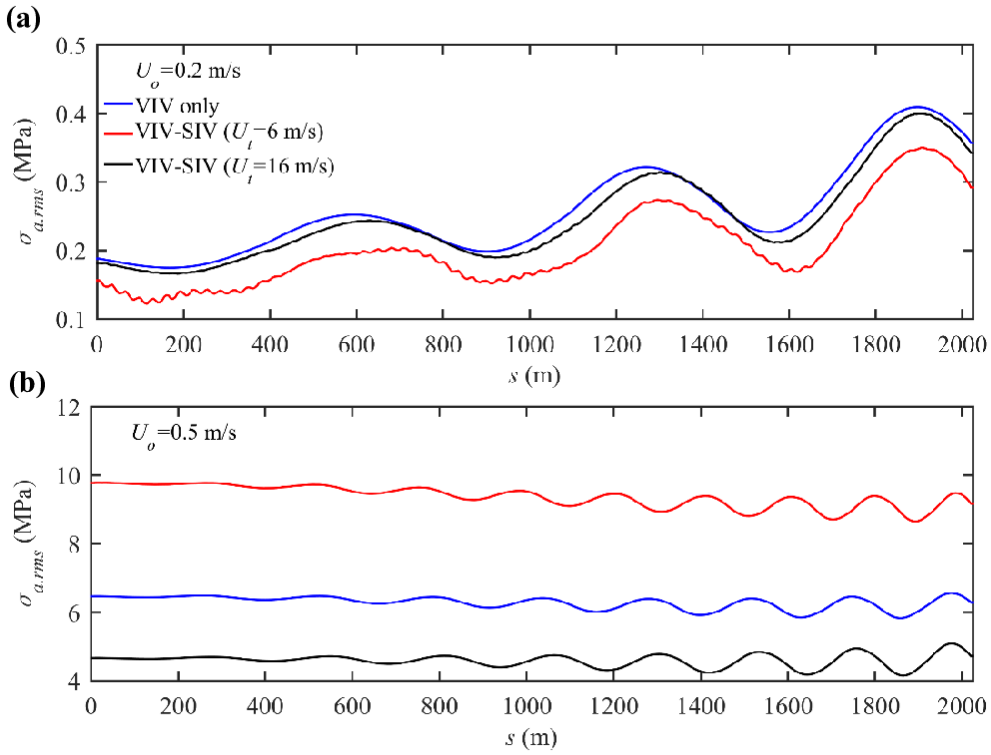


**Figure 5.18:** Spatial distribution of $\sigma_{a.rms}$ in case of (a) $U_o$ = 0.2 m/s and (b) $U_o$ = 0.5 m/s.

Figure 5.17 displays the associated $\sigma_a$ in case of (Figures 5.17a, c, e) $U_o$ = 0.2 m/s and (Figures 5.17b, d, f) 0.5 m/s for (a, b) VIV, (c, d) VIV-SIV of $U_t$ = 6m/s and (e, f) VIV-SIV of $U_t$ = 16 m/s. By the comparison between the case of (Figures 5.17a, c, e) low and (Figures 5.17b, d, f) high $U_o$, the former generally illustrates less uniform variations in space than those of the latter, especially for VIV-SIV at low $U_o$ (Figure 5.17c), which is subject to strong local modulations as presented in the bending stresses (Figures 5.14c, d). Further, the two groups demonstrate magnitudes of different orders, emphasizing again the effects of vibration modes. From the results, $\sigma_a$ from $U_o$=0.5 m/s are 10 times greater than those from $U_o$ = 0.2 m/s, exhibiting more comparable values with their associated bending stresses (Figures 5.15c-f). Such an amplification of $\sigma_a$ with $U_o$ is also addressed in Zanganeh and Srinil (2016), implying the non-negligible role of $\sigma_a$ in stress assessments. Associated with Figure 5.17, spatial RMS values ($\sigma_{a.\mathrm{rms}}$) are shown in Figure 5.18. For $U_o$ = 0.2 m/s (Figure 5.18a), it is interesting to see that $\sigma_{a.\mathrm{rms}}$ of the VIV-only case predominates over those of VIV-SIV cases although the responses and the associated bending stresses are found to be the other way around. This observation may be related with reduced $f_n$ due to stiffness-softening effects, which yields $f_o$ (VIV-only) > $f_o$ ($U_t$ = 16 m/s) > $f_o$ ($U_t$ = 6 m/s) as presented in Figure 5.10. Such a correlation has also been reported by Yang et al., (2018), where $\sigma_a$ is found to decrease with lower $f_n$. However, this is not the case for $U_o$ = 0.5 m/s (Figure 5.18b), where the VIV-SIV case ($U_t$ = 6

m/s) causes the largest $\sigma_{a.\mathrm{rms}}$ amongst the three cases. This is owing to its larger curvatures associated with the higher-modal oscillation.

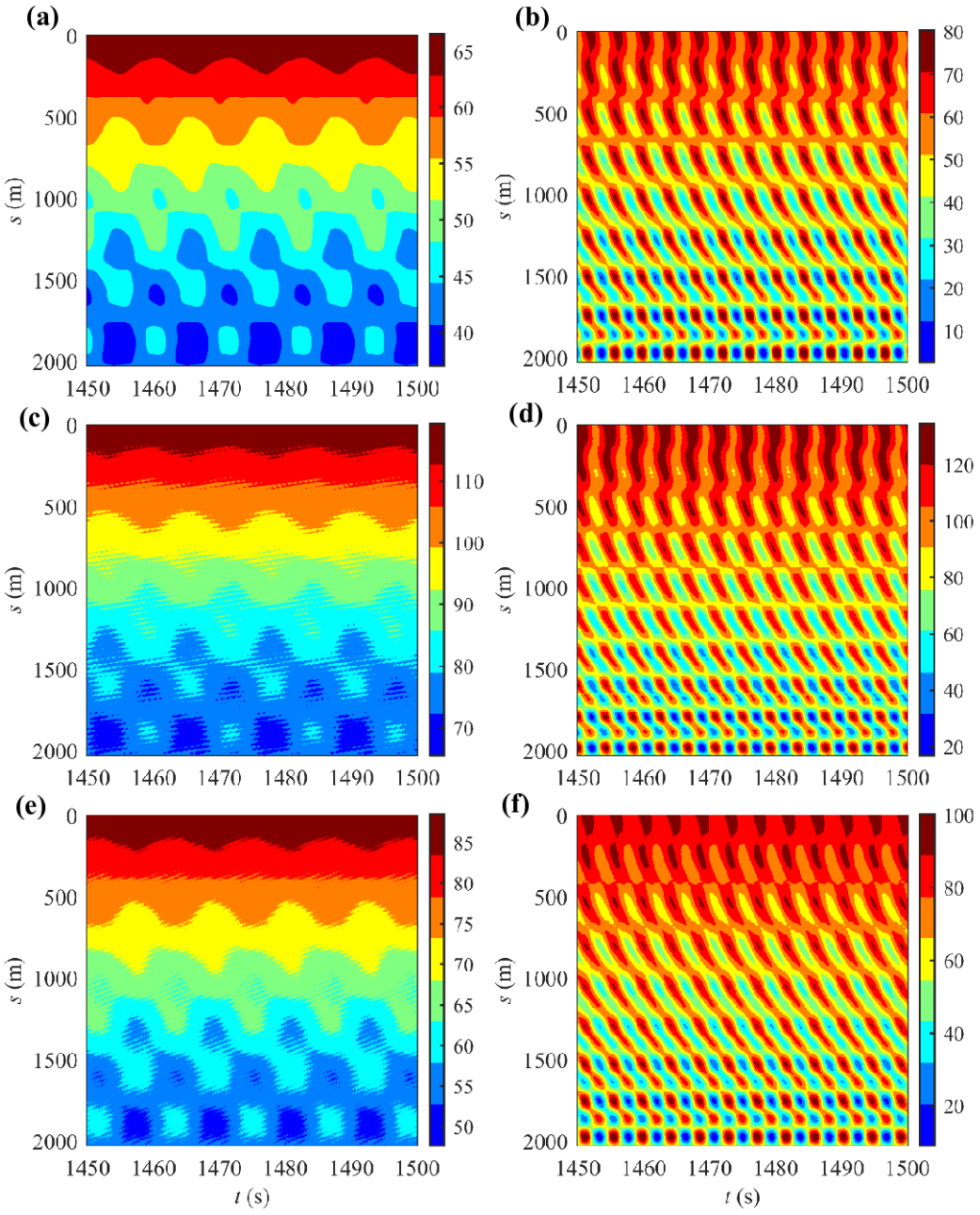


**Figure 5.19:** Space-time varying $\sigma_t$ at (a, c, e) $U_o$ = 0.2 and (b, d, f) 0.5 m/s, for (a, b) VIV-only, (c, d) VIV-SIV: $L_u/d$ = 80 at $U_t$ = 6 m/s and (e, f) VIV-SIV: $L_u/d$ = 80 at $U_t$ = 16 m/s.

The total steady-state stresses ($\sigma_t$) can be finally evaluated by the summation of static, dynamic bending and axial stresses. Figure 5.19 exhibits $\sigma_t$ in association with the above cases in Figure 5.17. Following $\sigma_u$, $\sigma_v$ and $\sigma_a$, variations of $\sigma_t$ display standing- and travelling-wave patterns for (Figures 5.19a, c, e) low and (Figures 5.19b, d, f) high $U_o$, respectively. Further, by comparisons between the two groups, higher maximum $\sigma_t$ but lower minimum $\sigma_t$ are observed in the group of $U_o$=0.5 m/s due to the greater dynamic stresses as demonstrated above. On the

other hand, VIV-SIV cases reveal overall larger $\sigma_t$ than the pure VIV case, highlighting the contribution from slug flow-induced dynamics and static stresses (i.e. mean $\sigma_a$ due to drifts) as discussed in Section 3.4.3. In the present study, the worst $\sigma_t$ scenario exists in the case of higher $U_o$ together with slug flows of lower $U_t$ (Figure 5.19d). Nevertheless, the pure VIV case with relatively more compressive $\sigma_t$ (Figure 5.19b) may signal a dynamic global buckling issue. Some main outputs in SIV and VIV-SIV at $U_o$=0.2 vs. 0.5 m/s are summarized in Table 5.1.

**Table 5.1:** Summary of main outputs in SIV vs. VIV-SIV responses for $U_o$=0.2 m/s and $U_o$=0.5 m/s.

| | | **$U_o$=0.2 m/s** | | | **$U_o$=0.5 m/s** | | |
|---|---|---|---|---|---|---|---|
| Scenarios | | **VIV** | **VIV+SIV ($U_t$=6 m/s)** | **VIV+SIV ($U_t$=16 m/s)** | **VIV** | **VIV+SIV ($U_t$=6 m/s)** | **VIV+SIV ($U_t$=16 m/s)** |
| $u_{max}$, $v_{max}$ (m) | | 0.49, 0.85 | 0.56,0.91 | 0.54, 0.9 | 0.42, 1.05 | 0.43, 1.07 | 0.45, 1.13 |
| $u_{rms}$, $v_{rms}$ (m) | | 0.35, 0.58 | 0.39,0.64 | 0.37, 0.63 | 0.3, 0.74 | 0.31, 0.76 | 0.32, 0.8 |
| Dominant $f_o$ (Hz) | | 0.09 | 0.08 | 0.084 | 0.244 | 0.24 | 0.229 |
| Mode participation | | $4^{th}$ - $6^{th}$ | $4^{th}$ - $6^{th}$ | $4^{th}$ - $6^{th}$ | $14^{th}$ - $16^{th}$ | $15^{th}$ -$22^{nd}$ | $13^{th}$ - $19^{th}$ |
| Dominant mode | | $5^{th}$ | $5^{th}$ | $5^{th}$ | $15^{th}$ | $18^{th}$ | $15^{th}$ |
| Oscillation pattern | | Standing | Standing | Standing | Travelling | Travelling | Travelling |
| $\sigma_u$ (MPa) | Max | 1.67 | 2.88 | 2.61 | 10.95 | 14.67 | 12.98 |
| | Min | -1.67 | -2.78 | -2.51 | -10.95 | -14.32 | -12.41 |
| $\sigma_v$ (MPa) | Max | 4.07 | 8.03 | 6.59 | 30.89 | 47.37 | 38.97 |
| | Min | -4.07 | -7.91 | -7.22 | -30.89 | -47.13 | -40.34 |
| $\sigma_a$ (MPa) | Max | 0.57 | 0.64 | 0.61 | 9.27 | 14.27 | 7.05 |
| | Min | -0.57 | -0.65 | -0.67 | -9.27 | -14.25 | -7.41 |
| $\sigma_t$ (MPa) | Max | 66.52 | 119.31 | 88.53 | 80.22 | 134.57 | 100.29 |
| | Min | 37.02 | 65.54 | 47.63 | 26.35 | 16.89 | 8.97 |

## 5.4 Summary

In this chapter, combined VIV and SIV phenomena of a long flexible catenary riser are investigated based on the slug-conveying model with a semi-empirical VIV model by spatially distributed van der Pol wake oscillators. The riser is subject to slug-induced gravity forces, internal fluid pressure variation, flow centrifugal and Coriolis forces as well as hydrodynamic forces due to VIV simultaneously. By applying $2^{nd}$ order finite difference in space and $4^{th}$ order Runge-Kutta in time, the VIV-SIV model is numerically solved for the coupled horizontal and vertical motions of the flexible catenary riser under various external-internal flow conditions. Through validating against the published experimental results, the proposed VIV model shows abilities in predicting qualitatively and quantitatively comparable riser responses to the tests.

Moreover, in case of the varying current velocities, several key VIV aspects of flexible risers are revealed through examining the riser response amplitude, modal distribution and oscillation frequency. As the current velocity increases, VIV of the riser is dominated by a high order of mode with enhanced multi-mode contribution, showing a tendency from standing to travelling oscillation patterns. The riser responses by pure external and combined external-internal excitations are assessed by comparing the space-time response, resonant frequency, dominant mode and mode distribution, dynamic and total stresses.

Overall, VIV is found to prevail in the VIV-SIV cases, while slug flows can result in more complicated VIV responses than those of VIV-only cases. Although not comparable with VIV in terms of amplitudes, SIV is prone to introduce small additional curvatures along the riser, especially for relatively low external flow velocities. These SIV effects are noticeable in bending stresses and subsequently responsible for the amplified magnitudes. Depending on the current velocity and slug flow translational velocity, slug flows can result in a modified VIV excitation mode with enhanced multi-modal contributions. Slug flow effects on the riser VIV responses are more significant at a lower slug translational velocity or a higher external flow velocity. Greater dynamic and static stresses are observed in VIV-SIV scenarios than those of VIV-only scenarios, which are attributed to the slug flow-induced additional curvature, mean drift and enhanced multimode oscillation.

# Chapter 6. Experimental Investigation on Slug Flow-Induced Vibration

In the present chapter, an experimental investigation into a flexible catenary pipe conveying gas-liquid flows is performed to explore SIV phenomena and to validate the numerical model proposed in Chapter 3. The experiment is carried out in an air-water test loop with a hanging tube section made of silica gel. High-speed cameras are employed to simultaneously acquire both slug-induced pipe motions and two-phase flow regimes in a non-intrusive way. Meanwhile, internal fluid pressures are measured at the pipe inlet and outlet via two pressure transducers. A wide range of gas-liquid flow rates are tested in the flow-conveying system and slug flows are captured at the relatively high ratios of gas to liquid superficial velocities, leading to SIV of the flexible pipe. Under various flow conditions, different levels of riser responses are observed accompanied by significant variations in slug flow characteristics including travelling velocities, slug unit lengths and slug frequencies. These highlight the correlations between the intermittent slug flows and the unsteady SIV with modulated amplitudes. Moreover, some aspects from the numerical SIV investigation are qualitatively exhibited in the laboratory tests. Model validations are carried out through comparisons with the experimental results in terms of riser responses and frequencies.

## 6.1 Experimental Setup

The experiments were conducted in an air-water test loop of the State Key Laboratory of Oil and Gas Reservoir Geology and Exploitation at the Southwest Petroleum University, China. The key test facilities comprise four parts, including the test segments, fluid supplies, measurement devices and data acquisition instruments as shown schematically in Figure 6.1.

The test loop consists of a 2 m long horizontal pipeline followed by a curved flexible pipe for a catenary configuration. In this experimental investigation, transparent silica tubes with 6 mm outer diameter ($D$), 1 mm thickness (e), density of 1041.8 kg/m$^3$ and Young's modulus ($E$) of 7.15 MPa were employed for the pipeline-riser system, which guarantee both the pipe flexibility and the visualization of internal flow contents. As displayed in Figure 6.2, the riser section was freely hanged in air with 0.915 m in horizontal span, 0.8 m in vertical height and 1.28 m in arc length, leading to aspect ratios of ($L$/$D$) 213 and ($L$/$d$) 320, respectively. The two ends of the riser are fixed axially and laterally on the floor and the support frames, respectively. More detailed pipe parameters are listed in Table 6.1. It is worth noting that the sag-to-span ratio is defined as the ratio of maximum sag (distance from the riser to its chord line) to $L$.

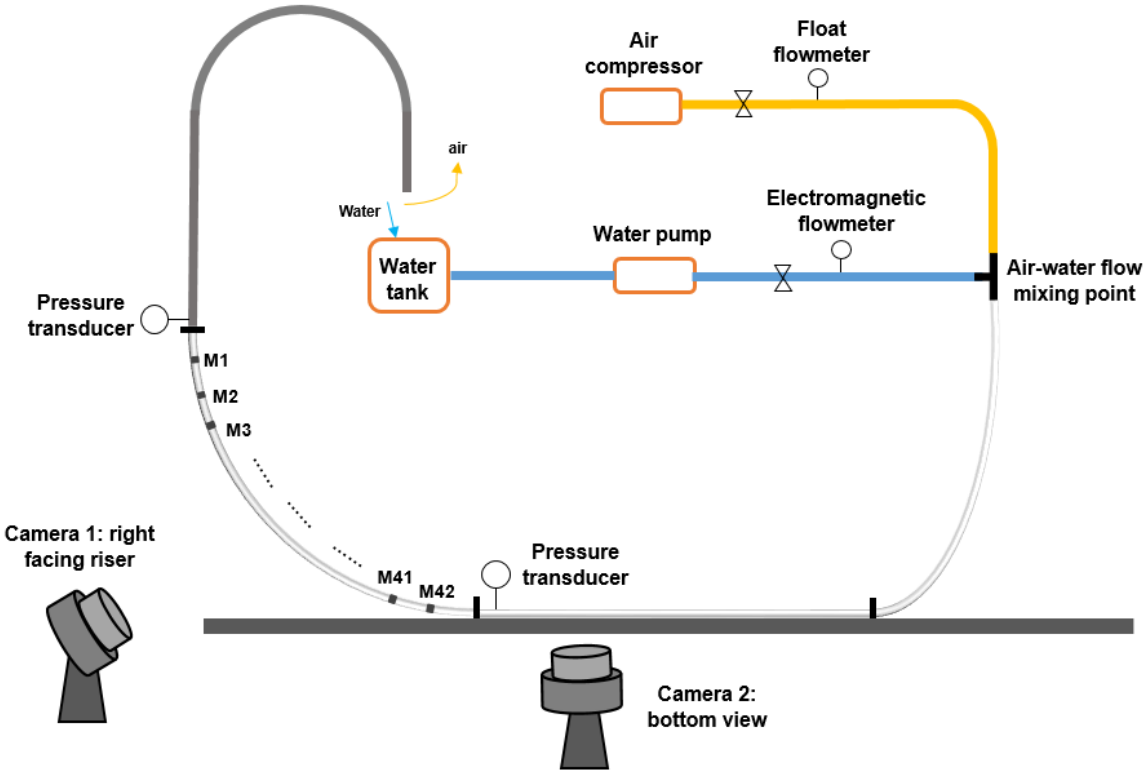


**Figure 6.1:** A schematic plot of SIV test loop.

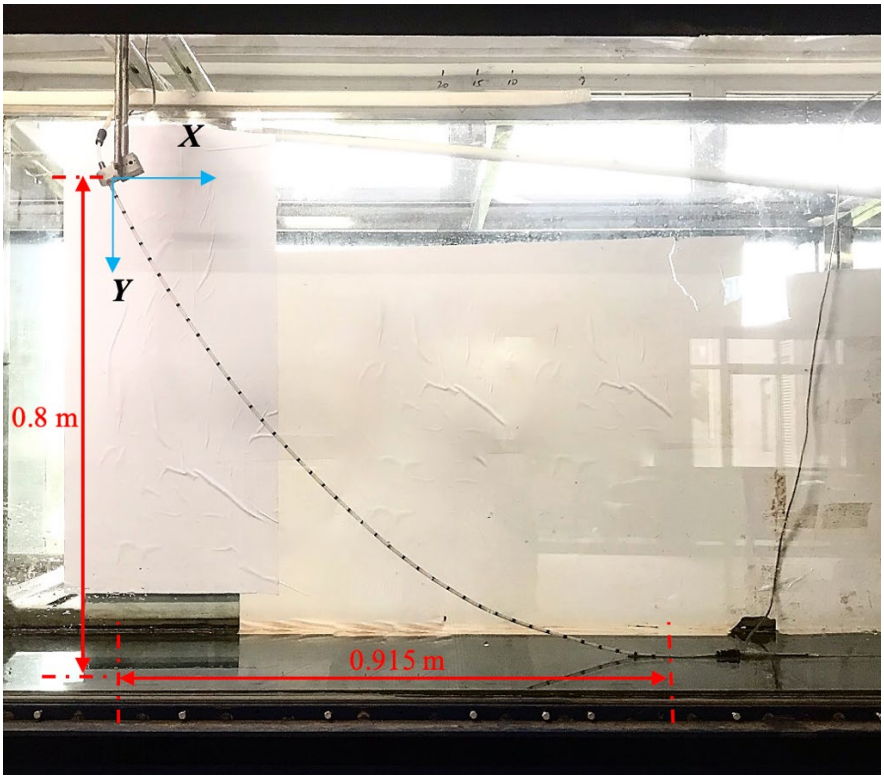


**Figure 6.2:** In-plane view of the riser segment.

**Table 6.1:** Key parameters of the riser segment.

| | |
|---|---|
| Length ($L$) | 1.28 m |
| Internal diameter ($d$) | 0.004 m |
| Outer diameter ($D$) | 0.006 m |
| Elastic modulus ($E$) | 7.15 MPa |
| Density of the riser | 1041.8 kg/m$^3$ |
| Horizontal span | 0.915 m |
| Vertical height | 0.8 m |
| Sag-to-span ratio | 0.124 |

Figure 6.3 has displayed the key measurement devices along the test flowlines. As for the internal gas-liquid phases, air-water flows are employed in the present tests. Dry air at 1 atmosphere pressure (101.325 kPa) and room temperature (20°C) was supplied by an air compressor with a maximum volumetric flow rate of 450 litre/minute (Figure 6.3a), which was connected to a float flowmeter (Figure 6.3b) of 3 litre/minute in maximum measurement capacity with an accuracy of 1%. A centrifugal pump (Figure 6.3c) with a maximum flow rate of 1.5 litre/minute was used to pump the liquid out from a water storage tank of 0.5 m$^3$ capacity and to circulate it throughout the test loop. An electromagnetic flowmeter (Figure 6.3d) with a measurement range up to 1.3 litre/minute and an accuracy of 0.5% was adopted to monitor the water flow rate. Liquid and gas flows were initiated at the same time in the respective flowlines (Figure 6.3f) and mixed at the connection section through a pneumatic tee adapter followed by a downward curved pipe (see Figure 6.1), where the air, water and mixing flowlines have $D$ ($d$) of 8 (6) mm. It is worth mentioning that the flow regime appeared to be a stratified flow in the downward part during the tests. This may be reasonable since the stratified flow takes place easily in a downward pipe (see Figures 2.4e, f). In fact, such a flow regime helps develop hydrodynamic slug flows due to the gas-liquid interface instabilities and it is typically taken as an initial condition for slug flow initiation in both experimental (Ansari and Nariai, 1989; Vaze and Banerjee, 2012) and numerical (Issa and Kempf, 2003; Carneiro and Nieckele, 2007) studies. Then, the inclined downward two-phase flow would enter the horizontal pipe and the downstream catenary pipe. According to several experimental tests for slug flows (Al-Hashimy et al., 2016; Ortiz-Vidal et al., 2017), an entrance length is necessary to allow the full development of intermittent flows. In order to have a negligible coalescence rate of liquid slugs, a minimum length of $L/d = 60$ is suggested in Van Hout et al. (2003). In the present study, the horizontal part ($L/d \approx 500$) is considered sufficient for this purpose.

Moreover, the two-phase flow rates were monitored by the flowmeters and adjusted by the respective valves according to the desired two-phase flow superficial velocities so that slug flow can be observed in the horizontal pipe and hence enter the following riser segment.

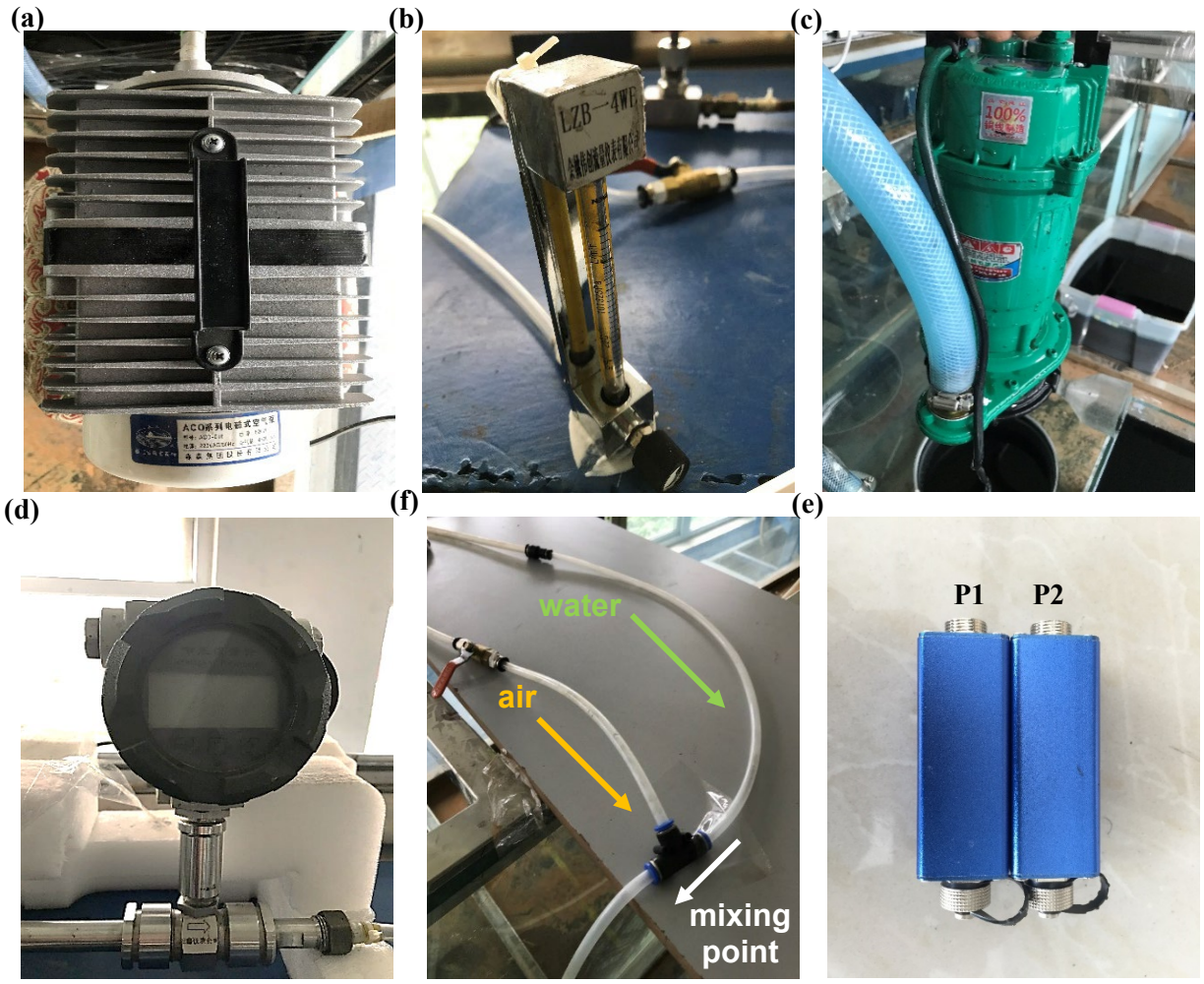


**Figure 6.3:** Key devices along flowlines: (a) air compressor, (b) float flowmeter, (c) water pump, (d) electromagnetic flowmeter, (e) air-water mixing point, (f) pressure transducers.

At the end of the loop, the air-water flows were separated naturally by gravity with discharging the air into the atmosphere and recycling the water in the storage tank. Two pressure transducers (P1 and P2) with an accuracy of 0.1% (Figure 6.3f) were applied at the inlet and outlet of the riser segment, recording local pressure variations and differential pressures.

### 6.2 Data Acquisition

Compared with some widely used methods such as strain gauges (Chaplin et al., 2005; Song et al., 2011; Mohmmed et al., 2019) and accelerometers (Al-Hashimy et al., 2016; Ortiz-Vidal et al., 2017; Liu and Wang, 2018), an optical measurement leads to no changes in the system mass, stiffness and damping due to its non-intrusive feature, which is especially important to the light-weight pipes with a low elasticity in this study. Laser vibrometers, as a viable way of vibration measurement, have also been considered in several FIV investigations (Zhang et al., 2004; Cheng et al., 2006; Qin et al., 2019). However, it only captures pipe dynamics without providing

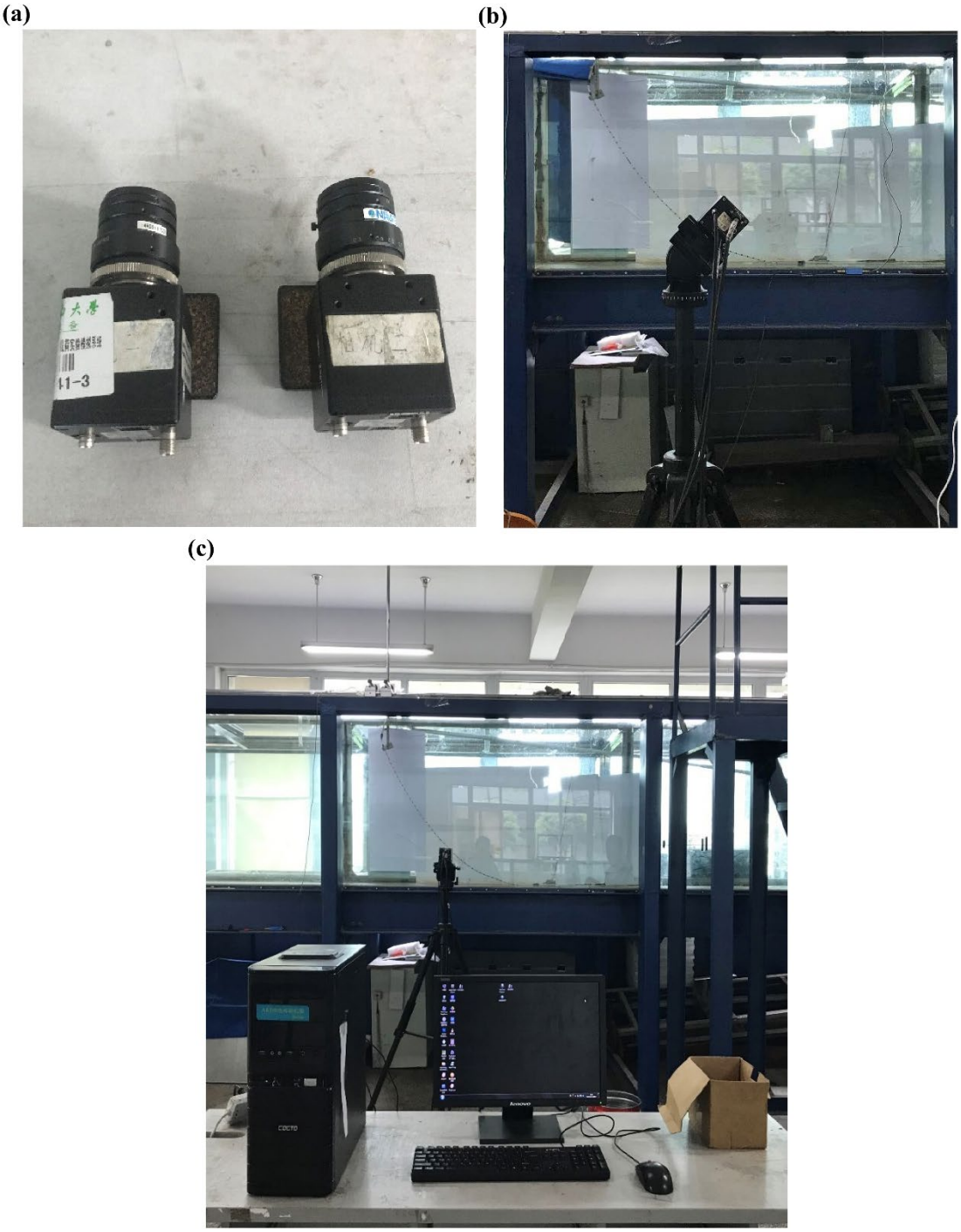


**Figure 6.4:** (a) High-speed cameras, (b) record view in front of the riser segment and (c) operation panel for data acquisition.

information of concerned flow contents. For understanding both pipe and flow behaviours of interests, a technique of digital imaging correlation and tracking was therefore employed in the present experiments to capture both pipe dynamics and internal flow regimes simultaneously in a non-contact manner (Zhu et al., 2018a; Zhu et al., 2018b). Also, detailed and comprehensive dynamic information can be gathered by setting a sufficient number of local tracking points along the concerned testing segment. Herein, such a technique was implemented through two Baumer HXG20 high-speed cameras (Figure 6.4). The cameras (Figure 6.4a) were turned on at

the same time, recording the slug-conveying riser dynamics and monitoring the upcoming slug flows in the horizontal section, respectively. One of them was placed right facing the testing segment and fully fitting the *XOY* view (Figure 6.4b) for capturing planar motions of the pipe, whereas the second one was arranged beneath the horizontal pipe looking into the real-time flow patterns. Also, pressures at the two ends of the riser were obtained simultaneously through the transducers for each considered case. This data acquisition procedure was conducted on an operation panel (Figure 6.4c), where cameras and pressure transducers were controlled by the associated software (Figure 6.5).

**(a)**

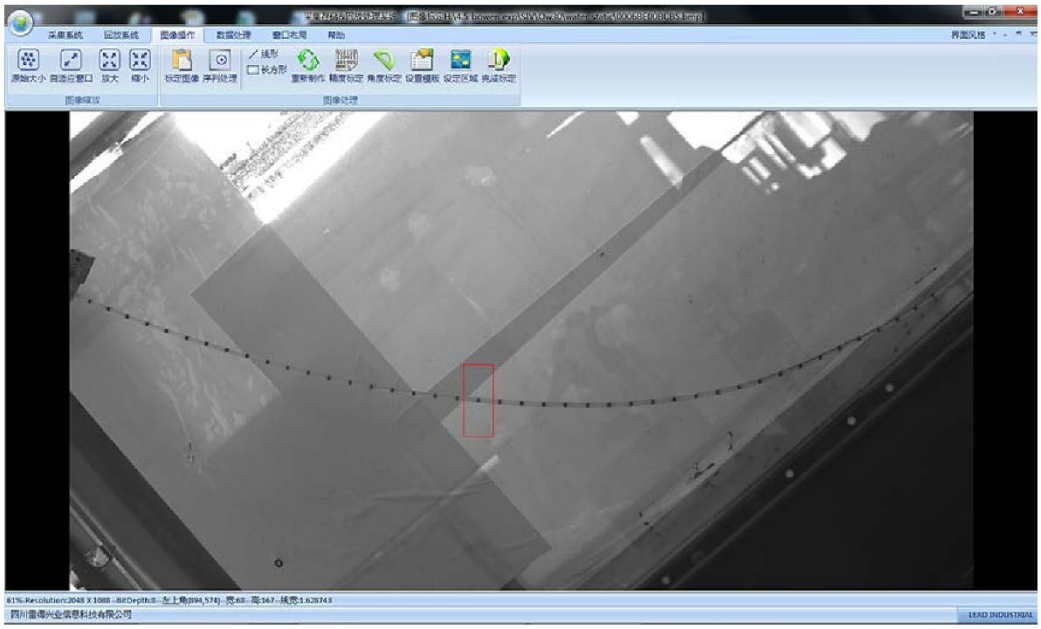

**(b)**

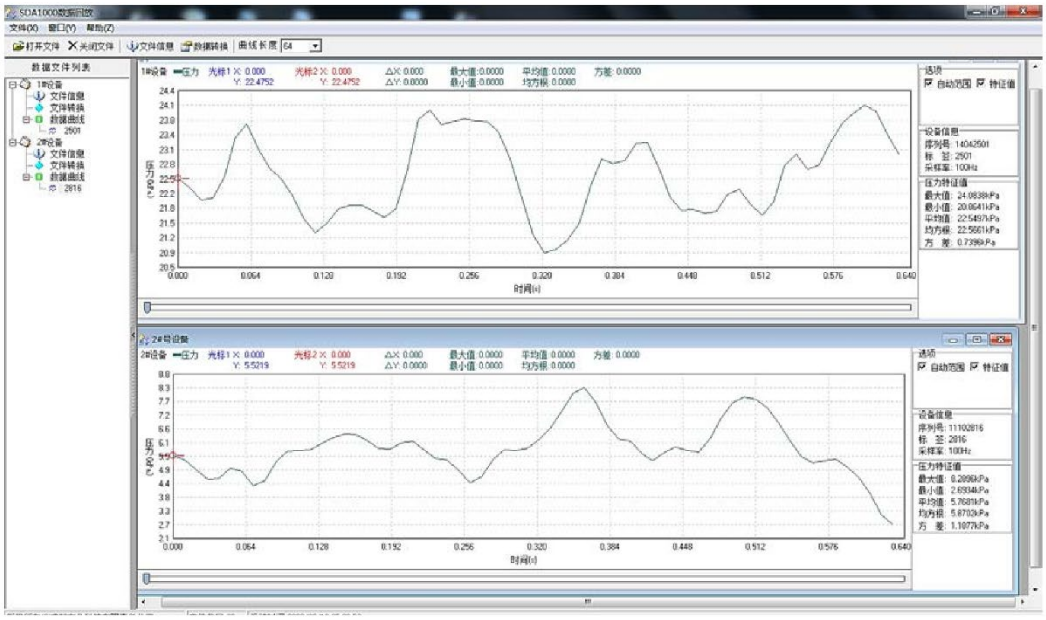

**Figure 6.5:** Software interface for (a) cameras and (b) pressure transducers, respectively.

Since slug flow is characterized by its non-uniform flow pattern of alternative liquid and gas sections, it is necessary to distinguish the air and the water phases due to their similarity in colour and transparency. Hence, the water in the storage tank was dyed into black to get better visibility on liquid slugs. Also, to capture riser responses at different locations, 42 markers (M1 to M42) were made by a black marker pen along the riser segment as illustrated in Figure 6.6. Each marker was 4 mm in length and arranged in a 30 mm centre-to-centre interval with the first and last markers 25 mm away from the associated ends of the riser. The number of markers is considered adequate for acquiring a comprehensive picture of pipe oscillation as well as guaranteeing enough space for visualizing the internal flow contents. Meanwhile, the markers can be regarded as reference coordinates along the arc length for statistically identifying flow characteristics such as the slug length, velocity and frequency.

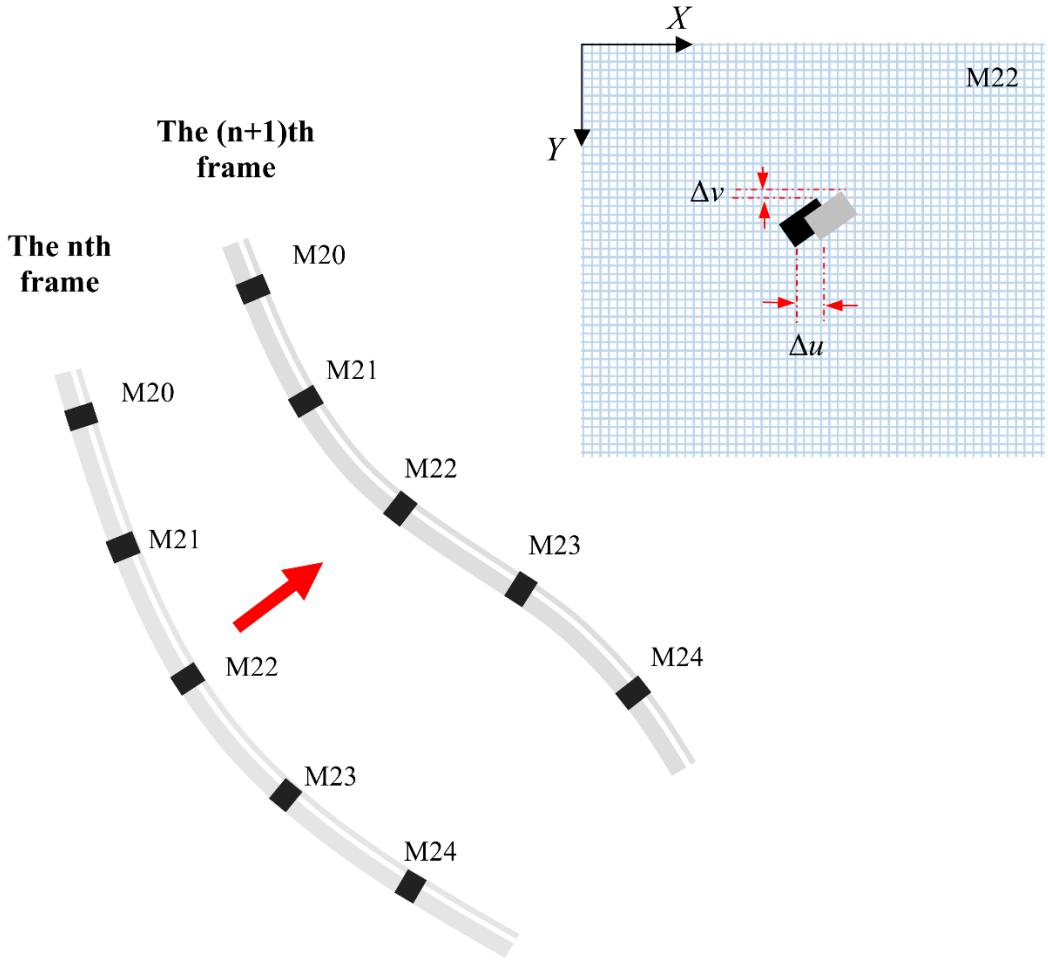


**Figure 6.6:** Illustrative plot of makers and image post-processing process by comparing different frames.

Displacements of various locations along the riser segment were traced by the markers and recorded through the cameras with a resolution of 2048 × 1088 pixels at a sampling frequency of 100 Hz (100 images per second). Before tests, cameras and pressure transducers

were calibrated to ensure the best focus and zero gauge pressure, respectively. Each test was allowed to run for 10 minutes so that the internal two-phase flow can be fully developed and then followed by a data acquisition process for about 80 seconds. Thus, approximate 8000 consecutive frames were stored after a single run, capturing successive motions of the target. To acquire the riser displacements, a static image (Figure 6.5a) was taken prior to tests, used for setting up a frame of reference for the following dynamic process. The direction of gravity was marked via a suspension line and the scale of pixels to actual distance was established by the length between any two neighbouring markers, which corresponds to an actual size of 30 mm. Figure 6.6 also exemplifies the process of how the riser motion was captured and extracted from images. The markers can be identified easily from the images due to the colour difference between them and the pipe. Translational pixel changes between two adjacent frames of each marker (e.g. nth vs. (n+1)th frame for M22) can be obtained in $X$ and $Y$ directions. Then, the pixel variation was converted to the displacements as $\Delta u$ and $\Delta v$. By processing all markers for the whole series of frames, time-varying responses of the riser were achieved.

### 6.3 Free Decay Tests

Free decay tests for the riser filled with air and water were performed to identify natural frequencies and damping of the pipe in both in-plane and out-of-plane directions. Giving the riser a certain amount of initial displacements and then release, the free damped vibration process was recorded. Repeated tests were conducted and the difference was found lower than 0.5%. Figure 6.7 displays response time histories at M15 in different directions with the associated frequency spectra obtained via Fast Fourier Transform (FFT). For the air-filled pipe (Figures 6.7a-c), it is interesting to observe a common frequency ($f_n$ = 1.4 Hz) between the in-plane (Figures 6.7a, b) and out-of-plane (Figure 6.7c) results. This is due to the fact that the planar disturbance imposed on the riser is not perfect which involves out-of-plane effects, and consequently leads to the appearance of the out-of-plane frequency in the in-plane free vibration. Thus, the fundamental in-plane natural frequencies should refer to the pronounced peaks, having $f_n$ = 2.72 Hz for both $X$ and $Y$. Similarly, free decay tests have also been conducted for the riser fully filled with stationary water and displayed in Figures 6.7d-f. Comparing with the air-filled condition, the pipe filled with water presents lower natural frequencies in both in-plane ($f_n$ = 2.52 Hz) and out-of-plane ($f_n$ = 1.33 Hz) directions. It is worth mentioning that the mass ratio of the internal water to the pipe per unit length under the fully-filled condition is 0.766. Such a significant change of system mass together with the internal pressure may be responsible for the decreased natural frequencies, which has been discussed in the numerical studies in Chapters 3 and 5.

Further, the damping ratio ($\xi$) can be calculated by the logarithmic decrement based on the decayed riser amplitudes $\xi = \ln(A_n/A_{n+1})/2\pi$, where $A_n$ and $A_{n+1}$ denotes any two consecutive amplitudes in the time history of riser displacements. $\xi$ was evaluated for different pairs of amplitudes peaks and an averaged value was adopted. Accordingly to the above analysis, natural frequencies and damping ratios of the present riser are summarized in Table 6.2.

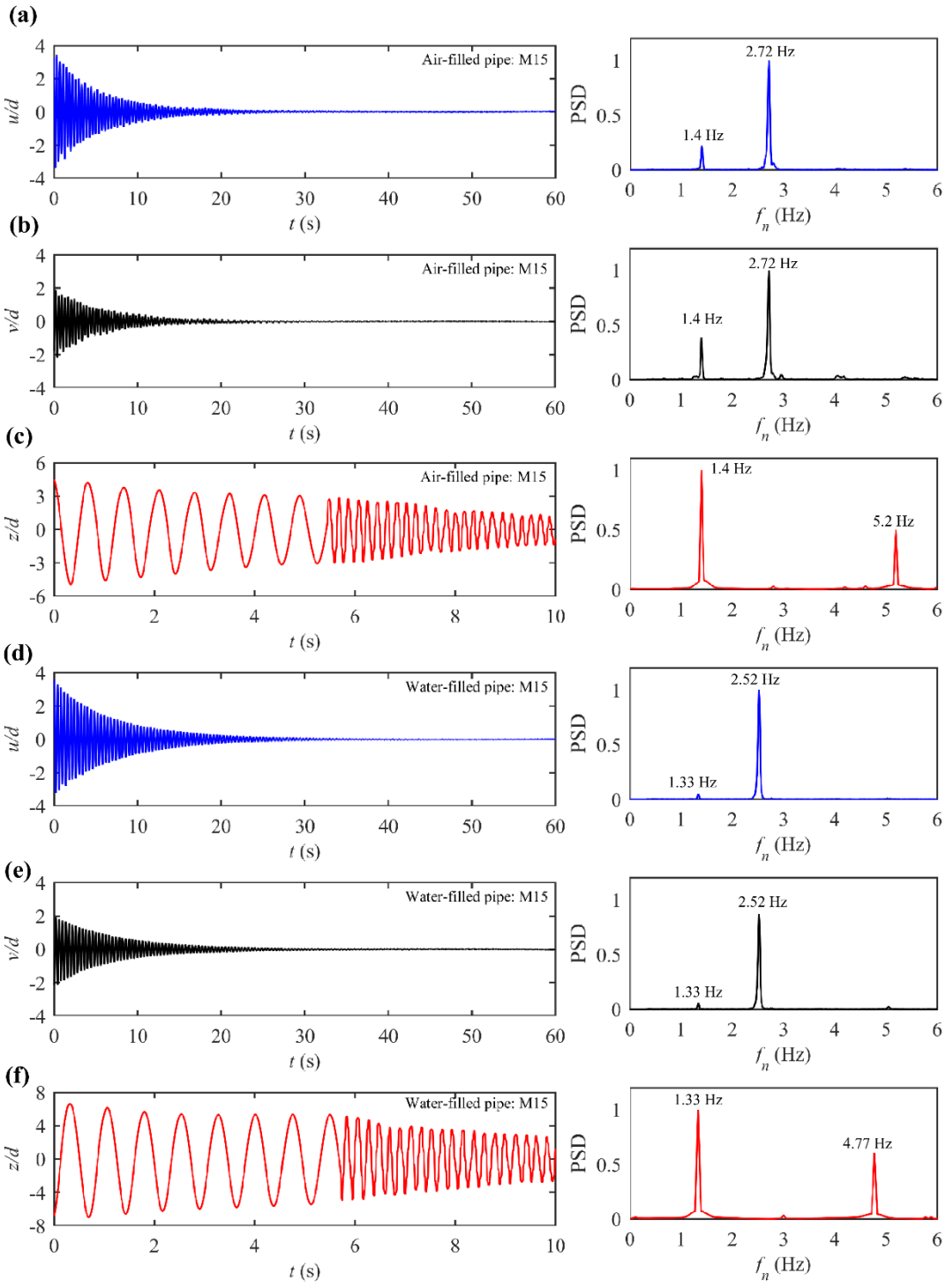


**Figure 6.7:** Time histories and frequency spectra of free decay tests for (a-c) air-filled and (d-f) water-filled riser in ($u$, $v$) in-plane and ($z$) out-of-plane directions.

**Table 6.2:** Natural frequencies and damping ratios of the riser.

| Parameters | Air-filled pipe | | Water-filled pipe | |
|---|---|---|---|---|
| | In-plane | Out-of-plane | In-plane | Out-of-plane |
| Fundamental $f_n$ (Hz) | 2.72 | 1.4 | 2.52 | 1.33 |
| Damping ratio (%) | 0.98 | 0.86 | 0.86 | 0.69 |

### 6.4 SIV Results and Discussion

In the present study, 15 different cases (C1-C15) were considered for SIV tests and listed in Table 6.3. Each case is described by a pair of superficial velocities, which can be achieved through adjusting air and water volumetric flow rates by the respective valves during the tests. The relationship between superficial velocities and flow rates are $u_{ls}= Q_l/A$ and $u_{gs} = Q_g/A$, where $Q_l$ and $Q_g$ denote the water and air flow rates. The below test matrix (Table 6.3) is designed by having three different $u_{ls}$ (0.553, 0.663, 0.774 m/s). For each $u_{ls}$, various $u_{gs}$ are taken so that the gas-liquid ratios ($R_{GL}$) reads $R_{GL}$= 1, 2, 3, 4, and 5, respectively. The effect of gas-liquid ratios has been discussed in Zhu et al. (2018a; 2018b) that it could lead to a variety of slug flows and hence different slug flow-induced behaviours. Compared with their flow conditions, the present tests have relatively larger $u_{ls}$-$u_{gs}$ pairs in a wider $R_{GL}$ range. During the tests, it was observed that slug flow has taken place in the majority of the test cases except for C1, C6, C11 ($R_{GL}$ = 1) and C2, C7, C12 ($R_{GL}$ = 2), where the liquid phase dominates over the gas phase showing negligible and small FIV, respectively.

**Table 6.3:** Test cases with observed FIV and flow patterns.

| Case No. | $u_{ls}$ (m/s) | $u_{gs}$ (m/s) | $R_{GL}$ | Flow pattern | FIV |
|---|---|---|---|---|---|
| C1 | Set 1: 0.553 | 0.553 | 1 | NS | NA |
| C2 | | 1.116 | 2 | NS | NA |
| C3 | | 1.659 | 3 | US | SA |
| C4 | | 2.212 | 4 | US | MA |
| C5 | | 2.765 | 5 | US | LA |
| C6 | Set 2: 0.663 | 0.663 | 1 | NS | NA |
| C7 | | 1.326 | 2 | NS | SA |
| C8 | | 1.989 | 3 | US | SA |
| C9 | | 2.652 | 4 | US | MA |
| C10 | | 3.315 | 5 | US | LA |
| C11 | Set 3: 0.774 | 0.774 | 1 | NS | NA |
| C12 | | 1.548 | 2 | NS | SA |
| C13 | | 2.322 | 3 | US | SA |
| C14 | | 3.096 | 4 | US | MA |
| C15 | | 3.870 | 5 | US | LA |

Note: NS, US denote no-slug and unsteady slug cases, respectively.
NA, SA, MA and LA represent negligible-, small-, moderate- and large-amplitude FIV

The cases of negligible FIV reflect the fact that the riser would remain still when a single-phase flow is transported at a low speed unless pulsation appears (Lee et al., 1995; Gorman, 2000). This is also consistent with features of single-phase FIV problems, where a uniform single-phase flow would not lead to pipe instabilities before reaching critical velocities (Paidoussis, 2014). In this section, the measured and observed experimental results of slug flow-induced riser dynamics as well as slug flow characteristics are reported and discussed.

### *6.4.1 Riser response amplitudes and frequencies*

Converted from the pixel variations, time histories of the riser responses can be achieved at different locations (M1 to M42). To refine the raw data by excluding environmental effects on the measured signals, e.g. noises, a low-pass filter is employed to eliminate irrelevant bands of high frequencies. In the present study, the highest SIV frequency is observed to be less than 6 Hz. To focus on the frequency range of interests (Figure 6.7), all the original data of riser responses are low-pass filtered in the frequency domain with a cutoff at 6 Hz, i.e. removing any frequencies higher than 6 Hz. In this section, SIV in C10 is exemplified owing to its largest responses among all the considered cases.

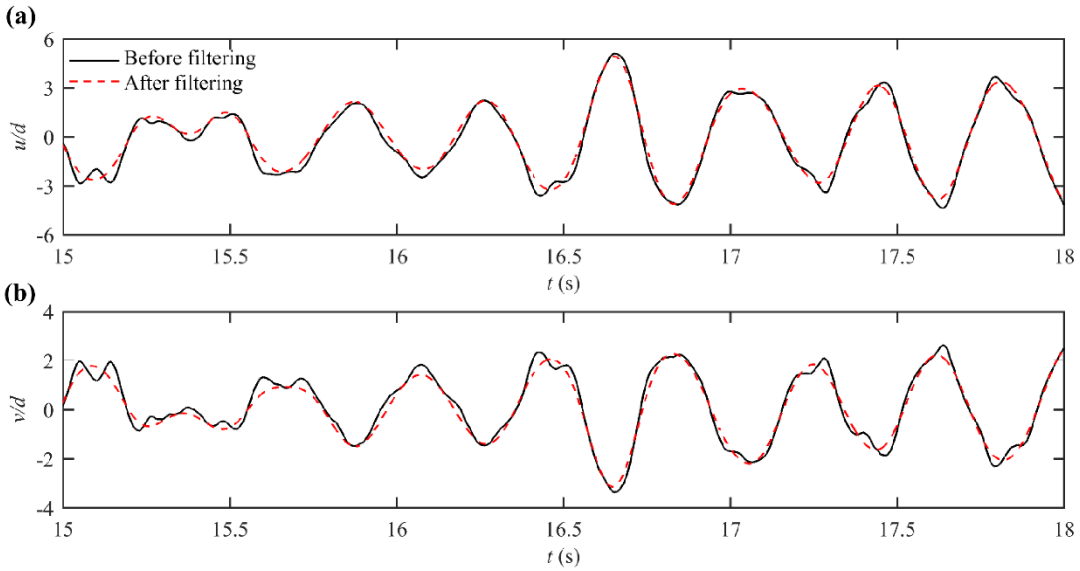


**Figure 6.8:** Time histories of riser responses for (a) *u* and (b) *v* before and after low-pass filtering (case 10).

Figure 6.8 exemplifies the data filtering process by showing riser response time histories at M14 for C10 before and after applying the filter. It can be seen from the comparison that the raw data become smoother with remaining the main vibration pattern when influences of the high-frequency noises are excluded, which would benefit the following analysis of SIV phenomena. Figure 6.9 exhibits planar response envelopes of the riser (solid lines) with the associated RMS values (dashed lines) for C10. It is interesting to observe that the riser responses

generally follow a typical fundamental modal oscillation of a catenary riser. The slug flow leads to larger responses in $X$ than the ones in $Y$. This is dependent on the combined effects of the riser geometry as well as the flow direction at the riser inlet, where the horizontal inlet flow potentially causes significant pipe motion in $X$. The riser vibrates in an asymmetric shape at each instantaneous moment, leading to coupled responses in $X$ and $Y$. However, the oscillation is strongly modulated without intersection points, i.e. the location with zero responses. This implies co-existing modal oscillations despite the fact that the fundamental mode is predominant. Such a multi-mode behaviour can also be confirmed by observing the RMS of riser displacements along the riser span. At the location of the maximum response, the ratios of RMS values to the associated maximum amplitudes are 0.419 and 0.376 in $X$ and $Y$, respectively. Compared with the ratio of 0.707 from a harmonic oscillation with a single frequency, such a significant difference between the maximum and the RMS values may be aroused by the modulated oscillation amplitudes due to a superposition of different modes. Besides, the RMS waveforms do not demonstrate any nodes (i.e. $u_{rms}$= 0, $v_{rms}$= 0) in between the boundaries, consistent with the aforementioned high modulation at the node of intersection. All of these observations imply the occurrence of multi-mode responses.

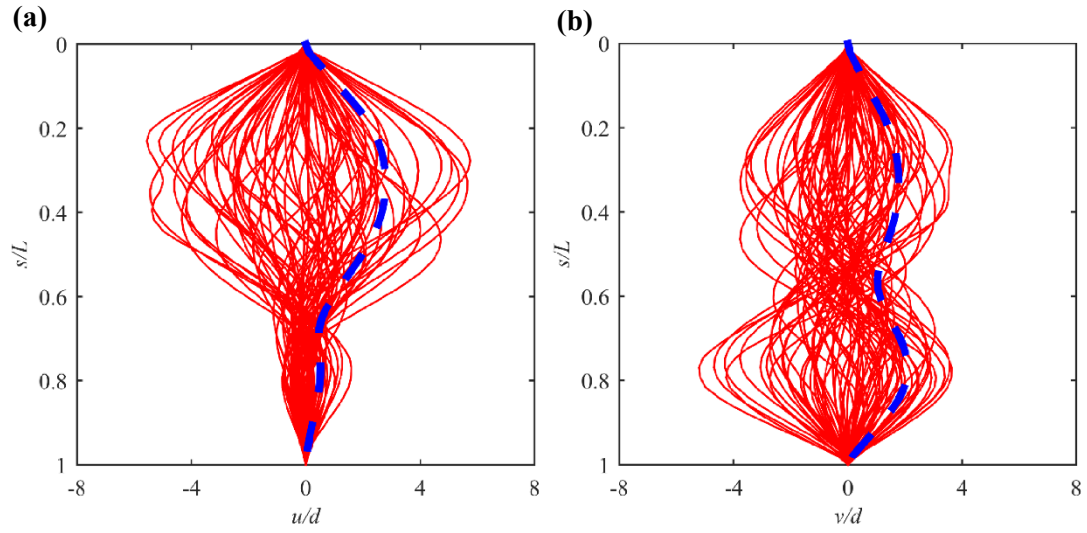


**Figure 6.9:** Time-varying spatial profiles (solid lines) with associated spatial RMS displacements (dashed lines) in (a) $X$ and (b) $Y$ for case 10.

To further visualize SIV, the pipe vibrations of C10 in the time domain at selected locations (M5, M14, M20, M24, M30, M33, M38) are displayed in Figure 6.10. Regardless of the different amplitudes along the pipe, similar oscillation patterns are observed across all locations with synchronized responses between $u$ and $v$. The riser experiences relatively small oscillations around $t$ = 40 s but persistent large ones around $t$ = 60 s for all the consider locations. For instance, the riser motion at M14 has demonstrated quite unsteady oscillations with strong

variations of amplitudes along time, showing maximum and minimum vibrations of 6.6*d* vs. 0.05*d* in *X* and 3.9*d* vs. 0.03*d* in *Y*. Such chaotic vibrations along time has explained the much smaller RMS values than the maxima (Figure 6.9). In fact, the oscillation variability reflects the transient flow characteristics associated with random slug geometries, which will be discussed in the following sections.

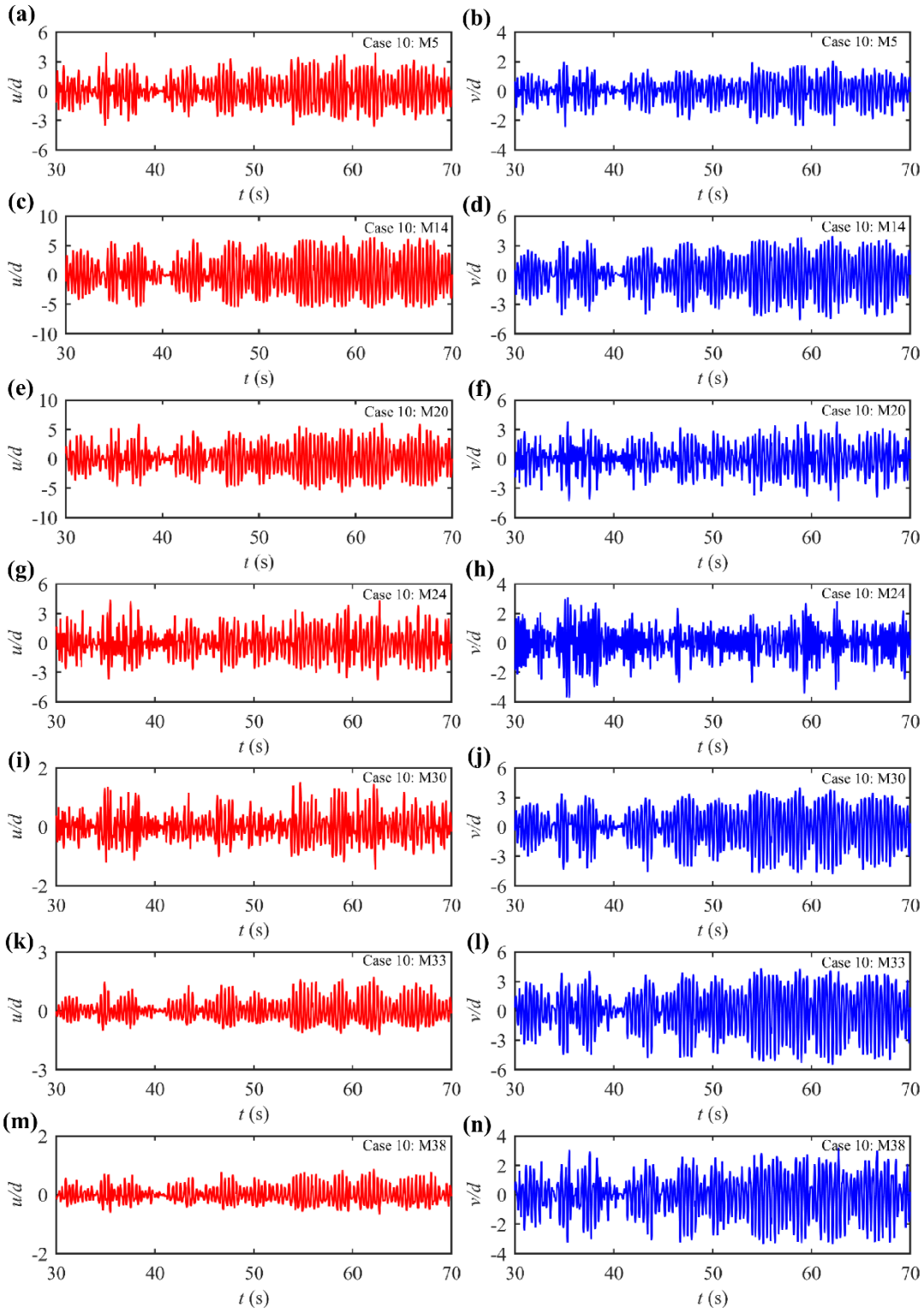


**Figure 6.10:** Time histories of (a, c, e, g, i, k, m) *u* and (b, d, f, h, j, l, n) *v* at different locations of riser for case 10.

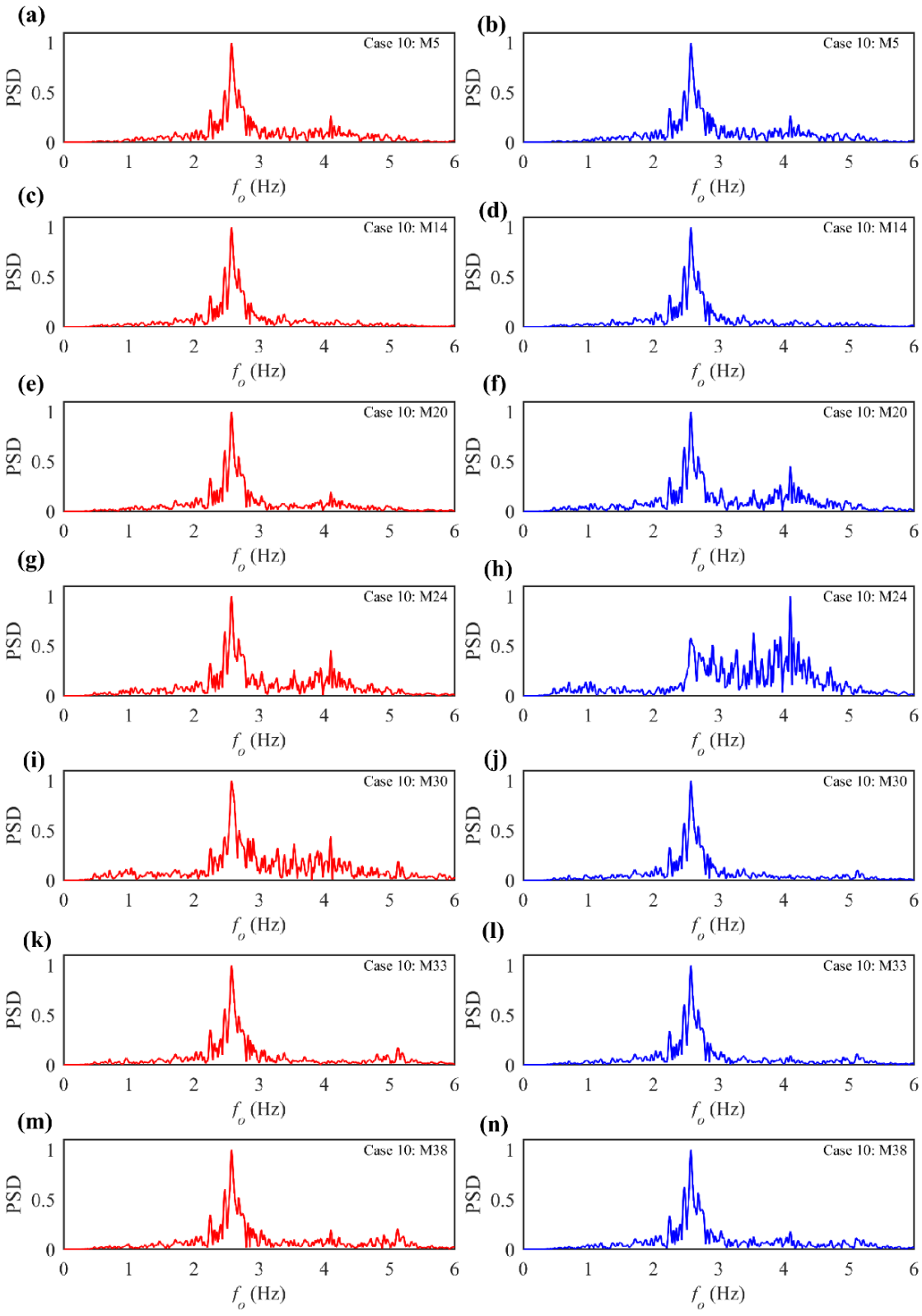


**Figure 6.11:** Frequency spectra associated with the responses in Figure 6.10.

Frequency spectra in association with the riser oscillation (Figure 6.10) are exhibited in Figure 6.11 to identify the system oscillation frequency ($f_o$). The results present a predominant $f_o$ of 2.58 Hz for nearly all the considered locations. It is worth noting that this $f_o$ falls between air-filled (2.72Hz) and water-filled $f_n$ (2.52 Hz) as listed in Table 6.2, indicating the occurrence of resonance at the fundamental mode as well as justifying the fundamental mode oscillation profiles in Figure 6.9. This in-between $f_o$ is expected since slug liquid holdup ranges from 0 to 100%, contributing to additional system mass. Plus, the internal pressures and centrifugal forces would alter pipe stiffness (Sparks, 2007), giving rise to a lower resonance frequency. This experimental observation is in an agreement with the numerical study in Chapters 3 and 5. In addition to the dominant $f_o$, a secondary peak is also noticed by some markers (M5, M20, M24, M30, M38), leading to a higher $f_o$ around 4.1 Hz. The higher $f_o \approx 4.1$ Hz may be related to the eigenmode next to the fundamental one. During the free decay tests, a second frequency peak about 4.4 Hz is observed at some locations (e.g. M32 and M35) of the riser. This value is checked through OrcaFlex (Orcina, 2016) by conducting a static analysis for this catenary pipe. The numerically obtained value of 2$^{nd}$ order natural frequency is about 4.6 Hz (error < 5%). This information justifies that $f_o \approx 4.1$ Hz is associated with the 2$^{nd}$ order eigenmode of the air-filled riser. Based on the discussion in Chapter 3 and Chapter 5, it is reasonable to see a lower value of $f_o$ (4.1 Hz) than the 2$^{nd}$ order natural frequency of the riser (4.4 Hz) due to the combined effect of internal fluid mass and centrifugal forces. Hence, the higher $f_o$ in Figure 6.11h is associated with the 2$^{nd}$ order modal vibration, which may be directly attributed to $f_s$. This aspect will be discussed in Section 6.4.3.

Although the fundamental mode prevails, this higher-order $f_o$ is found more pronounced at intersection points. For example, the frequency contents of M30 (Figure 6.11i) and M24 (Figure 6.11h), representing the intersection points in $X$ and $Y$ (Figure 6.9), show comparable PSD between the main $f_o$ and the secondary one, especially in Figure 6.11h, where the higher-order $f_o$ becomes predominant. This feature may explain the strong modulation around the corresponding location as seen in Figure 6.9, signifying the significant participation of higher modes in SIV. Moreover, it is noticeable to see the neighbouring frequencies around the main $f_o$. In this case, additional peaks always take place at 2.47 Hz and 2.68 Hz accompanying the highest one (2.58 Hz). This may account for the unsteady oscillation as displayed in the time histories of riser responses (Figure 6.10), where the riser vibrates unrepeatably with switching from one $f_o$ to another. Such an oscillation transition may be due to the flow randomness, suggesting strong fluid-structure interactions.

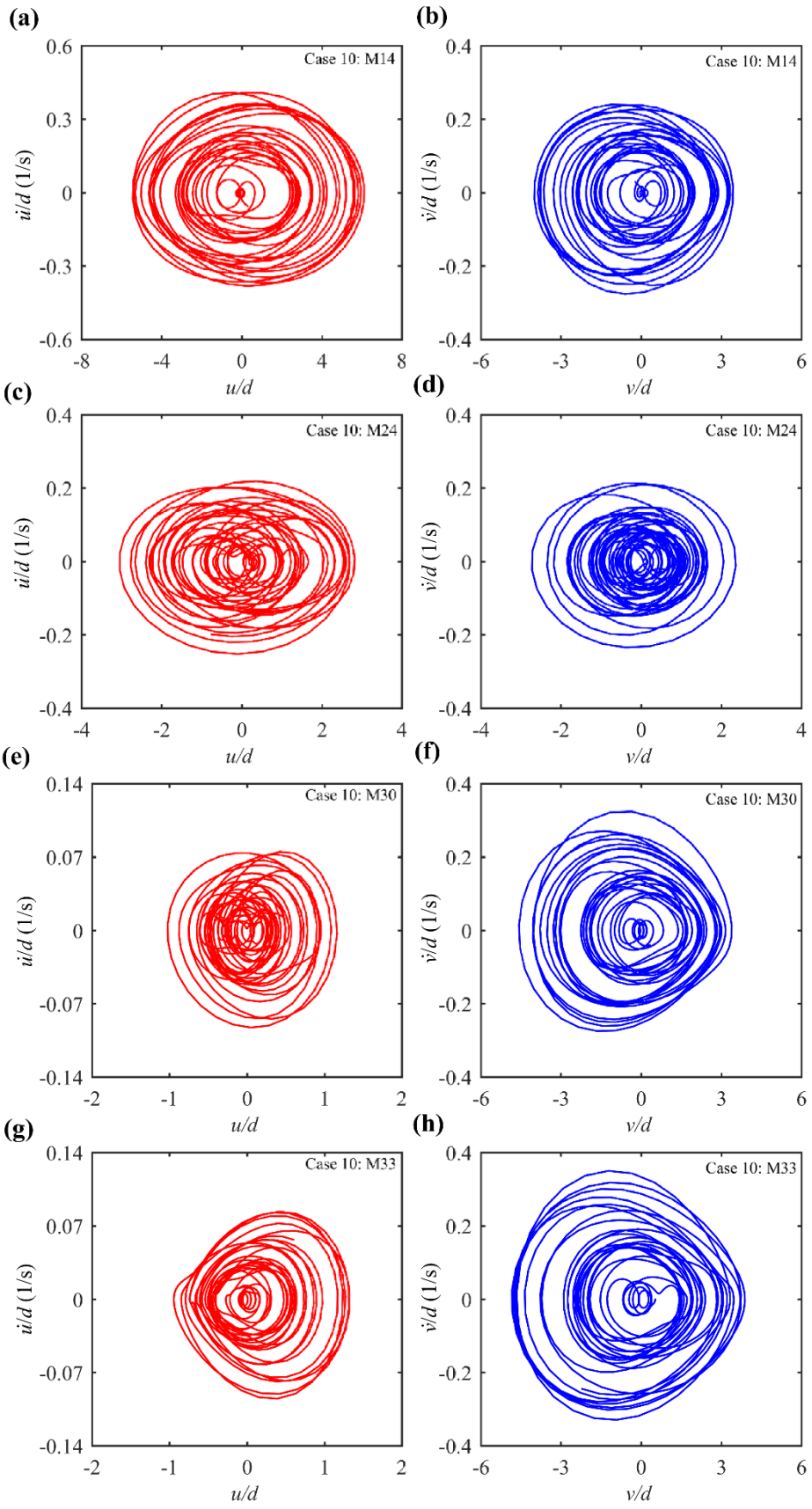


**Figure 6.12:** Phase plane trajectories associated with the responses of M14, M24, M30 and M33 in Figure 6.10.

Some selected phase plane trajectories in $X$ and $Y$ associated with the M14, M24, M30, M33 are illustrated in Figure 6.12. It is observed that all the considered trajectories show complex, aperiodic, and non-repetitive orbits. Strong modulation of the phase portraits are featured in the trajectories with inner and outer ellipses, which are mainly attributed to the unsteady and chaotic riser responses (Figure 6.10). Moreover, evident non-elliptic trajectories within one cycle are realized in the inner area, especially for M24 and M30 (Figures 6.12c, d and e, f). Such peculiar orbits may be due to the multi-frequency behaviour (Figure 6.11) and have also been demonstrated in the numerical study (see Section 3.4.4). The above riser responses are directly driven by the slug flows. To further understand SIV, the slug flow characteristics such as translational velocities and slug lengths, which yields the excitation forces, shall be qualitatively and quantitatively analysed alongside the riser responses.

*6.4.2 Non-uniform slug flow characteristics*

As seen in Section 6.4.1, rather unsteady SIV is observed with a wide range of local amplitudes. For an FSI problem, these phenomena can indirectly reveal the flow status. In this section, detailed flow contents are focused on to characterize the slug flow. Some of the key flow parameters in a strong correlation with SIV are presented with highlighting their corresponding effects on the riser oscillation.

Although different phases may have various velocities, the translational velocity, as one of the most important slug parameters, represents how fast the multiphase flow travels along the channel. Combined with the slug unit length, they could determine the slug frequency as investigated in Chapter 3. For the present experiment, the translational velocity is estimated by recording the travelling duration of a certain slug starting from the riser inlet to outlet. For instance, five consecutive frames ($t_1$-$t_5$) of a slug unit conveyed from the riser bottom to the top are displayed in Figure 6.13. The measurement procedure starts when the front of liquid slug just passes M42 (Figure 6.13a) until its arrival at M1 (Figure 6.13e). Then, $U_t$ can be calculated through the recorded duration and the arc length from M42 to M1 (123.4 cm). In each case, such a process is repeated for five different slug units and an average value is employed. For instance, the estimated $U_t$ of C10 range from 2.33 m/s to 2.47 m/s, which is lower than $u_{gs}$ (3.315 m/s) but higher than $u_{ls}$ (0.663 m/s). This is expected since the liquid phase travels slower than the gas phase, resulting in an intermediate velocity of the two-phase mixture.

As another important parameter, the slug lengths ($L_s$, $L_f$, $L_u$) play important roles in SIV. Different slug unit geometries would give rise to various distributions of slug flow-induced static and hydrodynamic forces along the pipe. For certain $U_t$, it is reported in Chapter 3 that $L_u$ would become predominant in deciding $f_s$ and consequently the pipe vibrations. For C10, the

$U_t$ range is rather small and the slug flow can be considered travelling at a constant speed, which suggests the dominating effects of slug lengths in this case. Thus, the interaction between the fluid and the structure could be analysed through inspecting the slug flow distribution together with the corresponding instant riser vibration.

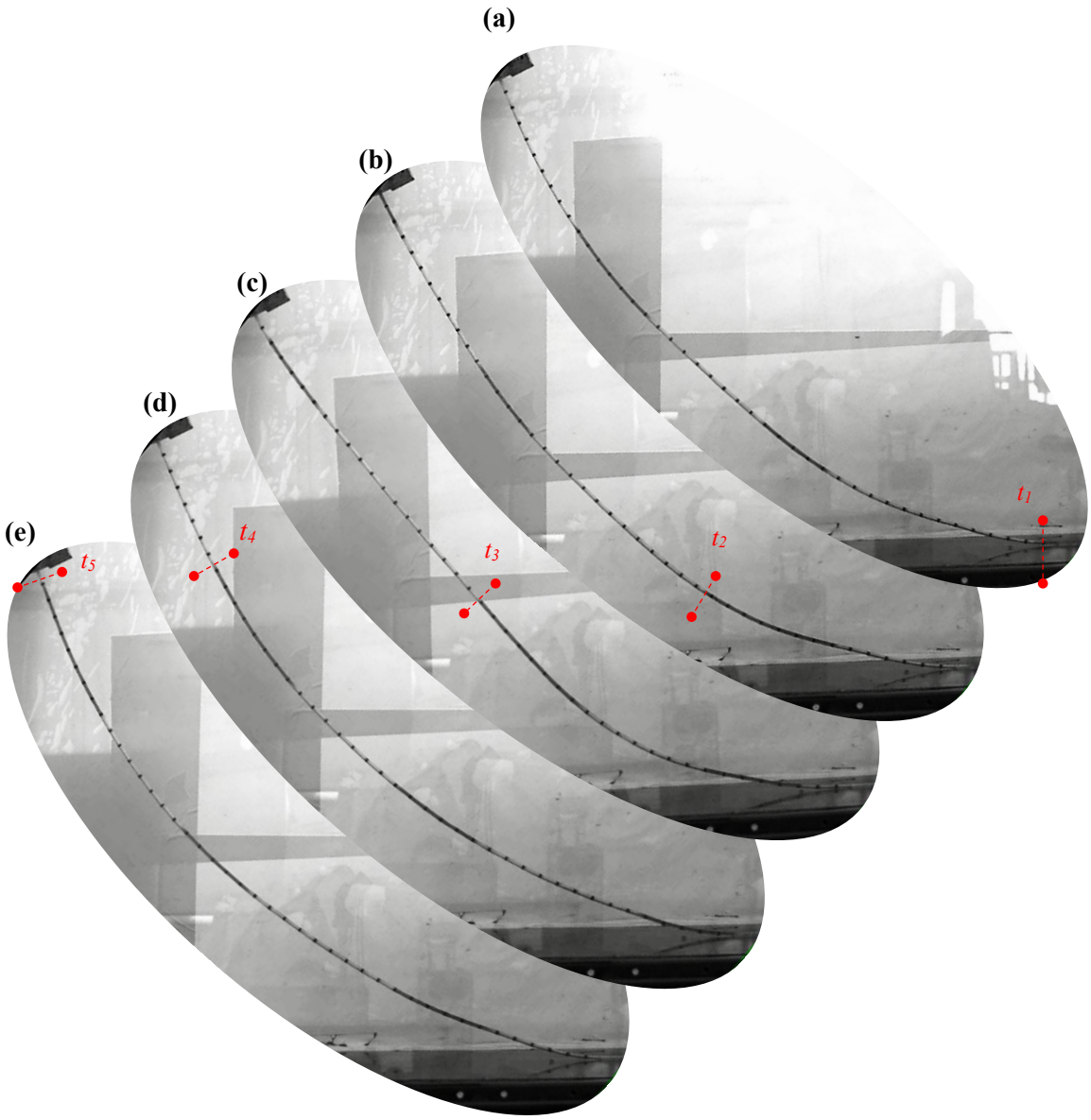


**Figure 6.13:** Illustration of $U_t$ measurement by a slug travelling path in five consecutive frames (a-e) for ($t_1$-$t_5$) in case 10.

Figure 6.14 exhibits the response time histories of M14 (30 s < $t$ < 42 s) with snapshots of flow regimes, in which relatively irregular oscillations take place with modulated amplitudes. Based on the time-varying riser responses (Figure 6.14a), three instant moments are selected (A-A, B-B, C-C) corresponding to the riser displacements of 0.25$d$, 5.6$d$, 0.3$d$ and 0.04d, 3.7$d$,

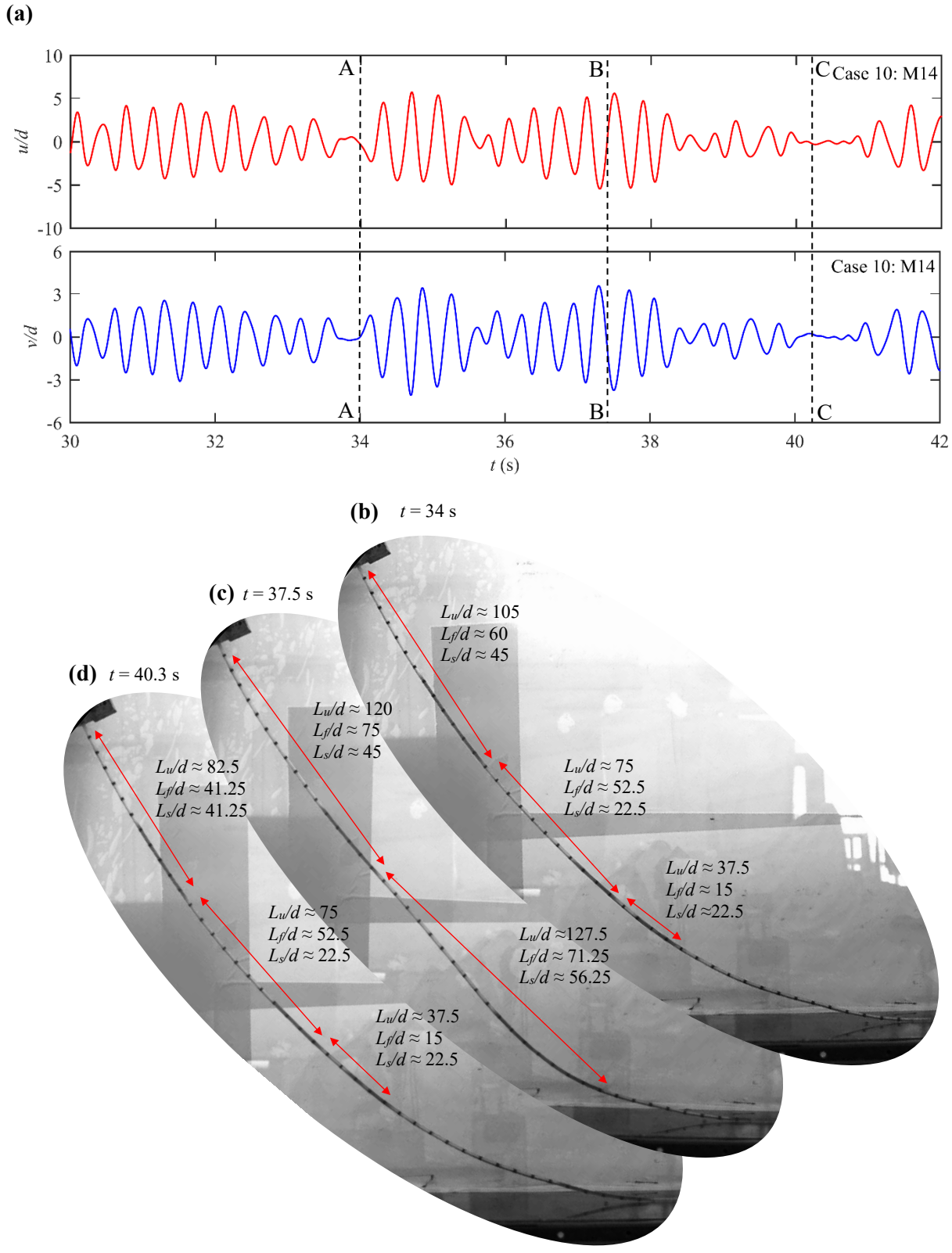


**Figure 6.14:** (a) Selected responses (30 s < $t$ < 42 s) for case 10 and their associated (b-d) flow information at three time instants (A-A: $t$ = 34 s, B-B: $t$ =37.5 s, C-C: $t$ =40.3 s): red arrows highlight slug units in the frames with estimated $L_u$, $L_f$, $L_s$.

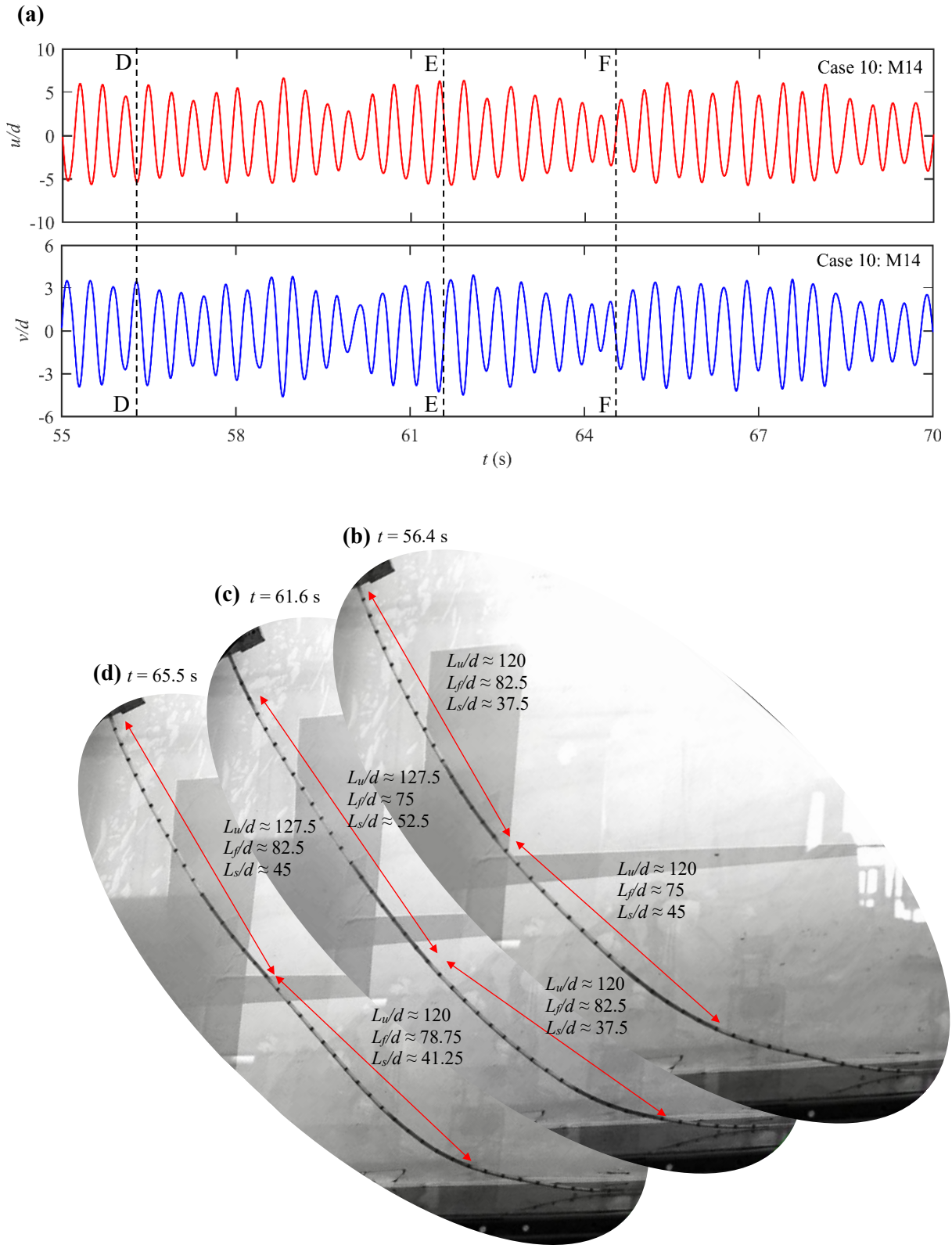


**Figure 6.15:** (a) Selected responses (55 s < $t$ < 70 s) for case 10 and their associated (b-d) flow information at three time instants (D-D: $t$= 56.4 s, E-E: $t$=61.6 s, F-F: $t$=65.5 s): red arrows highlight slug units in the frames with estimated $L_u$, $L_f$, $L_s$.

0.16$d$ at $t$ =34 s, 37.5 s and 40.3 s in $X$ and $Y$, respectively. The associated instantaneous moments of flow information are shown in Figures 6.14b-d. Through inspecting the distinguishable liquid (black) and gas phases (grey) in the frames, $L_u$ can be approximately measured by counting the number of markers contained in each slug unit. As shown in Figures 6.14b, d, three slug units can be identified at $t$ = 34 s and 40.3 s with various $L_u/d$ about 105, 75, 37.5 and 82.5, 75, 37.5, respectively. In contrast, only two slug units but with longer lengths about $L_u/d$ = 120 and 127.5 are observed at $t$ = 37.5 s (Figure 6.14c). These observations indicate the strong flow variability in this region, which may account for the unsteady riser displacements. Further, it shows a clear relationship between $L_u$ and the amplitudes that longer (Figure 6.14c) and shorter (Figures 6.14b, d) $L_u$ tend to cause larger (B-B) and smaller (A-A, C-C) riser displacements. Similarly, the time histories of M14 from $t$ =55 s to $t$ =70 s with the flow regimes at three time instants (section D-D, E-E, F-F) are demonstrated in Figure 6.15. Compared with Figure 6.14a, the riser response amplitudes in this duration are relatively larger and less modulated. The instantaneous flow contents at $t$ = 56.4, 61.6 and 65.5 s are exemplified in Figures 6.15b-d, having $L_u/d$ longer than 120 in all considered moments. Such flow condition may explain the sustainable significant riser vibration shown in Figure 6.15a. For example, two slug units can be seen from Figure 6.15c with about $L_u/d$=127.5 and 120, which are generally larger than the ones in Figures 6.14b-d. This is consistent with the observation in Figure 6.14c vs. Figures 6.14b, d, justifying the responsibility of longer $L_u$ for higher response amplitudes. A similar trend was also reported by Wang et al. (2018) for a horizontal pipe transporting slug flows, showing enhanced SIV due to longer liquid slug lengths. Moreover, by comparing Figures 6.15b-d with Figures 6.14b-d, the former shows relatively more steady slugs, i.e. less differences between consecutive slug units, than the latter, which may account for their different levels of steadiness in the oscillation. Overall, these results further emphasize the important role of slug flow characteristics in directing the riser dynamics.

### *6.4.3 SIV responses under various flow conditions*

To characterize the fundamental effects from slug parameters such as $u_{ls}$ and $u_{gs}$ on riser dynamics, SIV at different $R_{GL}$ will be presented and analysed in this section. Figure 6.16 displays the space-time variations (40 s < $t$ < 70 s) of riser responses in case of C7 (Figures 6.16a, e), C8 (Figures 6.16b, f), C9 (Figures 6.16c, g), C10 (Figures 6.16d, h), which correspond to different $u_{gs}$ from 1.326 m/s to 3.315 m/s and hence $R_{GL}$ = 2, 3, 4, 5, respectively. Inspecting the overall responses, it is seen that the riser experiences the fundamental mode oscillation in all the considered cases, where the vibration patterns clearly exhibit two peaks in standing waves in both $X$ (Figures 6.16a-d) and $Y$ (Figures 6.16e-h). Despite the same $f_o$ of $u$ and $v$, the

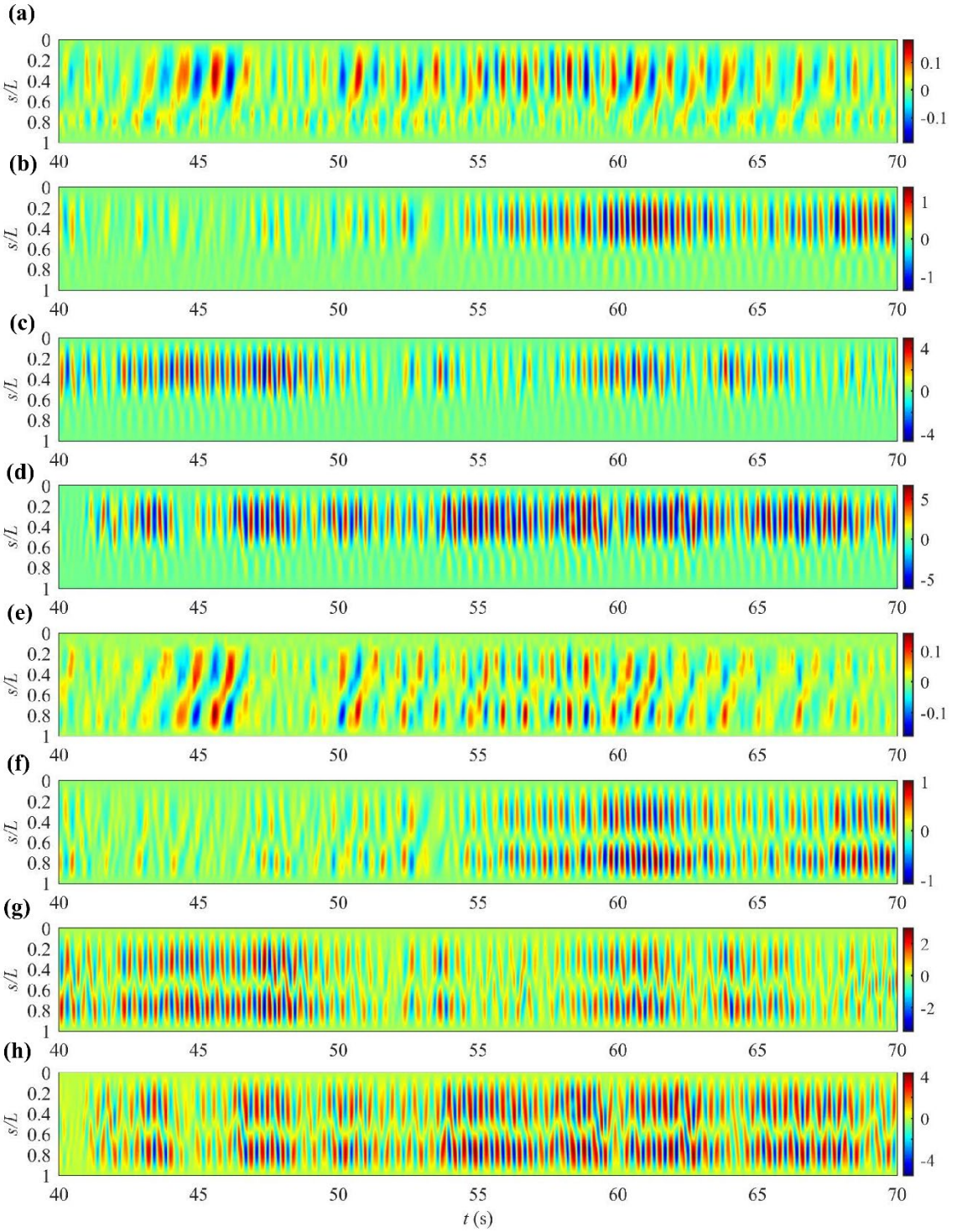


**Figure 6.16:** Space-time varying (a, b, c, d) *u* and (e, f, g, h) *v* of SIV for (a, e) case 7, (b, f) case 8, (c, g) case 9, (d, h) case 10.

response amplitudes in *X* are generally higher than the ones in *Y* for each case. From $R_{GL}$ =2 to 5, FIV become stronger as well as more regular. For instance, the maximum amplitude of C10 (Figures 6.16d, h) is about 6.7*d* (in *X*) and 5.5*d* (in *Y*), while riser can only attain 0.2*d* (in *X* and *Y*) for C7 (Figures 6.16a, e). Also, it is interesting to observe that C7 ($R_{GL}$ =2) seems to oscillate at relatively lower frequencies than the other cases (C8-C10). Regardless of different

amplitudes, Figures 6.16a-h have demonstrated various levels of variability with unsteady responses, switching between large and small vibrations. For example, relatively evident SIV is only observed after $t$ =55 s for C8 (Figures 6.16b, f), whereas C9 (Figures 6.16c, g) presents pronounced dynamics during about 40 s < $t$ <50 s as well as 58 s < $t$ < 66 s. Such intermittent structural behaviours are interrelated with the unsteady flow characteristics as discussed in Section 6.4.2.

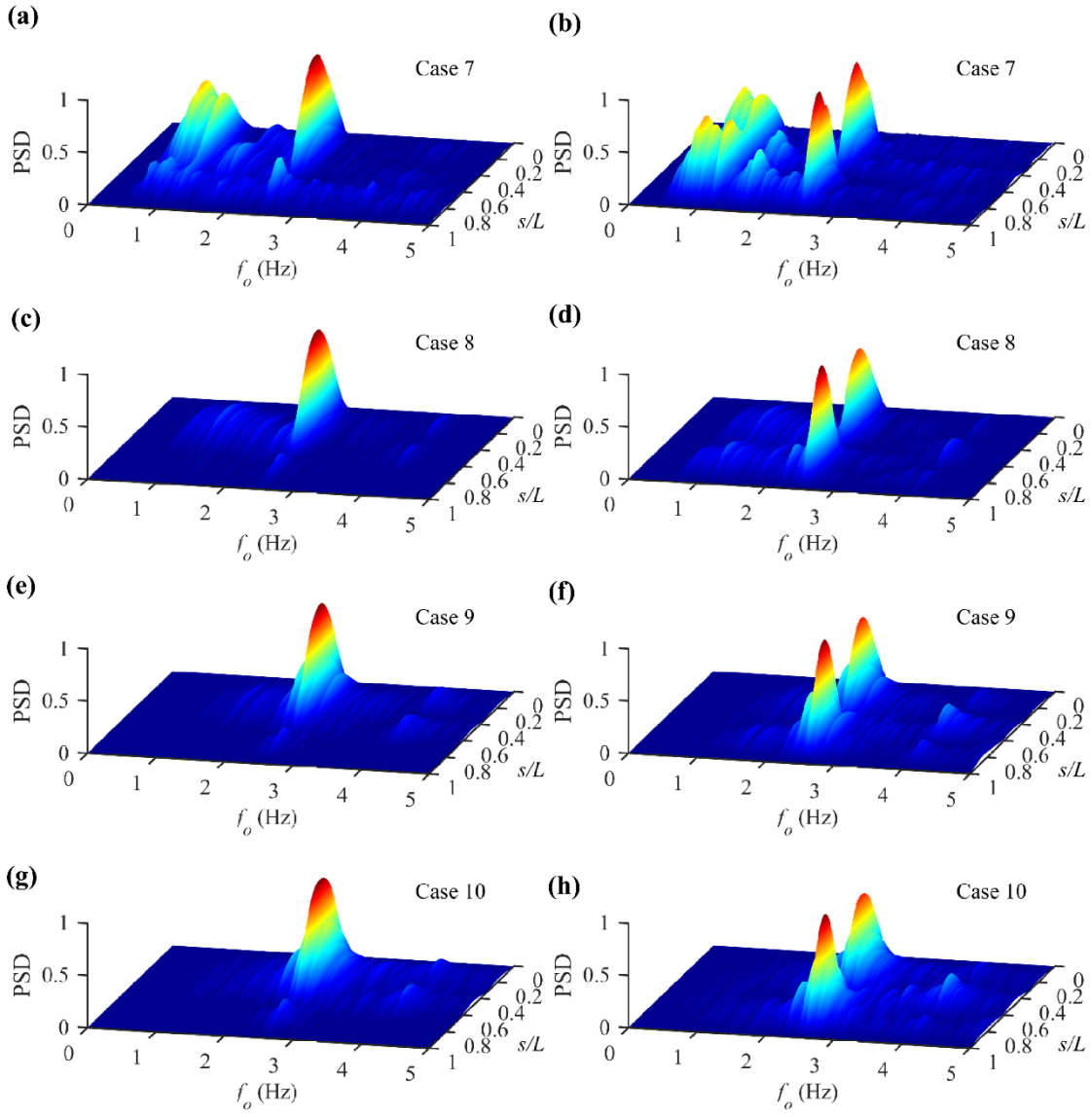


**Figure 6.17:** Spatial profiles of oscillation frequencies associated with responses in Figure 6.16.

In association with Figure 6.16, spatial frequency spectra vs. normalized PSD are demonstrated in Figure 6.17 for both $X$ (Figures 6.17a, c, e, g) and $Y$ directions (Figures 6.17b, d, f, h). It is noted that the main $f_o$ in all the considered cases are around 2.55 Hz, which is lower than $f_n$ of air-filled pipe and close to the water-filled one. Besides, the main $f_o$ increases with $R_{GL}$ from 2 to 5, yielding the frequencies at 2.5, 2.52, 2.56 and 2.58 Hz, respectively. Although

the fundamental mode oscillation is predominant across different cases, distinct frequency components can be remarked. For instance, C7 (Figures 6.17a, b) is quite distinguishable from the others (Figures 6.17c-h), showing a series of $f_o$ with comparable PSD at the lower frequency range to the predominant one ($f_o$= 2.5 Hz). These low frequencies may be due to the imperfect pipe geometry, which induces out-of-plane effects. The co-existing in-plane and out-of-plane oscillations have accounted for the relatively low-frequency oscillation patterns as observed in Figures 6.16a, e. Nevertheless, such out-of-plane SIV is negligible and only observable when the amplitude is less than 0.2$d$.

Similar to the previous analysis on C10 (Figure 6.11), some neighbouring frequencies around the main $f_o$ are also realized in C7-C9. Such concentrated narrowband of response spectra suggest the variability and intermittency of the corresponding slug flow, which induces the irregular oscillation as observed in Figure 6.16. Besides, non-negligible higher harmonics appear in C8, C9 and C10 around 4.1 Hz even though they are much less pronounced than the main peak. These frequency components could bring higher-order responses in SIV, causing additional vibrations. Observing the corresponding space-time responses in $Y$ (Figures 6.16f-h), it can be seen that the large response amplitudes take place around $s/L$ = 0.32 and 0.77, which can be regarded as antinodes in standing waves. However, the oscillations at the node (around $s/L$=0.56) have non-zero values, which is different from a single-mode oscillation. This is attributed to the observed higher harmonics, indicating multi-mode behaviours.

To further visualize SIV, the instantaneous slug distribution for C7-C10 are selected between 60 s < t < 65s, where the significant riser responses appear in all cases (Figure 6.16). Figure 6.18 displays four representative frames with showing detailed slug flow contents for C7-C10, respectively. It is worth noting that the flow pattern in C7 (Figure 6.18a) is distinctive, with only small bubbles entrained inside the liquid phase, i.e. no apparent form of slug flow. Such a flow pattern tends to behave like single-phase or uniform flows, hardly inducing riser oscillation. Thus, the small structural responses in C7 (Figures 6.16a, e) are reasonable. In contrast, evident slug flows are observed in C8, C9 and C10 (Figures 6.18b-d), comprising a series of alternative gas and liquid regions. By comparing $L_u/d$ among those cases, it can be seen that the case with higher $R_{GL}$ generally forms longer $L_u/d$. As for C8-C10, the maximum $L_u/d$ are about 90, 97.5 and 150, separately. In fact, the amplified SIV is led by the combined effects from higher $U_t$-$L_u$, which indicate the interrelationship between flow characteristics and structural dynamics via $R_{GL}$. Furthermore, it can be seen that the liquid slug and bubble regions are various as well. It is true and expected to see longer $L_f$ in case of higher $R_{GL}$ due to the larger $Q_g$. While both $L_u$ and $L_f$ increases with $R_{GL}$, the ratio of $L_f$ to $L_s$ turns to be higher, suggesting

the predominant role of $L_f$ at larger $Q_g$. For instance, as $R_{GL}$ decreases (C10, C9, C8), the length ratio ($L_f/L_s$) associated with the maximum $L_u/d$ are approximately 0.26, 1.17, 1.5. This indicates a trend of convergence to a uniform flow and the riser is almost fully occupied by liquid eventually without elongated bubble sections as shown in Figure 6.18a.

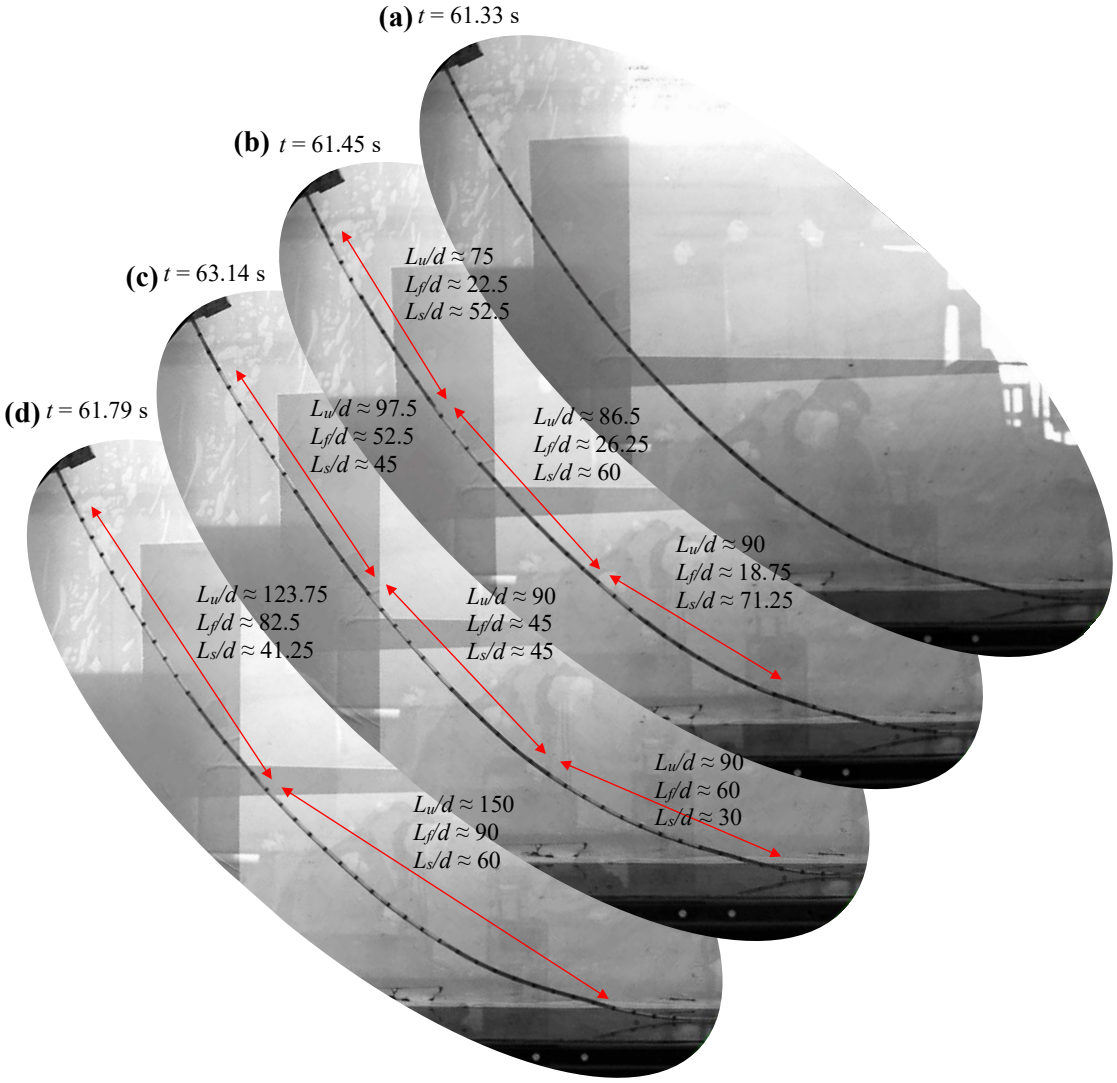


**Figure 6.18:** Representative flow information for (a) case 7, (b) case 8, (c) case 9 and (d) case 10: red arrows highlight slug units in the frames with estimated $L_u$, $L_f$, $L_s$.

For C7-C10, response time histories associated with the locations of spatially maximum RMS oscillations are exhibited in Figure 6.19. It is observed that unsteady oscillations take place in each case. As expected, the pipe in C7 demonstrate small oscillations with a lower $f_o$ than other scenarios (C8-C10). For the cases showing evident slug flows (C8-C10), the chaotic responses seem to have different levels of amplitude modulations, being more significant at lower $R_{GL}$. This may be correlated with the variability of slug lengths as discussed and shown

in Figures 6.14 and 6.15. To address these intermittent FIV behaviours, the riser responses in C7-C10 are analysed and compared through instantaneous frequencies. By performing a wavelet analysis in association with Figure 6.19, the frequency contents are demonstrated as a function of time for 0 s < $t$ < 70 s as shown in Figure 6.20. Overall, it can be seen in C7-C10 that the riser responds at unsteady $f_o$ at all times, illustrating time-varying contents along the time span. In C7, low frequencies (around 1 Hz) with comparable weights to the main $f_o$ (around 2.55 Hz) are captured, explaining the distinct riser responses as shown in Figures 6.19a, b. For C8-C10, it is true that the riser mainly oscillates around 2.55Hz, while other frequencies within a broad band also play roles in SIV and this is rather pronounced in C10. Inspecting Figures 6.20g and h, an obvious deviation from the main $f_o$ can be seen at 25 s < $t$ < 28 s, leading to a gradual variation of dominating $f_o$ approximately from 2.5 Hz to 3.4 Hz. Also, multiple dominating $f_o$ are found around $t$ = 34.5s, where the riser vibrates at 2.4 Hz and 3 Hz simultaneously.

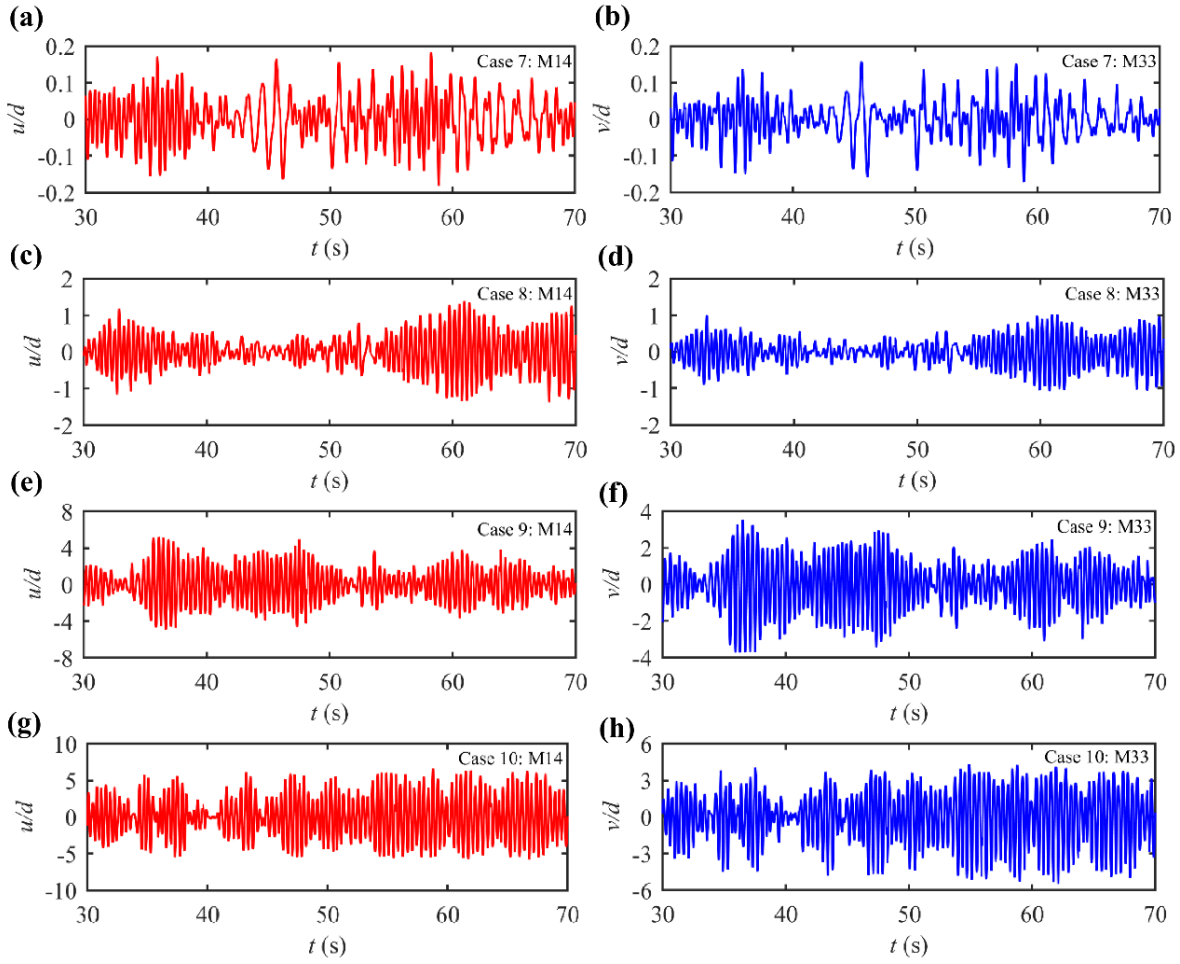


**Figure 6.19:** Response time histories of (a, c, e, g) $u$ and (b, d, f, h) $v$ associated with spatially maximum RMS displacements for (a, b) case 7, (c, d) case 8, (e, f) case 9 and (g, h) case 10.

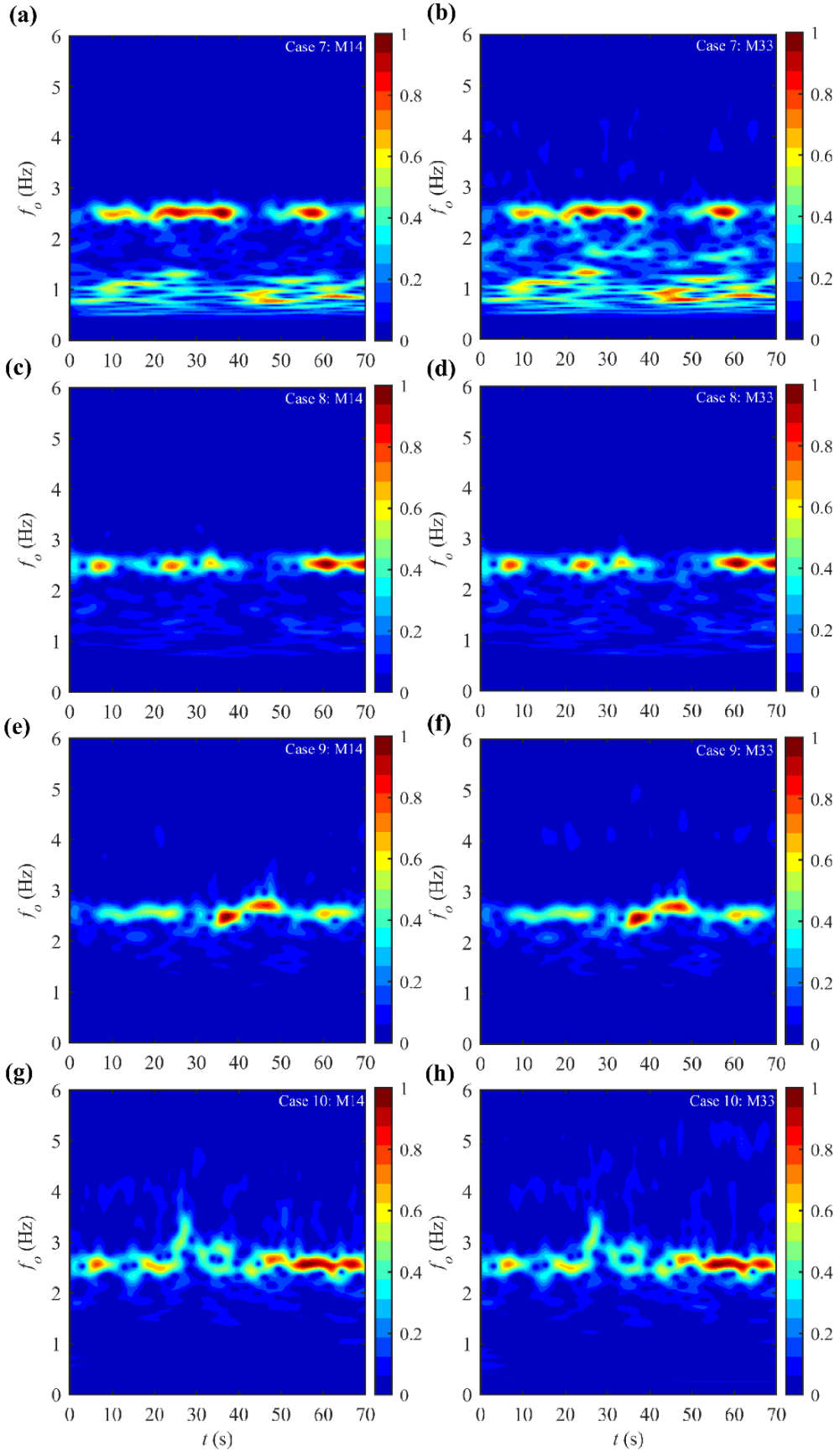


**Figure 6.20:** Wavelet contour plots associated with response time histories in Figure 6.19.

In fact, the contribution from the less significant frequencies, which neighbours the predominant $f_o$, can always be observed in a wide range, e.g. from around 0.8 Hz to 5.5 Hz for M33 in C10 (Figure 6.20h). Besides, the main $f_o$ in C8 seems to be more scattered along the time span than those of C10, where the former only exhibits some beats of the main $f_o$, while the latter shows continuously frequency contents around 2.55Hz. Such difference may verify the various levels of amplitude modulations between Figures 6.19c, d and g, h. These features in the frequency domain have once again supported the discussion in the above sections and reflected the slug flow behaviours with strong variability and intermittency that yield unsteady SIV under different flow conditions. The observed SIV and response frequencies are closely related to the modal loads exerted from slug flows. According to the numerical studies in Chapter 3 and Chapter 5, centrifugal and gravity forces are the main contributors to SIV, which depend on the slug characteristics including liquid holdup, travelling velocity and slug frequency. For the cases with evident slug flows (C8, C9 and C10), the increasing $R_{GL}$ (Table 6.3) potentially lead to larger $U_t$ from C8 to C10 and hence greater centrifugal effect. This can be partially responsible for the pronounced SIV (Figure 6.19) as $u_{gs}$ increases, resulting in the critical case with an amplitude up to 6.7$d$. The strong modal loads consequently lead the riser to vibrate at a persistent governing frequency as shown in Figures 6.20g and h. This may also be related to the long $L_u$, where the more unbalanced flow state gives rise to more pronounced modal loads and consequently enhanced SIV at a clear dominant $f_o$. On the other hand, the slower slug flow tends to result in more modulated SIV as discussed in Chapter 3. Thus, the scattered frequency contents at relatively low $R_{GL}$ (Figures 6.20c, d) may be reasonable. A further analysis based on the slug flow parameters under different flow conditions is carried out in the following.

Figure 6.21 has displayed the comparisons of spatial distribution of RMS responses with different $R_{GL}$ for Set 1, Set 2 and Set 3 (see Table 6.3), respectively. Note that FIV was not observed in C2 so that only three $R_{GL}$ (C3, C4, C5) are considered and displayed in Figures 6.21a, b. For each set, the spatial RMS responses increase with $R_{GL}$ and are predominated by the fundamental mode in both $X$ (Figures 6.21a, c, e) and $Y$ (Figures 6.21b, d, f). This is expected according to the previous discussion regarding C8-C10, where the higher $U_t$-$L_u$ pair is prone to drive more pronounced SIV. Such a consistent trend among different sets of $u_{ls}$ has again confirmed the effects from $R_{GL}$ in SIV with reflecting the significant correlation between the fluid and the structure. Table 6.4 has summarized the flow information as well as the maxima of spatial RMS responses for all the considered cases. Apart from the increasing trend of $u_{rms}$

and $v_{rms}$ with $R_{GL}$ in each set, the variation of oscillation can also be evaluated for a fixed $R_{GL}$, revealing the influences from various $u_{ls}$. For instance, it is evident to see that Set 2 has the

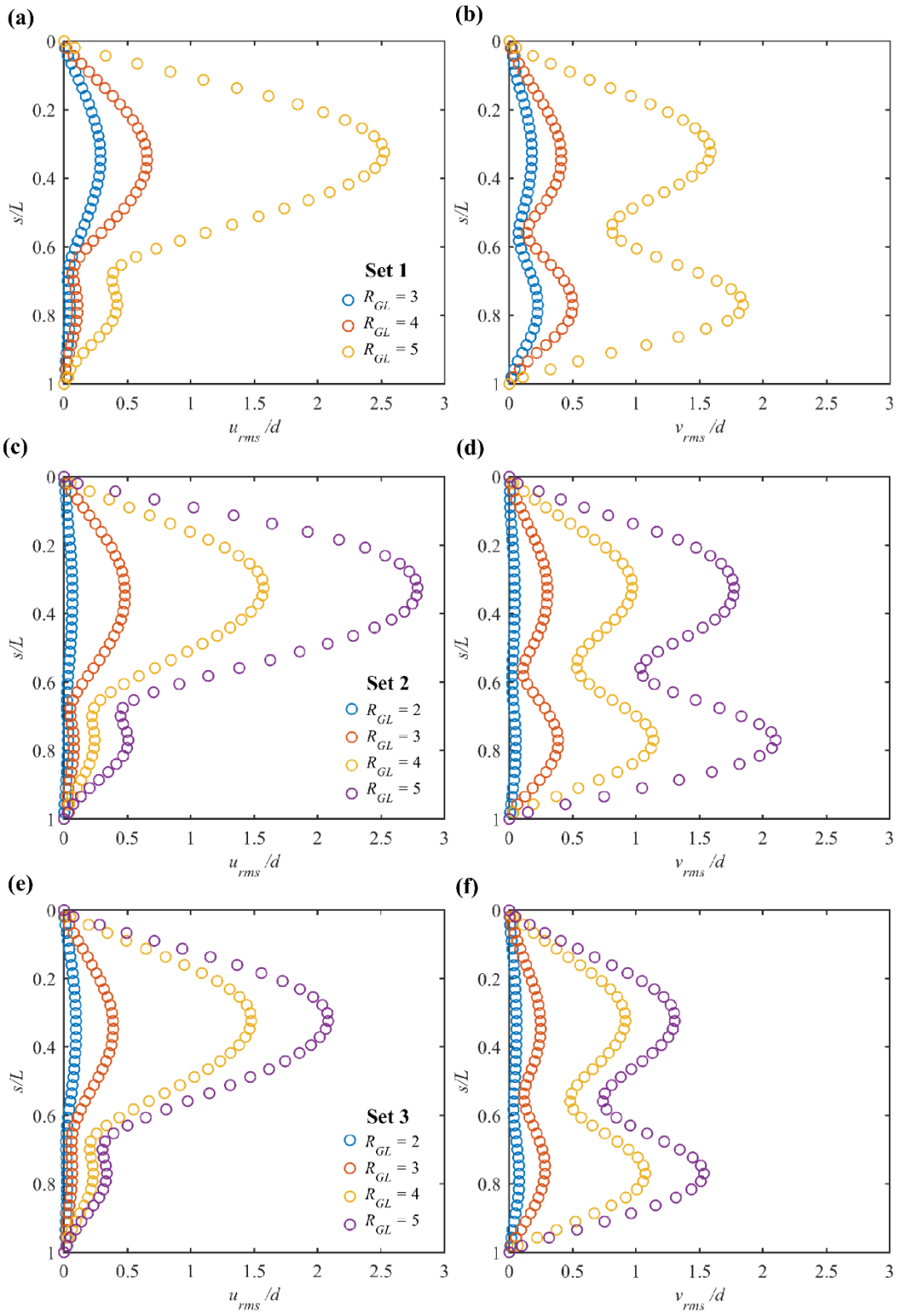


**Figure 6.21:** Spatial distribution of RMS responses for (a, b) case 3-5 in Set 1, (b, d) case 7-10 in Set 2 and (e, f) case 12-15 in Set 3.

largest RMS oscillation amplitudes when comparing with Set 1 and 3 for a fixed $R_{GL}$, representing the worst SIV scenario in the present study. Nevertheless, a wider range of $u_{ls}$ needs to be considered in order to determine its effects on SIV. In addition, flow information has been estimated and demonstrated in Table 6.4 for the cases exhibiting evident slug flow (Table 6.3) through inspecting a number of slug units in different frames.

**Table 6.4:** Summary of key flow characteristics and maxima of riser RMS responses.

| Set | Case | $R_{GL}$ | $U_t$ (m/s) | | $L_f/d$ | | $L_u/d$ | | $f_s$ (Hz) | | $u_{rms}/d$ | $v_{rms}/d$ |
|---|---|---|---|---|---|---|---|---|---|---|---|---|
| | | | Max | Min | Max | Min | Max | Min | Max | Min | | |
| 1 | C1 | 1 | - | - | - | - | - | - | - | - | - | - |
| | C2 | 2 | - | - | - | - | - | - | - | - | - | - |
| | C3 | 3 | 1 | 0.97 | 30 | 7.5 | 71.5 | 30 | 8.21 | 3.46 | 0.286 | 0.224 |
| | C4 | 4 | 1.39 | 1.37 | 56.25 | 15 | 101.25 | 45 | 7.67 | 3.4 | 0.654 | 0.499 |
| | C5 | 5 | 1.97 | 2.05 | 127.5 | 45 | 195 | 90 | 5.61 | 2.58 | 2.523 | 1.843 |
| 2 | C6 | 1 | - | - | - | - | - | - | - | - | - | - |
| | C7 | 2 | - | - | - | - | - | - | - | - | 0.066 | 0.052 |
| | C8 | 3 | 1.29 | 1.26 | 37.5 | 15 | 93.75 | 37.5 | 8.5 | 3.4 | 0.483 | 0.385 |
| | C9 | 4 | 1.96 | 1.87 | 86.25 | 30 | 142.5 | 71.25 | 6.68 | 3.34 | 1.576 | 1.138 |
| | C10 | 5 | 2.47 | 2.33 | 150 | 52.5 | 217.5 | 93.75 | 6.35 | 2.74 | 2.787 | 2.1 |
| 3 | C11 | 1 | - | - | - | - | - | - | - | - | - | - |
| | C12 | 2 | - | - | - | - | - | - | - | - | 0.094 | 0.079 |
| | C13 | 3 | 1.6 | 1.56 | 30 | 15 | 90 | 37.5 | 10.52 | 4.38 | 0.389 | 0.281 |
| | C14 | 4 | 2.24 | 2.16 | 90 | 30 | 150 | 60 | 9.1 | 3.64 | 1.476 | 1.075 |
| | C15 | 5 | 2.32 | 2.2 | 120 | 37.5 | 191.25 | 71.25 | 7.79 | 2.9 | 2.083 | 1.534 |

Overall, $U_t$ is found to be relatively stable within a small range, leading to a good quantitative approximation of the flow speed. From the results, it reasonable to see the increasing $U_t$ with $R_{GL}$, e.g. C5 > C4 > C3 in terms of $U_t$, where higher $u_{gs}$ drives faster slug flow in the riser. On the other hand, for a specific $R_{GL}$, the combination of higher $u_{ls}$ and $u_{gs}$ generally results in higher $U_t$, e.g. C13 > C8 > C3 in terms of $U_t$, although comparable ranges are identified between C10 and C15. In contrast, the slug characteristics in terms of lengths are strongly variable. In each case, $L_f/d$ and $L_u/d$ are observed to have values in wide ranges, which account for the irregular oscillation patterns and the multi-peak frequency domains (Figures 6.16 and 6.17). Nevertheless, the lengths have shown a positive correlation with $U_t$. With increasing $U_t$, $L_f$ seems to get larger and play a predominant part in contributing to a longer $L_u$. It is worth noting that $U_t$ and $L_u$ of C10 are found to be more critical than the ones of other cases, which give rise to the most pronounced SIV in the present study (Figure 6.21). Such an observation also confirms the previous discussion on the modal loads related to $U_t$ and $L_u$. As one of the most important slug parameters, the corresponding ranges of $f_s$ can also be evaluated by knowing $U_t$ and $L_u$, where the average $U_t$ is considered for convenience. Following $L_u$, a

wide range of $f_s$ is found in each case, which may fundamentally be responsible for the irregular SIV and justify the rich dynamics as shown in Figure 6.16. For instance, $f_s$ of C10 range from 2.74 to 6.35 Hz. This may account for the multi-modal SIV observed in Figure 6.11h as well as the time-varying $f_o$ in Figures 6.20g and h. It is noticeable that all the cases in the present study are mainly subject to the vibration at a fundamental mode. However, $f_s$ in some cases do not coincide with the natural frequencies, especially for the ones with lower $R_{GL}$. This may be due to the strong variation of $f_s$ in these cases, where the system is difficult to coincide with any of them, leading to a return at the fundamental mode oscillation. Besides, for the cases with low $R_{GL}$, slug units with short $L_f$ have been observed among the regular ones. The combined slugs may be equivalent to a long slug unit and hence lead to a lower $f_s$ that close to the fundamental natural frequency of the riser. For a given $u_{ls}$, it is seen that the estimated range of $f_s$ tends to be lower with higher $R_{GL}$, e.g. C3 > C4 > C5 in terms of $f_s$. A similar observation was remarked in Mohmmed et al. (2019), where smaller $f_s$ was found at higher $R_{GL}$.

As another key flow information, local pressures at the riser top and bottom are evaluated. Figure 6.22 compares the standard deviation of time-varying pressure ($P_{std}$) and pressure drop ($dP$) between the inlet and the outlet among SIV cases of the three sets. With higher $R_{GL}$, it can be observed that $P_{std}$ at both the riser top and bottom increase in all sets, implying more significant pressure fluctuation with larger $u_{gs}$. The rising $P_{std}$ may be corresponding to the larger $L_f$ and $L_u$, which contribute to the amplified riser responses for higher $R_{GL}$ (Figure 6.21). Besides, there is a noticeable change of trend in C15, where its $P_{std}$ becomes the least one at $R_{GL}$=5. This observation may be associated with the lower $L_u$ as shown in Table 6.4, i.e. C15 < C5 < C10 in terms of $L_u/d$. As for $dP$, it is noticed that Set 1 < Set 2 < Set 3 for a given $R_{GL}$. As analysed in Chapter 3, $dP$ can be due to the combined static and dynamic components corresponding to the gravitational and frictional contribution, respectively. Therefore, the increasing trend from Set 1 to Set 3 may be attributed to higher $U_t$, which is related to the pressure loss due to friction. Also, for larger $R_{GL}$, Set 1 gets smaller $dP$ whereas Set 2 and Set 3 tend to have larger ones. In Set 1, the gravity may predominate over the friction due to its generally lower $U_t$, whereby longer $L_f$ exists in higher $R_{GL}$ and consequently leads to less hydrostatic pressure loss. On the other hand, Set 2 and Set 3, whose $dP$ may be mainly caused by the friction, have larger $dP$ with larger $R_{GL}$ due to the increased $U_t$.

SIV of a catenary pipe with similar riser scales have also been experimentally observed in Zhu et al. (2018a; 2018b). In Zhu et al. (2018b), the flow conditions were set with $u_{ls}$ ranging from 0.436 m/s - 0.796 m/s for 0.5 < $R_{GL}$< 1.826, whereas smaller $u_{ls}$ range of 0.06 m/s - 0.3 m/s with a wider range of $R_{GL}$ up to10 was applied in Zhu et al. (2018a). In contrast, the current

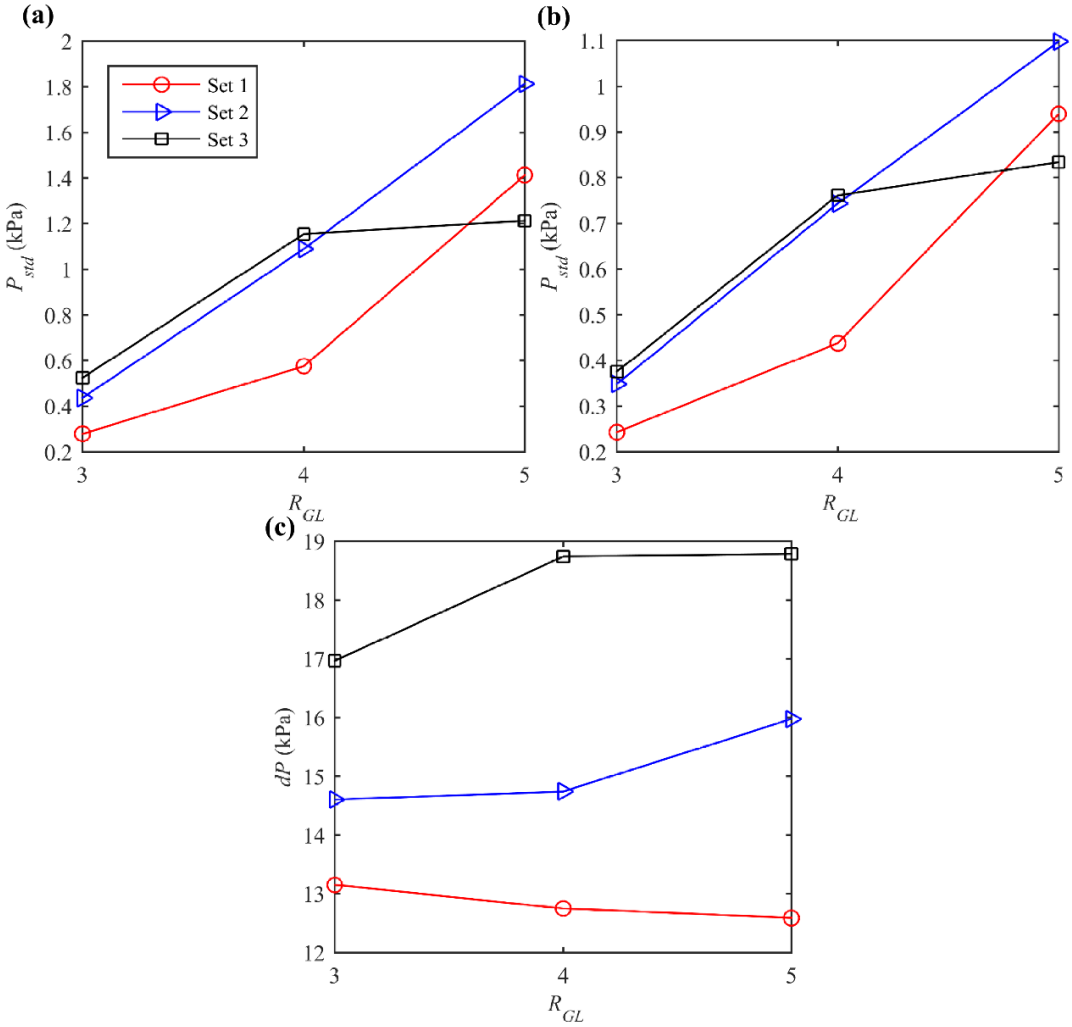


**Figure 6.22:** $P_{std}$ of (a) riser top and (b) bottom and (c) $dP$ associated for Set 1-3 at $R_{GL}$ = 3-5.

study focuses on relatively larger $u_{ls}$ than the latter and wider $R_{GL}$ than the former. Although quite different flow conditions are considered, some common SIV phenomena can be found between these two studies and the present experiment. For instance, they remarked that the slug flow mainly leads to in-plane SIV with greater vibrations in $X$ than $Y$, while the out-of-plane pipe motion is found negligible.These observations are also true herein. Besides, regardless of the various flow conditions, SIV seem to be dominated by the fundamental mode with strong modulations of amplitudes and non-zero displacements at the nodes across all the three works, which indicates the participation of multiple modes in the vibrations. Similar to the observations in the present tests and the discussion in Figures 6.14 and 6.15, the correlation between slug lengths and oscillation amplitudes were also addressed in Zhu et al. (2018a; 2018b), where longer liquid slugs are deemed responsible for more pronounced SIV. The important roles of $R_{GL}$ were highlighted in these two studies in which a high $R_{GL}$ generally results in pronounced SIV. Similarly, such a trend has been revealed in the present study as illustrated in Figure 6.21. Nevertheless, it is found in this study uniquely that evident slug flows are only detected in case

of $R_{GL} > 2$ with much longer slug lengths than those works, which in turn excite more significant SIV with amplitudes up to 6.7$d$ depending on the flow conditions. Moreover, only unsteady slug flows are found herein rather than other slug flow types, i.e. severe slugging, as reported in Zhu et al. (2018a), whilst various levels of unsteadiness are observed under different $R_{GL}$. In summary, some key aspects of those works and this study are listed in Table 6.5.

**Table 6.5:** Comparison of key experimental setups and SIV aspects between different studies.

| Key aspects | This study | Zhu et al. (2018b) | Zhu et al. (2018a) |
|---|---|---|---|
| $d$ (mm), $D$ (mm), $L/D$ | 4, 6, 213 | 4, 6, 158 | 8, 10, 134 |
| $u_{ls}$ (m/s) | 0.553-0.774 | 0.436-0.796 | 0.06-0.3 |
| $u_{gs}$ (m/s) | 0.553-3.87 | 0.398-0.796 | 0.1-0.6 |
| $R_{GL}$ | 1-5 | 0.5-1.826 | 0.333-10 |
| Flow regime | Unsteady slug flow; Uniform flow; | Unsteady slug flow | Severe slugging; Unsteady slug flow; Steady slug flow |
| $L_s/d$ | 22.5-72.5 | 15-60 | 6.8-52.5 |
| Out-of-plane SIV | Negligible | Negligible | Negligible |
| Dominant mode | fundamental | fundamental | fundamental |
| In-plane maximum $u_{rms}/d$, $v_{rms}/d$ | 2.79, 2.1 | 0.41, 0.27 | 1.1, 0.78 |

## 6.5 Experimental vs. Numerical Results

To further verify the numerical model as proposed in Chapter 3, numerical simulations are conducted for C5, C10, C15, corresponding to the limiting case with the most significant riser responses in Set 1, Set 2 and Set 3, respectively. The riser geometry is calculated based on Table 6.1 with adopting the measured slug characteristics including the translational velocities and slug flow lengths as empirical inputs. Since it is revealed that the most severe SIV is accompanied by the greatest $L_u$, extreme flow conditions are considered herein by having the $L_u/d$ = 195 for C5, 217.5 for C10 and 191.25 for C15. In the static analysis, the comparable riser static geometry, sag-to-span ratio and natural frequency to the measured ones (Tables 6.1 and 6.2) with differences less than 3% are yielded through adjusting the top effective tension. As for the dynamic simulation of the riser with fixed ends, a time step of 0.001 s and an element size of 0.01 m are applied for a simulation time of 100 s, which is found to provide a convergence of steady-state simulation results. As for the slug model, a spatial step of 0.0001m is considered sufficient for capturing the full information of slug profiles.

Figures 6.23-6.25 have displayed respective comparisons between numerical and experimental results for C5, C10, C15 via space-time response variations and time histories of

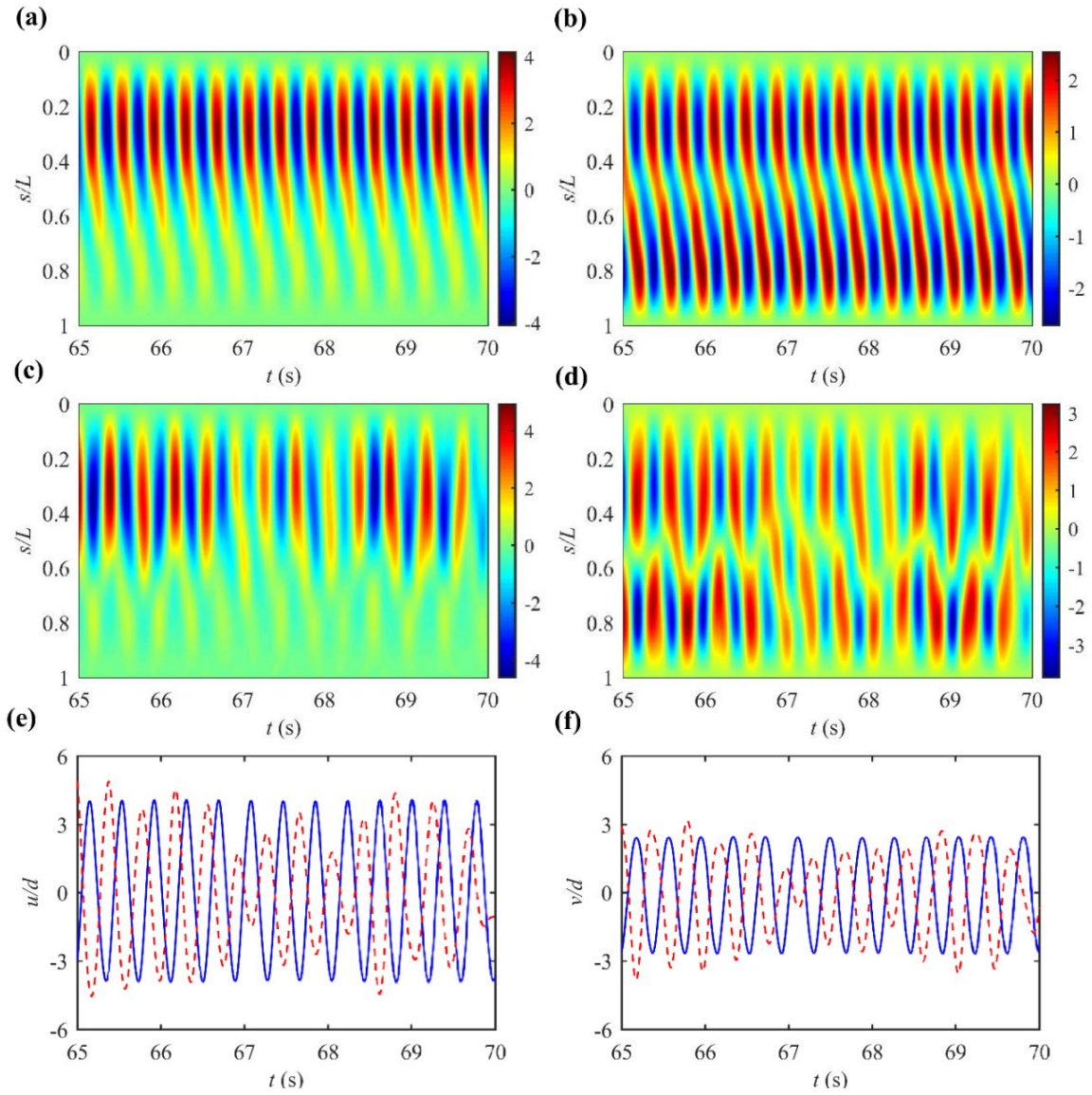


**Figure 6.23:** Comparison between (a, b) simulation and (c, d) experimental results (C5) via space-time varying responses and time-history displacements in (a, c, e) *X* and (b, d, f) *Y*: blue solid and red dashed lines denote results from model and experiment, respectively.

riser responses associated with the spatially maximum RMS oscillations. In the case of C5, similar vibration patterns can be found between the theoretical (Figures 6.23a, b) and experimental (Figures 6.23c, d) results, clearly presenting two peaks along the riser span. This implies that the predominant mode has been accurately predicted by the present model. Besides, non-zero values at the nodes as shown in the experimental results are also numerically captured, indicating the participation of multiple modes. Nevertheless, it is observed that numerical results illustrate more regular responses than the measured ones. Such a discrepancy is expected since the present model considers uniform slug flows, i.e. a constant slug length, which consequently result in relatively steady riser dynamics, while irregular SIV was observed taking place in the experiments due to the strong variability of the slug flow characteristics (Table 6.4).

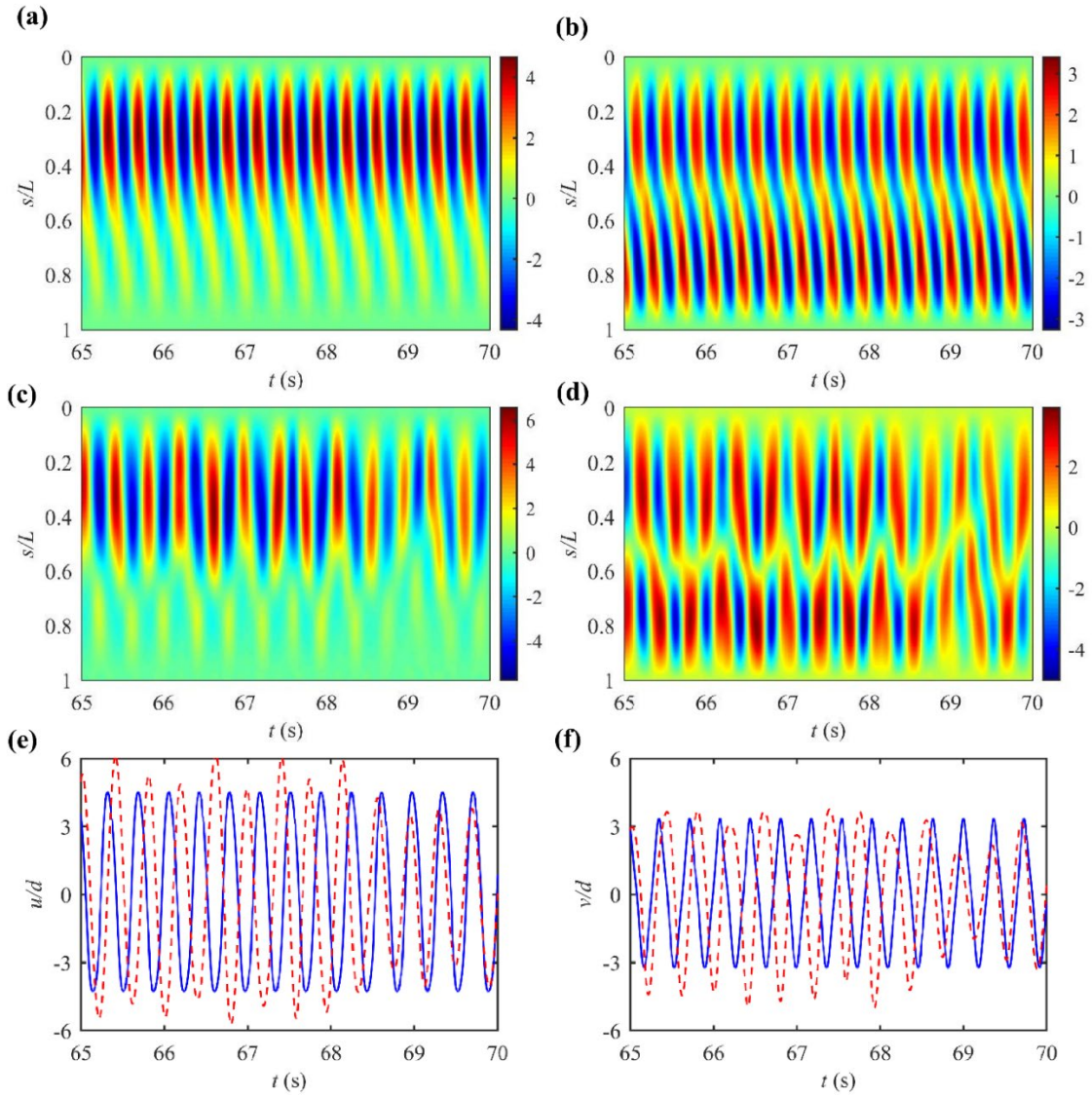


**Figure 6.24:** Comparison between (a, b) simulation and (c, d) experimental results (C10) via space-time varying responses and time-history displacements in (a, c, e) *X* and (b, d, f) *Y*: blue solid and red dashed lines denote results from model and experiment, respectively.

Further, SIV time histories are exhibited in Figures 6.23e, f to provide a closer inspection on the numerical prediction vs. experimental measurement. According to the aforementioned uniform vs. non-uniform slug flows, it is reasonable to see that the riser oscillates unsteadily with strongly modulated amplitudes during the test, whereas the predicted responses turn to be quite steady with time-invariant amplitudes. Nonetheless, it is true that the numerical simulation seems to match well with the experiment, where the modulated SIV amplitudes of the latter varies around those of the former. Besides, within the considered period of time (65 s < $t$ < 70 s), comparable oscillation cycles, i.e. 12 vs. 13 cycles, between the test and the simulation are revealed. In the case of C10 (Figure 6.24), similar conclusions of prediction vs. experimental observations to C5 can be made in terms of the mode order, oscillation pattern, response amplitude and frequency. However, although the time history responses are comparable

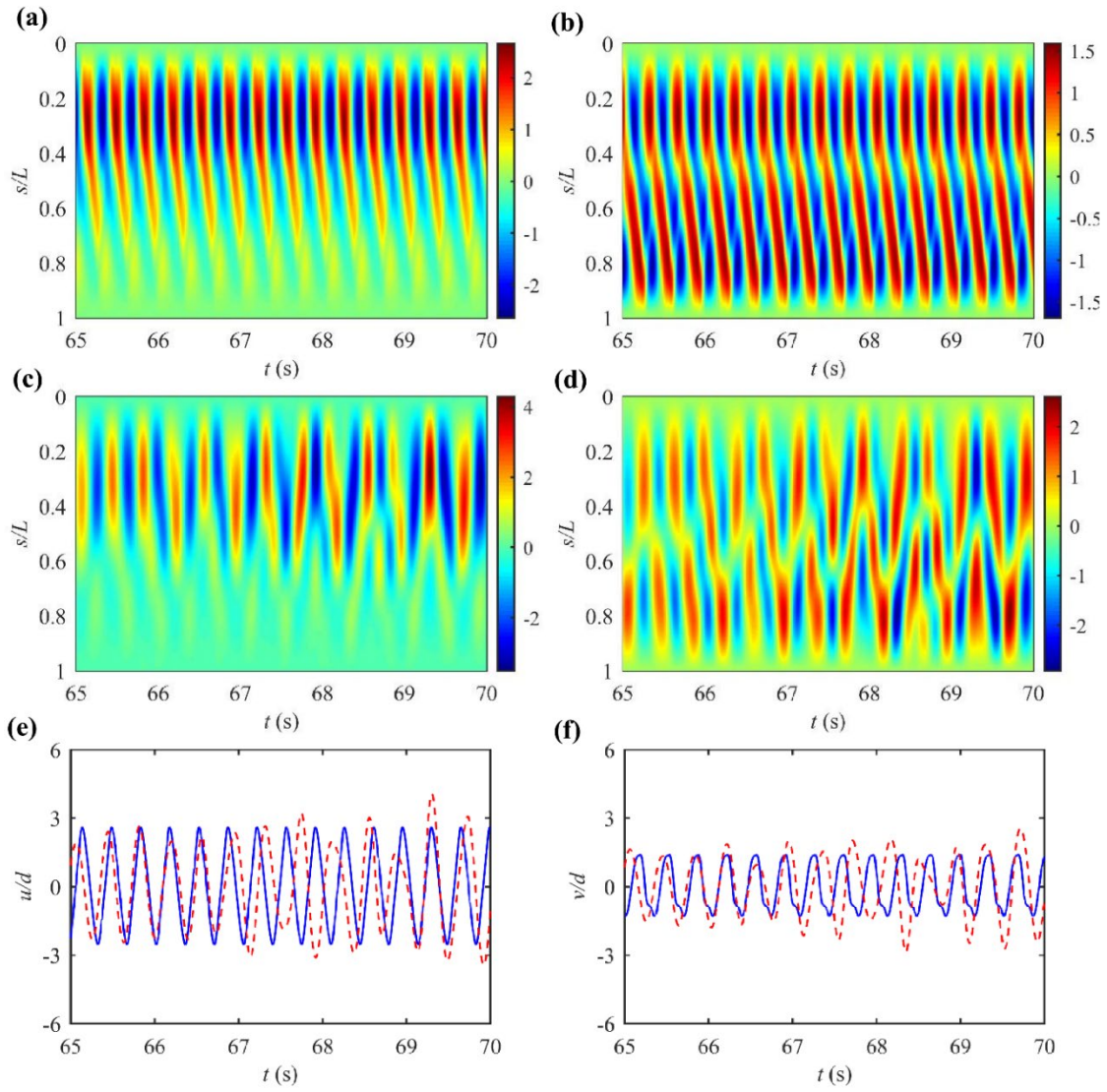


**Figure 6.25:** Comparison between (a, b) simulation and (c, d) experimental results (C15) via space-time varying responses and time-history displacements in (a, c, e) *X* and (b, d, f) *Y*: blue solid and red dashed lines denote results from model and experiment, respectively.

between the numerical and experimental results in case of C15 (Figures 6.25e, f), evident differences are realized in the oscillation patterns (Figures 6.25 a, b vs. c, d), where the formeris dominated by travelling waves and the latter follows standing-travelling waves. Comparing the oscillation patterns among the considered three cases, C15 seems to be a relatively more chaotic case than the others. Such strong unsteadiness from experiments is challenging for the numerical model, which is limited to steady-state slug flows, potentially resulting in evident theoretical-experimental discrepancies. Moreover, differences also exist with respect to $f_o$ although a good agreement of the main $f_o$ is reached between the test and the theoretical model. The riser responses turn to be quite chaotic with high intermittent frequency contents as informed by the FFT (Figure 6.17) and the wavelet analysis (Figure 6.20). In contrast, the numerical results present more steady and harmonic oscillations with little modulations,

signifying single-frequency-dominated responses throughout the time span. This is expected due to the model limitations as discussed. Also, according to the discussions on $L_u$ effects in Chapter 3, it is unsurprising to see that the large slug unit lengths ($L_u/L > 0.5$) applied in the current model tend to render a single-frequency SIV.

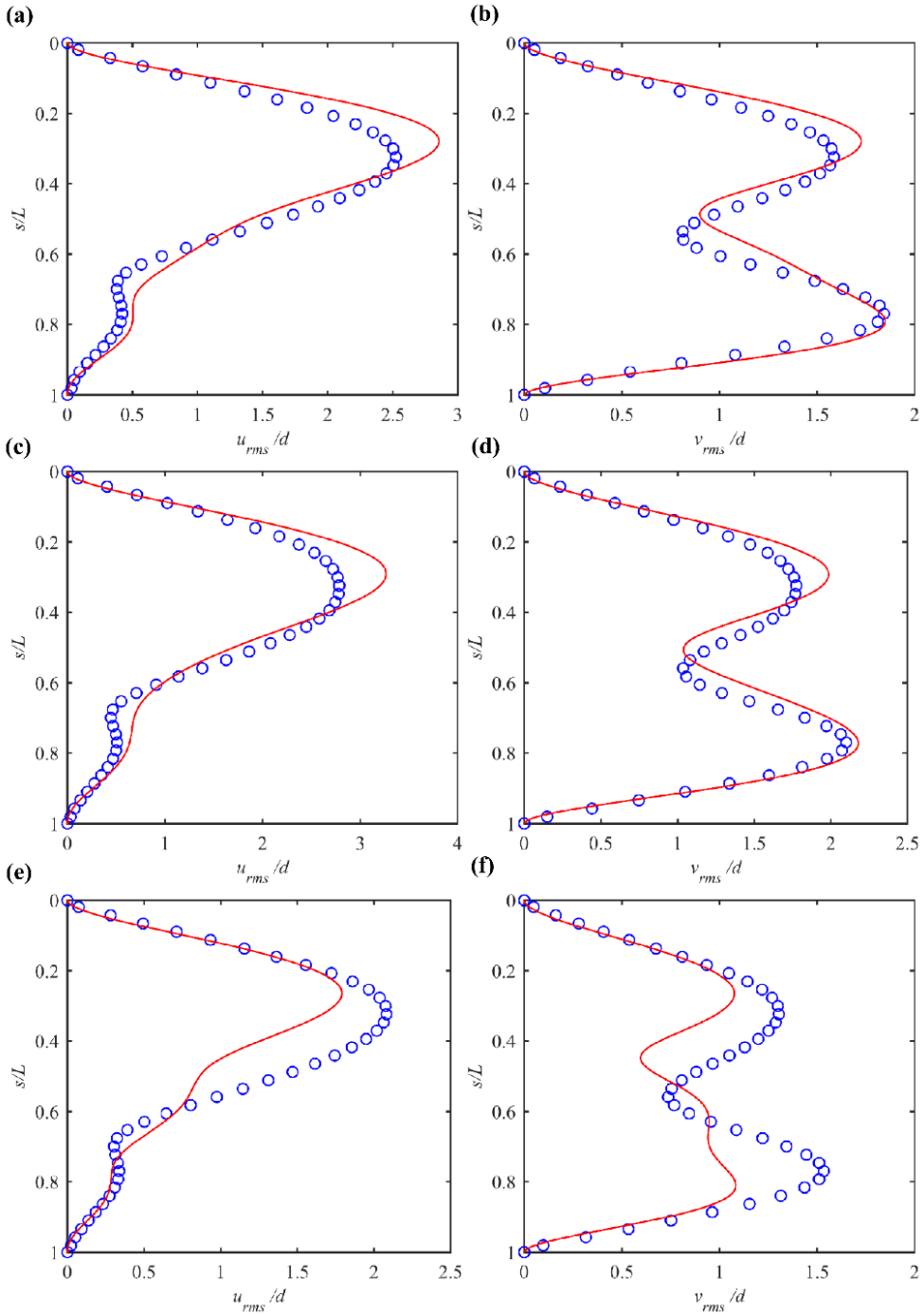


**Figure 6.26:** Comparison of (a, c, e) $u_{rms}$ and (b, d, f) $v_{rms}$: red line and circles denote numerical and experimental results, respectively.

In addition, as a better representation for the irregular oscillation, the associated spatial RMS displacements from the laboratory test and the simulation are compared and shown in

Figure 6.26. Though some differences are revealed between the numerical and experiment results, good qualitative and quantitative agreements are seen in both *X* (Figures 6.26a, c, e) and *Y* (Figures 6.26b, d, f), especially for C5 and C10. Numerical results demonstrate the same mode order as experimental observations and capture the locations of characteristic points with comparable magnitudes, indicating the overall satisfactory matches on RMS values. For instance, fairly good predictions of maxima are noted in *Y*, having a relative difference of only 0.32% and 3.6% for C5 and C10, respectively. Nevertheless, it is clear in C15 that the simulation results are less comparable to the measured ones than the other two cases, showing underestimated RMS values. As seen in the oscillation patterns (Figures 6.25a, b), the riser responses are dominated by travelling waves, which may imply a transition between the fundamental and the 2$^{nd}$ modes. Subsequently, the slightly overestimated mode order leads to the additional curvatures in the special RMS profiles (Figures 6.26e, f), which in turn render smaller magnitudes than the laboratory observations. Overall, by performing numerical-experimental comparisons for these limiting cases under different flow conditions, it is found that some important aspects are reasonably captured by the current numerical model, indicating its ability in predicting the slug flow-induced riser dynamics to a certain degree.

### 6.6 Summary

A small-scale laboratory test of a flexible pipe conveying gas-liquid flows has been conducted under various flow conditions to investigate SIV phenomena. A tube section made of silica gel with clamped ends was freely hanged for a catenary configuration in an air-water test loop. The pipe motions and the internal flow regimes were recorded at the same time by a digital imaging correlation and tracking technique using high-speed cameras. Meanwhile, the riser inlet and outlet pressures were measured through the pressure transducers. By varying gas-liquid flow rates, different flow regimes are observed. For relatively low ratios of gas to liquid superficial velocities, liquid-phase-dominated flows with small gas bubbles take place with resulting in negligible/small pipe motions, whereas the occurrence of slug flows is captured at high ratios, rendering pronounced SIV of the flexible pipe. Depending on the two-phase flow rates and the resultant superficial velocity ratios, slug flow characteristics are observed to vary significantly in terms of travelling velocities, slug unit lengths and slug frequencies, alongside unsteady SIV with modulated amplitudes.

Overall, the slug flows induce only in-plane vibrations, while out-of-plane ones are found negligible. Although mainly dominated by the fundamental mode across the considered cases, SIV is prone to possess multiple and time-varying oscillation frequencies. By increasing the gas-liquid superficial velocity ratios, amplified SIV is revealed up to 6.7*d* in the present study.

These are attributed to the intermittent and varying slug characteristics under different flow conditions. Unsteady slug flows are revealed with a wide range of slug lengths in each case, where longer slug unit lengths tend to result in larger SIV. For a specific liquid flow rate, a larger gas flow rate leads to faster and longer slug flows, which are accompanied by more pronounced riser responses. These phenomena have revealed the strong fluid-structure interaction. Through comparisons with experimental results from three limiting cases, the numerical model proposed in Chapter 3 has been validated with showing qualitative and quantitative agreements in riser vibration responses and frequencies.

# Chapter 7. Conclusions

The present thesis has investigated SIV of curved flexible pipes carrying slug flows by also involving external excitations from VIV. Numerical modelling approaches have been implemented for the two FIV scenarios individually and jointly, while SIV has also been experimentally explored. Numerical investigations have highlighted several important SIV features for the catenary riser, including the identification of individual role of the slug characteristics such as the slug unit length, translational velocity and frequency. This internal multiphase flow excitation has also been studied by a small-scale laboratory test, which sheds light on some SIV phenomena related to the unsteady slug flow conditions, the excited riser vibrations and the slug-pipe interactions. The SIV numerical model has been validated against in-house experimental results, manifesting abilities and limitations in the riser response prediction. The VIV effect is incorporated by adopting a phenomenological model of wake oscillators, which simulate the time-varying hydrodynamic forces coupled with the structural equations of motion. For an elastically-mounted rigid circular cylinder, several VIV features have been captured, serving as a preliminary study for the modelling application to a flexible riser subject to VIV. Numerical simulations in combined VIV and SIV cases have been performed under different internal and external flow conditions. Several pure-VIV aspects of flexible risers have been observed and discussed along with comparisons of VIV-SIV phenomena. A significant role of SIV in amplifying riser dynamic and static stresses in the presence of VIV has been revealed. The main contributions and outcomes are summarized as follows.

## 7.1 Slug Flow-Induced Vibration

- By accounting for the slug flow-induced forces including the space-time varying fluid weight, flow centrifugal and Coriolis effects, a planar dynamic model of an inclined curved bendable pipe conveying slug gas-liquid flows has been developed. Hydrodynamic steady slug flows have been considered and modelled by the mass-momentum balances of gas-liquid phases within an idealized slug unit cell. Depending on the pipe diameter, inclination, gas-liquid phase properties, superficial velocities and empirical functions, the approximation of phase fractions, local velocities and pressure variations have been obtained and employed as the time-varying, distributed parameters yielding SIV of a catenary pipe.
- The numerical model has been utilized for investigating SIV phenomena under different superficial gas-liquid velocities. Several features such as the slug flow-induced transient

drifts due to the entering masses, the mean displacements due to the combined slug weights and flow momenta, the tension changes due to a reconfiguration of pipe equilibrium and the steady-state SIV due to resonances have been revealed.

- Depending on the pipe inclination, slug unit length and translational velocity, the slug characteristic frequencies reveal several harmonic components which may trigger a multi-modal vibration of the flexible catenary riser. It is found that the slug translational velocity is a primary governing parameter enabling a transition from being a multi-mode SIV at a low velocity to a single-mode SIV at a high velocity. In the low velocity range, the single-mode SIV response may take place as the slug length increases.
- Planar SIV is found to be governed by an individual effect of the slug translational velocity and the slug unit length, regardless of the associated slug excitation frequency. To determine a critical SIV with maximum amplitudes of practical importance, the slug translational velocity should be parametrically varied for a given slug unit length, and vice versa. In some cases, a certain slug velocity-length combination may lead to a multiple resonant SIV involving two different excited modes switching intermittently along time.
- A small-scale experiment of a flexible pipe conveying liquid-gas flows has been conducted for a catenary configuration. Different flow regimes have been observed by varying the two-phase flow rates, which entail the dependence on the gas-liquid ratio of the slug flow formation. Actual physical tests reveal unsteady slug flows accompanied by a random-like SIV with modulated amplitudes and frequencies. Although mainly dominated by the fundamental planar mode, the riser responses at different locations possess multiple and time-varying oscillation frequencies.
- Strong interactions between the slug flow and the riser are experienced in the laboratory tests, and their correlations are analysed through comparing the pipe motions against the associated flow distributions. Depending on the gas-liquid superficial velocities, slug flow characteristics in terms of the travelling phase velocities, slug unit lengths and slug frequencies vary significantly in space and time. By increasing the gas-liquid superficial velocity ratios, amplified SIV responses have been remarked. It is found that a long slug unit length is responsible for a large SIV amplitude. For a specific liquid flow rate, a greater gas flow rate leads to a faster and longer unit slug flow strengthening the two-phase flow momentum forces. These reveal the interrelationship among the flow conditions, slug characteristics and pipe dynamics.
- Some aspects such as the individual effect of slug length and the multi-mode riser responses from numerical SIV investigations are qualitatively exhibited in the laboratory tests. The negligible out-of-plane riser vibration justifies the assumed modelling of planar SIV. Model

validation has been performed through comparing the numerical predictions of the three limiting cases for which a good agreement is justified in terms of the riser response displacements and frequencies.

### 7.2 Combined Vortex-Induced Vibration and Slug Flow-Induced Vibration

- A semi-empirical model based on wake oscillators has been applied and implemented for an elastically mounted rigid cylinder in uniform flows subject to cross-flow/in-line VIV. The dynamical system has been solved by a numerical-analytical approach and the results were compared with available experimental data. The model shows abilities in capturing several basic VIV features such as a lock-in range, amplitude jump, two-to-one resonant frequency and figure-of-eight trajectory. Additional investigation has been carried out by assessing the efficiency of linear and nonlinear damping in VIV active suppression.
- By distributing the van der Pol wake-oscillators along the structural span, the VIV numerical model has been applied to a long flexible riser. Numerical simulations have been carried out for cross-flow-only VIV in the case of straight and curved risers subject to uniform flows at various current velocities. For a curved riser, uniform flows are assumed to be perpendicular to the curvature plane. Some VIV features of flexible risers have been revealed. The order of the dominated structural vibration mode increases with the external flow velocities, showing a transition from standing- to travelling-wave patterns. Also, a linear modal analysis reveals a more pronounced multi-modal response at higher flow velocities.
- By comparing VIV-only and VIV-SIV scenarios, the prevailing role of VIV in the combined external-internal excitations and the significant effects from slug flows on VIV have been highlighted. Numerical results show that slug flows can lead to a modified VIV excitation mode with enhanced multimodal contributions. Through comparing the cases under various internal-external flow conditions, slug flows play a more significant role in the riser VIV response at a lower slug translational velocity or a higher external flow velocity. It is revealed that the combined VIV-SIV scenario results in greater dynamic and static stresses than those of the VIV-only scenario due to the slug flow-induced additional curvatures, mean drifts and enhanced multimode oscillations.

### 7.3 Recommendation for Future Research

There are several interesting research directions worthwhile for future investigations. Some suggestions are outlined as follows.

- Steady hydrodynamic slug flows have been numerically modelled and investigated in the present study. A further advancement of the proposed model to account for the unsteadiness (e.g. non-uniform slug length), intermittency (e.g. slug flow time-varying fluctuation) and dependence on riser dynamics (e.g. instantaneous time-space varying inclination), is recommended for developing towards a computationally efficient tool for a fully two-way coupled SIV of flexible pipes/risers. The structure model is presently limited to the linear riser dynamics. The importance of geometric nonlinearities has been revealed and addressed in some VIV studies, and therefore, it is worth investigating this aspect when considering SIV and three-dimensional VIV.
- Further research can be performed for coupled CF-IL VIV subject to different current profiles, e.g. uniform, linear and nonlinear sheared flows. Moreover, for combined internal-external flow excitations, it is recommended to consider other environmental factors such as wave, floater motion and heave-induced lateral motions, where the role of slug flow in riser responses may be distinctive. For numerical SIV studies, it is of interests to consider other structural configurations related to offshore applications, e.g. horizontal pipeline with free-spanning sections, M-shaped jumper and lazy-wave risers, where slug flow-induced forces and the resultant SIV may be different since slug flow characteristics are sensitive to the pipe geometry.
- Relatively large-scale experiments with a broader range of flow conditions are suggested. More detailed measurement in terms of riser dynamics (e.g. top-tension variation), detailed flow information (slug flow visualization and tracking) as well as the statistical slug parameter characterization is recommended. Experimental studies into combined SIV-VIV of flexible catenary risers are still lacking in the literature. In particular, VIV led by various flow directions, i.e. concave, convex and oblique flows, with respect to the riser plane requires further research.

# References


Al-Hashimy, Z.I., Al-Kayiem, H.H., Time, R.W., 2016. Experimental investigation on the vibration induced by slug flow in horizontal pipe. ARPN J. Eng. Appl. Sci 11, pp. 12134-12139.

Alexeyev, A.I., Filippov, Y.P., Mamedov, I.S., 1991. Flow patterns of two-phase helium in horizontal channels. Cryogenics 31, pp. 330-337.

Ansari, M.R., Nariai, H., 1989. Experimental investigation on wave initiation and slugging of air-water stratified flow in horizontal duct. Journal of Nuclear Science and Technology 26, pp. 681-688.

API-RP-1111, 2015. RECOMMENDED PRACTICE, Design, Construction, Operation, and Maintenance of Offshore Hydrocarbon Pipelines (Limit State Design).

Assi, G.R.S., Srinil, N., Freire, C.M., Korkischko, I., 2014. Experimental investigation of the flow-induced vibration of a curved cylinder in convex and concave configurations. Journal of Fluids and Structures 44, pp. 52-66.

Bai, X., Qin, W., 2014. Using vortex strength wake oscillator in modelling of vortex induced vibrations in two degrees of freedom. European Journal of Mechanics B/Fluids 48, pp. 165-173.

Baker, O., 1954. Simultaneous flow of oil and gas. Oil and Gas Journal 53, pp. 185-190.

Bakis, K., Srinil, N., 2019. Internal flow-induced instability analysis of catenary risers, in: Bensow, R., Ringsberg, J. (Eds.), The 8th Conference on Computational Methods in Marine Engineering (Marine 2019). (CIMNE), Gothenburg, pp. 1-12.

Barnea, D., 1990. Effect of bubble shape on pressure drop calculations in vertical slug flow. International Journal of Multiphase Flow 16, pp. 79-89.

Barnea, D., Shoham, O., Taitel, Y., Dukler, A.E., 1980. Flow pattern transition for gas-liquid flow in horizontal and inclined pipes. Comparison of experimental data with theory. International Journal of Multiphase Flow 6, pp. 217-225.

Baz, A., Ro, J., 1991. Active control of flow-induced vibrations of a flexible cylinder using direct velocity feedback. Journal of Sound and Vibration 146, pp. 33-45.

Bendiksen, K.H., 1984. An experimental investigation of the motion of long bubbles in inclined tubes. International Journal of Multiphase Flow 10, pp. 467-483.

Blevins, R.D., 1990. Flow-Induced Vibration. Van Nostrand Reinhold.

Bódai, T., Srinil, N., 2015. Performance analysis and optimization of a box-hull wave energy converter concept. Renewable energy 81, pp. 551-565.

Bonizzi, M., Andreussi, P., Banerjee, S., 2009. Flow regime independent, high resolution multi-field modelling of near-horizontal gas-liquid flows in pipelines. International Journal of Multiphase Flow 35, pp. 34-46.

Bordalo, S., Morooka, C.K., Cavalcante, C.C.P., Matt, C.G.C., Franciss, R., 2008. Whipping phenomenon caused by the internal flow momentum on the catenary risers of offshore petroleum fields, ASME 2008 27th International Conference on Offshore Mechanics and Arctic Engineering. American Society of Mechanical Engineers Digital Collection, pp. 315-323.

Bordalo, S.N., Morooka, C.K., 2018. Slug flow induced oscillations on subsea petroleum pipelines. Journal of Petroleum Science and Engineering 165, pp. 535-549.

Bossio, B.M., Blanco, A.J., Casanova, E.L., 2014. Numerical modeling of the dynamical interaction between slug flow and vortex induced vibration in horizontal submarine pipelines. Journal of Offshore Mechanics and Arctic Engineering-Transactions of the ASME 136.

Brennen, C.E., Brennen, C.E., 2005. Fundamentals of multiphase flow. Cambridge university press.

Brigham, E.O., 1988. The Fast Fourier Transform and Its Applications. Prentice Hall.

Cabrera-Miranda, J.M., Paik, J.K., 2019. Two-phase flow induced vibrations in a marine riser conveying a fluid with rectangular pulse train mass. Ocean Engineering 174, pp. 71-83.

Carneiro, J., Nieckele, A., 2007. Investigation of slug flow characteristics in inclined pipelines. Computational Methods in Multiphase Flow IV 56, pp. 185-194.

Chaplin, J.R., Bearman, P.W., Huarte, F.J.H., Pattenden, R.J., 2005. Laboratory measurements of vortex-induced vibrations of a vertical tension riser in a stepped current. Journal of Fluids and Structures 21, pp. 3-24.

Chaplin, J.R., King, R., 2018. Laboratory measurements of the vortex-induced vibrations of an untensioned catenary riser with high curvature. Journal of Fluids and Structures 79, pp. 26-38.

Chatjigeorgiou, I.K., 2017. Hydroelastic response of marine risers subjected to internal slug-flow. Applied Ocean Research 62, pp. 1-17.

Chen, S.-S., 1985. Flow-induced vibration of circular cylindrical structures. Argonne National Lab., IL (USA).

Cheng, L., Ribatski, G., Thome, J.R., 2008. Two-phase flow patterns and flow-pattern maps: fundamentals and applications. Applied Mechanics Reviews 61, p. 050802.

Cheng, L., Zhou, Y., Zhang, M.M., 2006. Controlled vortex-induced vibration on a fix-supported flexible cylinder in cross-flow. Journal of sound and vibration 292, pp. 279-299.

Chucheepsakul, S., Srinil, N., Petchpeart, P., 2003. A variational approach for three-dimensional model of extensible marine cables with specified top tension. Applied Mathematical Modelling 27, pp. 781-803.

Cohen, L.S., Hanratty, T.J., 1968. Effect of waves at a gas-liquid interface on a turbulent air flow. Journal of Fluid Mechanics 31, pp. 467-479.

Cook, M., Behnia, M., 1997. Film profiles behind liquid slugs in gas-liquid pipe flow. American Institute of Chemical Engineers Journal 43, pp. 2180-2186.

Dahl, J., Hover, F., Triantafyllou, M., 2006. Two-degree-of-freedom vortex-induced vibrations using a force assisted apparatus. Journal of Fluids and Structures 22, pp. 807-818.

Dahl, J.M., Hover, F.S., Triantafyllou, M.S., Oakley, O.H., 2010. Dual resonance in vortex-induced vibrations at subcritical and supercritical Reynolds numbers. Journal of Fluid Mechanics 643, pp. 395-424.

Dalheim, J., 2000. Numerical prediction of vortex-induced vibration on steel catenary risers, The Tenth International Offshore and Polar Engineering Conference. International Society of Offshore and Polar Engineers.

Danielson, T.J., 2012. Transient multiphase flow: past, present, and future with flow assurance perspective. Energy & Fuels 26, pp. 4137-4144.

DNVGL-RP-C205, 2017. RECOMMENDED PRACTICE, Environmental conditions and environmental loads.

DNVGL-RP-F105, 2017. RECOMMENDED PRACTICE, Free spanning pipelines.

DNVGL-RP-F204, 2017. RECOMMENDED PRACTICE, Riser fatigue.

DNVGL-ST-F201, 2018. STANDARD, Dynamic risers.

Domala, V., Sharma, R., 2018. An experimental study on vortex-induced vibration response of marine riser with and without semi-submersible. Proceedings of the Institution of Mechanical Engineers, Part M: Journal of Engineering for the Maritime Environment 232, pp. 176-198.

Dong, X., Shiri, H., 2019. The influence of nonlinear hysteretic seabed interaction on slug-induced stress oscillations in steel catenary risers. Applied Ocean Research 82, pp. 175-190.

Duns Jr, H., Ros, N.C.J., 1963. Vertical flow of gas and liquid mixtures in wells, 6th world petroleum congress. World Petroleum Congress.

Eaton, B.A., Knowles, C.R., Silberbrg, I.H., 1967. The prediction of flow patterns, liquid holdup and pressure losses occurring during continuous two-phase flow in horizontal pipelines. Journal of Petroleum technology 19, pp. 815-828.

Facchinetti, M.L., De Langre, E., Biolley, F., 2004. Coupling of structure and wake oscillators in vortex-induced vibrations. Journal of Fluids and structures 19, pp. 123-140.

Fan, Y.-t., Mao, H.-y., Guo, H.-y., Liu, Q.-h., Li, X.-m., 2015. Experimental investigation on vortex-induced vibration of steel catenary riser. China Ocean Engineering 29, pp. 691-704.

Fernandes, R.C., Semiat, R., Dukler, A.E., 1983. Hydrodynamic model for gas-liquid slug flow in vertical tubes. American Institute of Chemical Engineers Journal 29, pp. 981-989.

Filippov, Y.P., 1999. Characteristics of horizontal two-phase helium flows: Part I—flow patterns and void fraction. Cryogenics 39, pp. 59-68.

Furukawa, T., Fukano, T., 2001. Effects of liquid viscosity on flow patterns in vertical upward gas–liquid two-phase flow. International Journal of Multiphase Flow 27, pp. 1109-1126.

Fylling, I.J., Larsen, C.M., Sødahl, N., Ormberg, H., Engseth, A., Passano, E., Holthe, K., 1995. Riflex theory manual. SINTEF report no. STF70 F 95219, p. 53.

Gabbai, R.D., Benaroya, H., 2005. An overview of modeling and experiments of vortex-induced vibration of circular cylinders. Journal of Sound and Vibration 282, pp. 575-616.

Gallardo, J.P., Andersson, H.I., Pettersen, B., 2014. Turbulent wake behind a curved circular cylinder. Journal of Fluid Mechanics 742, pp. 192-229.

Gao, Y., Fu, S., Xiong, Y., Zhao, Y., Liu, L., 2017. Experimental study on response performance of vortex-induced vibration on a flexible cylinder. Ships and Offshore Structures 12, pp. 116-134.

GENESIS, http://www.genesisoilandgas.com. Accessed: 2019-09-18.

Ghajar, A.J., 2005. Non-boiling heat transfer in gas-liquid flow in pipes: a tutorial. Journal of the Brazilian Society of Mechanical Sciences and Engineering 27, pp. 46-73.

Govardhan, R.N., Williamson, C.H.K., 2006. Defining the 'modified Griffin plot'in vortex-induced vibration: revealing the effect of Reynolds number using controlled damping. Journal of fluid mechanics 561, pp. 147-180.

Govier, G.W., Omer, M.M., 1962. The horizontal pipeline flow of air ‐ water mixtures. The Canadian Journal of Chemical Engineering 40, pp. 93-104.

Gregory, G.A., Nicholson, M.K., Aziz, K., 1978. Correlation of the liquid volume fraction in the slug for horizontal gas-liquid slug flow. International Journal of Multiphase Flow 4, pp. 33-39.

Greskovich, E.J., Shrier, A.L., 1971. Pressure drop and holdup in horizontal slug flow. American Institute of Chemical Engineers Journal 17, pp. 1214-1219.

Halse, K.H., Mo, K., Lie, H., 1999. Vortex induced vibrations of a catenary riser, In proceedings of 3rd International Symposium on Cable Dynamics, Trondheim.

Hand, N.P., Spedding, P.L., 1993. Horizontal gas-liquid flow at close to atmospheric conditions. Chemical engineering science 48, pp. 2283-2305.

Hara, F., 1973. A theory on the two-phase flow induced vibrations in piping systems. Transactions of the 2nd International Conference on Structural Mechanics in Reactor Technology, Paper No. F5/15.

Hara, F., 1977. Two-phase-flow-induced vibrations in a horizontal piping system. Bulletin of JSME 20, pp. 419-427.

Harmathy, T.Z., 1960. Velocity of large drops and bubbles in media of infinite or restricted extent. American Institute of Chemical Engineers Journal 6, pp. 281-288.

Hartlen, R.T., Currie, I.G., 1970. Lift-oscillator model of vortex-induced vibration. Journal of the Engineering Mechanics Division 96, pp. 577-591.

Hasan, A.R., Kabir, C.S., 1992. Two-phase flow in vertical and inclined annuli. International Journal of Multiphase Flow 18, pp. 279-293.

Hewitt, G.F., Roberts, D.N., 1969. Studies of two-phase flow patterns by simultaneous x-ray and flast photography. Atomic Energy Research Establishment, Harwell, England (United Kingdom).

Hoogendoorn, C.J., 1959. Gas-liquid flow in horizontal pipes. Chemical Engineering Science 9, pp. 205-217.

Hoogendoorn, C.J., Buitelaar, A.A., 1961. The effect of gas density and gradual vaporization on gas-liquid flow in horizontal pipes. Chemical Engineering Science 16, pp. 208-221.

Huang, K., Chen, H.-C., Chen, C.-R., 2010. Flexible catenary riser VIV simulation in uniform current, The Twentieth International Offshore and Polar Engineering Conference. International Society of Offshore and Polar Engineers.

Huse Knudsen, T., Sævik, S., Thorsen, M.J., 2016. Numerical Analysis of Combined VIV and Slug Flow in Time Domain, ASME 2016 35th International Conference on Ocean, Offshore and Arctic Engineering.

Inman, D.J., 2006. Vibration with Control. Wiley.

Ishii, M., 1977. One-dimensional drift-flux model and constitutive equations for relative motion between phases in various two-phase flow regimes. Argonne National Lab., Ill.(USA).

Ishii, M., Hibiki, T., 2010. Thermo-fluid dynamics of two-phase flow. Springer Science & Business Media.

Issa, R.I., Kempf, M.H.W., 2003. Simulation of slug flow in horizontal and nearly horizontal pipes with the two-fluid model. International Journal of Multiphase Flow 29, pp. 69-95.

Jauvtis, N., Williamson, C., 2004. The effect of two degrees of freedom on vortex-induced vibration at low mass and damping. Journal of Fluid Mechanics 509, pp. 23-62.

Kaneko, S., Nakamura, T., Inada, F., Kato, M., Ishihara, K., Nishihara, T., Mureithi, N.W., Langthjem, M.A., 2013. Flow-induced vibrations: classifications and lessons from practical experiences. Butterworth-Heinemann.

Kaya, A.S., Sarica, C., Brill, J.P., 1999. Comprehensive mechanistic modeling of two-phase flow in deviated wells, SPE Annual Technical Conference and Exhibition, Houston, Texas.

Kim, J., Srinil, N., 2018. 3-D Numerical simulations of subsea jumper transporting intermittent slug flows, ASME 2018 37th International Conference on Ocean, Offshore and Arctic Engineering, pp. OMAE2018-77299.

Kovacic, I., Brennan, M.J., 2011. The Duffing Equation: Nonlinear Oscillators and Their Behaviour. Wiley-Blackwell.

Kurushina, V., Pavlovskaia, E., Postnikov, A., Wiercigroch, M., 2018. Calibration and comparison of VIV wake oscillator models for low mass ratio structures. International Journal of Mechanical Sciences 142, pp. 547-560.

Larsen, C.M., Passano, E., 2006. Time and frequency domain analysis of catenary risers subjected to vortex induced vibrations, 25th International Conference on Offshore Mechanics and Arctic Engineering. American Society of Mechanical Engineers Digital Collection, pp. 121-129.

Larsen, C.M., Vikestad, K., Yttervik, R., Passano, E., Baarholm, G.S., 2001. VIVANA theory manual. Marintek, Trondheim, Norway.

Lee, S.I., Chung, J., 2002. New non-linear modelling for vibration analysis of a straight pipe conveying fluid. Journal of Sound and Vibration 254, pp. 313-325.

Liang, F., Zheng, H., Yu, H., Sun, Y., 2016. Gas–liquid two-phase flow pattern identification by ultrasonic echoes reflected from the inner wall of a pipe. Measurement Science and Technology 27, p. 035304.

Lie, H., Kaasen, K.E., 2006. Modal analysis of measurements from a large-scale VIV model test of a riser in linearly sheared flow. Journal of fluids and structures 22, pp. 557-575.

Lie, H., Larsen, C.M., Tveit, Ø., 2001. Vortex induced vibration analysis of catenary risers, Offshore Technology Conference. Offshore Technology Conference.

Lin, P.Y., Hanratty, T.J., 1987. Effect of pipe diameter on flow patterns for air-water flow in horizontal pipes. International journal of multiphase flow 13, pp. 549-563.

Liu, G., Wang, Y., 2018. Study on the natural frequencies of pipes conveying gas-liquid two-phase slug flow. International Journal of Mechanical Sciences 141, pp. 168-188.

Low, Y.M., Srinil, N., 2016. VIV fatigue reliability analysis of marine risers with uncertainties in the wake oscillator model. Engineering Structures 106, pp. 96-108.

Ma, B., Srinil, N., 2018. Dynamic characteristics of deep-water risers carrying multiphase flows, ASME 2018 37th International Conference on Ocean, Offshore and Arctic Engineering, pp. OMAE2018-77381.

Mandhane, J.M., Gregory, G.A., Aziz, K., 1974. A flow pattern map for gas-liquid flow in horizontal pipes. International Journal of Multiphase Flow 1, pp. 537-553.

Maribus, 2014. World ocean review 3: Marine Resources - Opportunities and Risks.

Matsui, G., 1984. Identification of flow regimes in vertical gas-liquid two-phase flow using differential pressure fluctuations. International journal of multiphase flow 10, pp. 711-719.

Mehmood, A., Abdelkefi, A., Akhtar, I., Nayfeh, A., Nuhait, A., Hajj, M., 2014. Linear and nonlinear active feedback controls for vortex-induced vibrations of circular cylinders. Journal of Vibration and Control 20, pp. 1137-1147.

Meléndez, J.A.V., Julca, J.P.A., 2019. A parametric analysis of the influence of the internal slug flow on the dynamic response of flexible marine risers. Ocean Engineering 174, pp. 169-185.

Miliou, A., Sherwin, S.J., Graham, J.M.R., 2003. Fluid dynamic loading on curved riser pipes. Transactions-ASME Journal of Offshore Mechanics and Arctic Engineering 125, pp. 176-182.

Miwa, S., Mori, M., Hibiki, T., 2015. Two-phase flow induced vibration in piping systems. Progress in Nuclear Energy 78, pp. 270-284.

Moe, G., Chucheepsakul, S., 1988. The effect of internal flow on marine risers, Proceedings 7th International Offshore Mechanics and Arctic Engineering Symposium. American Society of Mechanical Engineers, Houston, TX, pp. 266–280.

Mohmmed, A.O., Al-Kayiem, H.H., Nasif, M.S., Time, R.W., 2019. Effect of slug flow frequency on the mechanical stress behavior of pipelines. International Journal of Pressure Vessels and Piping 172, pp. 1-9.

Monette, C., Pettigrew, M.J., 2004. Fluidelastic instability of flexible tubes subjected to two-phase internal flow. Journal of Fluids and Structures 19, pp. 943-956.

Monprapussorn, T., Athisakul, C., Chucheepsakul, S., 2007. Nonlinear vibrations of an extensible flexible marine riser carrying a pulsatile flow. Journal of Applied Mechanics 74, pp. 754-769.

Montoya-Hernández, D.J., Vázquez-Hernández, A.O., Cuamatzi, R., Hernandez, M.A., 2014. Natural frequency analysis of a marine riser considering multiphase internal flow behavior. Ocean Engineering 92, pp. 103-113.

Morooka, C.K., Tsukada, R.I., 2013. Experiments with a steel catenary riser model in a towing tank. Applied Ocean Research 43, pp. 244-255.

Mukherjee, H., Brill, J.P., 1985. Pressure drop correlations for inclined two-phase flow. Journal of energy resources technology 107, pp. 549-554.

Nayfeh, A.H., 1993. Introduction to Perturbation Techniques. Wiley.

Nydal, O.J., 2012. Dynamic models in multiphase flow. Energy & Fuels 26, pp. 4117-4123.

Nydal, O.J., Banerjee, S., 1996. Dynamic slug tracking simulations for gas-liquid flow in pipelines. Chemical Engineering Communications 141, pp. 13-39.

Omebere-Iyari, N.K., Azzopardi, B.J., 2007. A study of flow patterns for gas/liquid flow in small diameter tubes. Chemical Engineering Research and Design 85, pp. 180-192.

Orcina, 2016. OrcaFlex User Manual. Version 10.1b.

Ortega, A., 2015. Dynamic response of flexible risers due to unsteady slug flow. Ph. D. thesis, Norwegian University of Science and Technology, Trondheim, Norway.

Ortega, A., Rivera, A., Larsen, C.M., 2018. Slug flow and waves induced motions in flexible riser. Journal of Offshore Mechanics and Arctic Engineering 140.

Ortiz-Vidal, L.E., Mureithi, N.W., Rodriguez, O.M.H., 2017. Vibration response of a pipe subjected to two-phase flow: Analytical formulations and experiments. Nuclear Engineering and Design 313, pp. 214-224.

Ouyang, L.-B., Aziz, K., 2000. A homogeneous model for gas-liquid flow in horizontal wells. Journal of Petroleum Science and Engineering 27, pp. 119-128.

Paidoussis, M.P., 2014. Fluid-Structure Interactions. Volume 1, Slender Structures and Axial Flow, Second ed. Amsterdam : Academic Press.

Païdoussis, M.P., Luu, T.P., 1985. Dynamics of a pipe aspirating fluid such as might be used in ocean mining. Transactions of the ASME. Journal of Energy Resources Technology 107, pp. 250-255.

Patel, M.H., Seyed, F.B., 1989. Internal flow-induced behaviour of flexible risers. Engineering Structures 11, pp. 266-280.

Pesce, C.P., Franzini, G.R., Fujarra, A.L.C., Gonçalves, R.T., Salles, R., Mendes, P., 2017. Further Experimental Investigations on Vortex Self-Induced Vibrations (VSIV) With a Small-

Scale Catenary Riser Model, ASME 2017 36th International Conference on Ocean, Offshore and Arctic Engineering. American Society of Mechanical Engineers Digital Collection.

Petalas, N., Aziz, K., 1998. A mechanistic model for multiphase flow in pipes, Annual Technical Meeting. Petroleum Society of Canada.

Pollio, A., Mossa, M., 2009. A Comparison between Two Simple Models of a Slug Flow in a Long Flexible Marine Riser. ARXIV, Physics – Fluid Dynamics, 0911.1873.

Qin, B., Alam, M.M., Zhou, Y., 2019. Free vibrations of two tandem elastically mounted cylinders in crossflow. Journal of Fluid Mechanics 861, pp. 349-381.

Rouhani, S.Z., Sohal, M.S., 1983. Two-phase flow patterns: A review of research results. Progress in Nuclear Energy 11, pp. 219-259.

Rozenblit, R., Gurevich, M., Lengel, Y., Hetsroni, G., 2006. Flow patterns and heat transfer in vertical upward air–water flow with surfactant. International Journal of Multiphase Flow 32, pp. 889-901.

Safrendyo, S., Srinil, N., 2018. Slug flow-induced oscillation in subsea catenary riser experiencing VIV, ASME 2018 37th International Conference on Ocean, Offshore and Arctic Engineering, pp. OMAE2018-77298.

Sarpkaya, T., 2004. A critical review of the intrinsic nature of vortex-induced vibrations. Journal of Fluids and Structures 19, pp. 389-447.

Seyed-Aghazadeh, B., Budz, C., Modarres-Sadeghi, Y., 2015. The influence of higher harmonic flow forces on the response of a curved circular cylinder undergoing vortex-induced vibration. Journal of Sound and Vibration 353, pp. 395-406.

Seyed, F.B., Patel, M.H., 1992. Mathematics of flexible risers including pressure and internal flow effects. Marine Structures 5, pp. 121-150.

SINTEF, https://www.sintef.no/en. Accessed: 2019-09-18.

Skop, R.A., Balasubramanian, S., 1997. A new twist on an old model for vortex-excited vibrations. Journal of Fluids and Structures 11, pp. 395-412.

Song, J.-n., Lu, L., Teng, B., Park, H.-i., Tang, G.-q., Wu, H., 2011. Laboratory tests of vortex-induced vibrations of a long flexible riser pipe subjected to uniform flow. Ocean Engineering 38, pp. 1308-1322.

Sparks, C.P., 1984. The influence of tension, pressure and weight on pipe and riser deformations and stresses. Journal of Energy Resources Technology 106, pp. 46-54.

Sparks, C.P., 2007. Fundamentals of marine riser mechanics: basic principles and simplified analyses. PennWell Books.

Spedding, P.L., Chen, J.J.J., 1981. A simplified method of determining flow pattern transition of two-phase flow in a horizontal pipe. International Journal of Multiphase Flow 7, pp. 729-731.

Spedding, P.L., Hand, N.P., 1997. Prediction in stratified gas-liquid co-current flow in horizontal pipelines. International Journal of Heat and Mass Transfer 40, pp. 1923-1935.

Spedding, P.L., Nguyen, V.T., 1980. Regime maps for air water two phase flow. Chemical Engineering Science 35, pp. 779-793.

Srinil, N., 2010. Multi-mode interactions in vortex-induced vibrations of flexible curved/straight structures with geometric nonlinearities. Journal of Fluids and Structures 26, pp. 1098-1122.

Srinil, N., 2011. Analysis and prediction of vortex-induced vibrations of variable-tension vertical risers in linearly sheared currents. Applied Ocean Research 33, pp. 41-53.

Srinil, N., Ma, B., Zhang, L., 2018a. Experimental investigation on in-plane/out-of-plane vortex-induced vibrations of curved cylinder in parallel and perpendicular flows. Journal of Sound and Vibration 421, pp. 275-299.

Srinil, N., Opinel, P.-A., Tagliaferri, F., 2018b. Empirical sensitivity of two-dimensional nonlinear wake–cylinder oscillators in cross-flow/in-line vortex-induced vibrations. Journal of Fluids and Structures 83, pp. 310-338.

Srinil, N., Rega, G., Chucheepsakul, S., 2003. Large amplitude three-dimensional free vibrations of inclined sagged elastic cables. Nonlinear Dynamics 33, pp. 129-154.

Srinil, N., Rega, G., Chucheepsakul, S., 2004. Three-dimensional non-linear coupling and dynamic tension in the large-amplitude free vibrations of arbitrarily sagged cables. Journal of Sound and Vibration 269, pp. 823-852.

Srinil, N., Rega, G., Chucheepsakul, S., 2007. Two-to-one resonant multi-modal dynamics of horizontal/inclined cables. Part I: Theoretical formulation and model validation. Nonlinear Dynamics 48, pp. 231-252.

Srinil, N., Wiercigroch, M., O'Brien, P., 2009. Reduced-order modelling of vortex-induced vibration of catenary riser. Ocean Engineering 36, pp. 1404-1414.

Srinil, N., Zanganeh, H., 2012. Modelling of coupled cross-flow/in-line vortex-induced vibrations using double Duffing and van der Pol oscillators. Ocean Eng. 53, pp. 83-97.

Srinil, N., Zanganeh, H., Day, A., 2013. Two-degree-of-freedom VIV of circular cylinder with variable natural frequency ratio: Experimental and numerical investigations. Ocean Engineering 73, pp. 179-194.

Stanislav, J.F., Kokal, S., Nicholson, M.K., 1986. Intermittent gas-liquid flow in upward inclined pipes. International journal of multiphase flow 12, pp. 325-335.

Sumer, B.M., Fredsøe, J., 2006. Hydrodynamics Around Cylindrical Structures. World Scientific Publishing, London.

Taitel, Y., Barnea, D., 1990. Two-Phase Slug Flow. Advances in Heat Transfer 20, pp. 83-132.

Taitel, Y., Bornea, D., Dukler, A.E., 1980. Modelling flow pattern transitions for steady upward gas - liquid flow in vertical tubes. AIChE Journal 26, pp. 345-354.

Taitel, Y., Dukler, A.E., 1976. A model for predicting flow regime transitions in horizontal and near horizontal gas-liquid flow. American Institute of Chemical Engineers Journal 22, pp. 47-55.

Thorsen, M.J., Challabotla, N.R., Sævik, S., Nydal, O.J., 2019. A numerical study on vortex-induced vibrations and the effect of slurry density variations on fatigue of ocean mining risers. Ocean Engineering 174, pp. 1-13.

Tognarelli, M.A., Slocum, S.T., Frank, W.R., Campbell, R.B., 2004. VIV response of a long flexible cylinder in uniform and linearly sheared currents, Offshore technology conference. Offshore Technology Conference.

Tsukada, R.I., Morooka, C.K., 2016. A numerical procedure to calculate the VIV response of a catenary riser. Ocean Engineering 122, pp. 145-161.

Van Hout, R., Shemer, L., Barnea, D., 2003. Evolution of hydrodynamic and statistical parameters of gas–liquid slug flow along inclined pipes. Chemical Engineering Science 58, pp. 115-133.

Vaze, M.J., Banerjee, J., 2012. Prediction of liquid height for onset of slug flow. The Canadian Journal of Chemical Engineering 90, pp. 1295-1303.

Vieiro, J., Ita, E.I., Nydal, O.J., 2015. Two-way fluid-structure interaction in a flexible pipe conveying gas-liquid slug flow, OTC Brasil.

Vince, M.A., Lahey, R.T., Commission, U.S.N.R., Rensselaer Polytechnic, I., 1980. Flow regime identification and void fraction measurement techniques in two-phase flow. The Commission : Available from GPO Sales Program, Division of Technical Information and Document Control, U.S. Nuclear Regulatory Commission ; National Technical Information Service, Washington, D.C. : Springfield, Va.

Wallis, G.B., 1969. One-Dimensional Two-Phase Flow. McGraw-Hill.

Wang, J., Fu, S., Baarholm, R., Wu, J., Larsen, C.M., 2015. Out-of-plane vortex-induced vibration of a steel catenary riser caused by vessel motions. Ocean Engineering 109, pp. 389-400.

Wang, J., Fu, S., Larsen, C.M., Baarholm, R., Wu, J., Lie, H., 2017. Dominant parameters for vortex-induced vibration of a steel catenary riser under vessel motion. Ocean Engineering 136, pp. 260-271.

Wang, L., Yang, Y., Li, Y., Wang, Y., 2018. Dynamic behaviours of horizontal gas-liquid pipes subjected to hydrodynamic slug flow: Modelling and experiments. International Journal of Pressure Vessels and Piping 161, pp. 50-57.

Weisman, J., Duncan, D., Gibson, J., Crawford, T., 1979. Effects of fluid properties and pipe diameter on two-phase flow patterns in horizontal lines. International Journal of Multiphase Flow 5, pp. 437-462.

Weisman, J., Kang, S.Y., 1981. Flow pattern transitions in vertical and upwardly inclined lines. International Journal of Multiphase Flow 7, pp. 271-291.

Wu, X., Ge, F., Hong, Y., 2012. A review of recent studies on vortex-induced vibrations of long slender cylinders. Journal of Fluids and Structures 28, pp. 292-308.

Xiao, J.J., Shonham, O., Brill, J.P., 1990. A comprehensive mechanistic model for two-phase flow in pipelines, SPE Annual Technical Conference and Exhibition.

Yadigaroglu, G., Hewitt, G.F., 2017. Introduction to multiphase flow: basic concepts, applications and modelling. Springer.

Zaldivar, M., 2014. Quantification of Flow Rate during Slug Flow, SPEI Flow Assurance Technical Section.

Zanganeh, H., Srinil, N., 2014. Characterization of variable hydrodynamic coefficients and maximum responses in two-dimensional vortex-induced vibrations with dual resonances. Journal of Vibration and Acoustics 136, p. 051010.

Zanganeh, H., Srinil, N., 2016. Three-dimensional VIV prediction model for a long flexible cylinder with axial dynamics and mean drag magnifications. Journal of Fluids and Structures 66, pp. 127-146.

Zhang, H.-Q., Wang, Q., Sarica, C., Brill, J.P., 2003. A unified mechanistic model for slug liquid holdup and transition between slug and dispersed bubble flows. International Journal of Multiphase Flow 29, pp. 97-107.

Zhang, M.M., Cheng, L., Zhou, Y., 2004. Closed-loop-controlled vortex shedding and vibration of a flexibly supported square cylinder under different schemes. Physics of Fluids 16, pp. 1439-1448.

Zheng, G., Brill, J.P., Taitel, Y., 1994. Slug flow behavior in a hilly terrain pipeline. International journal of multiphase flow 20, pp. 63-79.

Zhu, H.-j., Zhao, H.-l., Gao, Y., 2018a. Experimental investigation of vibration response of a free-hanging flexible riser induced by internal gas-liquid slug flow. China Ocean Engineering 32, pp. 633-645.

Zhu, H., Gao, Y., Zhao, H., 2018b. Experimental investigation on the flow-induced vibration of a free-hanging flexible riser by internal unstable hydrodynamic slug flow. Ocean Engineering 164, pp. 488-507.

Zhu, H., Gao, Y., Zhao, H., 2019a. Experimental investigation of slug flow-induced vibration of a flexible riser. Ocean Engineering 189, p. 106370.

Zhu, H., Lin, P., Gao, Y., 2019b. Vortex-induced vibration and mode transition of a curved flexible free-hanging cylinder in exponential shear flows. Journal of Fluids and Structures 84, pp. 56-76.

Zhu, H., Zhou, D., Bao, Y., Wang, R., Lu, J., Fan, D., Han, Z., 2018c. Wake characteristics of stationary catenary risers with different incoming flow directions. Ocean Engineering 167, pp. 142-155.

Zhuang, X., Gong, M., Chen, G., Zou, X., Shen, J., 2016. Two-phase flow pattern map for R170 in a horizontal smooth tube. International Journal of Heat and Mass Transfer 102, pp. 1141-1149.

Zuber, N., Findlay, J., 1965. Average volumetric concentration in two-phase flow systems. Journal of Heat Transfer 87, pp. 453-468.